# Networks of influence: Water mediated hydrogen bond networks at anionic lipid interfaces and Hv1 proton channel

---

**Dissertation**

zur Erlangung des Grades eines Doktors der Naturwissenschaften

(doctor rerum naturalium)

am Fachbereich Physik

der Freien Universität Berlin vorgelegt von

Honey Jain

Berlin 2023

Erstgutachterin: Prof. Dr. Ana-Nicoleta Bondar
Zweitgutachter: Prof. Dr. Roland Netz
Tag der Disputation: March 11, 2024

# Abstract

Dynamic hydrogen-bonds (H-bonds) and H-bond networks govern essential biomolecular process. From providing conformational flexibility needed for the functioning of proteins, governing the fluidity, stability and permeability of cell membranes to serving as proton transfer pathways, H-bonds are observed abundantly in nature. It is thus crucial to understand the dynamics of H-bond networks in biological systems to guide drug discovery. In this thesis, I focus on characterizing and identifying the dynamic H-bond networks in mainly two biomolecular systems - (i) lipid membranes containing anionic lipids and (ii) Human voltage gated proton channel Hv1. I use atomistic molecular dynamics simulations along with graph theory based approach for efficient computations of dynamic H-bonds and H-bond networks of proteins and lipid membranes.

At the lipid bilayer interface, dynamic H-bonding can give rise to local lipid clusters of interest for reactions. The dynamics of these H-bonded lipid clusters can depend on the nature of lipid headgroups. To dive deeper into role of lipid headgroups in H-bonded lipid clusters, I use a previously developed graph theory based approach to analyze the topology of lipid clusters in zwitterionic and anionic lipid membranes including bacterial cell membranes. To understand the dynamics of anionic membranes, I further do a topology analysis of bilayers of phosphatidylserine containing varying concentrations of cholesterol. I find that presence of cholesterol can hinder the formation of extended water-mediated H-bond networks in phosphatidylserine membranes.

H-bond networks formed by clusters of carboxylate and histidine protein sidechains or anionic lipid headgroups can form pathways for proton transfer across and along the lipid membranes. To understand the functioning mechanism of proton transporters, it is crucial to identify and characterize these proton-binding clusters and the H-bond pathways between them. To this aim, I developed a graph theory based protocol to find the most frequently sampled water-mediated H-bond paths formed by titratable sidechains of transmembrane proteins and/or lipid headgroups. I implement this protocol to identify potential proton antennas of the human voltage gated proton channel Hv1. The functioning of Hv1 is regulated by a network of H-bonds formed between the titratable sidechains of the transmembrane protein. How does the pH and lipid composition of the membrane affects the H-bond network of Hv1 remains an open question. I apply the newly developed protocol to study the protonation-coupled and lipid-coupled H-bond dynamics of Hv1. I find that depending on the location of the protonated carboxylate or histidine, the H-bond network extends or collapses on either the intracellular or extracellular side. A continuous H-bond network spanning the proton channel is sampled only in phosphatidylserine bilayer in contrast to bacterial and zwitterionic bilayers. This suggest the role of lipid composition in regulating the H-bond network dynamics of Hv1. In this thesis, I also present the work done towards characterizing the impact of Hv1 inhibitors on H-bond networks of Hv1.

# Zusammenfassung

Dynamische Wasserstoffbrückenbindungen (H-Bindungen) und H-Bindungsnetze bestimmen wesentliche biomolekulare Prozesse. Von der Bereitstellung der für das Funktionieren von Proteinen erforderlichen konformativen Flexibilität über die Steuerung der Fluidität, Stabilität und Permeabilität von Zellmembranen bis hin zur Funktion als Protonenübertragungswege sind H-Bindungen in der Natur weit verbreitet. Es ist daher von entscheidender Bedeutung, die Dynamik von H-Bindungsnetzwerken in biologischen Systemen zu verstehen, um die Entwicklung von Medikamenten zu unterstützen. In dieser Arbeit konzentriere ich mich auf die Charakterisierung und Identifizierung der dynamischen H-Bindungsnetzwerke in hauptsächlich zwei biomolekularen Systemen - (i) Lipidmembranen, die anionische Lipide enthalten, und (ii) dem menschlichen spannungsgesteuerten Protonenkanal Hv1. Ich verwende atomistische Molekulardynamiksimulationen zusammen mit einem auf der Graphentheorie basierenden Ansatz zur effizienten Berechnung der dynamischen H-Bindungen und H-Bindungsnetzwerke von Proteinen und Lipidmembranen.

An der Grenzfläche von Lipiddoppelschichten können durch dynamische H-Bindungen lokale Lipidcluster entstehen, die für Reaktionen von Interesse sind. Die Dynamik dieser H-gebundenen Lipidcluster kann von der Art der Lipid-Kopfgruppen abhängen. Um die Rolle der Lipid-Kopfgruppen in H-gebundenen Lipidclustern zu ergründen, verwende ich einen zuvor entwickelten, auf der Graphentheorie basierenden Ansatz zur Analyse der Topologie von Lipidclustern in zwitterionischen und anionischen Lipidmembranen, einschließlich bakterieller Zellmembranen. Um die Dynamik anionischer Membranen zu verstehen, führe ich außerdem eine topologische Analyse von Phosphatidylserin-Doppelschichten mit unterschiedlichen Cholesterin-Konzentrationen durch. Ich stelle fest, dass das Vorhandensein von Cholesterin die Bildung ausgedehnter wasservermittelter H-Bindungsnetzwerke in Phosphatidylserinmembranen behindern kann.

H-Bindungsnetzwerke, die von Clustern aus Carboxylat- und Histidin-Protein-Seitenketten oder anionischen Lipid-Kopfgruppen gebildet werden, können Wege für den Protonentransfer durch und entlang der Lipidmembranen bilden. Um die Funktionsweise von Protonentransportern zu verstehen, ist es entscheidend, diese protonenbindenden Cluster und die H-Bindungswege zwischen ihnen zu identifizieren und zu charakterisieren. Zu diesem Zweck habe ich ein auf der Graphentheorie basierendes Protokoll entwickelt, um die am häufigsten untersuchten wasservermittelten H-Bindungswege zu finden, die von titrierbaren Seitenketten von Transmembranproteinen und/oder Lipid-Kopfgruppen gebildet werden. Ich wende dieses Protokoll an, um potenzielle Protonenantennen des menschlichen spannungsgesteuerten Protonenkanals Hv1 zu identifizieren, dessen Funktion durch ein Netzwerk von H-Bindungen zwischen den titrierbaren Seitenketten des Transmembranproteins gesteuert wird. Wie der pH-Wert und die Lipidzusammensetzung der Membran das H-Bindungsnetzwerk von Hv1 beeinflussen, bleibt eine offene Frage. Ich wende das neu entwickelte Protokoll an, um die protonations- und lipidgekoppelte H-Bindungsdynamik von Hv1 zu untersuchen. Ich stelle fest, dass sich das H-Bindungsnetzwerk je nach Lage des protonierten Carboxylats oder Histidins entweder auf der intrazellulären oder extrazellulären Seite ausdehnt oder zusammenbricht. Ein kontinuierliches H-Bindungsnetzwerk, das den Protonenkanal überspannt, wird nur in Phosphatidylserin-Doppelschichten beobachtet, im Gegensatz zu bakteriellen und zwitterionischen Doppelschichten. Dies deutet auf die Rolle der Lipidzusammensetzung bei der Regulierung der Dynamik des H-Bindungsnetzwerks von Hv1 hin. In dieser Arbeit stelle ich auch die Arbeiten vor, die zur Charakterisierung der Auswirkungen von Hv1-Inhibitoren auf die H-Bindungsnetzwerke von Hv1 durchgeführt wurden.

# Acknowledgement

I express my immense gratitude to my supervisor Prof. Dr. Ana-Nicoleta Bondar for guiding and supporting me through out the doctoral project. I received her support in every aspect from funding the project, relocation, doctoral study courses, training, seminars and conferences, presentations, manuscript writing to this dissertation writing. This research work was funded by the European Union's Horizon 2020 Research and Innovation Program under the Marie Sklodowska-Curie grant agreement No H2020 MSCA-ITN-2019-860592, Innovative Training Network 'Proton and proton-coupled transport' (to Ana-Nicoleta Bondar). I am very grateful for her time and consideration that made this dissertation possible.

I would like to express my gratitude to my co-supervisor Prof. Roland Netz for his support and guidance during the relocation process. I thank my internship supervisors Prof. Noam Agmon from Hebrew University of Jeruselam and Dr. Aniket Magarkar from Boehringer Ingelheim for the opportunity to work on exciting projects and their guidance and support during the internships. During my doctoral project and especially during the relocation process from Berlin to Bucharest, I received great help from Prof. Peter Pohl and Dr. Denis Kynazev from the ITN PROTON network, Dr. Iulian Costache and the Academic Diaspora Platform, Ms. Filuta Ionita from University of Bucharest and Ms. Endrias Sieglinde from Freie University Berlin. I am very grateful to them for making this dissertation possible. For outstanding technical support and computational resources, I would like to thank Dr. Christian Tuma of the North-German Super Computing Alliance HLRN, Dr. Loris Bennett, Dr. Boris Proppe, and Jens Dreger from the Physics Department at the High-Performance Computing Center of the ZEDAT. Many thanks to Mr. Andreas Heß for his patience and assistance during the dissertation submission procedure.

I dedicate this dissertation to my family expressing my gratitude to them. My mother taught me to ask questions and ignited the curiosity in my younger self whereas my father, brother and grandparents nurtured my curiosity and provided me with all the support I needed to follow my quest. Thank you for believing in me when I couldn't believe in myself.

I would also like to thank my friends and colleagues who were always there for a fun chat or intense discussions about science and life. Special thanks to my former colleagues Michalis Lazaratos and Konstantina Karathanou for helping me with all aspects of being part of the Bondar group. They not only helped me with learning software and programming scripts but also guided me to the life in Berlin and as a doctoral student. Without the company of wonderful friends and family, I would not have been able to complete this project.

# Publications arising from this thesis

**Jain, H**., Karathanou, K., & Bondar, A. (2023). Graph-Based analyses of dynamic Water-Mediated Hydrogen-Bond networks in phosphatidylserine: cholesterol membranes. Biomolecules, 13(8), 1238. https://doi.org/10.3390/biom13081238

*Manuscript in preparation*

**Jain, H**., Lazaratos, M., Pohl, P., & Bondar, A. Fluctuating hydrogen bond networks couple protonation, lipid interactions, and conformational dynamics of the Hv1 ion channel.

# List of Figures

# List of Tables

# List of abbreviations and symbols

| | |
|---|---|
| CHARMM | Chemistry at HARvard Macromolecular Mechanics |
| Chol | Cholesterol |
| DFS | Depth-first search |
| DMPC | 1,2-dimyristoyl-sn-glycero-3-phosphocholine |
| DNA | Deoxyribonucleic acid |
| DOPS | 1,2-Dioleoyl-sn-glycero-3-phospho-L-serine |
| *E. coli* | *Escherichia coli* |
| GUV | Giant unilamellar vesicle |
| H-bond | Hydrogen bond |
| HIF | Hv1 Inhibitor Flexibles |
| HPC | high-performance computing |
| JO | Joint Occupancy |
| MD | Molecular dynamics |
| NAMD | NAnoscale Molecular Dynamics |
| OPM | Orientations of Proteins in Membranes |
| PA | phosphatidic acid |
| PC | phosphatidylcholine |
| PDB | Protein Data Bank |
| PE | phosphatidylethanolamine |
| PG | phosphatidylglycerol |
| PI | phosphatidylinositol |
| PIP2 | phosphatidylinositol 4,5-bisphosphate |
| PMPE | 1-palmitoyl-2-cis-9,10-methylene-hexadecanoic-acid-sn-glycero-3-phosphoethanolamine |
| PMPG | 1-palmitoyl-2-cis-9,10-methylene-hexadecanoic-acidglycero-sn-3-phosphoglycerol |
| POPA | 1-palmitoyl-2-oleoyl-sn-glycero-3-phosphatidic acid |
| POPC | 1-palmitoyl-2-oleoylphosphatidylcholine |
| POPE | 1-Palmitoyl-2-oleoyl-sn-glycero-3-phosphoethanolamine |
| POPG | 1-palmitoyl-2-oleoyl-sn-glycero-3-phosphatidylglycerol |
| POPS | 1-palmitoyl-2-oleoyl-sn-glycero-3-phospho-L-serine |
| PS | phosphatidylserine |
| PYPG | 1-hexadecanoyl-2-(9Z-hexadecenoyl)-glycero-3-phospho-(1'-sn-glycerol) |
| QMPE | 1-pentadecanoyl-2-cis-9,10-methylene-hexadecanoic-acid-snglycero-3-phosphoethanolamine |

| | |
|---|---|
| RMSD | Root-mean-square deviation |
| RNA | Ribonucleic acid |
| SM | Sphingomyelin |
| TIP3P | Transferable Intermolecular Potential 3P |
| UB | Urey-Bradley |
| VMD | Visual Molecular Dynamics |
| VSD | Voltage Sensing Domain |
| YOPE | 3-palmitoleoyl-2-oleoyl-d-glycero-1-phosphatidylethanolamine |
| $\triangle$ pH | Change in pH |

# Contents

# 1

# Introduction

## 1.1 Proteins and Lipids

Proteins are essential biomolecules. They are made up of extended amino acid chains connected by peptide bonds [1]. The building blocks of proteins are twenty distinct naturally occurring amino acids. Amino acids comprise a $\alpha$-carbon bonded to a carbonyl group, an amino group, and a variable side chain that differs in all 20 amino acids [1]. The differing electronegativity of the side chains and the carbonyl & amino groups of amino acids gives them a unique ability to form hydrogen bonds (H-bonds). H-bonds between amino acids help stabilize the protein and facilitate its function [2]. A protein's precise amino acid sequence defines its distinct structure and function. Disruption in the structure of the protein can lead to a loss of functionality. This can happen due to changes in pH, temperature [3], or exposure to denaturing enzymes.

Lipids are biomolecules performing a variety of vital essential functions [4]. They are building blocks of cell membranes that give cells their form and regulate how chemicals enter and exit cells by providing the structural integrity needed. They also function as significant signaling molecules, as building blocks for the creation of hormones such as steroid and are essential for storing energy.

Lipid types, distinguished by their unique molecular structure supporting their role in specific biological systems, include phospholipids, triglycerides, and cholesterol [4]. Three fatty acid chains joined by a glycerol molecule form triglycerides. These fatty acids typically have a carboxyl group at one end of lengthy hydrocarbon chains. The main role of triglycerides is to store energy. Two hydrophobic fatty acid chains with a hydrophilic headgroup form a phospholipid. These amphipathic molecules allow the formation of a lipid bilayer in a hydrated environment and are thus the key components of cell membranes. Cholesterol, a sterol lipid, is also present in animal cell membranes [4]. It regulates the fluidity and stability of cell membranes by keeping the fatty acid chains in phospholipids from packing too tightly together.

## 1.2 H-bonds

H-bonds are potent forces of attraction essential to numerous chemical and biological processes. An H-bond is formed by the electrostatic attraction between an hydrogen donor and hydrogen acceptor in close proximity [5–7]. A hydrogen donor is usually a strong electronegative atom such as oxygen or nitrogen whereas an hydrogen acceptor is also an electronegative atom with a lone pair participating in H-bonding. The attractive force leading to formation of an H-bond is due to the difference in electronegativity between the H atom and the neighbouring electronegative atom. Although being weaker to covalent and ionic bonds, H-bonds contribute significantly to the unique properties of biomolecules. The strength of H-bonds in nature i.e the energy needed to break them range from 2-25 kcal/mol [8]. For weak H-bonds (1-3 kcal/mol) the H-bond length varies from 2.7-3.0 Å. As H-bond length decreased to 2.5-2.6 the energy required to break the H-bond increases to 7-25 kcal/mol [8–10]. Weak H-bonding is usual and occurs in biological systems with aqueous environments such as proteins due to the H-bonding competition with the solvent [8, 10].

H-bonds are extensively observed in nature from governing the molecular and physical properties of water to providing the structural shape and stability to DNA, RNA and proteins. The high boilling point of water and its surface tension can be attributed to the H-bonds formed by oxygen atom with upto four neighboring water molecules. In proteins, H-bonds contribute to structural stability [11, 12], folding [13–15] , formation of secondary structures [16, 17] and functioning of proteins including molecular recognition [18]. H-bonding between the titratable groups and water molecules also influence the $pK_a$s of ionizable amino acid residues [19]. The insertion and stability of transmembrane proteins [20, 21] in lipid bilayers, as well as the fluidity and stability of lipid bilayer [22–24] and its permeability to ions and small molecules [22, 25, 26], are all influenced by the H-bond network formed by lipid headgroups and protein sidechains. Proteins involved in proton transfer are particularly dependent on H-bond networks [27–30]. Breaking and formation of H-bonds at room temperature show a complex dynamics of H-bond network providing plasticity [20, 31] and conformational dynamics required for protein functioning [20, 28, 32]. Thus, understanding the dynamics of H-bond network is crucial for understanding the mechanisms behind protein functioning, protein-protein interactions, membrane transport functions reliant on lipids, and protein or lipid-mediated cellular signaling.

H-bond networks in transmembrane proteins and lipid bilayers have been studied using molecular dynamic simulations providing useful insights about

the functioning mechanism of proteins [28, 33–41] and formation of lipid clusters [42, 43]. H-bonds are typically identified using geometric criteria for the distance between the H-bond donor and acceptor heavy atoms, as well as for the H-bond angle. According to experimental and computational analysis of several crystal structures of proteins with varying H-bond geometries, the H-bond distance between an H atom and H-bond acceptor heavy atom ranges between 1.56-2.63 Å whereas the H-bond angle between the donor-acceptor axis in the range of 120°-180° [44, 45]. A distance and angle criteria of 3.5 Å and 60° has been used for H-bond analysis in proteins [28, 33–36]. A criteria of 2.5 Å distance between the H atom and the acceptor heavy atom is comparable to 3.5 Å distance and 60° H-bond angle and have been used to study H-bonding in lipid bilayers [42, 43].

While the mechanical perspective focuses on electrostatic interactions and provides insights on how H-bonds contribute to the unique physical properties of substances, a deeper understanding of H-bonds require quantum perspective. From the quantum perspective, H-bonding is seen as an electrostatic interaction between electron clouds with electron-rich and electron-poor regions formed by the electronegativity difference of the atoms involved [46]. Energy potentials and wave functions are used to describe the energy changes related to the formation and breaking of H-bonds [46, 47]. The distance between the donor and acceptor atoms, the angle between the donor-acceptor axis, and the presence of nearby molecules may have an impact on the strength of an H-bond, defined as the energy needed to break one [31, 48, 49]. In the work presented in this thesis, the dynamics of H-bond networks have been studied using classical molecular dynamics simulations.

## 1.3 Anionic lipid bilayers and cholesterol

Lipid membranes that surround cells and cell compartments host at their interfaces reactions essential for the survival of the cells. The charge and nature of the phospholipids, the main constituents of the membrane, influences the properties of the membrane [50]. Phosphoplipid are usually zwitterionic i.e. have a neutral charge or anionic i.e negatively charged. The most common zwitterionic phospholipids are phosphatidylcholine (PC) and phosphatidylethanolamine (PE) whereas anionic lipids include phosphatidylserine (PS), phosphatidylglycerol (PG), phosphatidic acid (PA) and phosphatidylinositol (PI). The specificity of lipids determine the physical properties of the membrane such as membrane curvature, fluidity and surface charge [51–53]. This makes role of anionic lipids important in various bi-

ological process. For example, PG is an abundant surfactant associated with pulmonary diseases [54] whereas PI and PG are suggested to have antiviral properties [55, 56]. These phospholipids play a role in modulation of membrane receptors and their signalling process [54]. Normally cells have a neutral total membrane charge attributed to the asymmetrical distribution of zwitterionic phospholipids on the outer plasma membrane and negatively charged phospholipids in the inner plasma membrane [57]. In cancerous cells, the asymmetry of lipid membranes is observed due to the exposure of PS and PE on the outer membranes of the cancerous cells. The exposure of PS on the outer leaflet is a characteristic of the cancer cell membranes [57, 58] and can be used as cancer biomarkers [58]. PS is associated with a number of human diseases [59], plays a role in protein localization in the cell [60] and controls the membrane curvature [61]. This makes it important and interesting to study and explore the structure of anionic lipid membranes containing phosphatidylserine.

Cholesterol is a crucial component of lipid membranes. Eukaryotic cell membranes contain 10-40 % cholesterol [62]. Presence of cholesterol influences the physical properties of membranes such as increase in the ordering of the lipid hydrocarbon chains [63–66], decrease in lateral lipid diffusion [67], increase in lateral pressure profile magnitudes [68, 69], and smaller area per lipid [70–74]. Apart from changes in physical properties of membranes, presence of cholesterol can induce formation of lipid rafts [75] that can act as a platform for membrane-associated signaling proteins. Cholesterol plays a role in functioning of G-proteins [76], signaling proteins for sperm activation [77] and proteases of amyloid precursors [78]. Cholesterol levels in cancer cell membranes drop to allow for membrane flexibility during metastasis [79, 80], while an increase in cholesterol concentration seems to be linked to chemotherapy resistance [81, 82]. Thus, the role of cholesterol in human physiology ranges from Alzheimer's disease [78], reproductive biology to cancer.

Lipid headgroups can form H-bond networks influencing the physical properties of membranes such as its stability and fluidity [42, 83]. Anionic lipid PS show high propensity to form H-bonds [42]. Whereas cholesterol shows a tendency to interact with anionic lipids and can H-bond due to the presence of the hydroxyl group [84]. In this thesis, H-bond dynamics of lipid membranes with anionic and zwitterionic lipids is presented (Chapter 3). To evaluate the impact of cholesterol on the lipid H-bond dynamics, atomistic simulations and graph-based algorithms are used to study the water-mediated H-bond clusters formed by PS in anionic lipid membranes containing cholesterol (Chapter 4).

## 1.4 Human voltage gated proton channel (Hv1)

Hv1 is a protein that functions as a voltage gated proton channel. It is a member of the voltage-gated ion channel superfamily that usually contain sodium or potassium ion channels. However, Hv1 is unique as it specifically allows only protons to pass through as a response to voltage change [85, 86]. It is thus essential for regulating intracellular pH in several animals, including humans. Hv1 plays a role in the respiratory burst in the immune cells, contributes to sperm motility and capacitation, and maintains pH for cancer cell survival and proliferation [85–89]. Certain types of cancer cells such as breast, colorectal, leukemia cancer cells show higher expression and high activity of the voltage-gated proton channel (Hv1) [87–89]. Recent studies report Hv1 as a novel target for neuroprotection since it is upregulated in Parkinsonian mice and mediates the generation of pro-inflammatory cytokines by microglia [90].

The main function of Hv1 is proton extrusion and maintenance of pH in cells [85, 86]. A network of H-bonds formed by the titratable sidechains of the protein regulates the proton transfer across Hv1 [27, 85, 91–93]. As Hv1 channel has a pH and voltage dependent gating, the change in protonation state of titratable sidechains can influence the H-bond network and thus the conformational dynamics and functioning of Hv1. In subsequent Chapter 5 of this thesis, the protonation-coupled and lipid-coupled H-bond network dynamics of Hv1 has been discussed.

In addition to the presence of protonatable carboxylates in the transmembrane region of Hv1, cluster of carboxylates and histidines on the extracellular and cytoplasmic sides suggest the formation of proton antennas. Proton antennas are molecular systems facilitating proton transfer over long distances [94–98]. Proton antennas usually consist of proton attractor sites and proton reservoir sites closely clustered within $\sim$10 Å [95]. Proton attractor sites are formed by low pK carboxylates - Aspartate (Asp) with pK = 3.5 [99] and Glutamate (Glu) with pK = 4.2 [95, 99]. Whereas proton reservoir sites on the other hand contain groups with neutral pK such as histidines with pK = 6.6 [95, 99]. Bulk exposed negatively charged protein side chains or lipid headgroups may form proton antennas at the lipid membrane interface, increasing the dwell time of the proton. Proton antennas have been discussed and identified for biological systems such as PsbO subunit of photosystem II [98, 100, 101], bacteriorhodopsin [102], green fluorescent protein [103] and cytochrome c oxidase [96].

Negatively charged groups situated within 12 Å of each other can transfer protons with high probability between them rather to the bulk, in case of overlapping Coulomb cages at zero ionic strength [95, 104]. At ionic strength of 100 mM monovalent salt, proton transfer may happen at smaller distances such as 8 Å or less [95, 96]. Anionic lipid headgroups are separated by 7-10 Å [104, 105] and protonatable sidechains of proteins are even closer. The close proximity of these groups might result in merging of their Coulomb cages, thus facilitating the formation of proton antennas [95, 96, 104, 106–110]. The space between a proton and protonatable group where the electrostatic interaction is stronger than the thermal energy (kBT) is defined as a Coulomb cage [96, 111]. The mobility of a proton in a Coulomb's cage is governed by electrostatic interactions rather than diffusion [111].

Proton transfer along and across lipid membranes can be explained by Grotthus mechanism [112] where protons jump along a proton wire formed by H-bonded water molecules and protonatable amino acid residues or lipid headgroups. The H-bond network formed at the membrane interface can change based on the lipid composition as water molecules rearranges around the lipid headgroups [42, 43, 113, 114]. In this thesis (Chapter 5), putative proton antennas forming H-bonded clusters at the protein-lipid interface are identified and characterized for Hv1 proton channel embedded in lipid bilayers with varying lipid compositions.

# 2

# Methodology

## 2.1 Force field used for Molecular dynamics (MD)

CHARMM36 force field was used for the description of potential energy of the lipids, protein, ions and water in all MD simulations presented in this work.

Force fields are essential for precisely describing the interactions between atoms and molecules in the world of molecular simulations. These mathematical models are essential for comprehending and forecasting the behavior of intricate molecular systems, giving researchers access to information that is often inaccessible through purely experimental approaches. The development of the CHARMM force field, which stands for Chemistry at Harvard Macromolecular Mechanics, is steeped in the history of accurate molecular modeling [115–120]. CHARMM36 force field provides precision in simulating a wide variety of biological macromolecules, including proteins, nucleic acids, lipids, and carbohydrates and has emerged as a widely adopted and extensively validated version [119, 121, 122].

CHARMM is an all-atom Class-I additive force field [115–120]. The potential energy function that lies at the core of the CHARMM force field is shown in the equation below:

$$\nu(\vec{R}) = \sum_{bonds} k_b(b - b_0)^2 + \sum_{angles} k_\theta(\theta - \theta_0)^2 + \sum_{dihedrals} k_\phi(1 + cos(n\phi - \gamma)) + \sum_{impropers} k_\omega(\omega - \omega_0)^2 + \sum_{Urey-Bredley} k_{UB}(S - S_0)^2 + \sum_{residues} U_{CMAP}(\phi, \psi) + \sum_{non-bonded} \left\{ \varepsilon_{ij}^{min} \left[ \left( \frac{R_{ij}^{min}}{r_{ij}} \right)^{12} - 2 \left( \frac{R_{ij}^{min}}{r_{ij}} \right)^{6} \right] + \frac{q_i q_j}{4\pi\varepsilon_0 \varepsilon r_{ij}} \right\}$$

This force field equation consists of several terms, each accounting for different types of interactions. In this section, the individual terms of the CHARMM36 force field equation will be discussed, along with their significance and contributions.

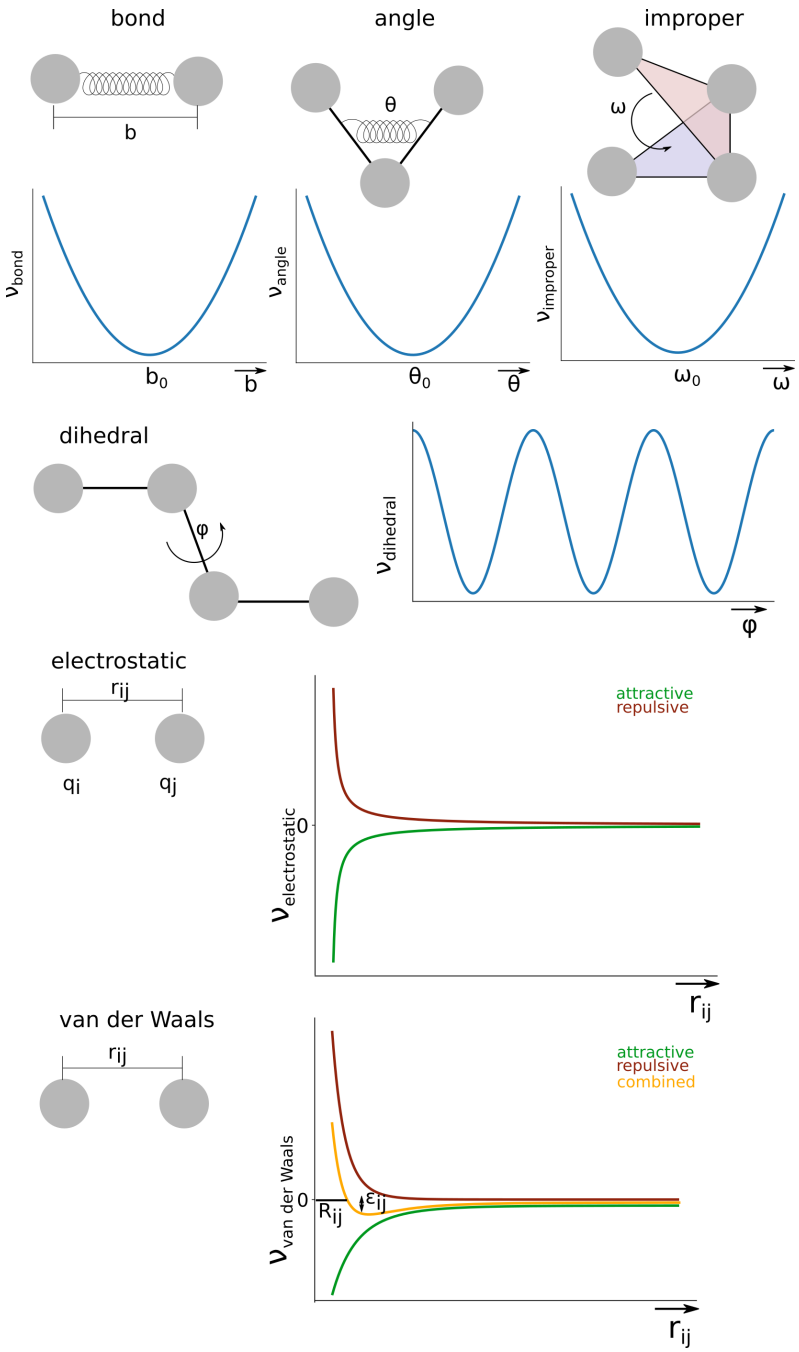


**Figure 2.1.** Force field terms. Graphical and schematic illustration for potential energy terms of CHARMM force field.

*Bonded interactions.*

The first four terms of the CHARMM force field equation are used to describe the covalent bonds, bond angles, dihedrals and improper angles. Harmonic potentials are used to characterize the stretching of the covalent bonds (bond distance *b*), with the force constant representing the stiffness of the bond ($k_b$) (Figure 2.1). Bond angle ($\theta$) bending and dihedral angles

also known as torsional angles ($\phi$, $\psi$) are defined using harmonic and cosine potentials (Figure 2.1), with the parameters coming from both ab initio calculations and experimental data. In the cosine potential term, $n$ and $\gamma$ represent dihedral multiplicity and phase. Torsional motions around bonds containing three atoms are related to improper angles ($\omega$), often known as out-of-plane angles. These angles are in charge of keeping certain functional groups flat and preventing undesirable distortions in the molecule structure. These terms ensure that the bond lengths, angles, and torsional angles seen in experimental structures are accurately represented in the force field.

A Urey-Bradley (UB) term is added in the force field equation as a harmonic function of distance between 1-3 atoms (*S*) [123]. It defines the interaction between bound atoms via the stretching and bending of covalent bonds. This enables a more accurate representation of the potential energy surface and the related vibrational modes as it takes into consideration that the potential energy is actually proportional to a more complex function than the square of the displacement. The equilibrium values for each term are shown with a subscript ($_0$) and the respective force constant as *k* ($k_\theta$, $k_\phi$, $k_\omega$, $k_\phi$, $k_{UB}$). CMAP term, a function of the backbone dihedral angles ($\phi$, $\psi$) is added as a correction term [116, 124, 125]. CMAP stands for the "crossterms and 2D dihedral energy grid correction map" term [126].

*Non-bonded interactions.*

Non-bonded interactions include the van der Waals interactions and electrostatic interactions. Coulomb's law, which defines the interaction between charged particles, governs electrostatic interactions (Figure 2.1). In the Coulombic law term, the atomic charges of interacting atoms are described as $q_i$, $q_j$, the interatomic distance as $r_{ij}$ and the dielectric constant as $\varepsilon$. The charge distribution on atoms is represented by a multipole expansion in the CHARMM36 force field, which enables a precise description of electrostatic interactions. Lennard-Jones (LJ) potentials, on the other hand, encapsulate the short-range repulsion and long-range attraction between atoms and are used to model van der Waals interactions. The LJ potential term has two parts: an attractive term that captures the dispersion forces at longer distances and a repulsive term that accounts for the steric repulsion at small distances (Figure 2.1). For two interacting atoms i and j in the LJ term, the interatomic distance is $r_{ij}$, the potential well depth is at $\varepsilon_{ij}^{min}$ and the minimum value of potential is found at $R_{ij}^{min}$. The well depth ($\varepsilon_{ij}^{min}$) and the distance at which the potential is zero $R_{ij}^{min}$, which are the parameters utilized in the LJ potential, are normally obtained from experimental data or quantum mechanical calculations.

To simulate the van der Waals interactions, the CHARMM36 force field includes specialized parameter sets for various atom types. These settings have been made to closely match experimentally measured observables including the energy of interactions in the gas phase.

## 2.2 Graph theory concepts

Graph theory stands out in the complicated fabric of mathematics due to its worldwide applicability, adaptability, and capacity to decipher the dense network of connections that underlies our world. It gave mathematicians and scientists a potent tool to model and examine a wide range of systems, including social networks, electrical circuits, molecular structures, and transportation networks. In this thesis, graph theory is used to model and analyze dynamic H-bond networks.

A *graph*, which is a mathematical structure made up of nodes and edges or connections between them, is the central notion in graph theory [127] (Figure 2.2). Graphs can be used to explore complex interactions in diverse circumstances. *Nodes* of a graph represent entities under study whereas *edges* connecting these nodes represent the relation between them. A *path* is defined as a series of nodes where each adjacent pair is connected by an edge (Figure 2.2). To model the structure and dynamics of H-bond networks, graphs can be used - the nodes can represent amino acid residues, lipid headgroups or H-bonding groups whereas the edges represent the direct or water mediated H-bonds [33, 34, 42, 43, 128].

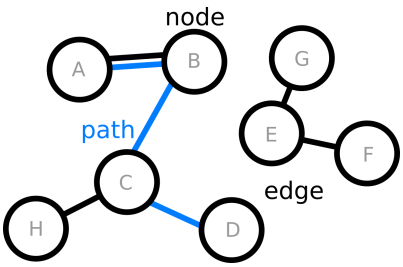


**Figure 2.2.** Illustration of a graph. The circles represent the nodes and the lines connecting the nodes represent the edges. Blue highlighted edges represent a path connecting A and D nodes via B, C nodes.

Graphs help us identify the most frequently sampled and important H-bonds in a network. It can be used to understand the dynamics of H-bond networks over time. For example, graph theory can help us understand how H-bond network in a transmembrane protein changes with activation-deactivation of the protein [129], temperature and pH [130–132]. This further helps in deciphering mechanism of proton transfer across transmembrane

proteins. Drugs that can disrupt the H-bond networks involved in disease can be developed. Using graph theory to study H-bond networks makes it an important and powerful tool with many applications.

*Depth-first search (DFS) algorithm*

DFS algorithm, a graph theory concept, is a recursive algorithm used to explore or traverse graphs [133]. A starting node is selected as the initial point of exploration in the beginning of the DFS algorithm. Following that, it investigates nearby nodes, designating them as visited and repeatedly probing into unexplored neighbors. DFS returns to the previous node after reaching a dead end or having fully explored a branch and then moves on to explore more unexplored branches. Until all of the graph's vertices have been reached, this recursive procedure keeps going.

DFS algorithm is used by NetworkX python library [134], to find all possible paths between two nodes. This algorithm starts at the source node, investigates nearby nodes, and then recursively traverse pathways, going backwards if needed. After arriving at the desired node, it records valid pathways and keeps exploring the graph, systematically locating all easy paths and avoiding cycles. This method efficiently finds all feasible connections between nodes, which makes it a useful tool for network connectivity analysis. When employing this approach, it's crucial to take computational complexity into account because the number of pathways might increase exponentially with the size of the graph, potentially resulting in high processing demands.

In this thesis, a protocol is developed to find the most frequent H-bond paths between aminoacid residues. This protocol uses NetworkX library's DFS based function to find all the paths between the nodes and Dijkstra's algorithm to find the shortest paths between nodes.

A previously developed DFS-based algorithm [42] is used in this thesis to catalogue the topologies of lipid clusters. This algorithm performs connected component searches using the DFS algorithm to find lipid clusters. Based on the presence of star nodes and back edges, the lipid clusters are classified into four topologies - circular with back edges and no star nodes, star & linear with star nodes and no back edges, circular & star & linear with back edges and star node, or else as linear with no back edges or star nodes.

## 2.3 Software used

In this section, the software used in the thesis are introduced briefly.

*CHARMM-GUI*

A user-friendly web-based platform called CHARMM-GUI [135–139], which stands for Chemistry at Harvard Molecular Mechanics Graphical User Interface, makes it easier to set up molecular dynamics simulations and carry out various tasks related to biomolecular modeling. For creating, parameterizing, and visualizing molecular systems, such as proteins, lipids, nucleic acids, and small molecules, it provides a wide range of tools and features. As CHARMM-GUI combines with various molecular modeling programs and the well-known simulation tool CHARMM [115], researchers may easily produce input files for simulations and carry out complex activities. CHARMM-GUI was used to setup simulation systems in this work.

*Modeller*

Modeller, developed by Sali's lab [140], is used for comparative protein structure modeling in computational biology and structural bioinformatics. It uses existing protein structures (templates) and applies comparative modeling methods to predict three-dimensional protein structures (targets). Modeller was used to model missing loops of the proton channel under study in this work.

*NAMD*

NAMD [141, 142] stands for NAnoscale Molecular Dynamics. It is a highly developed and parallelized software largely used to simulate complex molecular interactions, such as those found in proteins, nucleic acids, and membranes. Created and maintained by the Theoretical and Computational Biophysics Group at the University of Illinois at Urbana-Champaign, NAMD is recognized for its capacity to scale, which enables it to use supercomputers and high-performance computing clusters to carry out large simulations. NAMD at high-performance computing (HPC) cluster Curta [143] of the Zentral Einrichtung Datenverarbeitung (ZEDAT)-Freie Universität Berlin and HLRN Berlin was used to carry out MD simulations discussed in this work.

*VMD*

For the interactive visualization and analysis of complicated biomolecular systems, Visual Molecular Dynamics, or VMD [144], is a widely used molecular visualization program. Compatible to NAMD, VMD was also created by the Theoretical and Computational Biophysics Group at the University of Illinois at Urbana-Champaign. VMD allows viewing of three dimensional structures of biomolecules and acts as an interface for the Tcl scripting language, enabling scripting capabilities that are particularly useful for MD simulation analysis. VMD was used to produce molecular graphics and run Tcl scripts for analysis.

*Bridge*

Bridge is a graph-theory based algorithm with graphical interface developed by the Bondar group [34, 128] to efficiently analyse and visualize H-bond network dynamics in biomolecular systems such as transmembrane proteins embedded in lipid bilayers or hydrated lipid bilayers. Bridge was used in this work for H-bond network calculation and analysis. The protocol to find most frequent H-bond paths developed and discussed in this work uses Bridge core code.

*AutoDock Vina*

AutoDock Vina is a molecular docking software developed by the Trott group [145] at the Molecular Graphics Lab at the Scripps Research Institute. It is a state-of-the-art software used for predicting the binding modes and affinities of ligand-protein complexes. In this thesis, AutoDock Vina was used to dock Hv1 inhibitors to the open state model of Hv1.

*PyMol*

PyMol is a molecular visualization software from Schrödinger, Inc [146]. For the molecular graphics of the docking poses from AutoDock Vina, PyMol was used in this work.

## 2.4 Simulation setup used for MD simulations

*Atomistic simulations of hydrated lipid bilayers.*

Eleven independent simulations of hydrated lipid membranes were performed (Table 2.1, Sim1-11). Seven of these membranes are distinguished by the headgroup, as they are composed of i) 1-palmitoyl-2-

oleoylphosphatidylcholine (POPC) and ii) 1-palmitoyl-2-oleoyl-sn-glycero-3-phosphoethanolamine (POPE) lipids, which are zwitterionic; iii) acidic 1-palmitoyl-2-oleoyl-sn-glycero-3-phospho-L-serine (POPS), iv) 1-palmitoyl-2-oleoyl-sn-glycero-3-phosphatidylglycerol (POPG) and v) 1-palmitoyl-2-oleoyl-sn-glycero-3-phosphatidic acid (POPA) lipids; vi) a 5:1 mixture of POPE, which are zwitterionic lipids with higher propensity to H-bond than POPC, and of acidic POPG lipids; vii) the *E. coli* membrane model referred to as Top6 in ref. [147], which is a mixture of PE- and PG-type lipids (Table 2.1, Sim 1-7). The other four independent simulations of POPS bilayers were performed with 10, 20, 30 and 40 % of cholesterol (Chol) respectively (Table 2.1, Sim 8-11).

*Atomistic simulations of Hv1 in hydrated lipid bilayers.*

The crystal structure of mHv1 (PDB ID:3WKV) [148] was used as the initial protein coordinates for preparing simulations of hydrated membranes with Hv1. Modeller was used for modelling the missing internal loops [140]. Using the OPM server [149] and CHARMM-GUI [136, 139, 150], the Hv1 structure was put in the membrane with the normal orientation along the membrane. All titratable protein sidechains were considered in the standard protonation, meaning that all Asp/Glu are negatively charged, all Lys and Arg are positively charged, and all His are neutral and classified as N$\delta$1 tautomers. The concentration of the neutralizing KCl salt was 0.15M.

To investigate the effects of protonation on the dynamics of Hv1, I performed nine individual simulations using a hydrated POPC lipid bilayer (Table 2.1, Sim 12-21). In seven independent simulations, one of the following carboxylates was protonated: E115, D108, D119, E167, D170, or D181, in one simulation neutral H95 was described as an N$\epsilon$2 tautomer and in another simulation H136 was protonated at both the N$\delta$1 and N$\epsilon$2 atoms, i.e., it has a net charge of +1e (Table 2.1).

To probe the impact of composition of lipid bilayers and lipid-protein interactions, I performed five independent simulations of membranes with Hv1 embedded in membranes composed of i) POPC; ii) POPS; iii) POPE; iv) a 5:1 mixture of POPE:POPG lipids; v) the *E. coli* membrane model referred to as Top6 in ref. [147]

**Table 2.1.** Summary of simulations performed. 'Protonation' indicates whether all titratable sidechains were considered in their standard protonation or, when a sidechain has non-standard protonation, the identity of that sidechain.

| Sim | Lipid bilayer / #lipids | Protonation | #Atoms | Length (ns) | Membrane Thickness (Å) | RMSD (Å) [a] |
|---|---|---|---|---|---|---|
| Hydrated lipid bilayers with distinct lipid composition | | | | | | |
| 1 | POPC (218) | NA | 58,575 | 200 | 39.0 ± 0.5 | NA |
| 2 | POPE (218) | | 52,867 | 200 | 42.3 ± 0.6 | |
| 3 | POPG (218) | | 54,735 | 200 | 37.2 ± 0.6 | |
| 4 | POPA (218) | | 51,983 | 150 | 40.8 ± 0.6 | |
| 5 | 5:1 POPE:POPG (180/36) | | 52,731 | 200 | 41.6 ± 0.6 | |
| 6 | *E. coli* membrane model (Top6) [b] | | 54,120 | 200 | 38.6 ± 0.4 | |
| 7 | POPS (218) | | 53,680 | 500 | 41.2 ± 0.5 | |
| 8 | POPS/Cholesterol (196/22) | | 51,859 | 500 | 42.7 ± 0.5 | |
| 9 | POPS/Cholesterol (174/44) | | 49,790 | 500 | 44.2 ± 0.5 | |
| 10 | POPS/Cholesterol (152/66) | | 47,934 | 500 | 45.4 ± 0.5 | |
| 11 | POPS/Cholesterol (130/88) | | 46,065 | 500 | 46.0 ± 0.4 | |
| Hv1 embedded in hydrated lipid membranes | | | | | | |
| 12 | POPC (218) | standard | 107,348 | 500 | 39.3 ± 0.5 | 2.0 ± 0.2 |
| 13 | | D119 | 107,291 | 300 | 39.2 ± 0.5 | 2.8 ± 0.3 |
| 14 | | E167 | 107,297 | 300 | 39.3 ± 0.5 | 2.4 ± 0.3 |
| 15 | | D108 | 107,295 | 300 | 39.4 ± 0.5 | 2.9 ± 0.3 |
| 16 | | E115 | 107,267 | 300 | 39.4 ± 0.5 | 2.5 ± 0.5 |
| 17 | | D181 | 107,247 | 300 | 39.1 ± 0.5 | 2.4 ± 0.4 |
| 18 | | D170 | 107,396 | 300 | 39.4 ± 0.5 | 2.8 ± 0.2 |
| 19 | | D149 | 107,286 | 300 | 39.2 ± 0.5 | 2.8 ± 0.3 |
| 20 | | H95 | 107,331 | 300 | 39.2 ± 0.5 | 1.8 ± 0.3 |
| 21 | | H136 | 107,309 | 300 | 39.2 ± 0.5 | 2.4 ± 0.3 |
| 22 | POPE (218) | standard | 96,095 | 300 | 41.5 ± 0.4 | 3.2 ± 0.4 |
| 23 | 5:1 POPE/POPG (180/36) | | 95,918 | 280 | 42.0 ± 0.5 | 3.0 ± 0.2 |
| 24 | *E. coli* membrane model (Top6) [b] | | 99,141 | 300 | 41.0 ± 0.6 | 3.0 ± 0.3 |
| 25 | POPS (218) | | 97,775 | 300 | 38.3 ± 0.5 | 2.9 ± 0.3 |

[a] The C$\alpha$ RMSD and the standard deviation are computed from the last 200ns of each simulation., [b] The *E. coli* membrane model, which corresponds to the model known as Top6 in ref. [147] consists of 28 POPE lipids, 16 YOPE, 20 PYPG, 28 QMPE, 104 PMPE, and 22 PMPG lipids. YOPE: 3-palmitoleoyl-2-oleoyl-d-glycero-1-phosphatidylethanolamine; PYPG: 1-hexadecanoyl-2-(9Z-hexadecenoyl)-glycero-3-phospho-(1'-sn-glycerol), PMPE:1-palmitoyl-2-cis-9,10-methylene-hexadecanoic-acid-sn-glycero-3-phosphoethanolamine, PMPG: 1-palmitoyl-2-cis-9,10-methylene-hexadecanoic-acidglycero-sn-3-phosphoglycerol, QMPE:1-pentadecanoyl-2-cis-9,10-methylene-hexadecanoic-acid-snglycero-3-phosphoethanolamine

*Protocol for atomistic simulations of hydrated lipid bilayers.*

The simulation systems were set up using CHARMM-GUI [136, 139, 150], and the simulation trajectories were propagated using NAMD 2.13 [141, 142]. The simulation systems' atoms were described using the CHARMM36 force field [115–120] and the TIP3P water model [151]. For Coulomb interactions, the smooth particle mesh Ewald summation [152, 153] was employed, and for real space interactions, a switch function between 10 Å and 12 Å was used. The standard CHARMM-GUI protocol was followed during a 1 ns period of equilibration. All production runs were carried out using a Langevin dynamics scheme [154, 155] with an oscillation period of 200 fs, a damping time scale of 100 fs, and a damping coefficient of 5 $ps^{-1}$ in the NPT ensemble with constant number of particles N, constant pressure P = 1 bar, and constant temperature T = 310.15 K. Using SHAKE, covalent bonds to H atoms were fixed [156]. With a 1 fs integration step, equilibration and the first 1 ns of the production runs were completed. All subsequent production runs were carried out using a multiple time step integration method [157, 158], with integration steps of 1 fs for bonded interactions, 2 fs for short-range non-bonded forces, 2 fs and 4 fs for long-range electrostatics in the simulations of lipids (Sim 1-11) and Hv1 in lipids (Sim 12-25), respectively. Every 10 ps, coordinates were saved.

## 2.5 Protocol used to characterise topology of water-mediated hydrogen-bond clusters formed by lipid headgroups

A previously developed algorithm [42, 159] was used to characterize the topology of water-mediated H-bond networks formed by lipid headgroups. To probe topologies sampled by zwitterionic POPC, POPE, and anionic POPG, POPA and POPS lipid molecules in simulations (Figure 2.3), the DFS algorithm [42, 159] that identifies four main topologies - linear, star & linear, circular and complex combinations of these three arrangements (Figure 2.4) was used. The same algorithm was applied to simulations of POPS with varying cholesterol concentration.

*H-bond criteria, H-bonding groups*

For simulations distinguished by lipid headgroups and without cholesterol, the H-bond computation includes the oxygen atoms of phosphate, carboxyl and glycerol groups, the amine H atoms whereas in simulations with cholesterol, the hydroxyl group of cholesterol and the oxygens of ester group of

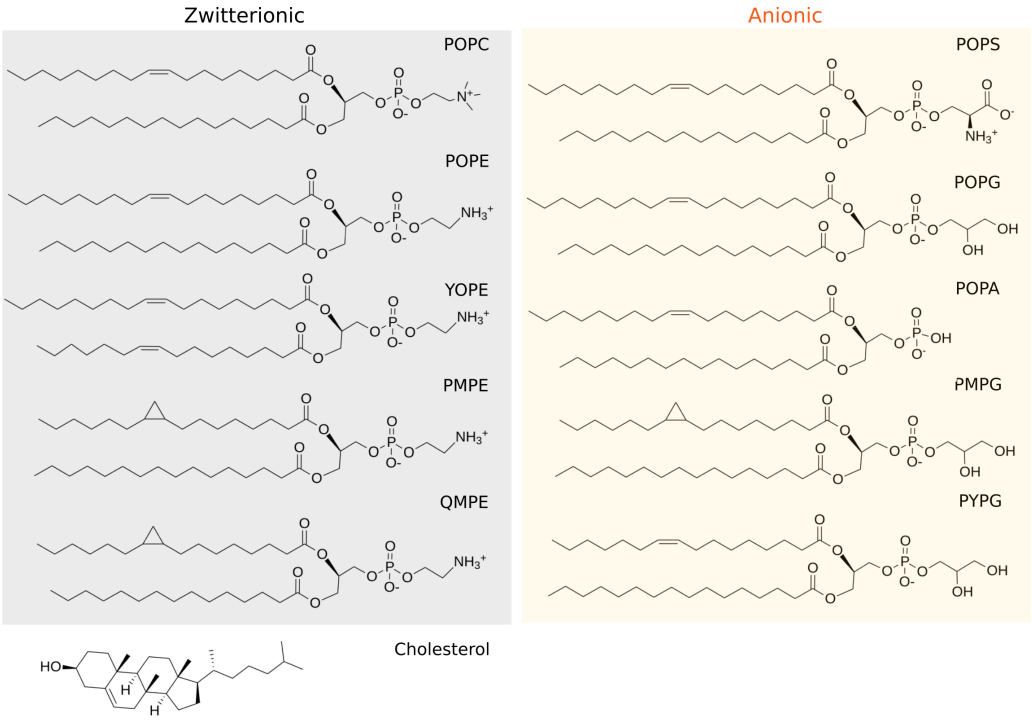


**Figure 2.3.** Lipid types used in the simulations.

POPS lipids are also included as H-bonding groups (Figure 2.4). To understand the distribution of H-bond networks at different depths of lipid bilayer, I calculated H-bonds formed by 5 different groups of POPS lipid headgroup - phosphate only, serine only, ester only, phosphate & serine and all the groups together (Figure 2.4A). In this case, I mainly take into account the following H-bond interactions - i) POPS-POPS - between POPS lipid head groups (Figure 2.4B), ii) POPS-Chol - between POPS lipid headgroups and cholesterol (Figure 2.4C) and iii) Chol-Chol - between cholesterol molecules (Figure 2.4D).

For H-bond calculation, a standard distance criterion was used. Two groups were considered as H-bonded if the distance between the donor and acceptor hetero-atoms is within 2.5 Å. For potassium ion-mediated bridges between two POPS lipid phosphate groups, a distance criterion of 4 Å was used.

*H-bond clusters, topology, cluster size, path length, occupancy and occurrence of lipid cluster*

An *H-bond cluster* is defined by the nodes and edges that interconnect with each other. The geometric arrangement of the nodes and edges in that cluster is *the topology of the H-bond lipid cluster* [42]. The *size of a lipid cluster* is given by the number of lipid headgroups, and the *topology path*

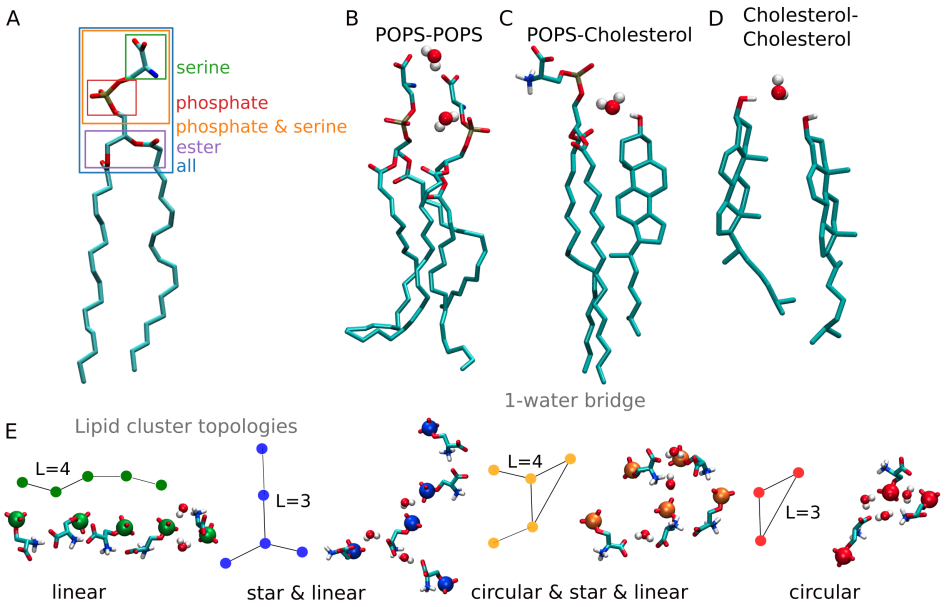


**Figure 2.4.** Protocol for topology analysis of lipid clusters sampled in hydrated POPS bilayers with and without cholesterol. (A) H-bonding groups. Five different H-bonding groups - serine, phosphate, ester, phosphate and serine, and all the groups together were used for topology analysis and H-bond calculations. (B-D) Molecular graphics illustrating 1-water mediated H-bond interaction between POPS headgroups (Panel B), POPS-cholesterol (Panel C) and cholesterol-cholesterol (Panel D). (E) Molecular graphics illustrating the topologies studied here for lipid H-bond clusters. The insets illustrate the main topologies that can be identified with the DFS algorithm [42]. This figure is taken from ref. [160].

*length* is defined as the number of edges in the longest path connecting two nodes of the H-bond cluster [42]. The *occurrence of a lipid cluster* is computed as the percentage of the trajectory frames where at least one lipid cluster of a specific topology is found. The *occupancy of lipid cluster* is the percentage of coordinate sets utilized in analyses in which the cluster is present [34, 43, 128]. All topology calculations were performed using the VMD and MATLAB data analysis scripts as deposited in the Mendeley repository [159]. A *geometrical cluster* is defined as a group of lipids with H-bonding atoms within 6 Å of each other. For data analysis, the complete trajectories were used. The H-bond networks and occupancies of H-bonds were calculated using Bridge [34, 128].

*Structure factors and the number of H-bonds per lipid molecule.*

The structure factors of lipid bilayers i.e. average thickness of lipid bilayers, the area per lipid molecule and the order parameters were calculated using MEMBPLUGIN [161] in VMD [144]. The H-bonds per lipid was reported as the average number of H-bonds formed by the specific lipid headgroup in every frame.

## 2.6 Protocol developed to extract the most frequent water mediated H-bond paths between titratable sidechains of a protein

*H-bond criteria, H-bond occupancy, H-bond graphs, local H-bond clusters, and H-bond paths.*

The standard distance and angle criteria for H-bonding, whereby two groups were considered as H-bonded if the distance between the donor and acceptor heavy atoms was within 3.5 Å, and the H-bond angle, within 60º was used. The *occupancy of an H-bond* gives the percentage of the coordinate sets used for analyses during which the H-bond criteria are met [33, 34, 43].

Protein or lipid H-bonding groups serve as the nodes of *an H-bond graph*, whereas direct or water-mediated H-bonds between protein sidechains or lipid headgroups serve as the edges. The nodes and edges that interconnect those two protein groups via intermediary H-bonds make up *an H-bond path* between two nodes (protein groups) of interest. The percentage of the coordinate sets utilized for analyses in which all intermediate path segments satisfy the H-bond criteria simultaneously is known as the *Joint Occupancy (JO)* of an H-bond path [34].

*Protocol for H-bond and H-bond path calculations.*

Bridge [34, 128] was used for all H-bond graph computations. Connected Component Analysis [34] in Bridge was used to extract local H-bond clusters. H-bond paths were extracted from the H-bond graphs. Unless otherwise stated, water-mediated bridges between protein sidechains contain up to three H-bonded water molecules. For the sake of clarity and to filter out statistically significant frequently sampled H-bonds and H-bond paths, we only consider H-bonds with occupancies greater than 30 % in data analyses and report H-bond paths with a joint occupancy of more than 5 %.

*Implementation of H-bond path calculations for titratable protein sidechains.*

The following steps were performed (Figure 2.5) to find H-bond paths that connect Asp, Glu, and His sidechains with water molecules and protein sidechains that might engage in proton transfer. The last 200 ns of each simulation trajectory were used to compute protein-water H-bond graphs;

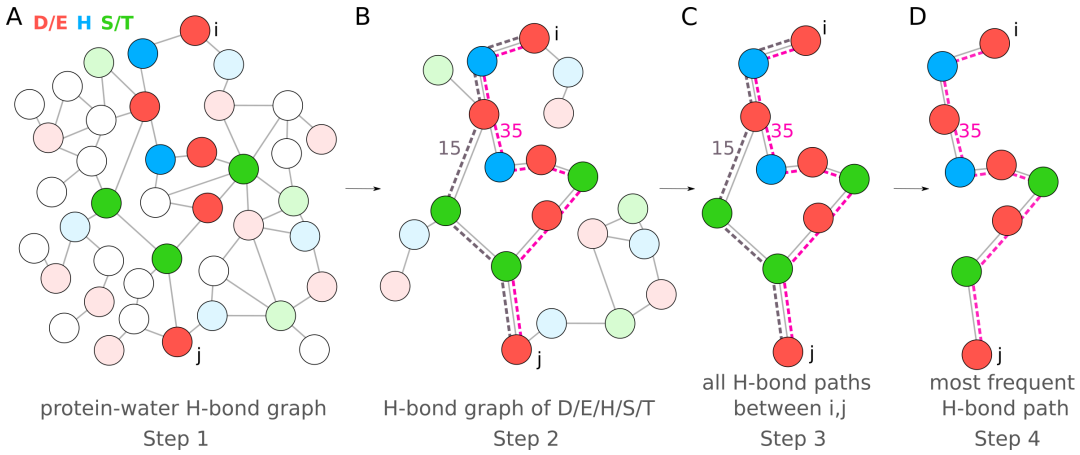


**Figure 2.5.** Protocol for extracting the most frequent paths between Asp, Glu, and His sidechains from protein-water H-bond graphs. (A) Complete protein-water H-bond graphs (Step 1). (B) Extracted graph of Asp, Glu, His, Ser, Thr (Step 2). (C) Computation of all H-bond paths and joint occupancies of these paths between carboxylates/histidines of interest (Step 3). (D) Most frequent H-bond path between carboxylates and/or histidines in MD simulations. Here, each circle represents an H-bonding group (Step 4). An edge represents an H-bond. Asp/Glu, His, Ser/Thr are shown as red, blue and green circles. Amino-acid residues in the selected paths are shown as bright colors whereas the faded circles represent the remaining amino acid residues in the extracted H-bond graph. This figure is taken from ref. [162] (manuscript in preparation).

water bridges with up to three H-bonded waters were taken into account. The Asp, Glu, His, Ser, and Thr H-bond graph is extracted in the following step. The DFS algorithm from the NetworkX package [134] is then used in the third step to compute all the H-bond pathways mediated by up to three water molecules for all distinct pairs of Asp, Glu, and His side chains. Then each path's JO value is calculated and the paths are ranked in the fourth step.

The protocol and scripts presented here uses core code of Bridge [34] and MDAnalysis [163, 164]. The scripts will be made available in an open repository with the manuscript publication. A class called *Path Analysis* with attributes required for H-bond path analysis is added to the core code of Bridge.

# 3

# Role of lipid headgroups in H-bond dynamics of lipid bilayers

The algorithm used for topology analysis in this chapter was developed by Konstantina Karathanou [42, 159]. I prepared all of the system setups, performed MD simulations, and did H-bond network and topology analysis on those systems that are described in this chapter. Under the direction and close supervision of Prof. Dr. Ana-Nicoleta Bondar, I prepared the figures and wrote the text.

Parts of the work presented in this chapter are originally published in the deliverable report of the Innovative Training Network on Proton and proton coupled transport project.

Lipid headgroups are the polar ends of the lipids that engage in highly complex interactions and reactions, such as proton transfer, at the lipid membrane interface. They are exposed to the aqueous environment where they interact and form H-bonds with the water molecules. A key question is whether the nature of lipid headgroups plays a role in the mechanism of proton transfer. Proton transfer at the lipid membrane interface generally occurs via dynamic H-bonds between lipid headgroups and water. In this chapter, I use atomistic MD simulations along with a recently developed graph-theory based algorithm [42] to effectively analyse and evaluate dynamic H-bonds and H-bond networks as a function of the composition of the lipid headgroup.

H-bonds play a crucial role in the structure and function of lipids in biological systems. In lipid bilayers, H-bonds are responsible for the stability of lipid bilayers and the maintenance of their fluidity [22–24]. H-bond networks in lipids also affect the insertion and stability of transmembrane proteins [20, 21], as well as the permeability of the lipid bilayer to ions and small molecules [22, 25, 26]. The H-bond network in lipids are sensitive to changes in temperature and pH, which can alter the strength and stability of H-bonds and affect the properties of lipid bilayers [22, 165]. Understanding the H-bond network in lipids is important for gaining insights into the mechanisms of lipid-protein interactions, lipid-based membrane transport processes, and lipid-mediated cellular signaling.

The composition of the lipid membranes impacts their structural and functional characteristics [50]. Van Klompenburg in 1997 showed that anionic phospholipids interact with positively charged amino acids and contribute to topology of membrane proteins and the membrane itself [166]. For example, phosphatidylserine (PS) shows high propensity to form H-bonds as compared to phosphatidylcholine (PC) [83, 167]. Among negatively charged lipid headgroups, PS lipids have the most inter-lipid H-bonds due to its additional carboxyl as compared to the zwitterionic phosphatidylethanolamine (PE) and additional amine group as compared to anionic phosphatidylglycerol (PG) and phosphatic acid (PA) [165]. The high intermolecular hydrogen bonding in PS and PE lipids may also be a factor in the tight packing of these lipids resulting in large bilayer thicknesses [165].

Molecular dynamics studies have shown that lipids can form lipid clusters. These clusters are defined as groups of lipids in close proximity of each other [83] or H-bonded via direct H-bond, water molecules or ions [42, 83]. Water mediated and direct H-bonding in PC [24, 168] and PE [169] membranes reduces lipid mobility and contributes to the stability of the membrane. H-bonded PE headgroups are more likely to diffuse and reorient as groups

rather than individual lipids because the internal H-bonds in a cluster remain stable longer than the cluster maintains its size [169]. This suggests the presence of H-bond networks lead to formation of small lipid clusters or micro-domains that are prominent for lateral organization of extended lipid domains on the membrane interface. The temporal characteristics and spatial extent of H-bonded lipid clusters can provide insights into the time evolution of the lipid membrane interface and its organization.

The properties of H-bond mediated lipid clusters vary depending upon the nature of the lipid headgroup and the composition of the membranes. PS, PE and PA tend to form larger clusters with more lipids as compared to PG and PC [165]. This tendency can be attributed to the H-bonding between lipid headgroups and lipid-ion interactions. The presence of PS along with PC has been reported to increase the cluster size as compared to PC [83, 170]. Anionic lipids forming larger clusters with higher number of H-bonds can enhance proton transfer [171]. Larger lipid clusters with highly connected H-bond network can contribute to the formation of stable and extensive lipid domains [168, 169], enhancing membrane rigidity and mechanical stability [22–24], providing concentrated binding sites for proteins [172–174], and impede lipid diffusion [168, 169, 175]. Moreover, cluster size can impact membrane permeability, with H-bonding in larger clusters creating denser lipid packing and restricting solute diffusion, while smaller clusters or more dispersed lipids lead to increased permeability [22, 25, 26].

The potential for understanding, controlling, and predicting specific and nonspecific interactions between membranes and ions, small molecules, peptides, polycations, proteins, coated and uncoated nanomaterials ultimately lies in the ability to probe hydrogen-bond networks over lipid bilayers. In this chapter, I identify and characterize dynamic water-mediated clusters of different lipid headgroups using a recently developed DFS-based graph algorithm [42]. In order to characterize four different types of lipid H-bond clusters according to their characteristics, such as cluster size and cluster length, this algorithm explores the nodes of the H-bond graphs using Connected Component searches. I characterize the water-mediated H-bond clusters at the interface of hydrated lipid bilayers made up of various lipids, such as zwitterionic POPC, POPE, anionic POPS, POPG, POPA, and 5:1 POPE:POPG, and an *E. coli* lipid membrane model. The topology analysis of all lipid bilayers commonly sample small linear H-bond configurations, typically two-three lipid headgroups that form an H-bond either directly or indirectly with one water molecule. As the most favoured topology of the lipid H-bond clusters is independent of the lipid headgroup, the mechanism for proton transfer at lipid membrane interfaces can be assumed to be mostly

**Table 3.1.** Number of H-bonds per lipid in simulations of hydrated lipid bilayer distinguished by lipid headgroups.

| | Number of H-bonds/lipid | | |
|---|---|---|---|
| Simulation | direct | 1-water bridge | ion bridge |
| POPC | - | 1.5 ± 0.1 | 1.0 ± 0.1 |
| POPE | 0.9 ± 0.1 | 1.4 ± 0.1 | 1.0 ± 0.1 |
| POPS | 1.4 ± 0.1 | 1.9 ± 0.1 | 1.3 ± 0.1 |
| POPG | 0.7 ± 0.0 | 1.6 ± 0.1 | 1.3 ± 0.1 |
| POPA | 0.6 ± 0.1 | 1.7 ± 0.1 | 1.3 ± 0.1 |
| 5:1 POPG:POPE | 0.6 ± 0.1 | 1.4 ± 0.1 | 1.1 ± 0.2 |
| *E. coli* | 0.6 ± 0.1 | 1.4 ± 0.1 | 1.1 ± 0.2 |

independent of the kind of lipid headgroup. However, POPS tend to more often engage in extended and complex H-bonded lipid clusters of 3 or more lipids. In this case, interactions between lipids and lipid clusters may momentarily position the water in the wire while protons would travel along H-bonded water wires.

*Dynamic H-bond clusters at the anionic and zwitterionic membrane interface*

*Acidic POPS lipids show higher propensity to form lipid H-bond clusters as compared to zwitterionic POPC, POPE and acidic POPG, POPA lipids.*

Number of H-bonds formed by POPS and POPE headgroups is higher than POPC, POPG or POPA (Table 3.1, Figure 3.1). Acidic POPS shows a higher propensity to form direct and water mediated H-bonds (Table 3.1, Figure 3.1) as compared to the other lipid headgroups. The negatively charged carboxyl group in the acidic POPS headgroup increases the likelihood to form H-bonds with other molecules. Among lipid bilayers under study, POPS and POPE shows higher tendency to form lipid clusters with 86 % and 74 % of the total lipids participating in H-bond cluster formation respectively (Table A.3.1). Although more lipids participate in H-bond formation in POPS bilayer, the number of clusters sampled in POPE is higher than in POPS bilayer (Table A.3.1). This suggests the formation of bigger clusters in POPS bilayer as compared to POPE bilayers.

Lipid headgroups form highly dynamic H-bonds with low occupancies (Figure 3.2A). Most of the H-bonds have occupancies within 10 %. In POPC and POPA membranes, H-bonds have occupancies less than 1 % and 10 % respectively. This indicates that the H-bonds are only present occasionally and that they are constantly breaking and reforming. In contrast to POPC,

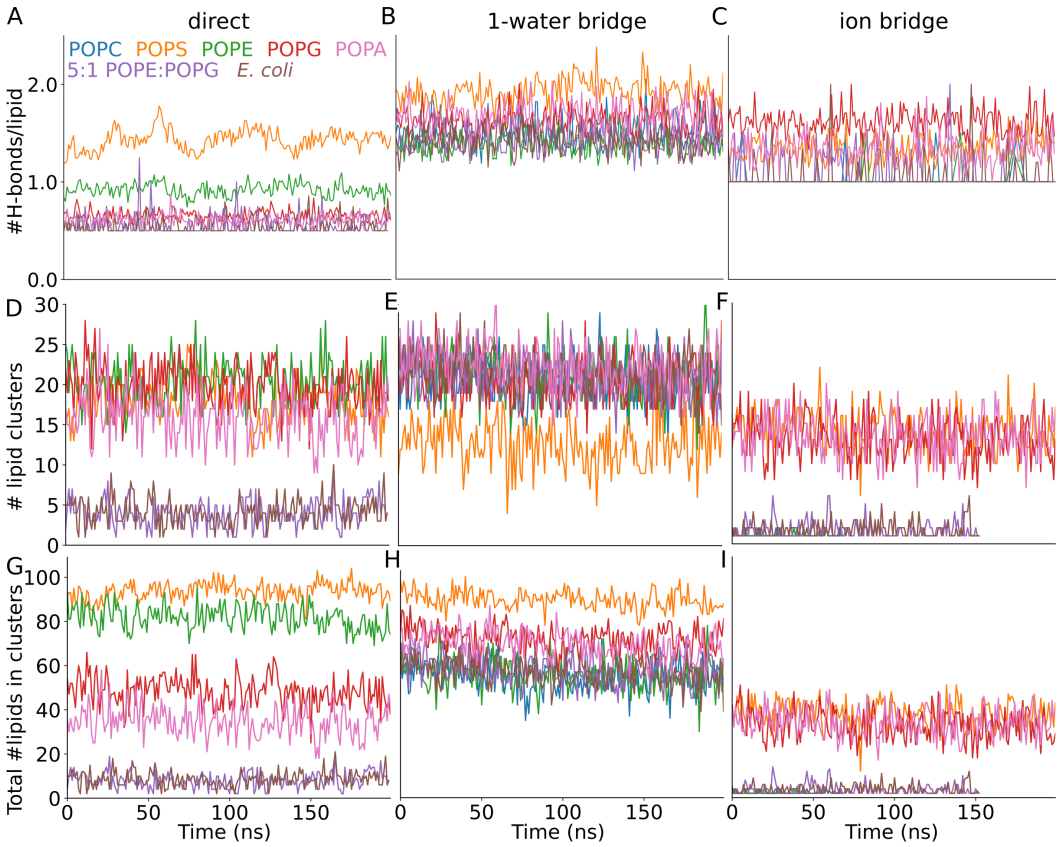


**Figure 3.1.** Dynamics of H-bonds and H-bond clusters in anionic and zwitterionic lipid bilayers. (A-C) Time series of the number of direct (Panel A), one-water mediated bridges (Panel B), and potassium-ion-mediated bridges between lipid headgroups (Panel C) in simulations of POPC (brown), POPE (blue), POPS (orange), POPG (green), POPA (pink), 5:1 POPE:POPG (red), and *E. coli* (purple) bilayers. (D-F) Time Series of #lipid cluster formed by direct (Panel D), one-water mediated (Panel E) and ion mediated (Panel F) H-bonds. (G-I) Total #lipid in clusters per frame forming lipid clusters mediated by direct (Panel G), one-water mediated (Panel H) and ion mediated (Panel I) H-bonds.

POPA, and POPG bilayers, membranes with POPS and POPE form extended 1-water mediated H-bond networks (Figures 3.2B-F). This can be attributed to the differing characteristics of the lipid headgroups. POPS and POPE have headgroups that are more polar than POPC, POPA, and POPG. The carboxyl group and amine groups in POPS and the amine group in POPE are more prone to form hydrogen bonds with water molecules because of their polarity (Figures 3.3A,B). The hydroxyl groups of POPG lipids may make contacts with one another (Figure 3.3C) although rarely sampled (Figure 3.2C). Zwitterionic and acidic lipids form lipid clusters mediated via molecules as depicted in Figure 3.3. The headgroups of POPC, POPA, and POPG, on the other hand, are less polar and more likely to form hydrogen bonds with one another. Acidic lipids can be discovered in groups with zwitterionic lipids in the membranes of POPE:POPG, and *E. coli* (Figures 3.3F-G).

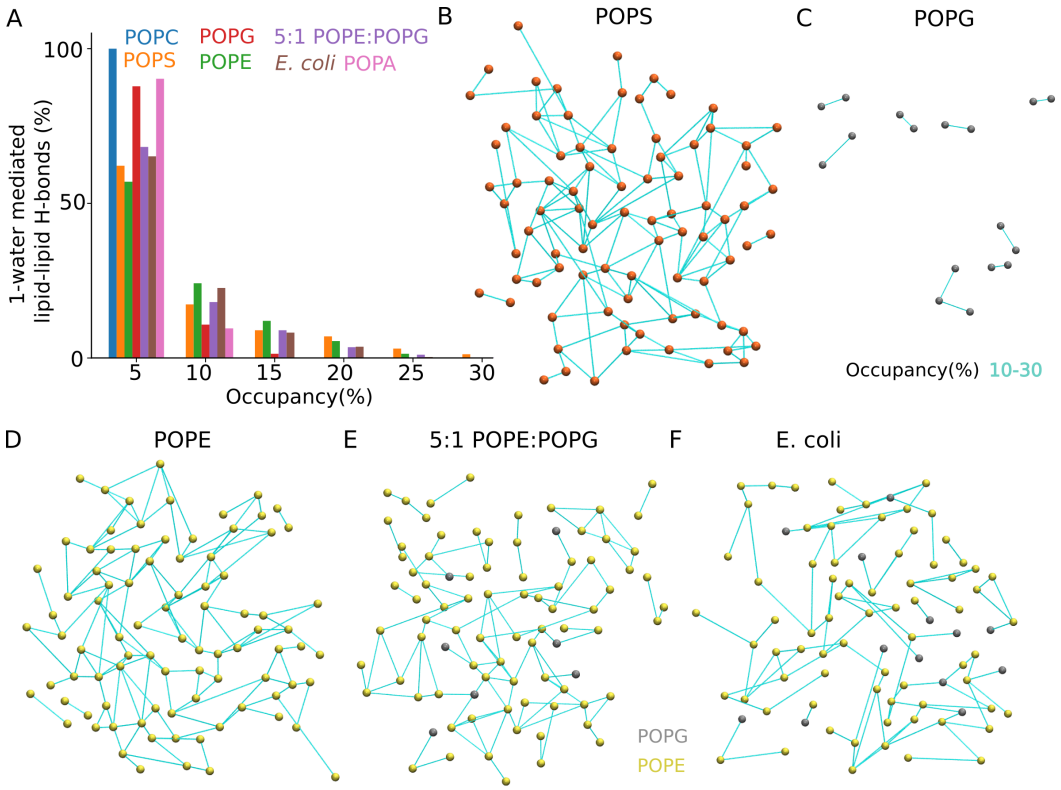


**Figure 3.2.** Water-mediated H-bond network at membrane interfaces. (A) Percentage of 1-water mediated lipid-lipid H-bonds in a particular occupancy range. (B-G) Illustration of water mediated H-bond network at the interface of POPS (Panel B), POPG (Panel C), POPE (Panel D), 5:1 POPE:POPG (Panel E), and *E. coli* (Panel F) membranes. The H-bond networks were computed using Bridge [34, 128]. H-bonds with occupancy greater than 10 % are shown here. In POPC and POPA membranes, H-bonds are sampled with less than 1 % and 10 % occupancy respectively.

*Topology analysis of H-bond lipid clusters formed by anionic and zwitterionic lipid headgroups*

All lipid headgroups have a tendency to form linear H-bond paths rather than star, star & linear, or combination arrangements of the three, according to topology analysis of lipid membranes (Figure 3.4). Linear H-bond paths show a 100% occurrence i.e at any given time, there is at least one linear H-bond path in any of the simulations reported here. By contrast, circular paths are sampled less frequently. Direct, 1-water mediated or ion-mediated lipid clusters of all the four main topologies are more likely to be sampled by POPS and POPE lipid headgroups (Figure 3.4). POPE and POPG tend to form direct H-bond clusters with different topologies whereas 5:1 POPE:POPG and Top6 bilayers only samples linear clusters with direct H-bonds. This suggests that the inter-lipid H-bonding interactions between PE and PG headgroups prefer linear arrangements (Figures 3.3F,G). POPC headgroups

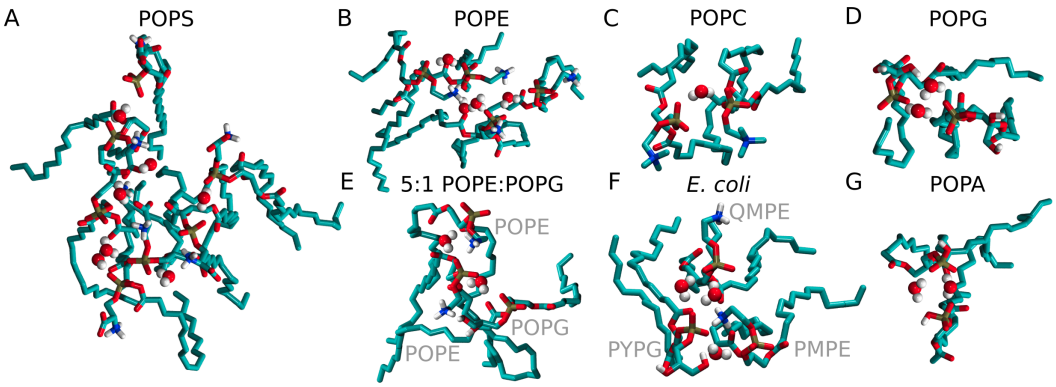


**Figure 3.3.** Illustration of H-bond clusters sampled in hydrated lipid membranes distinguished by lipid headgroups. (A-G) Molecular graphics of H-bonded clusters formed by POPS (Panel A), POPE (Panel B), POPC (Panel C), POPG (Panel D), 5:1 POPE:POPG (Panel E), *E. coli* (Panel F), and POPA (Panel G) lipids connected via one-water bridges.

do not form direct H-bonds. All lipid headgroups tend to form water mediated H-bond clusters with the four main topologies.

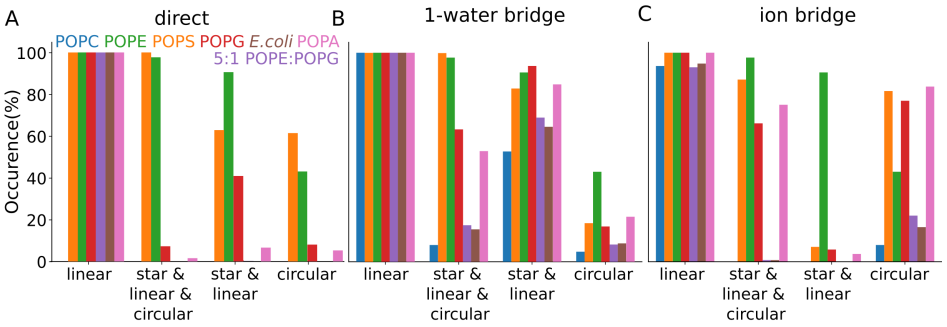


**Figure 3.4.** Topology analysis of lipid H-bond clusters. Main cluster topologies are identified with the DFS algorithm [42]. (A-C) Occurrence (%) of direct (Panel A), one-water bridge (Panel B) an ion-bridged (Panel C) H-bond clusters. Here, occurrence (%) as the percentage of the analysed trajectory where at least one lipid cluster of a specific lipid topology type is present irrespective of its size.

The H-bonded lipid clusters formed by lipid headgroups are highly transient. 1-water mediated lipid clusters show an occupancy of less than 0.3 % (Figure 3.5). Circular clusters are rarely sampled but when sampled show higher occupancies ($\geq$ 0.2 %) compared to other topologies in POPS, POPE, POPG and POPA bilayers.

A time series of linear H-bond clusters of varying lengths L, from L = 1 with two lipid headgroups bridged by one H-bonding water molecule to L = 6 highlights the dynamics of lipid H-bond clusters (Figure 3.6). Short H-bond clusters are persistently sampled throughout the simulation regardless of the lipid headgroup composition under test, though the precise number of paths (clusters) varies throughout the simulation. The number of H-bond paths

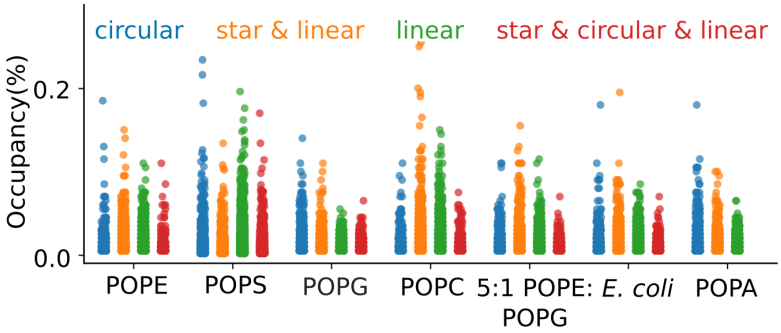


**Figure 3.5.** Occupancy of H-bond clusters sampled in hydrated lipid membranes distinguished by lipid headgroups and topology. Here, occupancy is defined as the percentage of the simulation where a specific lipid cluster is sampled. (A-C) Occupancy (%) of H-bond lipid clusters formed by lipid headgroups via direct (Panel A), 1-water bridged (Panel B) and ion bridged (Panel C) H-bonds.

and clusters would also depend on the size of the lipid bilayer under study for instance, L > 4 is rarely sampled.

Compared to other lipid headgroups being studied, POPS has a higher possibility of sampling extended H-bond clusters. All lipid headgroups prefer to sample linear clusters. This aligns with the results from Karathanou & Bondar [42]. However the H-bonding atoms considered for H-bonding calculation include the serine group of POPS, ethanolamine of PE, glycerol of PG and hydroxyl of POPA in addition to the phosphate group considered in the study by Karathanou & Bondar [42]. The transient linear arrangements of the lipid headgroups may affect the water H-bond networks close to the lipid headgroup clusters and these transiently oriented water H-bond networks may act as proton wires. In this case, the type and specifics of the phospholipid headgroup may have only a minor effect on the H-bond dynamics of lipid membranes involved in proton transfer.

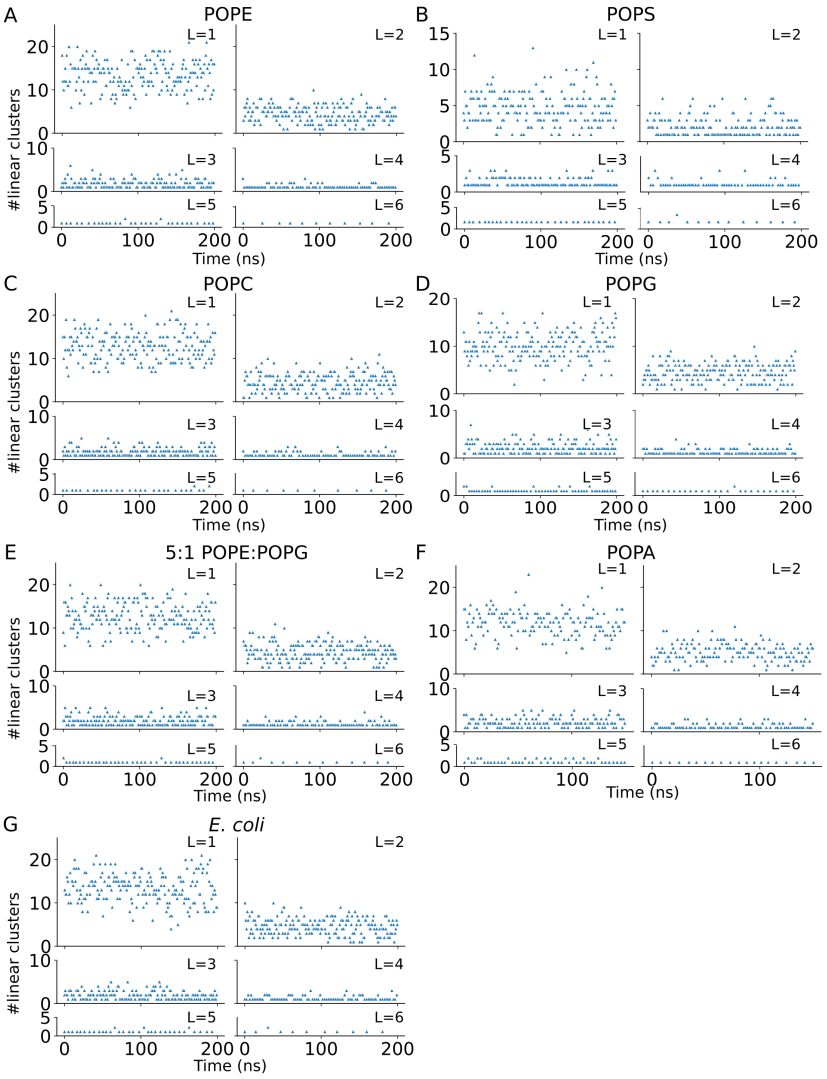


**Figure 3.6.** Path lengths of linear H-bond clusters formed by zwitterionic and anionic lipids. (A-G) Time series of number of linear H-bond clusters between POPE (Panel A), POPS (Panel B), POPC (Panel C), POPG (Panel D), 5:1 POPE:POPG (Panel E), POPA (Panel F), *E. coli* (Panel G) lipids connected via one-water bridges.

# 4

# Influence of cholesterol on the dynamics of hydrogen-bond clusters of POPS lipids

This work is based on the following publication:

Jain, H., Karathanou, K., & Bondar, A. (2023). Graph-Based analyses of dynamic Water-Mediated Hydrogen-Bond networks in phosphatidylserine: cholesterol membranes. Biomolecules, 13(8), 1238. https://doi.org/10.3390/biom13081238

The algorithm used for topology analysis in this chapter was developed by Konstantina Karathanou [42, 159]. Konstantina Karathanou's original work was modified by me to adapt to lipid bilayers with cholesterol for this project. I prepared all of the system setups, performed MD simulations, and did H-bond network and topology analysis on those systems that were described in the aforementioned study. Under the direction and close supervision of Prof. Dr. Ana-Nicoleta Bondar, I prepared the figures and wrote the text. In the publication, the phosphatidylserine bilayers without cholesterol and with 10% cholesterol were discussed. In this chapter, I also include analysis of phosphatidylserine bilayers with 20, 30 and 40 % cholesterol.

Parts of the work presented in this chapter are originally published in the journal Biomolecules. Figures and text originally published in the journal are modified in order to be presented in this chapter. Adapted figures and tables will be noted with "Adapted from ref. [160]."

The concentration of cholesterol in mammalian plasma membranes may vary significantly, which could impact the dynamics of lipid interactions and interactions at the membrane interface. As discussed in Chapter 3, anionic phosphatidylserine tends to form extended H-bond networks. Cholesterol can H-bond with phosphatidylserine (PS) impacting the H-bond dynamics of lipid bilayers. To characterize interactions at the interface of cholesterol-containing membranes, I carried out atomistic simulations and graph-based analyses of H-bonding patterns at different depths of hydrated phosphatidylserine membranes without and with cholesterol. I find that the extended H-bond networks are more likely to be formed by the serine group at the water-lipid interface as compared to the buried ester or phosphate groups. Phosphatidylserine tends to form linear H-bond paths. The presence of cholesterol decreases the likelihood that phosphatidylserine lipids engage in relatively complex and extended water-mediated hydrogen-bond networks at the membrane interface. This suggests that cholesterol shapes the dynamics of the lipid-water hydrogen-bond network, which could impact the binding of biomolecules and drugs at the membrane interface.

Cholesterol is present in a significant amount in eukaryotic membranes. Presence of cholesterol straightens the acyl chains of phospholipids resulting in a decrease in the area per lipid [70–74, 176]. This is termed as condensing effect [70–74, 176]. Cholesterol causes causes higher lipid hydrocarbon chain ordering [63–66] that allow tighter packing of lipids. This further restricts lateral lipid diffusion along the membrane plane [67], and increases lateral pressure profile magnitudes [68, 69]. Cholesterol shows a condensing effect on phospholipid bilayers .

The altered concentration and distribution of cholesterol in membranes is associated with a number of diseases, such as Alzheimer's disease [177] and cancer [178–180]. Typically healthy mammalian plasma membranes contain between 10 to 40 % cholesterol [62], whereas membrane cholesterol content varies among types of cancer cells. For example, Jurkat cell lines show about $\sim$20 mol % cholesterol content [181] whereas certain breast cancer cell lines show up to $\sim$35 mol % [182]. Cancer cells undergoing metastasis regulate their membrane fluidity by varying the cholesterol content [178–180]. Reduction in cholesterol levels provides membrane fluidity that helps in metastasis [183, 184] and an increase in the cholesterol concentration appears to associate with chemotherapy resistance [185, 186].

Cholesterol interacts with lipids in the membrane leaflets and alters their structure and dynamics. Due to the presence of the hydroxyl group, cholesterol can H-bond to lipid headgroups [187]. A stable H-bond network of

numerous lipid complexes can be formed due to the property of PS lipids to form inter-lipid H-bonds, which considerably lessen the rotational movements of the lipid headgroups [165] (Chapter 3). Cholesterol prefers to interact with anionic lipids i.e PS and PG rather than the zwitterionic PC and PE [84, 188, 189]. This preference can be attributed to the charged lipid head groups' tendency to form additional free volume in the membrane due to their electrostatic repulsion, which results in a less tightly packed arrangement of the head groups. This makes it easier for cholesterol molecules to intercalate between anionic lipids. When cholesterol is added to lipid bilayers, the packing becomes looser at the lipid headgroups and tighter at the tails [190] and a reduction is observed in the Na+ binding to the lipid membrane interfaces [191].

Molecular dynamics studies and H-bond network analysis show that anionic lipids can form water mediated H-bond clusters between lipid headgroups (Chapter 3). In comparison to the bulk, the water dynamics at the lipid interface are slower [192–194]. The slower relaxation rates of interfacial waters H-bonded to lipids than bulk water suggest that the lipid-lipid interactions are facilitated by H-bond networks in the hydration layer of membranes [192]. H-bonding interactions are more common at the hydrophilic region close to the lipid-water interface due to the presence of water. As we go deeper from the membrane surface, the number of waters decreases and H-bonding is less profound as compared to the interface. However esters and phosphate groups of lipids can still engage in H-bonding with nearby lipids and water molecules. Interfacial waters have been shown to H-bond at different depths with the carbonyl, phosphate and glycerol or serine group of PC [192] or PS [195] bilayers respectively. With increasing membrane depth, less H-bonds exist between water molecules at the interface of DMPC [192] and DOPS [195] bilayers. In case of POPS, the serine group with two H-bonding groups explains its high propensity for forming H-bonds as compared to other phospholipids. The glycerol group of anionic PG membrane, an additional H-bond acceptor as compared to PC membrane, has been proposed to contribute in stabilizing the H-bonds formed by water molecules with phosphate [196]. The presence of sodium cation close to the anionic PG interface may disturb the H-bond network formed in the bulk and stabilizes the H-bond network near the phosphate group [196]. This suggests that the dynamic interaction between hydrophilic and hydrophobic forces inside lipid membranes is reflected in the depth-dependent variation in H-bonding, which eventually affects the structure and behavior of the membrane.

Anionic POPS lipids have a higher propensity to form lipid H-bond clusters as compared to zwitterionic POPC, POPE and acidic POPG, POPA

lipids (Chapter 3). These lipid clusters H-bonded via direct H-bond, water molecules or ions are highly transient. PS lipids can form clusters of 3-6 lipids [42, 83] (Chapter 3). These PS clusters can further form nanometer-sized domains [172, 197, 198] that provides a platform for electrostatic interactions at the plasma membrane and cytosolic interface for peripheral protein recruitment. PS clustering enhances viral assembly in Ebola virus [174] and the interaction of the influenza A virus matrix protein with lipid membranes [172].

Presence of cholesterol can influence the PS clustering. Cholesterol binds to PS while keeping the headgroups of PS sufficiently apart to prevent spontaneous curvature [198]. It prefers to H-bond to a single lipid carbonyl or phosphate oxygen atom rather than forming cholesterol clusters [199–201]. Cholesterol does not serve as a link between two H-bonded PS clusters creating a bigger cluster that can span the entire leaflet [201]. Instead, cholesterol tends to join the H-bonded cluster formed by lipid headgroups and expand its size [201].

Lipid cluster formation can also be aided by ion interactions, particularly with anionic lipids like phosphatidylserine (PS) [42, 202, 203], phosphatidylglycerol (PG) [42] or phosphatidylinositol 4,5-bisphosphate (PIP2) [204]. Interactions between charged lipid headgroups and cations such as - sodium [42, 202, 205–208], potassium [202], cesium [202], calcium [203, 207, 208] or magnesium [209] may influence and induce clustering of lipids. For example, sodium ions tend to form larger clusters in PIP2 bilayers [210] and show a higher affinity to POPC/POPS lipid headgroups [202] as compared to potassium ions. The presence of anionic PS lipids in POPS/POPC bilayer reduces sodium ion mobility around the ester group [202] increasing the possibility of stable ion-mediated cluster formation. In comparison to PC bilayers, PE lipid bilayers show weak binding to sodium and potassium ions, which can be attributed to PE lipids' capacity to form both intra- and intermolecular H-bonds and, as a result, to adopt a more densely packed bilayer structure [211]. These ion interactions can affect the mechanical and dynamic properties of the lipid membranes [212] and further stabilize lipid clusters. Presence of cholesterol in the lipid membrane reduces the surface charge density resulting in reduced ion binding at the interface [191].

In this chapter, the focus lies on H-bond networks formed by the anionic lipid phosphatidylserine (PS) and cholesterol. PS lipid headgroups have a high propensity to form H-bonds. This suggests formation of extended H-bond networks that can lead to PS clustering. The ability of cholesterol to intercalate between PS headgroups and form H-bonds with PS lipids can

influence the H-bond dynamics of PS lipids. These H-bond networks formed by PS and cholesterol can influence physical and structural properties of the membranes making them an important target for understanding and regulating biological functions. As discussed above, the clustering of POPS and the role of cholesterol in modulating the structural properties of lipid membranes have been studied separately before. It has also been reported that PS lipids can form H-bonds via water at different depths of lipid bilayers between the phosphate, ester and serine groups. However, the H-bond dynamics of POPS clusters in the presence of cholesterol and at different depths of the lipid bilayers is yet to be explored. Here, I use molecular dynamics simulations and a graph-based analysis to characterize the properties of H-bonded lipid clusters in hydrated bilayers of POPS without and with 10, 20, 30 and 40 % concentration of cholesterol. Lipid bilayers with $\geq$ 20 % cholesterol concentration might show morphological changes such as a standing wave with local concave curvature resulting from partitioning of cholesterol [213]. I identify H-bond clusters formed by phosphate, serine and ester groups of PS lipid headgroups and characterize these direct, 1 water-mediated H-bonded and ion-mediated lipid clusters into 4 main topologies using the DFS algorithm [42]. Water mediated H-bond clusters formed by phosphatidylserine (PS) are transient as compared to the direct H-bond clusters. The water mediated H-bond network formed by the serine group is more frequently sampled as compared to the phosphate or ester group. PS lipids tend to form linear clusters rather than complex arrangements. In the presence of cholesterol, the tendency of phosphatidylserine lipids to form extensive and complex clusters even decreases further. The approach used here to study anionic lipid membranes with cholesterol provides insights into the dynamics of the lipid-water hydrogen-bond network at different depths of the lipid bilayers, which may have an effect on how biomolecules interact at the membrane interface. The approach to study lipid bilayers with cholesterol discussed in this chapter can be applied to any lipid membranes of different compositions.

*Influence of cholesterol on physical properties of phosphatidylserine membranes*

The presence of cholesterol is associated with a thickening of lipid bilayer, an increase in lipid tail order and a decrease in area per lipid in the presence of cholesterol [70–74, 176] key properties of condensing effect. Cholesterol can intercalate between lipid molecules leading to tighter lipid packing, increased membrane rigidity and decreased lipid mobility [67]. With increase in cholesterol content the condensing effect increases up to a certain threshold

of cholesterol concentration (40-50 %) beyond which the membrane integrity might be disrupted [214].

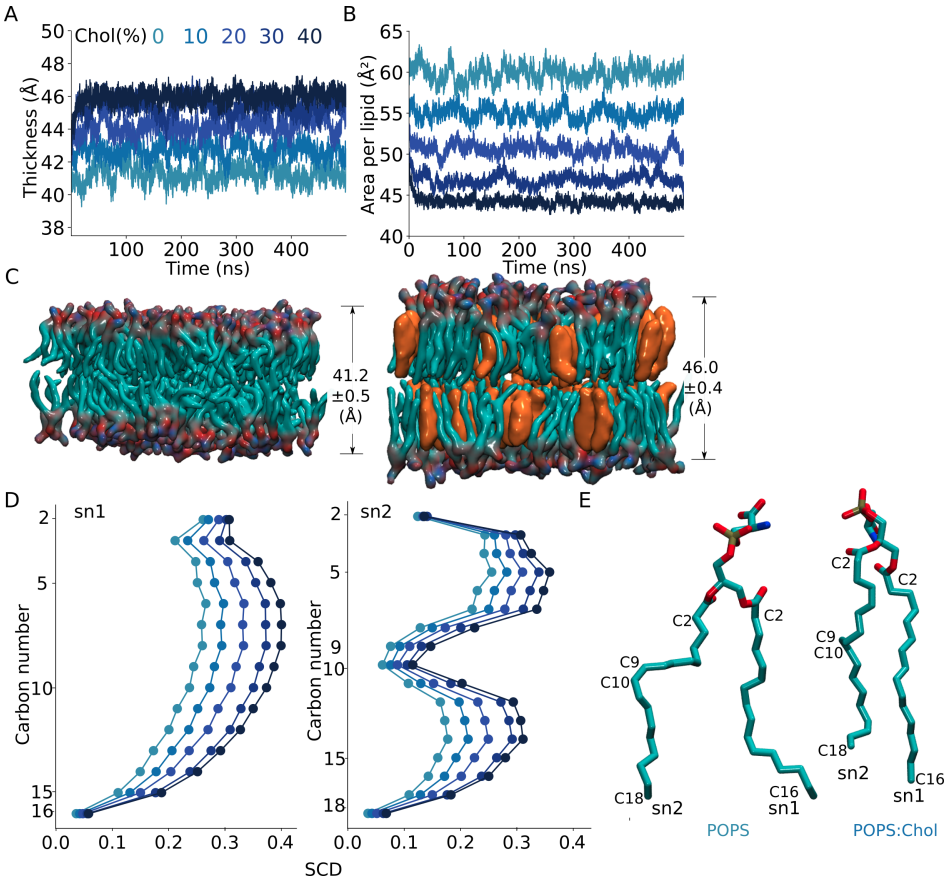


**Figure 4.1.** Structure factors of hydrated POPS lipid bilayers with varying cholesterol concentration. (A) Thickness of lipid bilayer. (B) Area per lipid. (C)Molecular graphics based on a coordinate snapshot showing average membrane thickness of POPS lipid bilayers without (left) and with 40 % (right) cholesterol content. POPS tails and headgroups are shown as cyan and red-blue lines respectively. Cholesterol is shown in orange. (D) Order parameters SCD *sn*1 and *sn*2. (E) Molecular graphics showing increase in order parameters of POPS due to presence of cholesterol. Adapted from ref. [160].

In the simulations reported here (Table 4.1), a change in physical properties of bilayer is observed due to the presence of cholesterol is observed. The average membrane thickness for POPS membrane without cholesterol is 41.2 ± 0.5 Å. This value is close to previously reported values of 43.2 ± 0.5 Å [66], 40.6 Å [215], 42.3 Å [216], 42.1 ± 0.5 Å [42] determined by MD simulations and 42.2 Å measured by neutron and X-ray scattering in presence of NaCl [215]. As the concentration of cholesterol increases from 0 to 40 %, the membrane thickness increases from 41.2 ± 0.5 Å to 46.0 ± 0.4 Å (Figure 4.1A). The thickness of the POPS membrane increases by 1.5Å in the presence of 10 % cholesterol (Table 4.1), which is consistent with

a 2.2 Å increase in the thickness of the DMPC/cholesterol membrane with 10 % cholesterol [217] compared to pure DMPC. Each 10% increase in the cholesterol concentration associates with ∼1.0-1.5 Å increase in the average membrane thickness (Table 4.1) such that, in the presence of 40 % cholesterol, the membrane is ∼5 Å thicker than in the absence of cholesterol. An increase of the membrane thickness by ∼6 Å has been previously reported for POPC/POPS/cholesterol [218]. Presence of cholesterol straightens the acyl chains of the POPS lipids (Figure 4.1E) that could result in an increase in the membrane thickness.

The area per lipid for the POPS membrane was calculated to be 59.8 ± 1.9 Å$^2$, which is relatively close to previously published values from MD simulations (58.4 Å$^2$ [219], 57.5 ± 1.2 Å$^2$ [216], and 62.0 Å$^2$ [215]). With an increase in cholesterol concentration from 0 to 40 %, the area per lipid drops from 59.8 ± 1.0 Å$^2$ to 44.2 ± 0.5 Å$^2$ (Figure 4.1B). A decrease of ∼5 Å$^2$ in the area per lipid (Figure 4.1B) is in reasonable qualitative agreement with a decrease of ∼6-7 Å$^2$ in the area per lipid of a DOPC/cholesterol membrane with 10 % cholesterol [73, 176]. The SCD order parameters of POPS membrane without cholesterol (Figure 4.1D) are also compatible with previous studies [216, 219]. The *sn*1 and *sn*2 SCD order parameters show an increase with increase in cholesterol (Figures 4.1D,E).

**Table 4.1.** Structure factors of POPS bilayers without and with cholesterol.

| Sim | Membrane thickness (Å) | Area per lipid (Å$^2$) |
|---|---|---|
| POPS | 41.2 ± 0.5 | 59.8 ± 1.0 |
| POPS:Chol (10%) | 42.7 ± 0.5 | 54.9 ± 0.8 |
| POPS:Chol (20%) | 44.2 ± 0.5 | 50.6 ± 0.7 |
| POPS:Chol (30%) | 45.4 ± 0.5 | 46.9 ± 0.7 |
| POPS:Chol (40%) | 46.0 ± 0.4 | 44.2 ± 0.5 |

## 4.1 Dynamic H-bond network formed by POPS headgroups and cholesterol

*H-bonds formed by POPS lipid headgroups at different depths of lipid bilayer.*

To understand the distribution of H-bond networks at different depths of lipid bilayer, I calculated H-bonds formed by 5 different groups of POPS lipid headgroup - phosphate, serine, ester, phosphate & serine and all the groups together (Figure 2.4). I identified and characterised direct and 1-water

mediated H-bond networks formed by these five groups. In this section as the focus lies on understanding the distribution of H-bond network at different depths of lipid bilayers, I only include data analysis for the simulations of POPS bilayers without and with 10% cholesterol. Direct interactions show a consistent number of H-bonds between POPS lipid headgroups and POPS-Cholesterol, with an average of 1.5 ± 0.1 H-bonds (Table 4.2, Figure 4.2A), which is very close to the 1.1-1.2 H-bonds/POPS lipid headgroup reported previously from MD simulations with CHARMM36 force field [165]. In the case of 1-water mediated interactions, there is an increase in the number of H-bonds, averaging 2.3 ± 0.2 H-bonds (Table 4.2, Figure 4.2B). Whereas ion bridge interactions also exhibit an average of 1.5 ± 0.1 H-bonds (Table 4.2, Figure 4.2C). Comparing specific H-bonding groups, interactions involving phosphate-only and serine-only groups demonstrate slightly higher 1-water mediated H-bonds 1.4 ± 0.1 and 1.3 ± 0.1 respectively as compared to interactions involving ester alone with an average of 1.1 ± 0.1 H-bonds per lipid (Table 4.2, Figure 4.2). When the ester group is included as an H-bonding group along with phosphate and serine, the number of 1-water mediated H-bonds increases from 1.9 ± 0.1 to 2.3 ± 0.2 (Table 4.2, Figure 4.2). This suggests that ester group is likely to be involved in water mediated H-bonding with the serine or phosphate group. H-bonds formed by the ester-only and phosphate-only groups have very low occupancies of <1 % whereas serine-only groups can form H-bonds with occupancies upto 15-20 %. No significant difference is observed in occupancies when ester group interactions are considered with the phosphate & serine group. The presence of cholesterol does not seem to affect the total average number of H-bonds per POPS molecule (Figure 4.2).

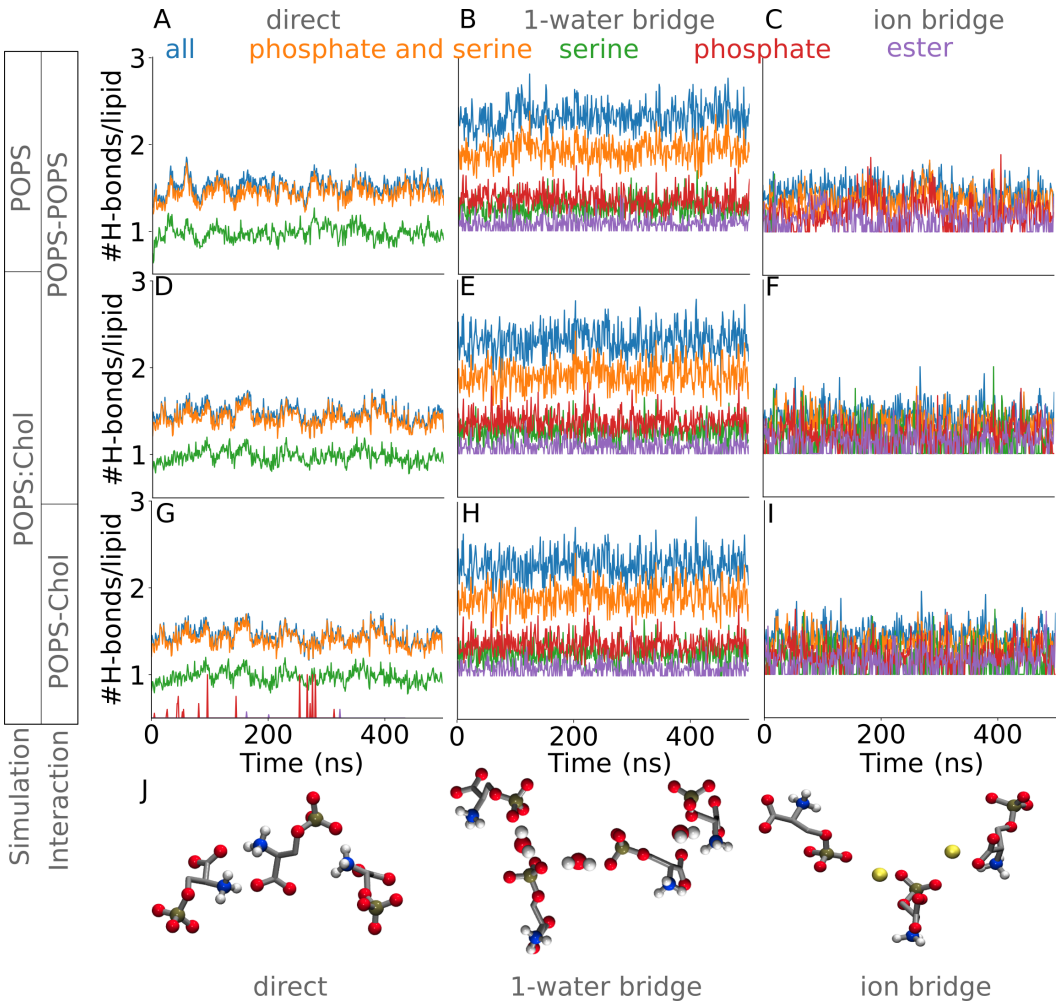


**Figure 4.2.** H-bonds per POPS. (A-C) Time series of the number of direct lipid H-bonds (Panel A), 1-water mediated (Panel B) and ion-mediated bridges between POPS (Panel C) sampled in simulations of the POPS membrane without cholesterol. (D-F) Time series of the number of direct lipid H-bonds (Panel D), 1-water mediated (Panel E) and ion-mediated bridges between POPS (Panel F) sampled in simulations of the POPS membrane with 10% cholesterol. (G-I) Time series of the number of direct lipid H-bonds (Panel G), 1-water mediated (Panel H) and ion-mediated bridges between POPS (Panel I) sampled between POPS-cholesterol in simulations of the POPS membrane with 10 % cholesterol. The blue profile shows the total number of H-bonds per POPS. The following color code is used for the groups of atoms of POPS: serine, green, phosphate, red, ester, purple, phosphate and serine, orange. The coordinate sets were read every 1 ns for clarity. (J) Molecular graphics showing direct POPS H-bonds (left), 1-water bridging (middle), and potassium ion-mediated bridges (right). This figure is taken from ref. [160].

**Table 4.2.** Number of H-bonds per lipid in simulations of POPS without and with 10 % cholesterol.

| Simulation | Interaction | H-bonding groups | direct | 1-water bridge | ion bridge |
|---|---|---|---|---|---|
| POPS | POPS-POPS | all | 1.5 ± 0.1 | 2.3 ± 0.2 | 1.5 ± 0.1 |
| | | phosphate & serine | 1.4 ± 0.1 | 1.9 ± 0.1 | 1.3 ± 0.1 |
| | | phosphate | - | 1.4 ± 0.1 | 1.2 ± 0.2 |
| | | serine | 1.0 ± 0.1 | 1.3 ± 0.1 | 1.2 ± 0.2 |
| | | ester | - | 1.1 ± 0.1 | 1.1 ± 0.1 |
| POPS:Chol (10%) | | all | 1.5 ± 0.1 | 2.3 ± 0.2 | 1.4 ± 0.1 |
| | | phosphate & serine | 1.4 ± 0.1 | 1.9 ± 0.1 | 1.3 ± 0.1 |
| | | phosphate | - | 1.4 ± 0.1 | 1.2 ± 0.1 |
| | | serine | 1.0 ± 0.1 | 1.3 ± 0.1 | 1.1 ± 0.2 |
| | | ester | - | 1.1 ± 0.1 | 1.1 ± 0.1 |
| | POPS-Chol | all | 1.4 ± 0.1 | 2.3 ± 0.1 | 1.5 ± 0.1 |
| | | phosphate & serine | 1.4 ± 0.1 | 1.9 ± 0.1 | 1.3 ± 0.1 |
| | | phosphate | 0.5 ± 0.1 | 1.4 ± 0.1 | 1.2 ± 0.1 |
| | | serine | 1.0 ± 0.1 | 1.3 ± 0.1 | 1.1 ± 0.2 |
| | | ester | 0.5 ± 0.0 | 1.1 ± 0.1 | 1.1 ± 0.1 |

The analysis shows that both direct and water-mediated H-bonds between POPS headgroups have low occupancies. Around 83-93 % of direct H-bonds have occupancies within 10-15 % (Figures 4.3A,C) whereas 69-100 % of the one-water bridges computed for the different POPS H-bonding groups have occupancies within about 5 % (Figures 4.3B,D). This indicates that these interactions are highly dynamic, with frequent formation and dissolution of the H-bonded bridges by lipid molecules during the course of the simulation. Within the distribution of occupancy of both direct H-bonds and one-water-mediated bridges, a number of data points stand out as outliers (Figure 4.3). These outliers show certain instances of H-bonding interactions that are persistent in the highly dynamic environment and exhibit occupancy levels that are noticeably greater than the average. Figure 4.3 shows about 4-8% of H-bonds (Table 4.3) that fall into this category of outliers. A closer look at the outliers reveal that an average of 35 lipids (32 % of total lipids) engage in direct H-bonding whereas 49 lipids (45 % of total lipids) are bridged via one water molecule at any moment of time during the POPS bilayer simulation (Table 4.3, Figure 4.4). Within specific H-bonding groups at increasing different depths from serine to ester group of POPS, the average number

of lipids forming high occupancy H-bonds decreases significantly (Figure 4.4). In POPS membranes with cholesterol, a similar trend is observed with 24 and 39 % of total lipids participating in direct and one-water mediated H-bonds showing an overall decrease in average number of lipids forming high occupancy H-bonds as compared to POPS membranes without cholesterol. The lipid outliers forming the highest-occupancy H-bonds in POPS simulation (Figures 4.5A,C) remain within H-bond distance for 306.2ns (61.2 % of POPS simulation) (Figure 4.5E) and in the POPS:cholesterol simulation (Figures 4.5B,D) for 360.2ns (72 % of the simulation) (Figure 4.5F).

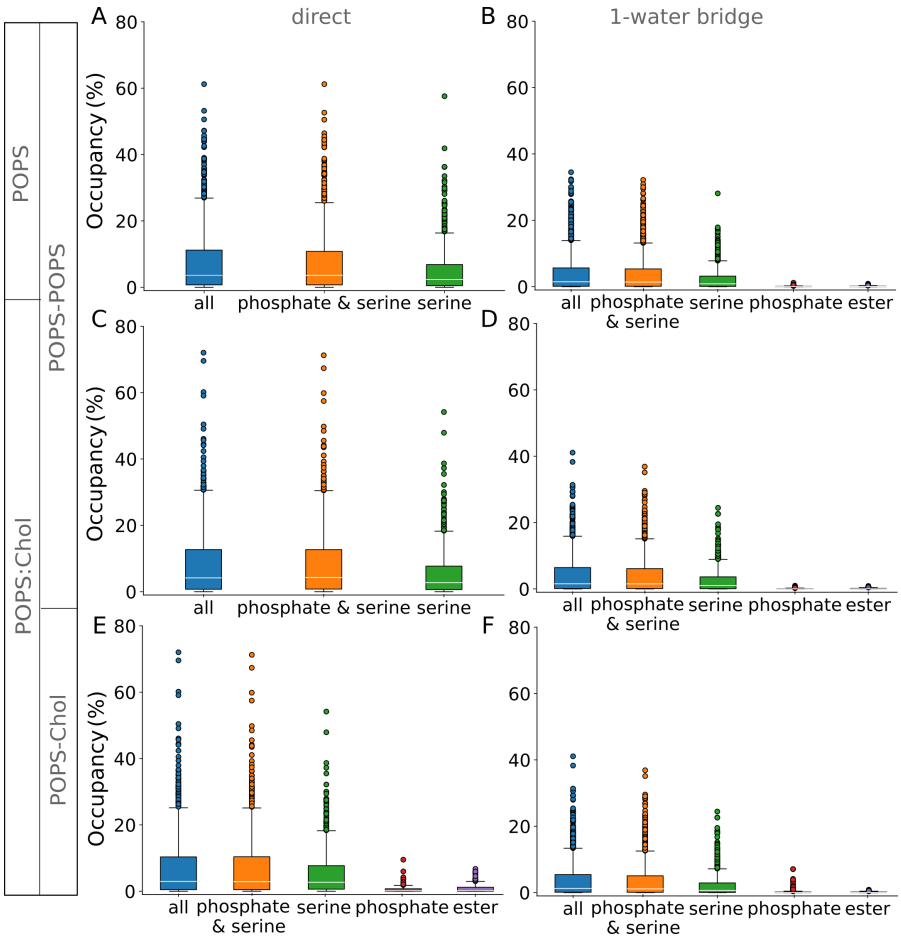


**Figure 4.3.** Occupancies of H-bonds and water-mediated bridges. The boxplots show H-bond occupancy values extracted with Bridge [34, 128] for interactions between phosphate groups, serine, ester groups, and for all these three groups (see Scheme 1A). (A-D) Direct H-bond (Panels A, B) and 1-water bridges (Panels C, D) occupancies (%). Note that, there are no direct H-bonds sampled between phosphate or ester groups in Panels A and C. (E-F) Direct POPS-cholesterol H-bond (Panel E) and 1-water bridges (Panel F) occupancies (%). Overall, the high-occupancy H-bonding and water bridging shown here for the various moieties are usually formed by the same pairs of headgroups. The boxplots were generated using Python. This figure is taken from ref. [160]

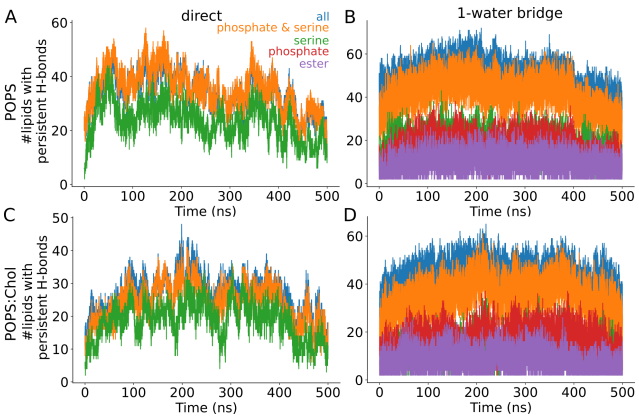


**Figure 4.4.** Time evolution of number of POPS forming high occupancy H-bonds. (A-B) Number of lipids forming high occupancy direct (Panel A) and 1-water bridged (Panel B) between different H-bonding groups of POPS headgroups at any moment of time in POPS simulations without cholesterol. (C-D) Number of lipids forming high occupancy direct (Panel C) and 1-water bridged (Panel D) between different H-bonding groups of POPS headgroups in POPS simulations with 10% cholesterol.

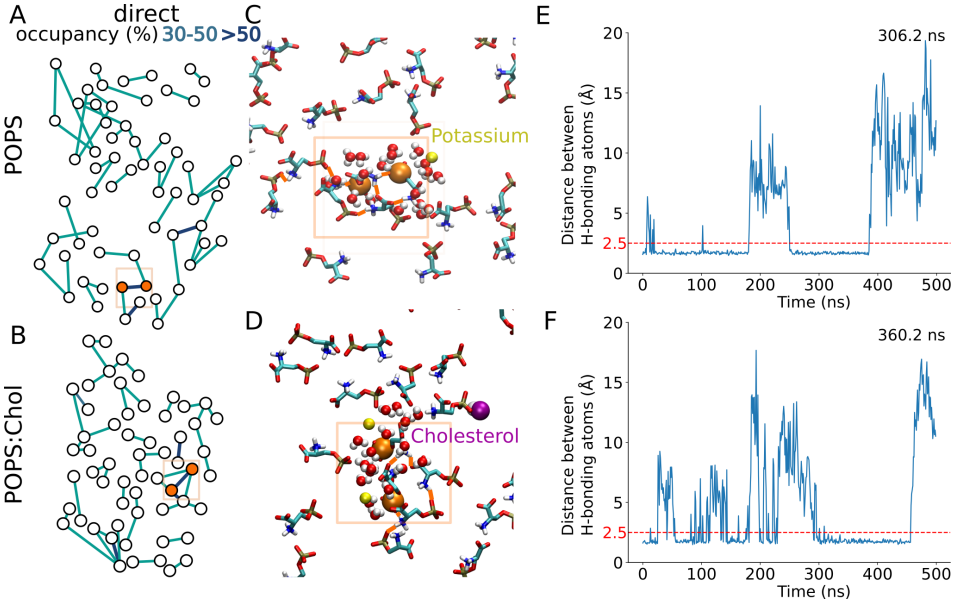


**Figure 4.5.** High occupancy direct H-bonds formed by POPS headgroups. (A-B) Graph representation of direct H-bond network formed between POPS headgroups in POPS simulations without (Panel A) and with 10 % (Panel B) cholesterol. Orange highlighted lipid headgroups form the highest occupancy H-bond. (C-D) Molecular graphics of illustrating interactions of high occupancy direct H-bonds in POPS simulations without (Panel C) and with 10 % (Panel D) cholesterol corresponding to Panels A and B respectively. (E-F) Time series of distance between H-bonding groups of lipid headgroups forming highest occupancy H-bond in POPS simulations without (Panel E) and with 10 % (Panel F) cholesterol shown as highlighted orange circles in Panels A,C and Panels B,D respectively.

**Table 4.3.** Number of lipids forming high occupancy H-bonds in simulations of POPS without and with 10 % cholesterol.

| Simulation | | H-bonding groups | Average #lipids with high occupancy H-bonds | % of average #lipids with high occupancy H-bonds | #high occupancy H-bonds | Total #H-bonds | % high occupancy H-bonds |
|---|---|---|---|---|---|---|---|
| POPS | direct | all | 35 | 32 | 69 | 1254 | 5.5 |
| | | phosphate & serine | 36 | 33 | 74 | 1233 | 6.0 |
| | | serine | 24 | 22 | 67 | 1162 | 5.8 |
| | 1-water bridge | all | 49 | 45 | 131 | 1617 | 8.1 |
| | | phosphate & serine | 42 | 38 | 124 | 1596 | 7.8 |
| | | serine | 18 | 16 | 112 | 1526 | 7.3 |
| | | phosphate | 17 | 16 | 67 | 1596 | 4.2 |
| | | ester | 10 | 9 | 62 | 1026 | 6.0 |
| POPS: Chol (10%) | direct | all | 27 | 24 | 45 | 985 | 4.6 |
| | | phosphate & serine | 25 | 23 | 41 | 966 | 4.2 |
| | | serine | 19 | 17 | 50 | 904 | 5.5 |
| | 1-water bridge | all | 43 | 39 | 89 | 1284 | 6.9 |
| | | phosphate & serine | 36 | 33 | 86 | 1263 | 6.8 |
| | | serine | 13 | 12 | 78 | 1207 | 6.5 |
| | | phosphate | 17 | 15 | 45 | 1263 | 3.6 |
| | | ester | 8 | 7 | 39 | 785 | 5.0 |

*H-bond networks formed by POPS lipid headgroups at different depths of lipid bilayer.*

The 1-water mediated H-bond networks formed by POPS headgroups between the serine-only and ester-only groups are more extended as compared to phosphate-only groups (Figure 4.6) and exclusively sampled for serine-only groups when direct H-bonds are considered (Figure 4.7). At the water-membrane interface, the carboxyl and amine of the serine groups have a higher propensity for H-bonding due to their exposure to the aqueous environment. As the depth increases, the hydrophobic environment hinders the formation of H-bonds with water molecules. The number of water molecules interacting with the serine group are significantly higher than the phosphate and ester groups (Figure 4.8). High occupancy H-bond networks with H-bond occupancies >30 % for direct and >15 % for 1-water mediated H-bonds are observed between serine-only, phosphate & serine and phosphate & serine & ester groups (Figures 4.6,4.7). Due to the transient nature of interactions between ester groups, there is no significant difference between high occupancy H-bond network when ester is considered as H-bonding group along

with phosphate & serine compared to when it is not (Figures 4.6,4.7). For this reason, phosphate & serine groups are used as H-bonding groups for further analysis. The comparison of H-bonding between POPS only and POPS-Chol systems reveals similar trends with slight variations in the H-bond counts for different H-bonding groups.

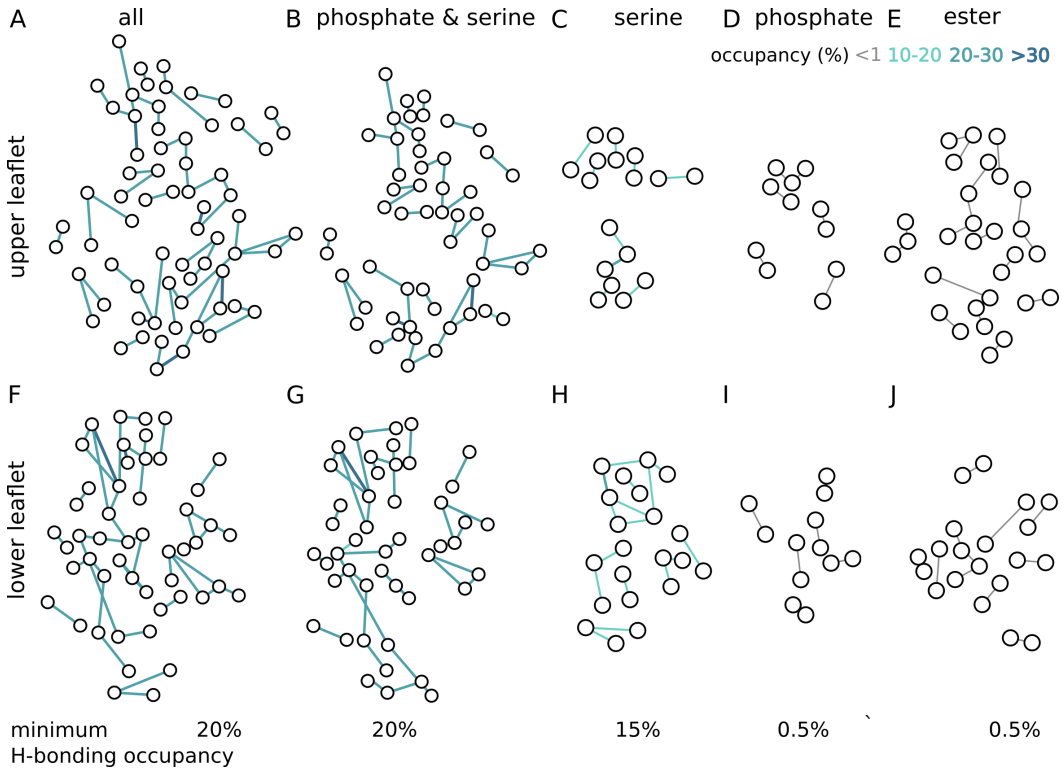


**Figure 4.6.** Water-mediated H-bond network of the hydrated POPS membrane. H-bonds were computed using Bridge [34, 128] and are shown in the Principal Component Analysis (PCA) projection onto the two-dimensional plane of the Cartesian coordinates of the lipid groups used as nodes of the graph computation [34]. H-bonding groups (graph nodes) are represented by circles, and one-water-bridges, by the edges between nodes. For simplicity, the two bilayer leaflets are referred as 'upper' vs. 'lower', which are meant to indicate, respectively, positive vs. negative values of the z coordinates of the lipid headgroups. Only one-water bridges were included in the graph computation. The minimum H-bond occupancy (%) is indicated at the bottom of the figure. (A-J) Illustration of H-bond networks computed for all H-bonding POPS groups ('all' in Scheme 1) (Panel A, F), for phosphate and serine groups (Panels B, G), serine (Panels C, H), phosphate (Panels D, I) and ester (Panels E, J).

To gain further insights and to visualise the H-bonding pattern of POPS at the interface of each leaflet of the lipid bilayer, the H-bond networks formed by phosphate and serine groups of POPS headgroups were calculated using Bridge [34, 128]. Extended H-bond network formed by direct or water mediated H-bonding is observed on each leaflet. Both leaflets show sim-

ilar distribution of H-bond networks and occupancies of H-bonds. Higher occupancy direct H-bonds are sampled as compared to 1-water mediated H-bonds (Figures 4.9A,B,D,E,G). With 3 water molecules forming a water wire, a dense and high occupancy H-bonded network is observed (Figures 4.9C,F,G).

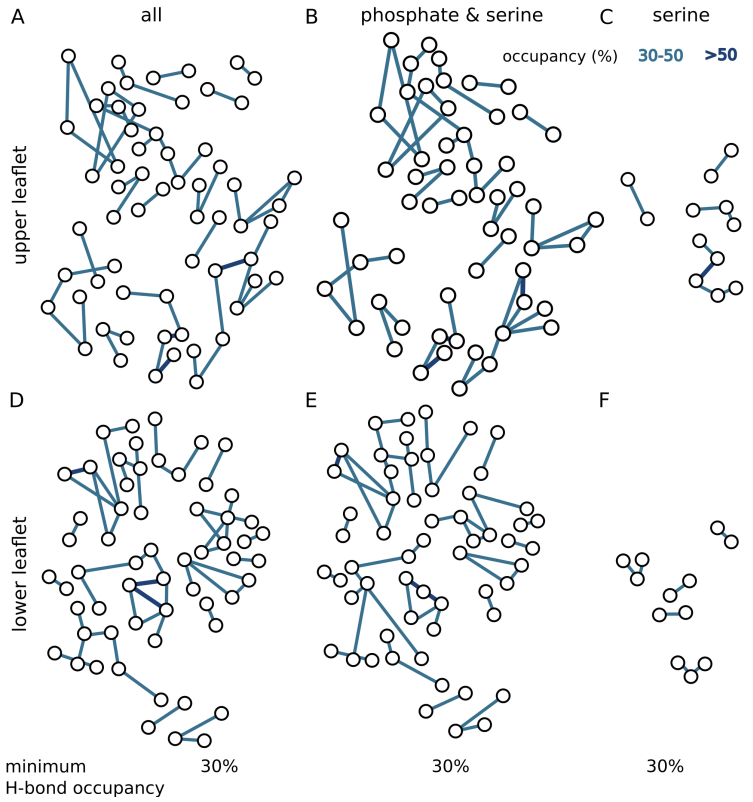


**Figure 4.7.** Illustration of transient networks of direct H-bonds between POPS headgroups. Bridge [34, 128] was used to compute H-bonds for all H-bonding groups of POPS, for phosphate and serine and serine, only. (A-F) H-bond networks of direct H-bonds for all POPS H-bonding groups as defined in Scheme 1 (Panels A, D), phosphate and serine (Panels B, E) and serine (Panels C, F).

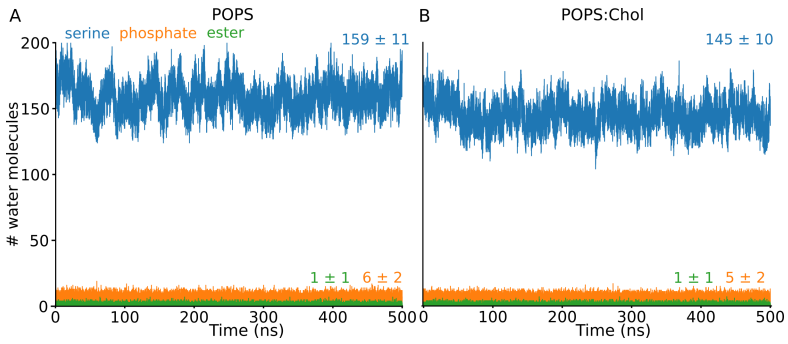


**Figure 4.8.** Number of water molecules interacting with lipid headgroups. (A-B) Number of water molecules within 2.5Å of H-bonding atoms of serine (blue), phosphate (orange) and ester (green) group of POPS lipids in pure POPS bilayers (Panel A) and in POPS bilayers with cholesterol (Panel B).

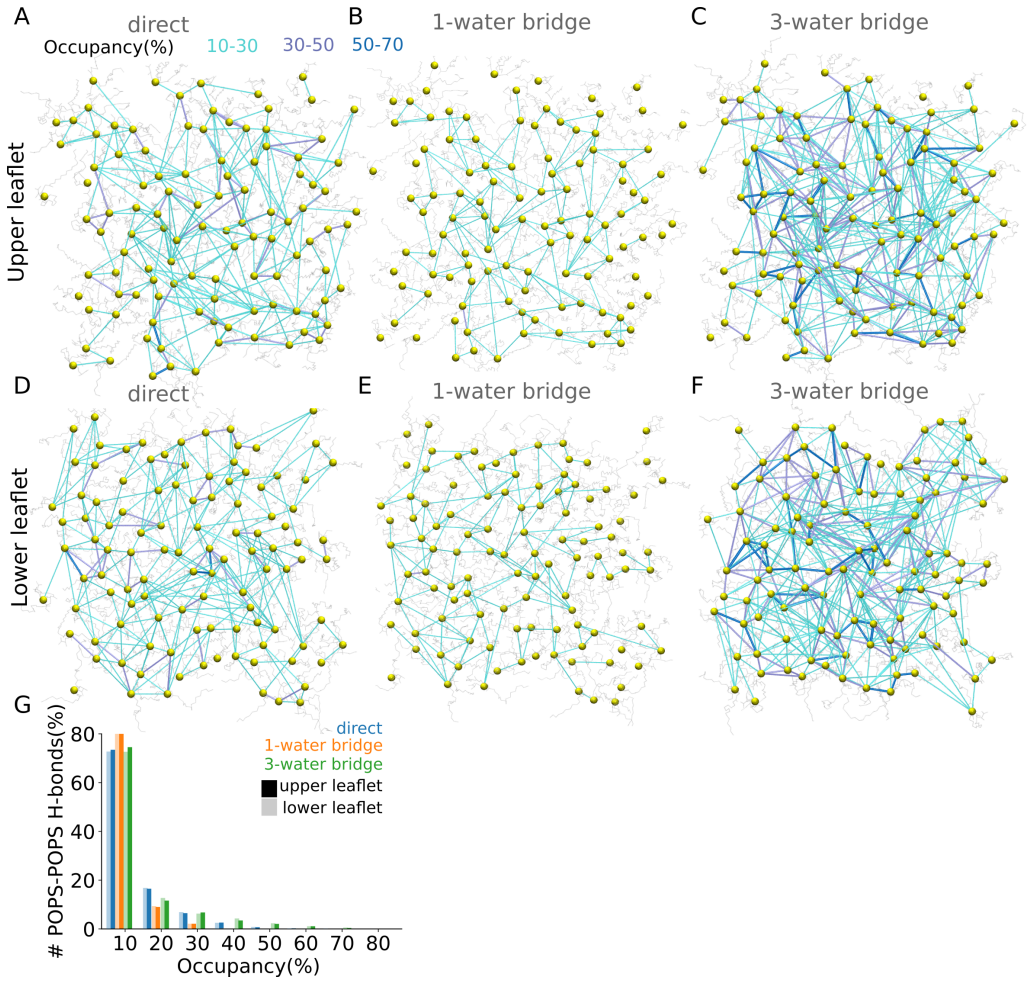


**Figure 4.9.** H-bond dynamics of POPS lipids in the absence of cholesterol. (A-C) Network visualisation of direct (Panel A), 1-water bridged (Panel B), 3-water bridged (Panel C) H-bond lipid pairs in upper leaflet. (D-F) Network visualisation of direct (Panel D), 1-water bridged (Panel E), 3-water bridged (Panel F) H-bond lipid pairs in lower leaflet. (G) Number of direct, 1-water and 3-water mediated H-bonds (%) formed by POPS lipid headgroups within specific occupancy ranges.

To illustrate how dynamic the H-bond networks are, Figure 4.10 presents one-water-mediated H-bond networks with a minimum H-bond occupancy of 30 %. About 9 water mediated POPS lipid networks with a joint occupancy above 1 % are sampled regardless of the presence of cholesterol (Figures 4.10A,C). Out of these 9, 8 have linear topology and 1 is circular (Figure 2.4). The circular network in both simulations may rarely (<1 % joint occupancy) form a larger and complex network. The more frequently sampled linear networks with 6-8 % joint occupancy tend to have 1-water bridged 3-4 POPS lipids/path in membranes without cholesterol and 3 POPS/path in the presence of cholesterol. The frequency of sampling complex topologies is rare and in the presence of cholesterol it decreases even further. The joint occupancy of the circular network decreases from 8 to 2 % in the presence of

cholesterol (Figures 4.10B,D). That the presence of cholesterol disfavors the sampling of longer H-bond paths is further illustrated by the finding that there are, on the average, 2 linear H-bond paths with 4 POPS lipids in simulations without cholesterol (Figure 4.10A), and just one when cholesterol is present (Figure 4.10B). These results concur with the previous study by Bhide et al. [201], stating that cholesterol does not act as a bridge connecting two H-bonded POPS clusters to form a larger cluster that can span the entire leaflet. Despite the altered clustering behaviour of POPS in presence of cholesterol, the average number of H-bonds per POPS lipid remained similar (Figure 4.2) indicating that cholesterol primarily influences the spatial organisation of POPS lipids rather than directly affecting their H-bonding interactions. These observations instigate the further investigation of the topologies preferred by POPS headgroups in the presence of cholesterol.

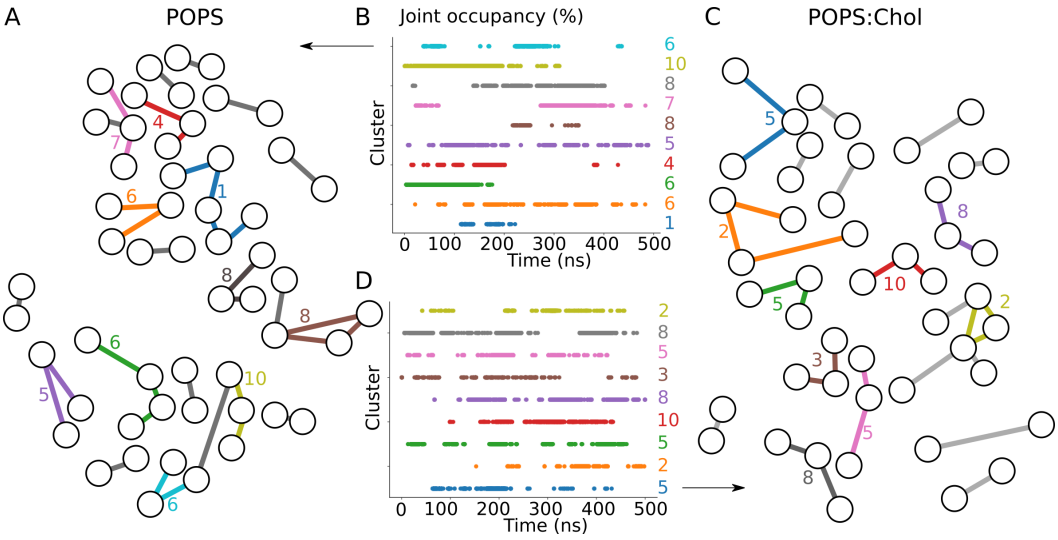


**Figure 4.10.** Illustration of most frequently sampled one-water mediated POPS. (A, B) Selected H-bond clusters sampled in the POPS membrane simulation shown as graphs (Panel A) and time series of the corresponding joint occupancy value (Panel B). Edges and numbers indicating the average joint occupancy (Panel A) and the time series profiles (Panel B) are colored according to the corresponding path. (C, D) Selected H-bond clusters sampled in the POPS:Chol membrane simulation shown as graphs (Panel C) and time series of the corresponding joint occupancy value (Panel D). H-bond graphs were computed with a minimum H-bond occupancy threshold of 20%, and paths, with a minimum joint occupancy of 1%.

## 4.2 Topology analysis of POPS-Cholesterol H-bond clusters

Presence of cholesterol and its interaction with POPS headgroups can influence the formation of H-bonded lipid clusters (Refer Section 4.2). In

this section, the focus lies on characterizing these lipids clusters formed by POPS headgroups in presence of cholesterol and their properties. To understand how these lipid clusters arrange spatially, a recently developed DFS algorithm [42] is used to classify the clusters into the four main topologies - linear, circular, star & linear and star & linear & circular (Figure 2.4).

The temporal evolution of significant factors that define the dynamics of cluster formation are shown in Figure 4.11 in order to illustrate the convergence of the MD simulations with respect to cluster formation. The timeseries data for all simulations include the number of H-bonds per lipid, the count of lipid clusters, and the overall number of lipids forming these clusters. The number of direct, one-water, and ion mediated lipid clusters fluctuates between ∼10-28, ∼8-22 and ∼2-20 respectively for all concentrations of cholesterol (Figures 4.11D,E,F). As the fluctuations of number of clusters (Figures 4.11D,E,F) and total number of lipids in clusters (Figures 4.11G,H,I) remain in a specific range for MD simulations throughout the trajectories, the entire trajectories were considered for topology analysis.

**Table 4.4.** Occurrence (%) of topologies of H-bond clusters identified with the DFS algorithm. We report the occurrence (%) of lipid clusters that involve direct H-bonds and one-water bridges between lipids. Here, occurrence is the percentage of the analysed trajectory where at least one lipid cluster of a specific lipid topology type is present irrespectively of its size.

| | Topology of clusters | Occurrence (%) | | | | | | | | | | | | | | |
|---|---|---|---|---|---|---|---|---|---|---|---|---|---|---|---|---|
| | | All H-bond clusters | | | | | POPS-POPS clusters | | | | | Cholesterol-Cholesterol clusters | | | | |
| | | Cholesterol (%) | | | | | Cholesterol (%) | | | | | Cholesterol (%) | | | | |
| | | 0 | 10 | 20 | 30 | 40 | 0 | 10 | 20 | 30 | 40 | 0 | 10 | 20 | 30 | 40 |
| direct | Linear | 100 | | | | | 100 | | | | | 100 | | | | |
| | Circular | 61 | 60 | 43 | 51 | 45 | 61 | 62 | 47 | 58 | 55 | 0 | | | | |
| | Star & Linear | 63 | 65 | 71 | 74 | 70 | 63 | 61 | 61 | 59 | 48 | 0 | | | | |
| | Circular & Star & Linear | 100 | | | | | 100 | | | | | 0 | | | | |
| 1-water bridge | Linear | 100 | | | | | 100 | | | | | 100 | | | | |
| | Circular | 18 | 20 | 16 | 16 | 14 | 18 | 21 | 18 | 19 | 19 | 0 | | | | |
| | Star & Linear | 83 | 85 | 86 | 89 | 91 | 83 | 84 | 81 | 83 | 82 | 0 | | | | |
| | Circular & Star & Linear | 100 | 99 | 99 | 96 | 91 | 100 | 99 | 99 | 95 | 89 | 0 | | | | |
| Ion bridge | Linear | 100 | | | | | 100 | | | | | 100 | | | | |
| | Circular | 82 | 86 | 84 | 79 | 71 | 82 | 83 | 75 | 68 | 52 | 0 | | | | |
| | Star & Linear | 7 | 8 | 6 | 4 | 2 | 7 | 8 | 6 | 3 | 2 | 0 | | | | |
| | Circular & Star & Linear | 87 | 86 | 74 | 68 | 46 | 87 | 84 | 66 | 57 | 30 | 0 | | | | |

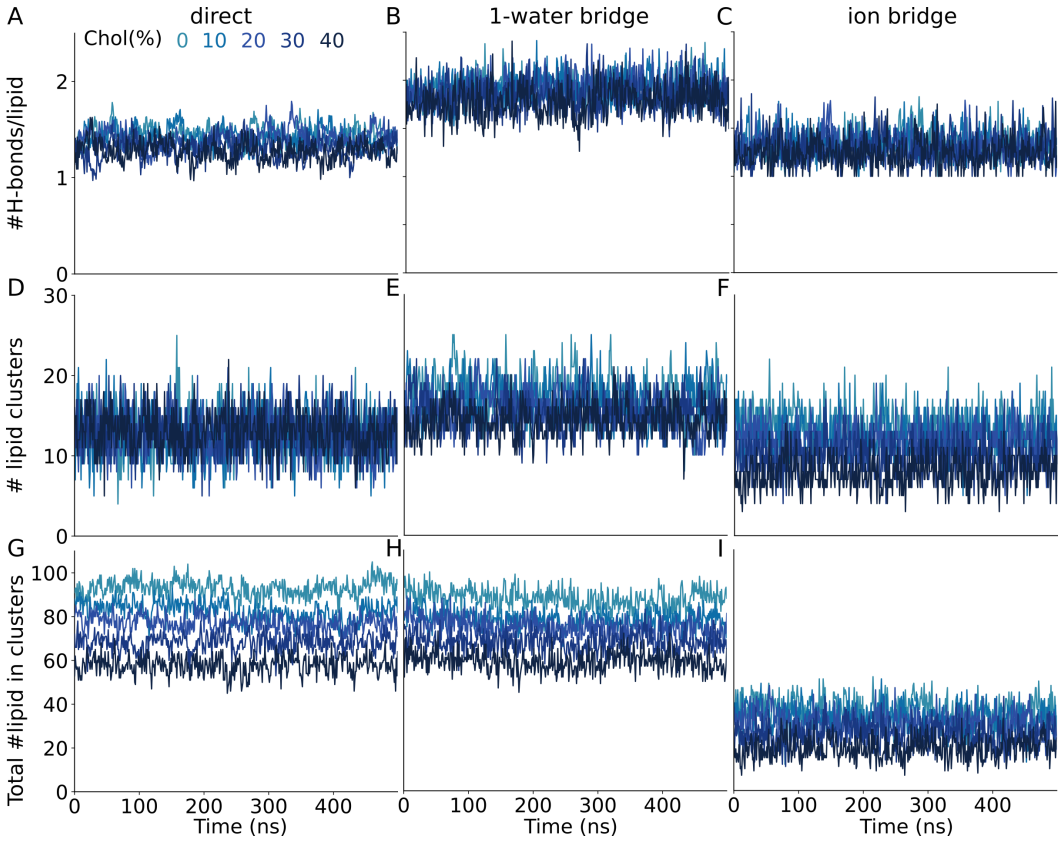


**Figure 4.11.** Dynamics of H-bond lipid clusters sampled in POPS membranes with various concentrations of cholesterol. (A-C) Time series of direct (Panel A), 1-water mediated (Panel B) and ion mediated (Panel C) H-bonds/lipid. (D-F) Time Series of #lipid cluster formed by direct (Panel D), 1-water mediated (Panel E) and ion mediated (Panel F) H-bonds. (G-I) Total #lipid in clusters per frame forming lipid clusters mediated by direct (Panel G), 1-water mediated (Panel H) and ion mediated (Panel I) H-bonds.

At any given time, 85 % of lipids out of 109 lipids in each leaflet of POPS bilayer participate in forming dynamic H-bonds with low occupancies. About 18 direct H-bonded lipid clusters are likely to be sampled in the POPS membrane and this number decreases to 14 in the POPS:cholesterol membrane with 40 % cholesterol (Table A.4.1). As the cholesterol concentration increases, a significant decrease from 85 % to 53 % and 80 % to 54 % is observed in the total number of lipids forming direct and water mediated H-bonded clusters respectively (Table A.4.1, Figures 4.11G,H,I). However, the number of lipid clusters (Figures 4.11D,E,F) or the number of H-bonds per lipid (Figures 4.11A,B,C) do not have a significant effect of the presence of cholesterol. This indicates a reduction in size of POPS clusters with a rise in the cholesterol content. As cholesterol rises from 0 to 40 %, the proportion of low occupancy POPS-POPS H-bonds reduces by 4-6 % while the percentage of POPS-cholesterol H-bonds rises by 3-10 % (Figure 4.12). As

a result, the total average number of H-bonds per POPS lipid is independent of the cholesterol concentration (Figures 4.11A,B).

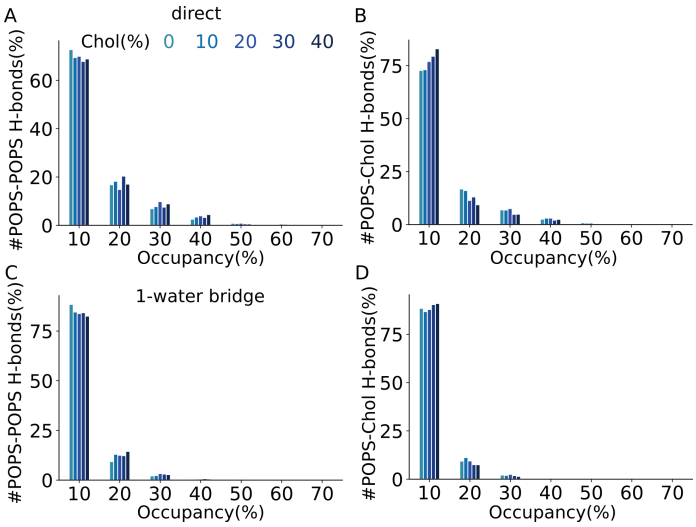


**Figure 4.12.** Occupancy of H-bonds identified in POPS-cholesterol bilayers. (A-B) Percentage of number of direct (Panel A) and 1-water mediated (Panel B) POPS-POPS H-bonds within a specific occupancy range. (C-D) Percentage of number of direct (Panel C) and 1-water mediated (Panel D) POPS-cholesterol H-bonds within a specific occupancy range.

*Linear H-bond paths are favoured by POPS irrespective of cholesterol concentrations and exclusively sampled in cholesterol clusters.*

Cholesterol tends to engage in water or ion-mediated H-bond clusters with POPS (Figure 4.13A). The average number of POPS-cholesterol clusters and cholesterol-cholesterol clusters increases with increasing cholesterol concentration (Figure 4.13A). As reported previously [42], linear H-bond paths are preferred by the POPS lipid headgroups in the membrane without cholesterol (Figures 4.13C,D, Table 4.4). The values for occurrence reported are higher as compared to the previously reported values [42] as both studies differ in the H-bonding atom selections. Here, additional to H-bonding atoms of phosphate group, the H-bonding atoms of serine group of POPS are included in H-bond calculations for water mediated H-bonds in contrast to the study by Karathanou & Bondar [42]. At least one linear path is sampled at any moment during the entire simulation length. More complex cluster topologies as circular, star & linear and star & linear & circular are sampled but very rarely (Figure 4.13C,D, Table 4.4). For H-bonded clusters formed by cholesterol molecules, linear paths are exclusively sampled (Figure 4.13E, Table 4.4).

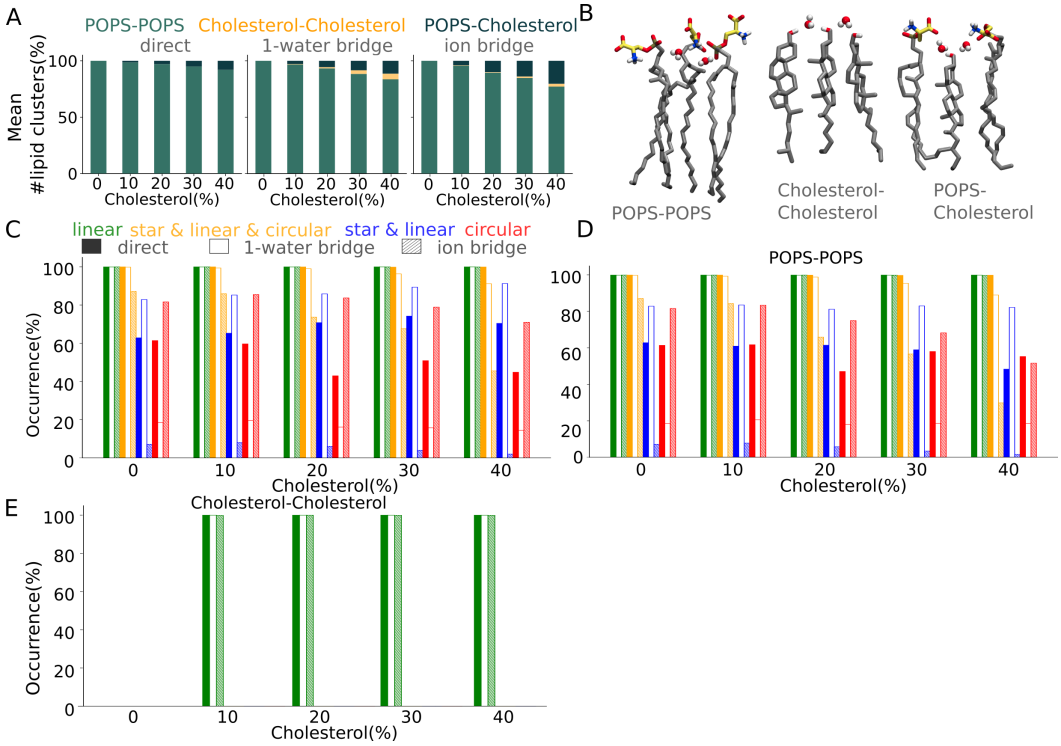


**Figure 4.13.** Occurrence of lipid cluster topologies and number of H-bond clusters sampled in POPS and POPS-cholesterol bilayers. Main cluster topologies that can be identified with the DFS algorithm [42] are reported here. (A) Percentage of average number of direct, 1-water bridged, and ion-bridged POPS-POPS, cholesterol-cholesterol and POPS-cholesterol lipid clusters. (B) Molecular graphics illustrating POPS-POPS, cholesterol-cholesterol and POPS-cholesterol lipid clusters with 3 lipids. (C-E) Occurrence (%) of all lipid H-bond clusters (Panel C), POPS-POPS (Panel D) and cholesterol-cholesterol (Panel E) H-bond clusters. We report the cluster occurrence (%) as the percentage of the analysed trajectory where at least one lipid cluster of a specific lipid topology type is present irrespectively of its size.

*Presence of cholesterol associates with the decreased sampling of complex H-bond paths*.

In POPS simulation, around 15-18 lipid clusters are likely to be sampled. Out of these, the most frequently sampled are linear and star & linear & circular with an average of 8-9 and 1-6 clusters per frame respectively (Figure 4.14C). Circular and star & linear clusters are rare but when found are likely to be of cluster size = 3 and 4-5 respectively (Figures 4.14C, D). The size and number of circular, star & linear and linear clusters do not seem to be affected by the cholesterol concentration. However, the average number and cluster size of a complex lipid cluster decreases as cholesterol concentration increases (Figures 4.14C,D). The number of lipids in a complex lipid cluster decreases by about 25 % with an increase of cholesterol concentration from

0-40 % (Figure 4.14C). This suggests that the presence of cholesterol hinders the formation of complex H-bond mediated lipid clusters. Three or four POPS are likely to H-bond directly, through one water mediated H-bond bridge or ion mediated bridge for most of the time (Figures 4.15,4.16,4.17). Extended and large clusters with cluster size more than 6 are rarely sampled (Figures 4.15,4.16,4.17).

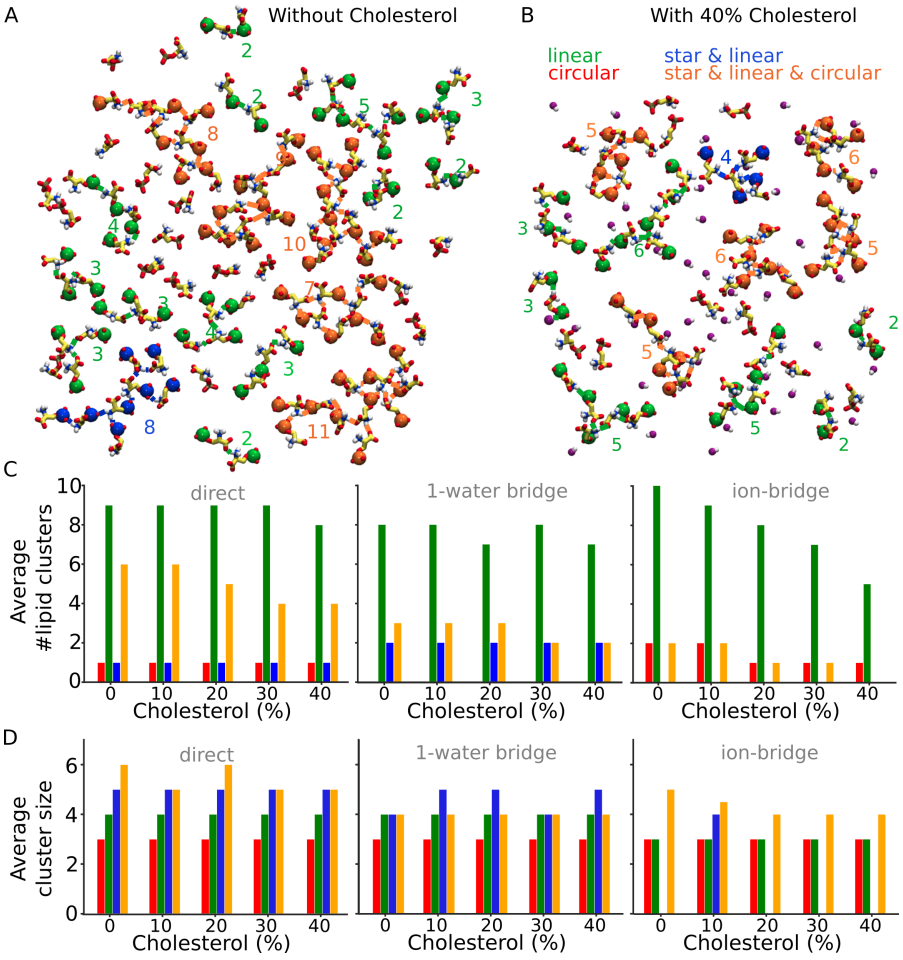


**Figure 4.14.** POPS lipid cluster distribution based on topology. (A-B) Molecular graphics illustrating direct POPS-POPS lipid clusters in a snapshot from MD simulations of POPS bilayers without cholesterol (Panel A) and with 40 % cholesterol (Panel B). POPS lipid headgroups are shown as yellow lines and oxygen of cholesterol is shown as purple sphere. The phosphorus of POPS headgroups of linear, star & linear, star & linear & circular clusters is shown as green, orange or blue spheres respectively. (C-D) Average number (Panel C) and average cluster size (Panel D) of direct, 1-water bridged and ion bridged lipid clusters sampled in one frame of MD simulations with and without cholesterol. Adapted from ref. [160].

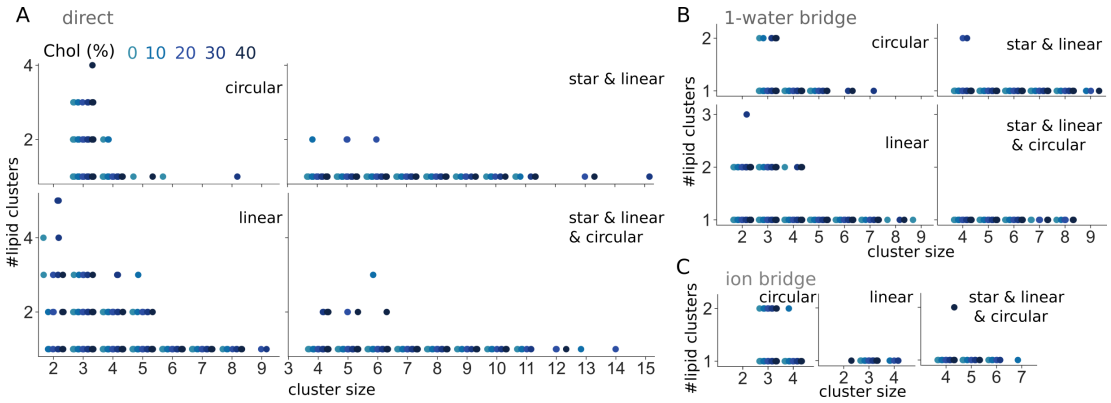


**Figure 4.15.** Cluster size of lipid clusters sampled in POPS and POPS-cholesterol bilayers. (A-C) #POPS lipid clusters mediated by direct (Panel A), 1-water (Panel B) or ion (Panel C) H-bonds as a function of cluster size and concentration of cholesterol. Cluster size is the number of lipids in a cluster.

*POPS tend to form short linear clusters with 3 lipids whereas cholesterol clusters in pairs.*

Linear H-bond paths mediated by one water molecule are sampled in hydrated POPS bilayers (Chapter 3). This supported by the previous discussion in this chapter, which demonstrates that one water mediated H-bond paths are also present in POPS bilayers with cholesterol. The most frequently sampled POPS linear H-bond paths are typically with 2–3 lipids (Figures 4.15, 4.16). The occurrence of linear H-bond paths between cholesterol molecules and POPS molecules is significantly influenced by the length of the path (Figures 4.16, 4.17). Longer paths are less likely to be sampled and thus have lower occurrences. For example, less than 1 % of linear clusters with five or more lipids are sampled (Figures 4.16A,B). This is because it becomes harder for the molecules to arrange themselves in a way that permits all of the H-bonds sampled simultaneously to form the longer the path. These observations are consistent with earlier research on hydrated POPS membranes [42] and 4:1 POPC:POPG membranes [43].

Direct singular H-bonds (H-bond paths with length L = 1) between POPS headgroups are slightly less common in the presence of cholesterol than they are in the POPS membrane (Figure 4.16). Such paths are still sampled over all of the simulations, nevertheless. The time series of the H-bond paths of various lengths, when combined with the H-bond occupancy analysis, indicate that the majority of H-bond clusters at the POPS headgroup interface are short and transient (Figure 4.16). It is significant to note that the size of the lipid bilayer affects the precise number of H-bond paths, or clusters, sampled across the simulation trajectories. The purpose of the time series

employed in the study is to depict the dynamics of H-bonds at the lipid headgroup interface of the hydrated membrane patches used here (Table 4.1).

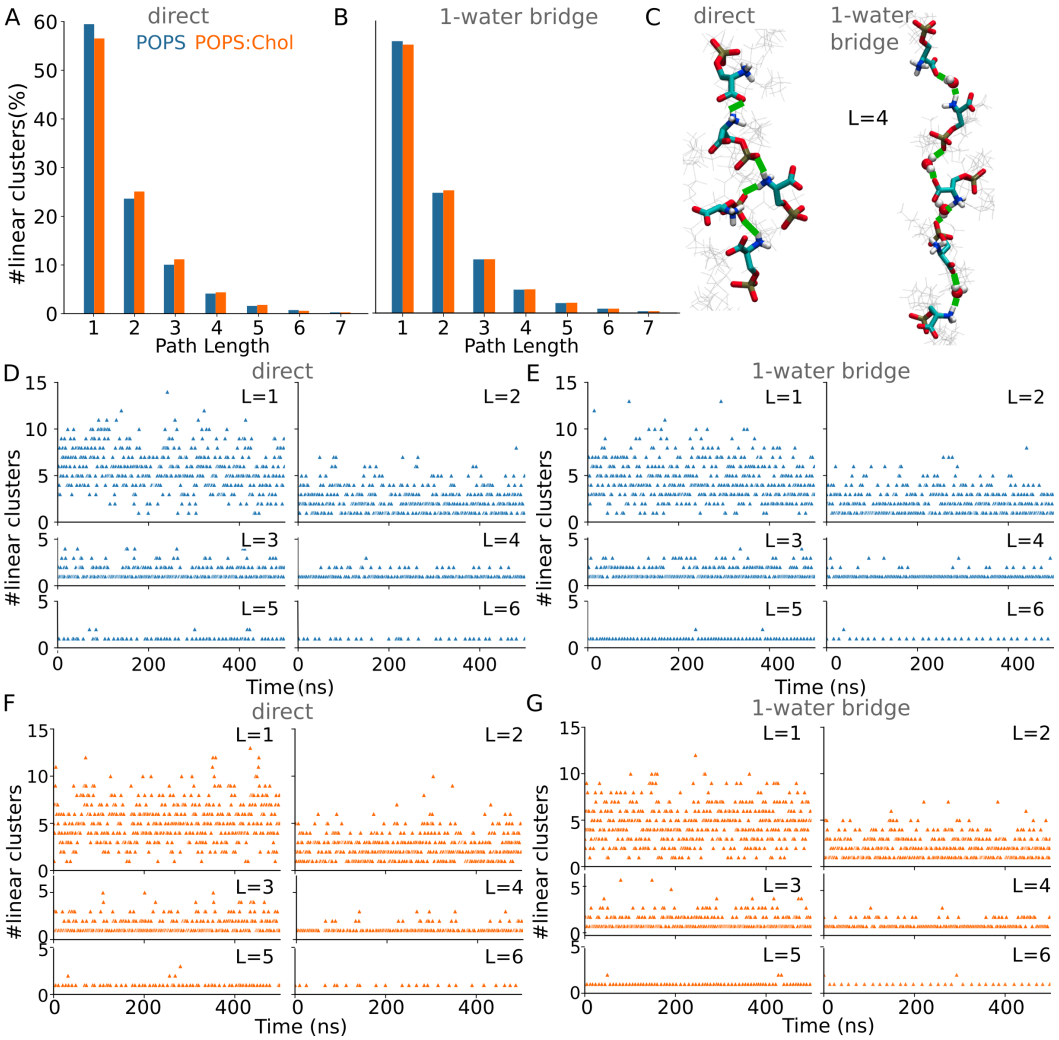


**Figure 4.16.** Path lengths for linear clusters formed by POPS headgroups. (A-B) The percentage of linear clusters in POPS (blue) and POPS:Chol (10 %) (orange) bilayers with various path lengths mediated by direct H-bonds (Panel A) and one-water bridges (Panel B). (C) Molecular graphics illustrating water-mediated linear cluster with path length L = 4. Four H-bonds are represented as thick green lines. (D-E) Time series of the number of direct (Panel D) and one-water bridge (Panel E) linear clusters with path lengths ranging from 1-6 derived from simulations of POPS without cholesterol. (F-G) Time series of the number of direct (Panel F) and one-water bridge (Panel G) linear clusters with path lengths ranging from 1-6 derived from simulations of POPS with 10 % cholesterol. The figure is taken from ref. [160].

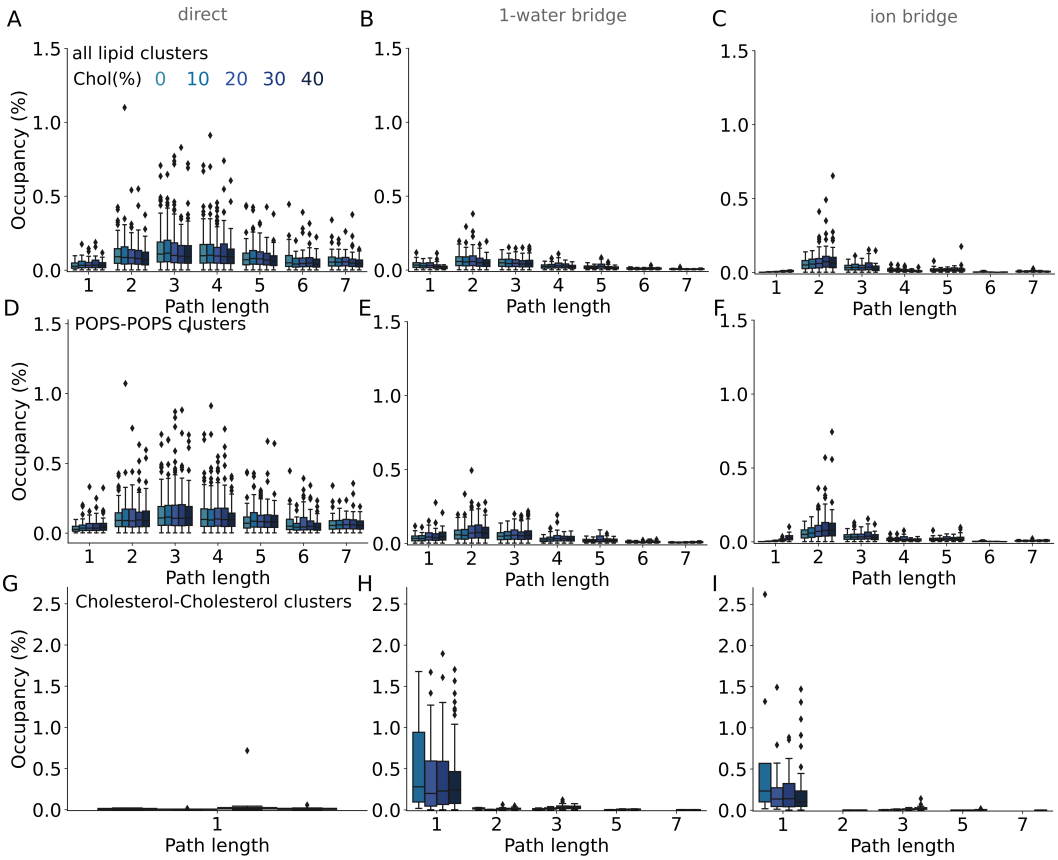


**Figure 4.17.** Occupancies and path lengths of linear H-bond lipid clusters in simulations of membranes with POPS and cholesterol lipids. Occupancy (%) of linear H-bond lipid clusters sampled by (A-C) POPS headgroups and cholesterol via direct (Panel A), 1-water bridged (B) and ion bridged (Panel C), (D-F) POPS headgroups via direct (Panel D), 1-water bridged (E) and ion bridged (Panel F) and, (G-I) cholesterol via direct (Panel G), 1-water mediated (H) and ion bridged (Panel I) H-bonds as a function of concentration of cholesterol. Path length of a linear cluster is the minimum number of H-bonds forming a particular cluster. Occupancy is the percentage of the trajectory frames in which a specific cluster is present.

## 4.3 Topology analysis of cholesterol-cholesterol H-bond clusters

Cholesterol tends to cluster in pairs of two (Figure 4.18). Larger linear clusters with 3-4 cholesterol H-bonded via 1-water bridges are rarely sampled (Figure 4.18). These findings match with the previous study by Bandara et al. (2016) [220] that reports the preference of cholesterol to form dimers. The average lifetime of cholesterol dimers in POPC bilayers has been reported to be 0.35-0.37 ns for 10 and 20 % cholesterol concentration [220]. Cholesterol clustering reported in previous publications consider the distance criteria of 5-6 Å between heavy atoms [213, 220, 221] or 9 Å between center of mass of two cholesterol molecules [73] in contrast to the standard H-bond

distance criteria of 2.5 Å between H-bonding groups in this study. In those publications, the hydrophobic interactions between the cholesterol molecules were also considered and the simulations were run upto microseconds. To consider the geometric clustering, I performed topology analysis with a 6 Å distance criteria [222] between hydroxyl groups of cholesterol molecules. The 500 ns simulations reported here are limited in length to show phase separation or lipid raft formation due to cholesterol clustering. For lipid raft formation, a cholesterol-rich and cholesterol-poor nanodomain is observed around 3 microseconds in POPC:DPSM:Chol membranes with 10-20 % of cholesterol [75]. However, cholesterol-cholesterol clustering via direct or water mediated H-bonds have been previously reported in MD simulation less than 50 ns long [199–201]. The cholesterol clusters are unstable and disperse into monomers within a 200 ns simulation, according to a prior study by [73]. To minimize contact with water, the cholesterol clusters adopt a frustum structure [73]. 2:1 POPC:Chol appeared to be a homogeneous mixture in experimental studies on GUV at 24 °C, whereas POPC/SM/Chol 2:1:1 formed micron-sized domains [223]. This suggests that cholesterol clustering may only occur in systems with 2 distinct lipid components in addition to cholesterol - one with high-Tm and one with low-Tm component in relation to the experimental temperature [223].

In this study, an incipient cholesterol clustering in POPS bilayers with 40 % cholesterol is observed (Figure 4.19). However the number of cholesterol-cholesterol clusters and the size of the clusters don't show a significant and/or gradual change as POPS with 40 % cholesterol simulation progresses (Figure 4.19). A geometrical cluster of cholesterol is defined as the group of cholesterol molecules whose hydroxyl group are within 6 Å [222] of each other. Geometrical cholesterol clusters are more frequent and larger in size as compared to the H-bonded cholesterol clusters (Figures 4.18, 4.20) due to the relaxation in the distance criteria between hydroxyl groups of cholesterol molecules. In both cases, cholesterol molecules prefer to arrange in linear topology (Figure 4.20). In agreement with the previous studies, we suggest that cholesterol-cholesterol clusters are rarely formed and if formed they are very transient (Figures 4.18, 4.20). The number and size of lipid clusters sampled during simulations might vary based on the length of simulations and the size of the membrane patch under study. The simulations reported in this chapter are limited to 500 ns and 81 Å X 81 Å X 85 Å membrane patch and thus only serve as model simulations.

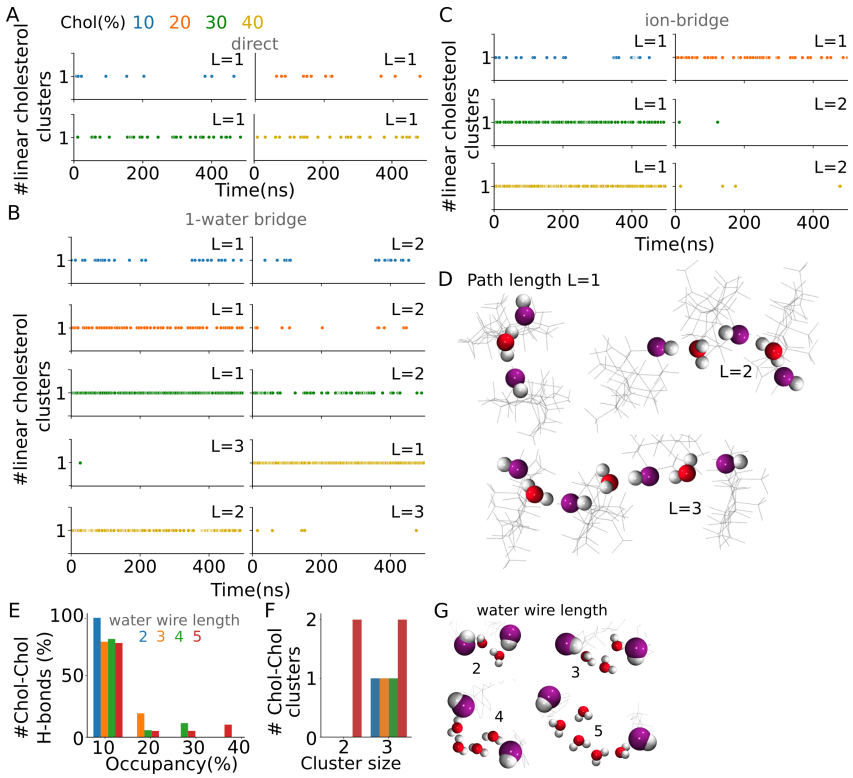


**Figure 4.18.** Dynamic cholesterol clusters. (A-C) Time Series of number of direct (Panel A), 1-water bridged (Panel B) and ion-bridged (Panel C) linear clusters with path lengths between 1-3. (D) Molecular graphics of linear paths of path length 1,2 and 3 formed by cholesterol. (E) Occupancy (%) of cholesterol-cholesterol H-bonds mediated by 2,3,4 or 5 water molecules. (F-G) Cluster size (Panel F) and time series (Panel G) of cholesterol clusters formed via H-bonds with water wire length of 2,3,4 or 5 water molecules. Joint occupancy of the cholesterol cluster is mentioned above the time series for each cluster. (H) Molecular graphics of linear cholesterol paths formed via water wires of length 2,3,4 or 5 water molecules. Panels A-D are adapted from ref. [160]. Panels E-G are taken from [160].

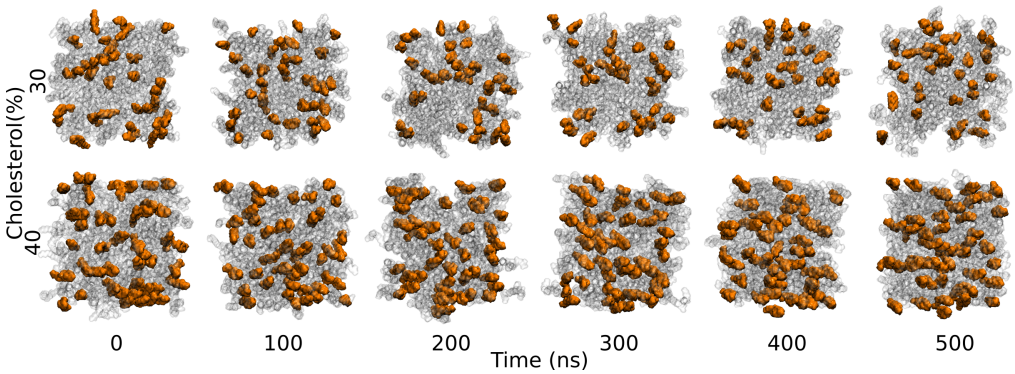


**Figure 4.19.** Cholesterol distribution in POPS lipid bilayers with respect to time. Cholesterol is shown in orange and POPS headgroups are shown as a white transparent surface. Incipient cholesterol clustering is observed in POPS bilayers with 40 % cholesterol.

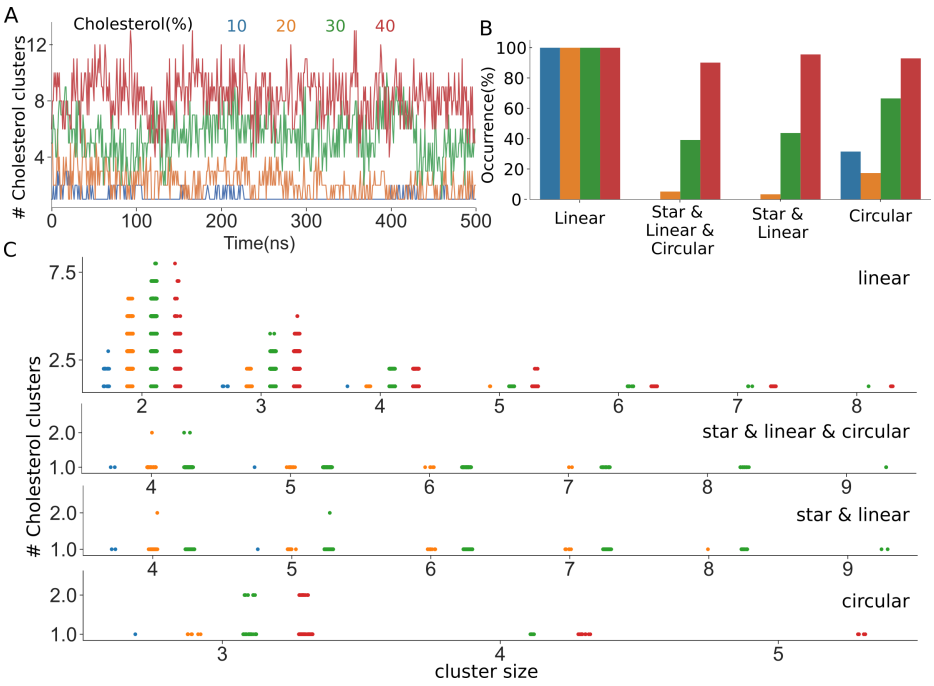


**Figure 4.20.** Geometrical cholesterol clusters. (A) Time Series of number of cholesterol-cholesterol clusters. (B) Occurrence (%) of cholesterol-cholesterol clusters based on their topology. (C) Number of cholesterol clusters of different cluster sizes. Here, a geometrical cholesterol cluster is formed by cholesterol molecules with their hydroxyl group within 6 Å of each other.

# 5

# Water mediated H-bond networks of Hv1 proton channel

I wrote the code and developed the protocol used in this chapter for finding the most frequent H-bond paths between titratable protein sidechains or lipid headgroups. I prepared all of the system setups, performed MD simulations, and did H-bond path analysis on those systems. Under the direction and close supervision of Prof. Dr. Ana-Nicoleta Bondar, I prepared the figures and wrote the text in the following Chapter. The following manuscript based on this chapter is under preparation:

Jain, H., Lazaratos, M., Pohl, P., Bondar, A. Fluctuating hydrogen bond networks couple protonation, lipid interactions, and conformational dynamics of the Hv1 ion channel.

Figures and tables adapted or taken from the manuscript under preparation are noted as “Adapted/Taken from ref. [162].”

The protocol and scripts presented here uses core code of Bridge [34] and MDAnalysis [163, 164]. I added a class called *Path Analysis* with attributes required for H-bond path analysis to the core code of Bridge.

The work on docking of inhibitors presented here was done under the supervision of Dr. Aniket Magarkar from Boehringer Ingelheim. I prepared the systems, did MD simulations, performed docking of inhibitors on Hv1, did H-bond network analysis and protein-ligand interaction analysis during my internship at Boehringer Ingelheim.

The voltage-gated proton channel Hv1 is a transmembrane protein that plays a role in several physiological processes, including pH regulation, neurotransmitter release, respiratory burst in the immune cells, sperm motility and capacitation, and cancer cell survival and proliferation [85–89]. This makes Hv1 a key target for the development of therapeutics and may serve as a biomarker for cancer [89, 224]. The Hv1 channel is regulated by a network of H-bonds within the protein and with its surroundings. Studies have shown that changes in the H-bond network within Hv1 play a crucial role in its activation and gating behavior [27, 85, 91–93]. The formation and breaking of H-bonds in specific regions of the protein can alter the orientation of transmembrane domains, leading to changes in ion permeation and channel gating. The functioning of Hv1 is also influenced by factors such as pH and the presence of inhibitors, which can alter the dynamics of the H-bond network of Hv1. Understanding the H-bond network in Hv1 is important for gaining insights into the mechanism of its activation and regulation, and for developing new therapeutic strategies for diseases involving pH regulation. In this chapter, a graph-based approach is used to investigate dynamic water mediated lipid-protein H-bond networks at Hv1-lipid membrane interfaces relevant to proton binding. The protocol developed and implemented here identifies the most frequent H-bond paths between the protein sidechains. I identify and characterize the dynamic H-bond network of Hv1 embedded in 5 different lipid bilayers and with different protonation states of the titratable protein sidechains.

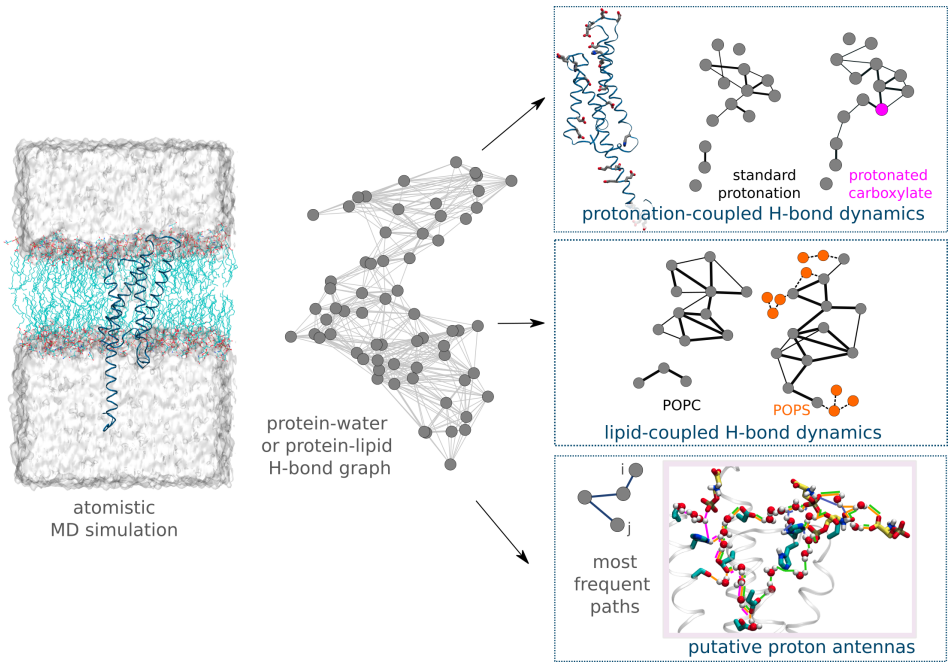


**Figure 5.1.** Hv1 water-mediated H-bond Networks: Insights into impact of protonation and lipid composition, and identification of putative proton antennas.

Hv1, a membrane of the superfamily of voltage sensing proteins, is a proton selective channel with 5 helices : S0-S4 [91] (Figure 5.2A). S1-S4 transmembrane helices form the pore domain and voltage sensing domain (VSD). The VSDs are conserved modules that regulate the opening of the voltage gated channels. Hv1 has 3 Arginines - R205, R208, R211 (mouse Hv1 numbering, mHv1) (Figure 5.2A) in the VSD that are reported to form salt bridges with Aspartates D108, D170 in the resting state of Hv1 [27, 91]. Two stages of structural changes happen when the channel is activated: R201 first adjusts its orientation in relation to F146, followed by a reorientation of R204 and R207 for interactions with D108 and D170 respectively. Then, in the subsequent phase, movement of helix S4 is associated with the formation of the salt bridge pairs R201-D119, R204-E192/E115, and R207-D108, as well as a reorientation of R201 and R204 towards the extracellular side [27]. When the channel is closed, a hydrophobic cluster composed of V105, F146, I173, V174 (V109, F150, V177 and V178 in hHv1) known as the hydrophobic gasket (Figure 5.2B) obstructs the flow of water and ions [225].

Hv1 maintains the pH of biological cells by extruding protons [85, 86]. The ability of Hv1 to transfer protons rely on the titratable side chains present in the hydrophobic cavity of the channel [27, 85, 91, 92] (Figure 5.5B). Of particular importance are the carboxylates and histidines, as they have been reported to be potential proton binding sites in membrane transporters [226, 227]. Site-directed mutagenesis studies show the effect of mutations of the carboxylates and histidines on proton selectivity, voltage threshold for detecting proton currents and binding of inhibitors of Hv1 (Table A.5.1). The carboxylates forming salt bridges with the Arg of the VSD are conserved and important for the functioning of the channel. The highly conserved D108 is responsible for proton selectivity [228]. Mutation of D108 to Ala [92, 228], Phe [228], Lys [228], His [228], Asn [92, 228], Ser [228] results in loss of proton selectivity and leads to anion permeation. In case of substitution to highly hydrophobic residues such as Val [228] or Ile [229], Hv1 becomes impermeable to ions. Proton transfer through Hv1 is robust as long as D108 is mutated to Glu [228–230]. D170 is an Hv1 inhibitor binding site [231–233] and mutating it to Ala causes the opening of the channel at 0 mV [234].

A number of carboxylate and histidine groups line up the transmembrane region of Hv1 (Figure 5.2A). Seven of them are in the pore domain - E115, D108, D119, D149, D170, D181, E167 and have been reported to regulate opening of the channel and participate in the proton transfer pathway [27, 85, 91, 92, 235]. van Keulen et al. [235] proposed that protons localize among three pairs of conserved carboxylates: D170/D149, D108/D181 and E115/D119. Mutation of the carboxylates towards the extracellular side

increases the voltage threshold for detecting proton current with respect to the wild type: D119 [92], E115 [92], D108 [92, 228], D181 [228] to Ala, D108 to Phe[228], Lys [228] His [228], Asn [92, 228], Ser [228] and D181 to Asn, Met and Val [228]. Whereas the mutation of carboxylates towards the cytoplasmic side - D170 to Ala, Asn, His and Glu, D149 (E153 in hHv1) to Ala, Asn, Cys, Glu, E167 to Ala and H95 to Ala decreases the voltage threshold for detecting proton current [92]. Close to the extracellular side, H136 is known to be critical for Zn2+ binding, an inhibitor of hHv1 [148]. H136A mutants show decreased Zn2+ binding. Depending on the inhibitor under study, the effects of mutations affect the binding of inhibitors to Hv1. For example, D181A prevents the binding of hanatoxin [236] but binds to HIFs (Hv1 Inhibitor Flexibles) [231, 232]. E167Q and D170E reduces HIF inhibition whereas D149 (E153) to Cys reduces the ability of Hv1 to release HIF from its binding site [231, 232]. D108E mutant of Hv1 interacts with guanidine derivatives [237] and HIFs [231, 232] whereas D170A yields a non-functional channel with saturating concentration of YHV98-1 [233].

The sidechains of titratable amino acids alter their protonation state in response to pH changes, which in turn significantly influences the functioning of voltage-gated proton channel Hv1 [238, 239]. Constant pH MD simulations gave insights about the pH- and $\triangle$pH-dependent gating of the human Hv1 channel in both symmetrical and asymmetrical pH conditions [240]. Increase in outer pH, resulted in a network of interactions between amino acids extending from the extracellular side of the channel down to the hydrophobic gasket. On the other hand, amino acids close to the channel's cytoplasmic side form extended network of interactions upto the hydrophobic gasket when the inner pH decreases [240].

Although mammalian Hv1 is a dimer, each monomer has its own proton-conduction pathway and is capable of functioning independently [241]. The S4 helix, extending on the cytoplasmic side, creates a dimeric interface and forms a coiled coil region that induces cooperative gating of the dimer [242–244] and mediates thermosensitivity of the channel [245]. In the crystal structure of *Mus musculus* Hv1 chimera (PDB ID: 3WKV), this C-terminal coiled coil region is replaced by the GCN4 leucine-zipper transcriptional activator from *S. cerevisiae* to increase the thermostability of the channel [148]. Conserved residues of the coiled coil domain present in heptad repeats stabilize the dimer formation by hydrophobic interactions, salt bridges, disulfide bonds, and H-bonds [244]. Multiple sequence alignment of the cytoplasmic coiled coil region shows conserved carboxylates E221, E235, and E237 whose functional role remains to be explored (Figure A.5.22). Truncated N- and C- terminal monomeric units are functional however truncating of the

C-terminal coiled coil region affects the localization of Hv1 [241]. While Li et al. [241] and Mony et al. [246] hypothesized the S1-S4 contacts between dimers and the Okuda group proposed that in Hv1 dimers VSDs interact via S4 segments [148, 247], the dimer interface of Hv1 still remains uncertain. Thus for simplicity, all computations in this chapter were performed on a monomer of Hv1.

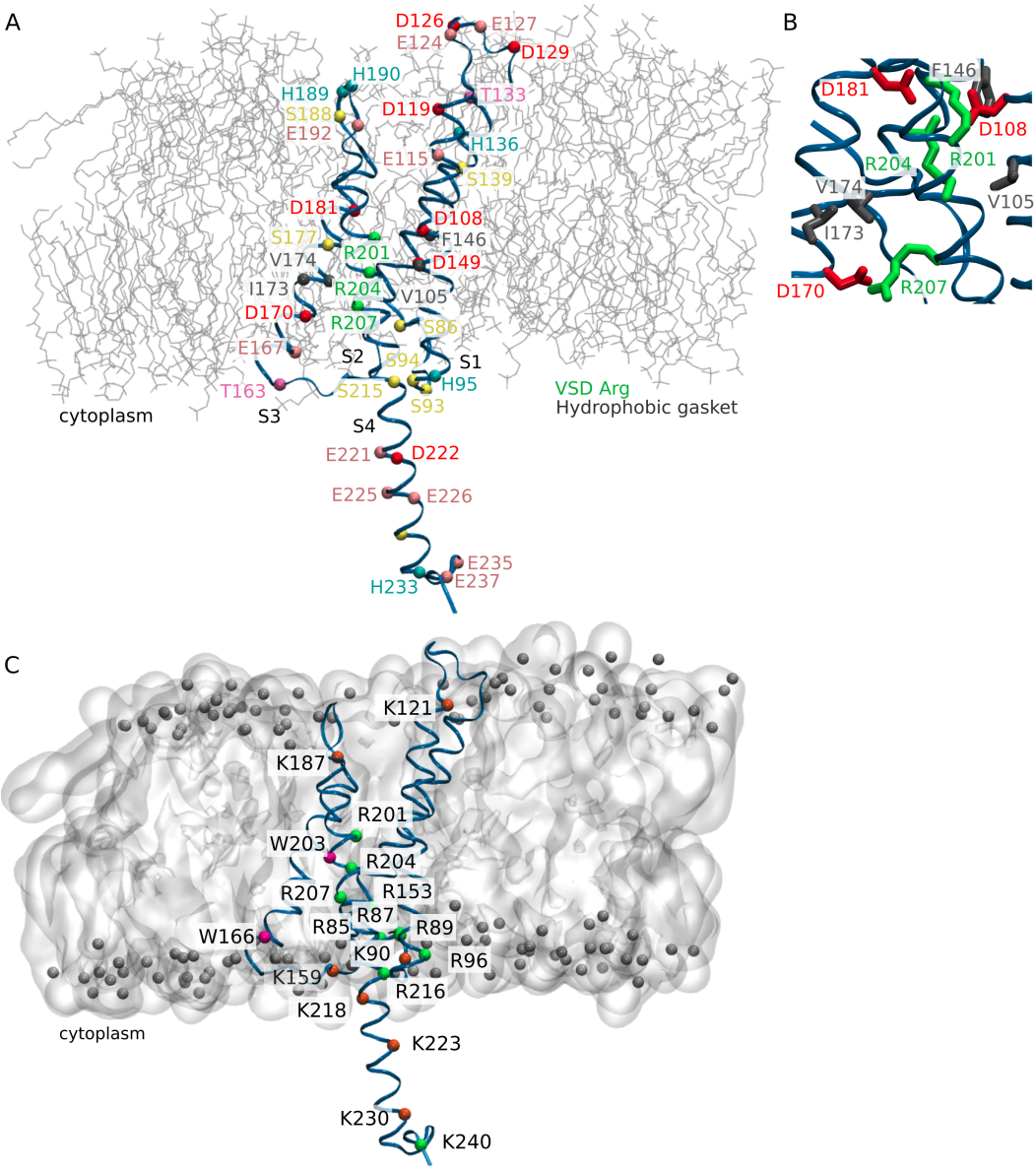


**Figure 5.2.** Architecture of Hv1. (A) Cut-away view of Hv1 embedded in lipid membrane. (B) Hydrophobic gasket of Hv1. (C) Potential lipid anchors - Arg, Lys and Trp sidechains that could anchor to lipid membranes and Arginines forming the Voltage sensing domain (VSD). Grey lines (Panel A) and a grey surface (Panel C) represents the lipid membrane whereas blue ribbons are used to show the protein. Small spheres represent the C$\alpha$ atoms of selected amino acid residues. Adapted from ref. [162] (manuscript under preparation).

Hv1 includes a number of Arg, Lys, and Trp sidechains at the lipid bilayer interface that may serve as membrane anchors (Figure 5.2C). R96, K121, and W203, previously identified important residues in Hv1 function, are examples of potential lipid anchors for Hv1. The voltage threshold for detecting proton currents is increased when K121 is changed to Ala rather than decreased when R96 is changed to Ala [92]. W203 (207 in hHv1), highly conserved along with the voltage sensing Arginines in Hv1, has been reported to be important for four unique properties of Hv1: proton selectivity, slow channel opening, highly temperature-dependent gating kinetics, and $\triangle$pH-dependent gating [238]. Although the relationship between Hv1 and the lipid bilayer that surrounds it is not well understood, voltage-gated ion channels are known to link to the lipid bilayer. For KvAP, a voltage-gated potassium channel, changes in the lipid composition of a bilayer cause the voltage sensing domains to alternate between open and closed states without altering the transmembrane voltage [248, 249]. When the lipid phospho-head groups are removed, voltage sensors on potassium channels embedded in lipid bilayers become immobile [249–252], whereas removal of the choline group results in the channels' apparent activation [249, 250, 252]. It has been proposed that the Arginines on the S4 helix of the voltage sensing domains interact with the lipids, maintaining the channel's open or closed state depending on the composition of lipid bilayer [249, 251].

Hv1 can function in lipid bilayers of various compositions. This includes the lipid membranes reconstituted in lab, *E. coli* bilayers and those with lipid compositions that differ greatly from those of the tissues in which it is expressed. On the extracellular and intracellular side of Hv1, a number of carboxylates and histidines are present in close proximity to the lipid interface. These carboxylates that could serve to be proton donor-acceptor pairs tend to locate within distances of $\sim$11-13 Å that could be bridged via 3-4 waters [132]. The presence of clusters of closely spaced carboxylate groups at the membrane interface in Hv1 suggests formation of proton antennas [132] (Chapter 1). These clusters can further interact with lipid headgroups and modulate functioning of Hv1 in different cells with varying composition of lipid bilayers. For instance, high expression of Hv1 and exposure of negatively charged lipids such as phosphatidylserine (PS) and phosphatidylethanolamine (PE) on the outer membrane [57–59, 253] in cancer cells seems to play a combined role in functioning and survival of cancer cells. Thus, understanding and describing how Hv1 collects protons via a cluster of protein sidechains and lipid headgroups, delivers the proton to an internal carboxylate/histidine sidechain, and then transfers protons along transient H-bonded wires between titratable sidechains could guide design of drugs with desired Hv1 binding properties.

To this aim, I performed MD simulations and characterized water-mediated protein-protein and protein-lipid dynamic H-bond networks of Hv1. To analyse the dynamic H-bond network of Hv1, I developed and implemented a protocol to find the most frequent H-bond paths (Chapter 2, Sec 2.6) between carboxylates and histidines of Hv1 sampled during the MD simulations. To study the effect of protonation and lipid interactions on the dynamic H-bond networks of Hv1, I analyzed Hv1 systems with different protonation states of the internal carboxylates and histidines and embedded in lipid bilayers of different composition.

*Comparison of the most frequent path protocol to the shortest path protocol*

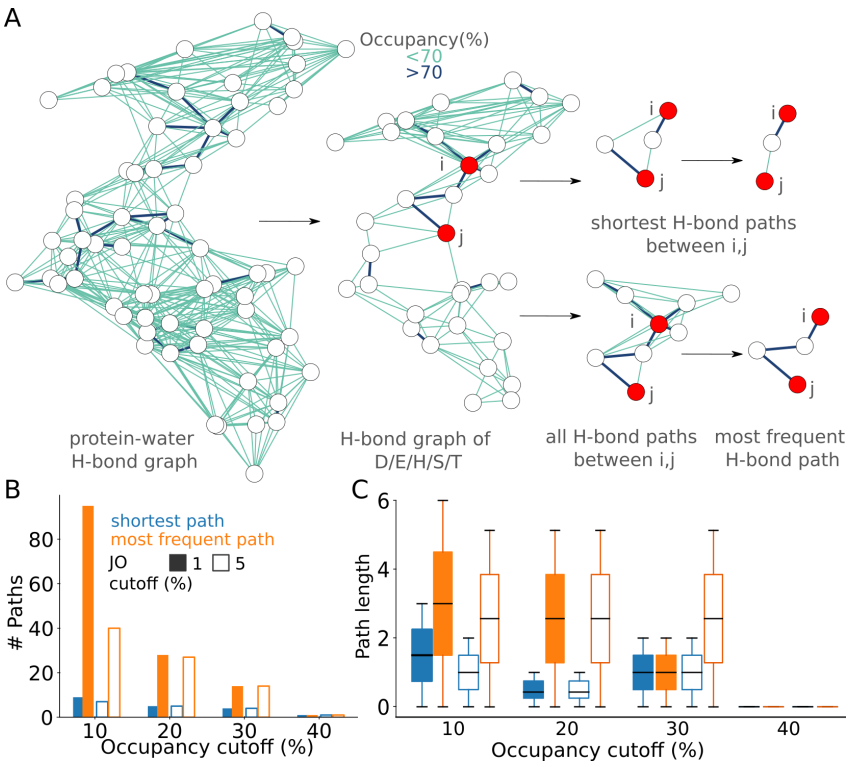


**Figure 5.3.** Protocol for finding the most frequent paths of Hv1 in comparison to the shortest path protocol.(A) Graphical illustration of comparison of the most frequent paths protocol with shortest path approach. (B) Number of H-bond paths from D108 sampled using both the protocols at occupancy cutoffs from 10-40 % and JO cutoff 1 and 5 %. (C) Path lengths of H-bond paths from D108 sampled using both the protocols at occupancy cutoffs from 10-40 % and JO cutoff 1 and 5 %. Here H-bond paths from D108 are shown as an illustration. Panel A of the figure is taken from ref. [162] (manuscript under preparation).

The protocol developed and implemented in this work enriches the sampling of H-bond paths for calculation of the most frequent paths by taking into account all the H-bond paths rather than only the shortest path i.e. the

H-bond paths with minimum number of nodes (Figures 5.3, 5.4, Tables A.5.2, A.5.3). The number of H-bond paths sampled using the most frequent paths approach is 3 to 10 times more compared to the shortest path approach. As the occupancy cutoff for filtering H-bonds increases from 10 to 40 % the difference between both the approaches to sample H-bond paths becomes less significant (Figure 5.3B). The most frequent path approach also samples paths with higher paths lengths as compared to the shortest path approach (Figure 5.3C). As the shortest path approach does not include all the paths in H-bond path calculations, some high joint occupancy paths might not be sampled. The most frequent path approach overcomes this shortcoming of shortest path approach. For illustration, Figure 5.4 shows H-bond path analysis between E115 and E192. In case of the most frequent path approach, E115-D119-E192 path with a high joint occupancy (68 %) is sampled in contrast to the shortest path approach.

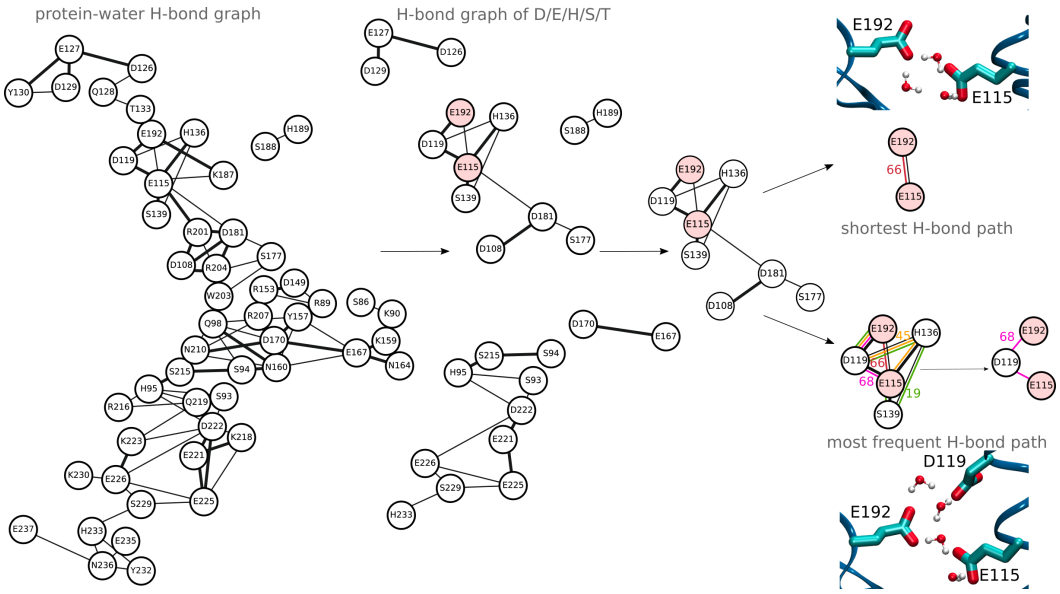


**Figure 5.4.** Illustration of the most frequent path and shortest path protocol applied to Hv1. Graphical illustration of most frequent paths and shortest path protocol applied to Hv1 with carboxylates of interest as E115 and E192. Note the sampled H-bond paths are different using the two different approaches.

In this chapter, I report analysis of 14 independent simulations of crystal structure of Hv1 (PDB ID:3WKV) [148] embedded in hydrated lipid bilayers. The chimeric *Mus musculus* crystal structure [148] used here shows high sequence similarity to the human Hv1 whose crystal structure is not yet available (Figure A.5.1). The system preparation and MD simulation protocol are mentioned in Chapter 2, Section 2.4. With a total sampling time of 4.38 µs, twelve of the simulations reported here are 300 ns, one is 500 ns and one is 280 ns long (Table 2.1, Sim 12-25). These simulations are distinguished

by the lipid bilayer composition and the protonation of selected titratable carboxylate and histidine sidechains (Figure A.5.2).

For the transmembrane helical region and the loops and termini of the Hv1 protein, time series of the C$\alpha$ RMSD profiles were tracked independently. Average RMSD values were calculated from each simulation's last 200 ns. The C$\alpha$ RMSD of transmembrane helices in all simulations remain within 3.5 Å relative to starting crystal structure with resolution of 3.45 Å [148] (Figure A.5.3). The dynamic modeled loops and non-helical regions show C$\alpha$ RMSD values as high as 45 Å. The cytoplasmic part of S4 helix orients towards the lipid headgroups in 5:1 POPE:POPG and Top6 bilayers, resulting in high RMSD values for non-helical regions of Hv1.

## 5.1 Dynamic H-bond network of Hv1

*A dynamic H-bond network inter-connects acidic and histidine sidechains of Hv1.*

Hv1 with standard protonation of all titratable sidechains and embedded in a hydrated POPC lipid membrane (Table 2.1) is considered as a reference simulation. A dynamic water-mediated H-bond network formed by carboxylates and histidines is sampled in the reference simulation (Figure 5.5A). This internal H-bond network is interrupted around the middle of the membrane plane at D108 and D170 (Figure 5.5A). The reason for this could be the presence of a hydrophobic gasket [225] formed by hydrophobic side chains - V174, I173, V105, and F146 (Figure 5.2B).

The interruption of the H-bond network was further analyzed by calculating the minimal distances between the carboxylates D108, D181, and D170 and their respective interaction partners. A stable salt bridge is found between D108 and R204 whereas D181 toggles between R201 and R204 (Figure 5.5D). D170, on the cytoplasmic side, prefers R207 as its interaction partner for most of the trajectory (Figure 5.5D). These salt bridge interactions are consistent with earlier research [27, 91].

D108 forms an extensive H-bond network on the extracellular side whereas D170 is connected via H-bond network to the cytoplasmic side. The most frequent water mediated H-bond paths between acidic and histidine sidechains were sampled for the internal H-bond network. The results show that the internal water mediated H-bond network extends from D108 to E115, H136, D119, E192 via D181 on the extracellular side whereas D170

H-bonds to E167 (Figures 5.5B,C). These H-bond paths are mediated by 1, 2 or 3 water molecules and have joint occupancy values ranging from 7 to 27 % on the extracellular side whereas on the cytoplasmic side D170 connects to E167 with a H-bond path mediated by an average of 2 water molecules and 91 % occupancy (Figure 5.5C).

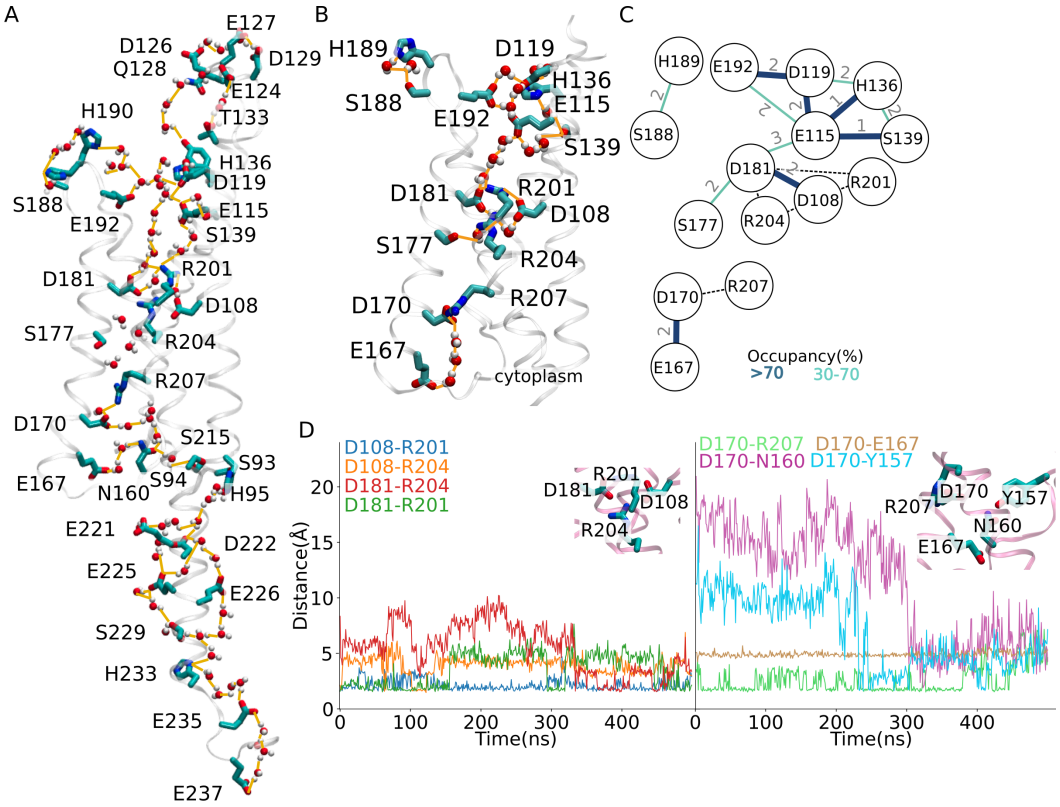


**Figure 5.5.** Dynamic H-bond network of Hv1 is interrupted at the middle of the transmembrane region.(A) Molecular graphics representing the water mediated H-bond network between selected protein sidechains. (B) The internal H-bond network and interruption at D108-D170. The orange lines show the most frequent water mediated H-bond paths connecting the hydrophobic core to the extracellular and cytoplasmic side. (C) Graph representation of the H-bond networks computed from simulations illustrated in Panel B. The thickness and color of the edges represent the occupancy of H-bonds whereas the numbers on edges represent the average number of waters per water wire of the graph. (D) Aspartate salt-bridge formation dynamics in the VSD of Hv1. Time series of the minimal distance between H-bond forming groups of D108-R201, D108-R204, D181-R201, D181-R204 (left) and D170-R207, D170-N160, D170-Y157, D170-E167 (right). Every 1 ns from 500 ns trajectory, the coordinates were read. The molecular graphics were prepared based on a coordinate snapshot from the simulation of Hv1 with standard protonation and embedded in a hydrated POPC lipid membrane environment. The protein is shown as white ribbons, the selected protein groups are shown as licorice and water molecules are shown as CPK representation. The Panels of the figure are taken from ref. [162] (manuscript under preparation).

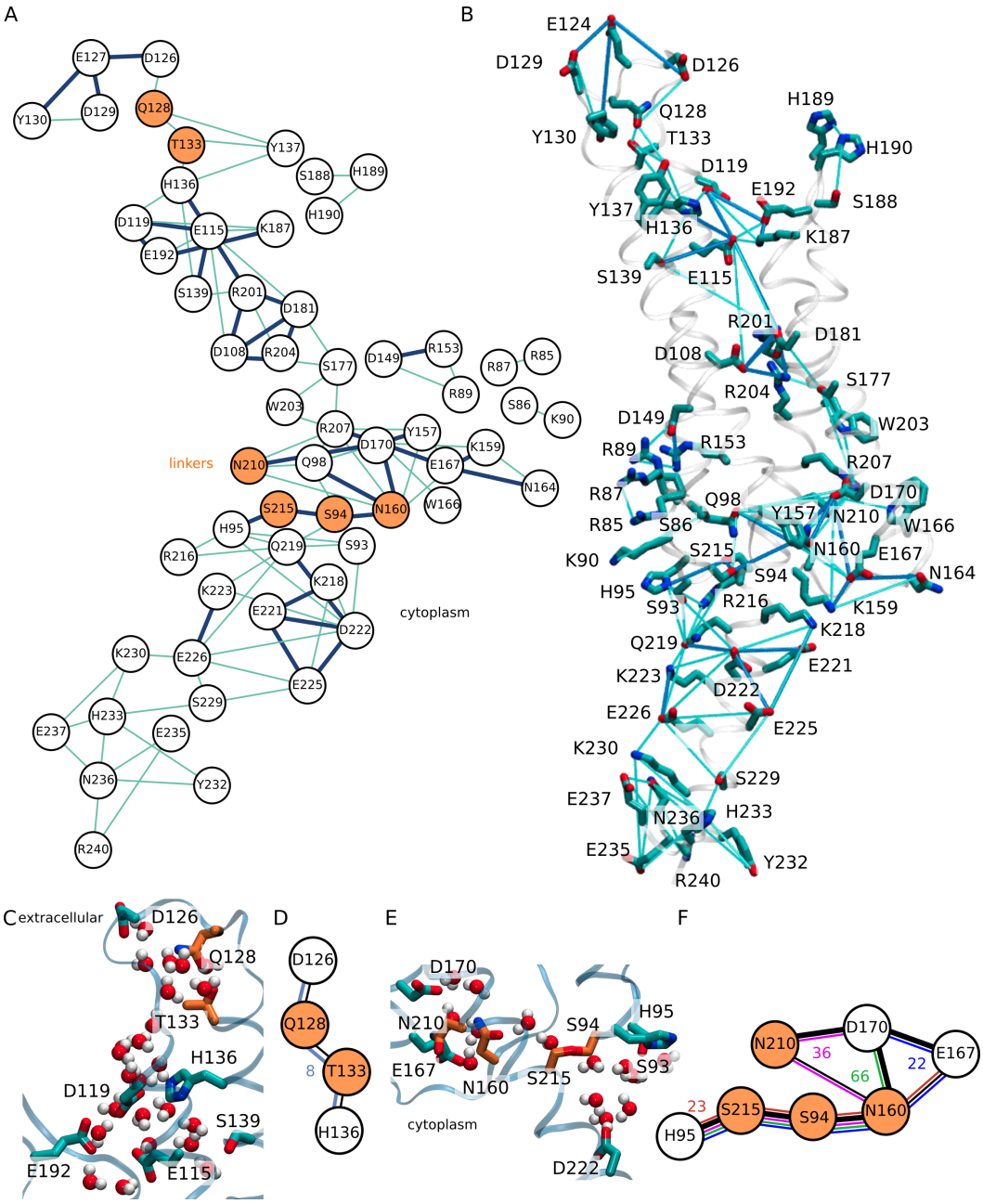


**Figure 5.6.** Linkers connecting the internal H-bond network to cytoplasmic and extracellular sides of Hv1. (A) Graph representation of complete water-mediated H-bond network of Hv1 with linkers highlighted in orange spheres. (B) Molecular graphics of Panel A. Here the occupancy cut-off is 20 % and maximum waterwire length is 3. (C) Molecular graphics showing linkers, Q128 or T133, which form water-mediated H-bonds to connect H136 from the internal H-bond network to D126 of the extracellular H-bond network. (D) H-bond path formed by D126-Q128-T133-H136. (E) Molecular graphics representing the linkers - N160, N210 and S215 connecting D170 and E167 via water mediated H-bonds to the cytoplasmic H-bond network. (F) H-bond path formed between D170 to H95. The numbers on the edges in Panels D and F represent the JO (%) of the highlighted paths. Linkers and specific H-bonding groups are depicted as orange and blue licorice, respectively. The molecular graphics were prepared based on a coordinate snapshot from the simulation of Hv1 with standard protonation and embedded in a hydrated POPC lipid membrane environment. The Panels A-C and E are adapted from ref. [162] (manuscript under preparation).

*Uncharged polar amino acid residues might serve as linkers connecting the internal H-bond network to cytoplasmic and extracellular sides.*

In close proximity to the carboxylates and histidines that make up the H-bond network in Hv1, many Ser, Thr, Asn, and Gln are present. The H-bond network calculations show that the connection between internal and cytoplasmic H-bond network is mediated by N160, N210 or S215 whereas the extracellular carboxylates and internal H-bond network are connected by T133 or Q128 (Figure 5.6). I refer to these H-bonding groups as "linkers" (Figure 5.6). The H-bond paths formed between D170 or E167 from the internal H-bond network to the cytoplasmic H-bond network via S215, N160, N210 or S94 have JOs ranging from 22 to 66 % (Figure 5.6F) whereas H-bond path from D126 to H136 via Q128-T133 has a JO of 8 % (Figure 5.6D). The amino acid residues forming the extracellular and cytoplasmic H-bond network of Hv1 lie in the highly dynamic loops of Hv1. However, N210 and S215 are largely conserved (Figure A.5.22). While N210R is proton permeable, N210C or N210A blocks proton permeation [92, 230, 254]. Mutation of N210 to Lys decreased the voltage threshold for detection of proton currents whereas Arg had the opposite effect [92, 230]. S215, located at the beginning of the cytoplasmic helix, has been reported to interact with Hv1 inhibitor and its mutation to Ala showed reduced inhibitory effect [233]. This suggests that the linker groups N210 and S215 might play a role in determining the connectivity between the internal H-bond network and extracellular and cytoplasmic networks.

## 5.2 Effect of protonation of acidic and histidine sidechains on the H-bond network dynamics of Hv1

*Protonation of acidic and histidine sidechains affects the internal H-bond dynamics of Hv1.*

To probe the effect of protonation state on the H-bond network dynamics of Hv1, I analyzed 10 independent simulations (Table 2.1, Sim 12-21) with different protonation states of carboxylates and histidines present in the most frequent H-bond paths (Figures 5.5B,C) and of significance in the proton conduction pathway as described in the literature. The analysis shows that the protonation state of the carboxylates and histidines forming the most frequent paths affects the waterwire span across Hv1 (Figures 5.7, 5.8). Only in simulations when D108 and D181 are protonated does a continuous H-bonded waterwire between D/E/H/S/T spans the transmembrane area

(Figures 5.7B, 5.7C, 5.8). The continuous water mediated H-bond network is broken at either E115 or D119. The interruption is at E115 when carboxylates on the extracellular side D119 or E115 are protonated (Figures 5.7D,E) and at D108/D181 when carboxylates on the cytoplasmic side of D170, E167, or D149 are protonated or in standard protonation state of Hv1 (Figures 5.7F-H). Only two specific locations where Hv1's waterwire is disrupted indicates that carboxylates D108, D181, and E115 play a key role in mediating the proton transfer pathway.

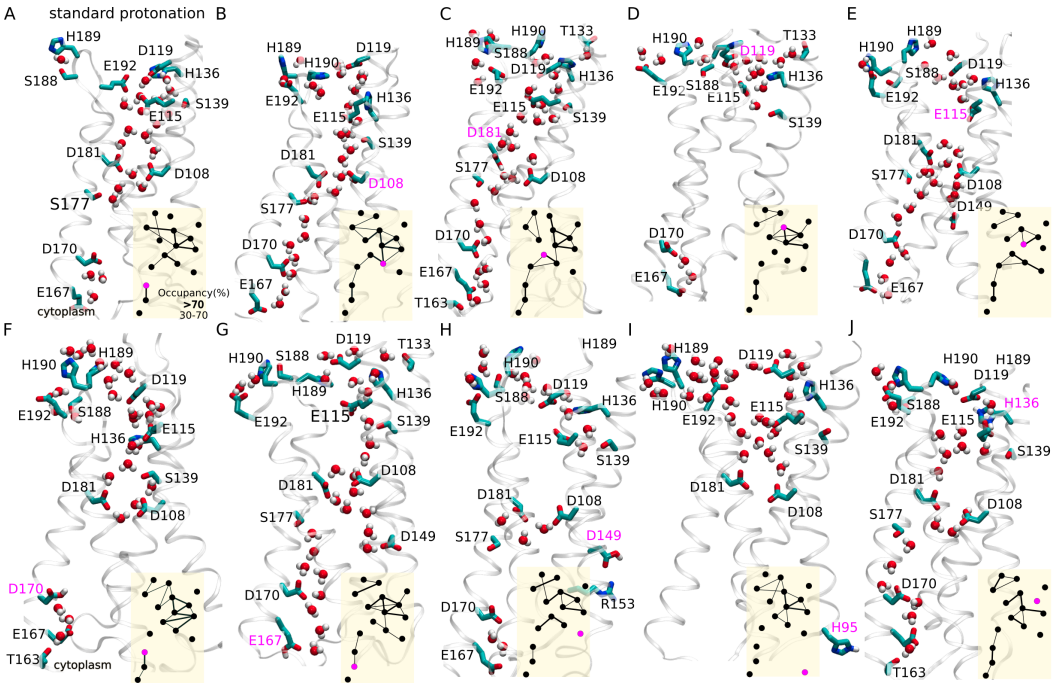


**Figure 5.7.** Dynamics of protonation coupled H-bond network of Hv1. (A-J) Molecular graphics showing water mediated H-bond networks of Hv1 from simulations with different protonation states: standard protonation for all titratable sidechains (Panel A), neutral D108 (Panel B), neutral D181 (Panel C), neutral D119 (Panel D), neutral E115 (Panel E), neutral D170 (Panel F), neutral E167 (Panel G), neutral D149 (Panel H), N$\epsilon$ protonated H95 (Panel I) and doubly protonated H136 (Panel J). Thin white ribbons are used to show the protein whereas licorice and CPK representation is used to show selected titratable groups and water molecules respectively. H-bond paths shown here are mediated by water bridges with up to 3 H-bonded waters in chains. Graphs of the H-bond networks computed from simulations illustrated as insets on the bottom right of each Panel. The figure is taken from ref. [162] (manuscript under preparation).

On double protonation, H136 is no longer a member of the H-bond network (Figure 5.8J), whereas when H95 is epsilon protonated, the cytoplasmic H-bond network is lost (Figure 5.8I). The cytoplasmic H-bond network cluster either expands or contracts depending on where the protonated amino acid residue is located (Figures A.5.5-A.5.14C,D, A.5.15). When carboxylates

on the cytoplasmic side below E115 are protonated, a cytoplasmic cluster is seen; however, when carboxylates at the extracellular side E115 or D119 are protonated, an interruption is observed (Figures 5.7, 5.8). The protonation state of the amino acid residues constituting the H-bond network affects the joint occupancy, length and presence of particular amino acid residues in the most frequent H-bond pathway from D108 and D170 to carboxylates and histidines of Hv1.

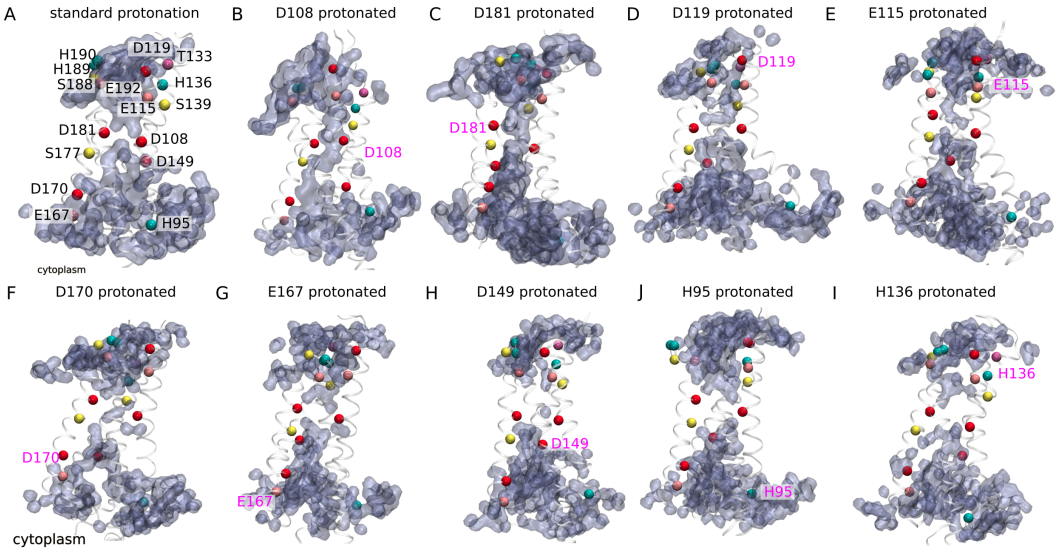


**Figure 5.8.** Water-wire span modulation across Hv1 based on the protonation state of carboxylates and histidines forming the most frequent H-bond paths. (A-J) Molecular graphics showing water-wire span of Hv1 from simulations with different protonation states: standard protonation for all titratable sidechains (Panel A), neutral D108 (Panel B), neutral D181 (Panel C), neutral D119 (Panel D), neutral E115 (Panel E), neutral D170 (Panel F), neutral E167 (Panel G), neutral D149 (Panel H), N$\epsilon$ protonated H95 (Panel I) and doubly protonated H136 (Panel J). Water molecules are shown as iceblue surface whereas thin white ribbons are used to show the protein. The selected protein groups Asp, Glu, His, Ser, Thr are shown as red, pink, cyan, yellow and purple spheres. The figure is taken from ref. [162] (manuscript under preparation).

The rearrangement of the dynamic H-bond network based on the protonation state of carboxylates and histidines is also shown by the conserved graph analysis using Cgraphs software [129] (Figure A.5.15). This suggests that location of protonated amino acid residues regulates the continuity and extension of the waterwire on a specific side of the Hv1. It aligns with the discussion of increase in outer or inner pH leading to extended H-bond network on the extracellular or intracellular side [240]. On inclusion of all the titratable sidechains of Hv1 in H-bond network calculations, the interruption of H-bond network is still observed in simulations with standard protonation (Figure A.5.5), protonated D119 (Figure A.5.7), D149 (Figure A.5.10), D170 (Figure

A.5.8), E115 (Figure A.5.11), H95 (Figure A.5.13) and a continuous H-bond network when D108 (Figure A.5.6), D181 (Figure A.5.9) are protonated. For simulations with E167 protonated (Figure A.5.11) and H136 doubly protonated (Figure A.5.14), R204, R207 and W203 form water mediated H-bonds with neighbouring carboxylates D108, D181, D149 and D170 leading to a formation of continuous H-bond network. These H-bonds are usually mediated by 2-3 water molecules on an average (Figures A.5.12-A.5.14).

## 5.3 Influence of lipid composition on the internal H-bond network Hv1

*Lipid composition influences the internal H-bond network dynamics.*

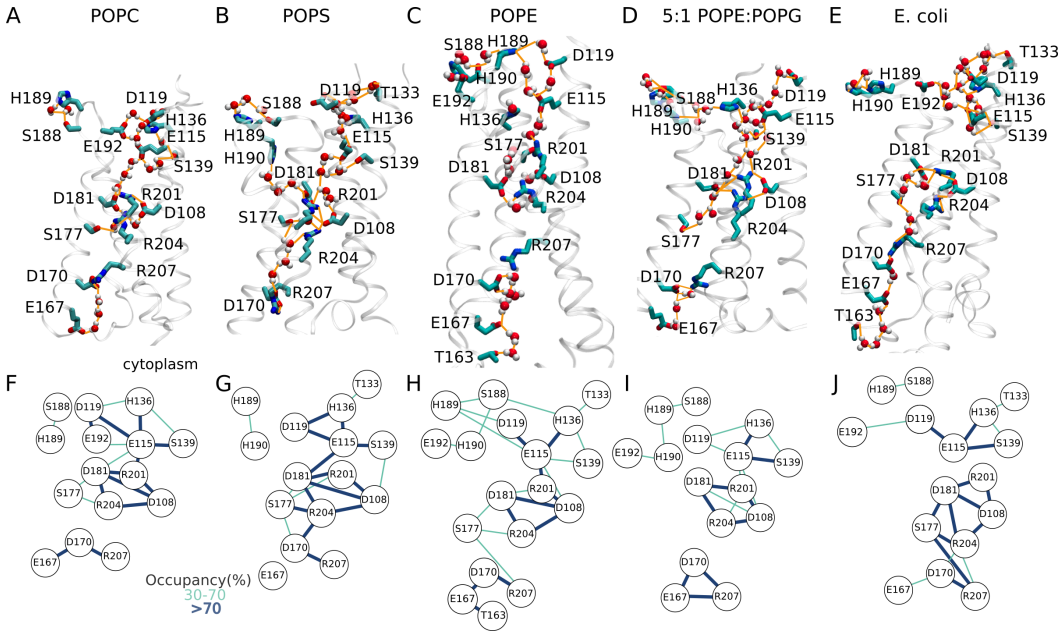


**Figure 5.9.** Dynamics of internal H-bond network of Hv1 in bilayers distinguished by lipid composition. (A-E) Molecular graphics of the water mediated H-bond network of Hv1 in POPC (Panel A), POPS (Panel B), POPE (Panel C), 5:1 POPE:POPG (Panel D) and the *E. coli* membrane (Panel E, I). (F-J) Graphical representation of H-bond network depicted in Panels A-E respectively. The figure is taken from ref. [162] (manuscript under preparation).

To probe the effect of lipid composition on the H-bond network dynamics of Hv1, I analyzed 5 independent simulations of Hv1 embedded in lipid bilayers with varying lipid composition - i) POPC; ii) POPS; iii) POPE; iv) a 5:1 mixture of POPE:POPG lipids; v) the *E. coli* membrane model referred to as Top6 in ref. [147], which is a mixture of PE- and PG-type lipids (Table 2.1, Sim 12, 22-25). In POPC, POPE, and 5:1 POPE:POPG bilayers the

internal H-bond network of Hv1 is interrupted at D108-D170 surrounded by the hydrophobic gasket (Figures 5.9, A.5.5, A.5.17-A.5.18). In *E. coli* bilayer, this interruption is observed at E115-D108 (Figures 5.9, A.5.20). In contrast to other bilayers, in the POPS bilayer, the internal H-bond network of Hv1 may become continuous (Figures 5.9B,F, A.5.16, A.5.19). In POPS bilayer, the S3 helix of Hv1 reorients with respect to other helices, which is linked to the rearrangement of the amino acid residues and this could result in changing the internal H-bond network. Titratable sidechains of Hv1 can form dynamic, water-mediated H-bond clusters with lipid molecules in all simulations including acidic lipids. This implies that the Hv1 sidechains and lipid headgroups may bind or trap protons on the membrane interface.

## 5.4 Putative proton antennas of Hv1 in different lipid bilayers

Protons may transiently bind to bulk exposed proton antennas containing negatively charged protein sidechains or lipid headgroups at lipid membrane interfaces, increasing the dwell time of the proton. These anionic groups along with histidines can create H-bonded lipid clusters that form pathways for proton transfer along the membrane interface while also collecting them from the bulk. Hv1 has closely spaced clusters of carboxylates and histidines at the membrane interface suggesting the formation of proton antennas. Using the protocol developed to find the most frequent H-bond paths between carboxylates and histidines (Chapter 2, Sec 2.6), I characterize dynamic lipid-water H-bond clusters at Hv1-lipid membrane interfaces. In 5 different lipid membranes, I identify the most frequently sampled water-mediated Hv1-lipid H-bonded clusters that might serve as putative proton antennae.

*Acidic lipids can participate in water-mediated H-bond clusters with Hv1.*

Hv1 carboxylates and histidines are in close proximity to the lipid headgroups. It is thus possible that an extended water mediated H-bond network is formed on the extracellular and cytoplasmic sides including the lipid headgroups (Figure 5.2C). In Chapter 3, anionic lipids have been shown to possess the tendency to form extended H-bond networks. In agreement to these observations, atomistic simulations of Hv1 in different lipid bilayers reveal an extended H-bond network at the membrane interface of Hv1-POPS bilayer. As compared to POPS, POPE and POPG in 5:1 POPE:POPG and the *E. coli* bilayer tend to engage in less extended protein-lipid H-bond network. In contrast, POPC lipids barely participate in water-mediated H-bond networks with protein sidechains. In membranes with PE and PG, PE is shown to

more frequently interact with Hv1 and neighbouring lipid headgroups rather than PG (Figure A.5.21). This observation can be attributed to the tendency of PG to engage in intramolecular rather than intermolecular H-bonding.

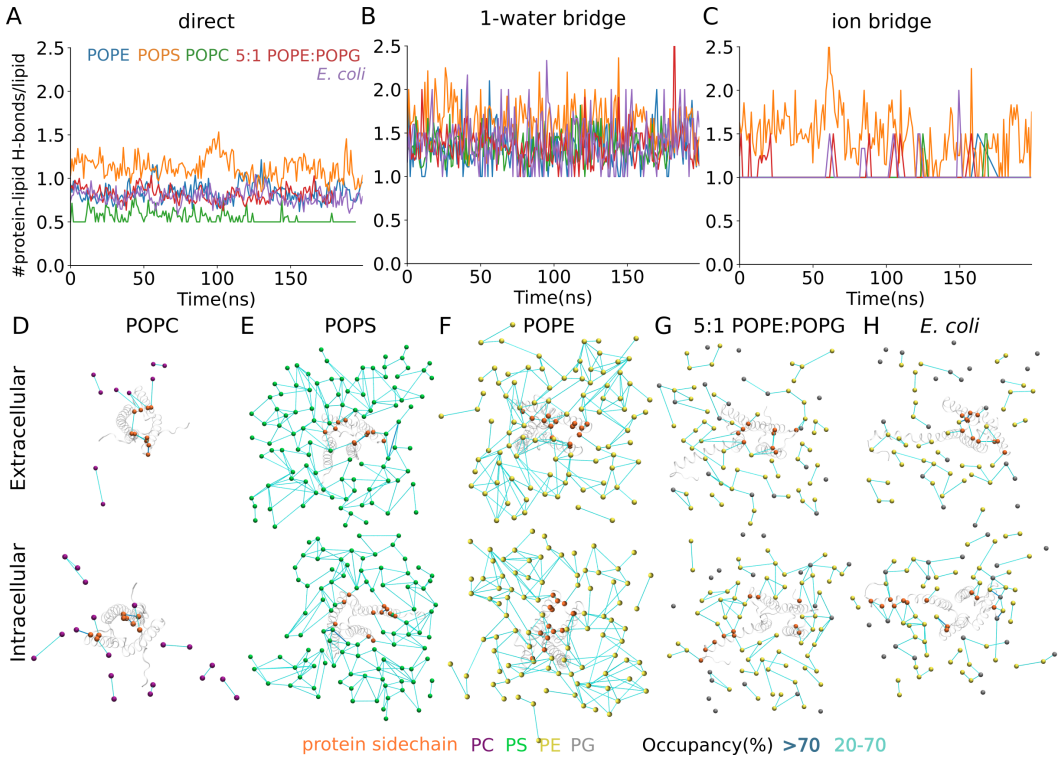


**Figure 5.10.** H-bond network mediated by water at membrane interfaces with Hv1. (A-C) Time series showing the number of direct (Panel A), one-water mediated bridges (Panel B), and potassium-ion-mediated bridges between lipid headgroups (Panel C). Coordinate sets were read each 1 ns for clarity. (D-H) Illustration of H-bond network mediated by upto 3 water molecules at membrane interfaces with Hv1. The top panel shows a view from the extracellular side of Hv1, and the bottom panel, from the cytoplasmic side. H-bond network at the interfaces of POPC (Panel D), POPS (Panel E), POPE (Panel F), 5:1 POPE:POPG (Panel G), and *E. coli* Top6 membranes (Panel H). The H-bond networks were computed using Bridge [34, 128]. H-bonds with occupancy greater than 20% are shown here. The figure is taken from ref. [162] (manuscript under preparation).

*Putative proton antennas of Hv1.*

Using the graphical approach for calculating water-mediated H-bond paths, I further characterize the dynamic H-bond pathways that can momentarily link internal titratable sidechains and lipid headgroups to the bulk. Based on the newly developed protocol (Chapter 2, Sec 2.6), I then rank the paths according to the frequency with which all intermediate path segments are sampled during the independent simulations, providing information regarding possible proton wire paths. POPS lipid headgroups and carboxylic

sidechains of Hv1 were found in water-mediated H-bond clusters (Figure 5.11). From D108 to the POPS lipid headgroups, an H-bond cluster runs along the extracellular side of Hv1 (Figure 5.11A). Two H-bond clusters are found on the cytoplasmic side - one with the E167 and lipid headgroups and another protein-water-lipid H-bond cluster with the S4 helix carboxylic sidechains (Figure 5.11A).

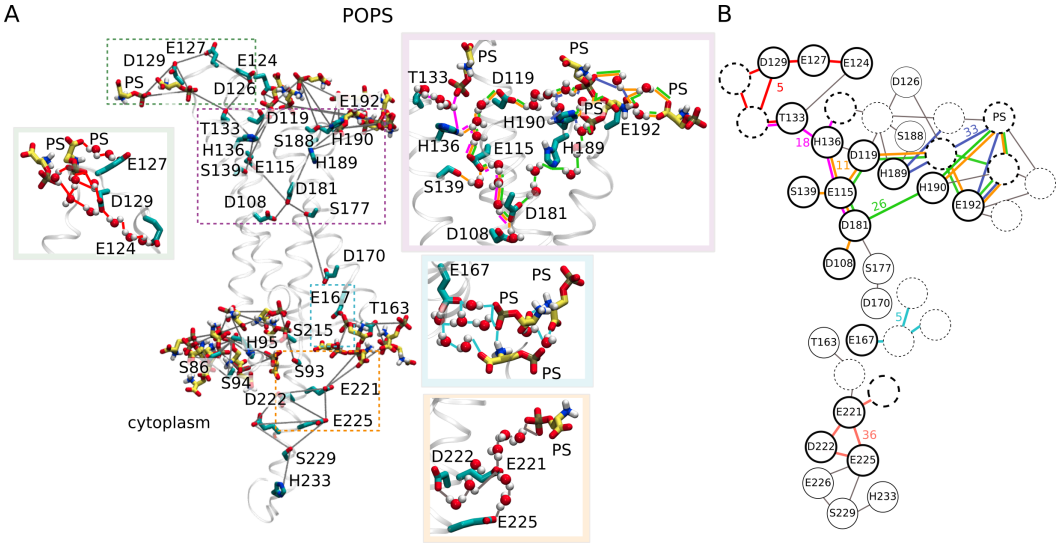


**Figure 5.11.** Hv1-POPS water-mediated H-bond clusters. (A) Molecular representation of specific H-bond clusters at extracellular and intracellular sites of Hv1. (B) A schematic representation of Panel A's H-bond clusters. For clarity, only H-bonds present during at least 30 % of the time and paths with minimum *JO* value of 5 % are reported. The figure is taken from ref. [162] (manuscript under preparation).

According to two simulations of Hv1 embedded in bilayers containing acidic PG-type lipids (Table 2.1), PG-type lipids may be a component of dynamic H-bond clusters at membrane interfaces of Hv1 (Figures 5.12, 5.13), just like the POPS membrane. PG-type lipids are a component of water-mediated H-bond clusters with H189, S188, and D129 on the extracellular side and with E167, E226, H233, and S86 on the cytoplasmic side in both the POPE:POPG and *E. coli* membranes (Figures 5.12, 5.13). At the extracellular E115 location, both lipid membranes permit water-mediated clusters of lipid-Hv1 H-bonds (Figures 5.12, 5.13). Given that E115 is assumed to be crucial for proton transfer via Hv1 [27, 85, 91, 92, 235], the discovery that E115 participates in H-bonding with water molecules and PG-type lipids is important for proton transfer considerations. Relative to the wild-type channel, the voltage threshold at which proton current could be detected was higher when E115 was mutated to Ala [92].

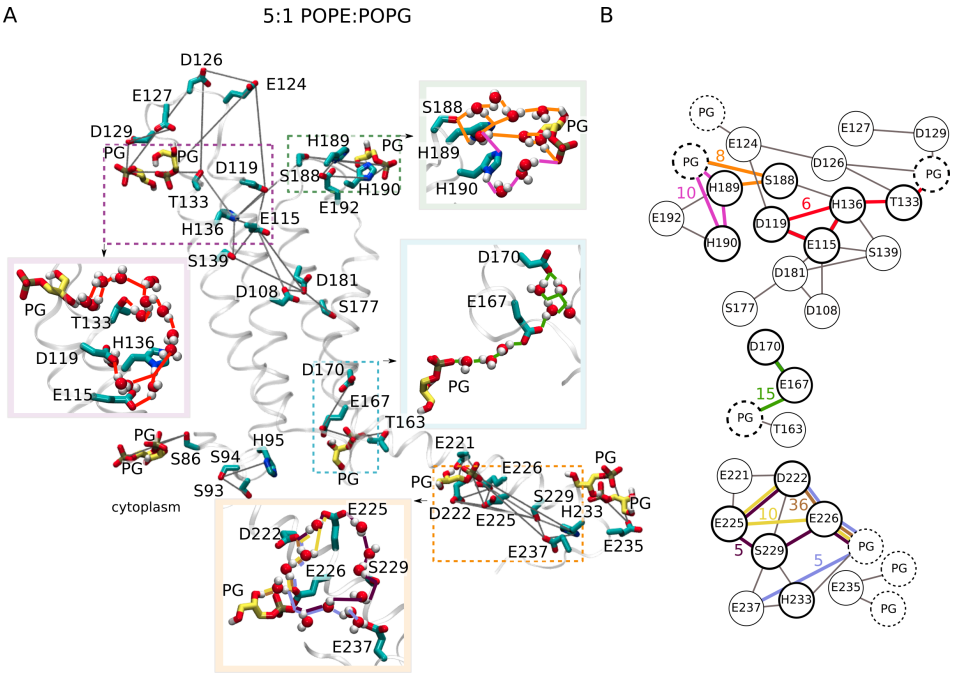


**Figure 5.12.** Hv1-lipid water-mediated H-bond clusters in a hydrated 5:1 POPE:POPG bilayer. (A) Molecular representation of specific H-bond clusters at extracellular and intracellular sites of Hv1. (B) A schematic representation of Panel A's H-bond clusters. For clarity, only H-bonds present during at least 30 % of the time and paths with minimum *JO* value of 5 % are reported. The figure is taken from ref. [162] (manuscript under preparation).

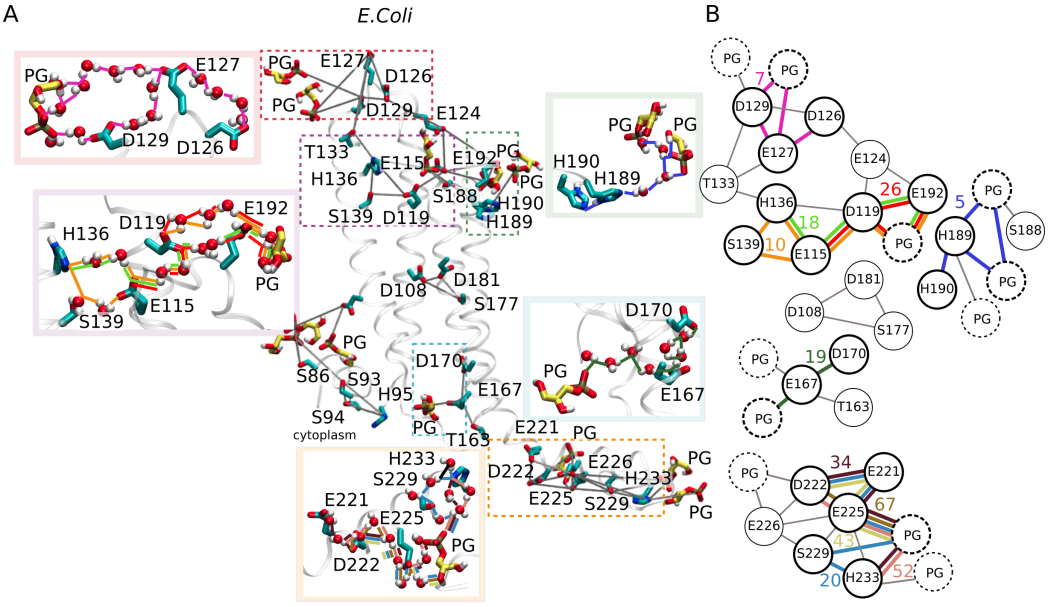


**Figure 5.13.** Hv1-lipid water-mediated H-bond clusters in a model *E. coli* bilayer. (A) Molecular representation of specific H-bond clusters at extracellular and intracellular sites of Hv1. (B) A schematic representation of Panel A's H-bond clusters. For clarity, only H-bonds present during at least 30 % of the time and paths with minimum *JO* value of 5 % are reported. The figure is taken from ref. [162] (manuscript under preparation).

## 5.5 Lipid anchors of Hv1

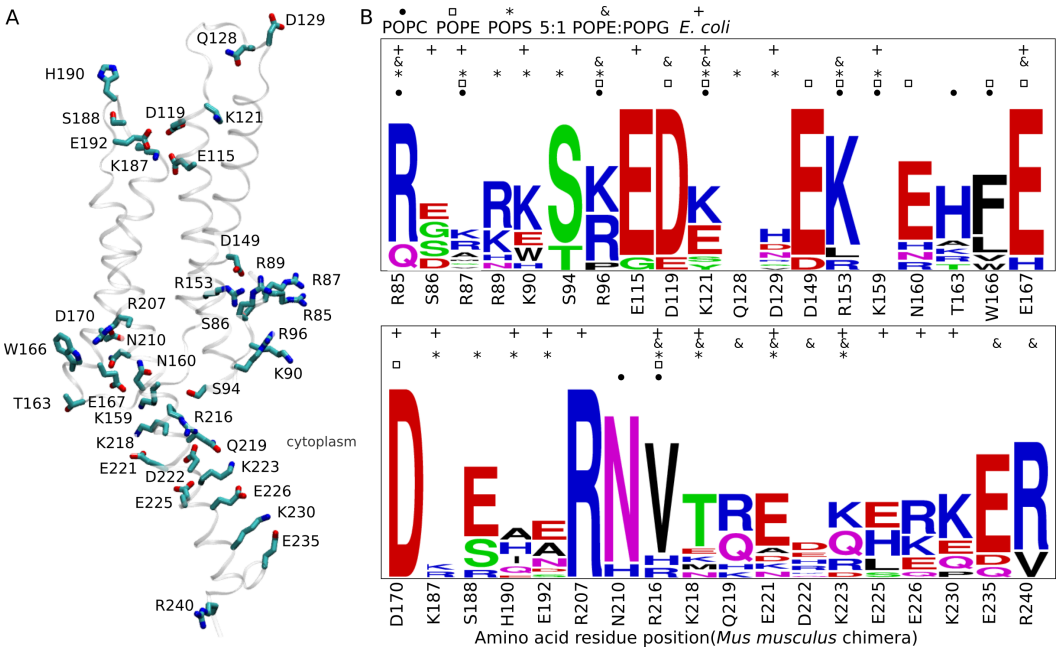


**Figure 5.14.** Hv1's conserved lipid anchors. (A) Molecular representation of lipid anchors of Hv1. Thin white ribbons represent the protein whereas the lipid anchoring protein groups are shown as cyan licorice. A coordinate snapshot from the simulation of Hv1 with standard protonation and embedded in a hydrated POPC lipid membrane environment was used to prepare the molecular graphics. (B) Logos diagram for Hv1 lipid anchor multiple sequence alignment. Each symbol's height indicates the conservation of that residue in 10 different Hv1 sequences from 9 species. WebLogo was used to generate the Logos diagram [255, 256]. The figure is taken from ref. [162] (manuscript under preparation).

Hv1 has several Arg, Lys and Trp in close proximity to the lipid interface (Figure 5.2C). These amino acid residues of Hv1 can serve as lipid anchors. Further analyzing the Hv1 simulations distinguished by lipid bilayers, I identified amino acid residues of Hv1 that interact with lipid headgroups of nine different types of lipids: neutral POPC, zwitterionic POPE, PMPE, QMPE, YOPE, negatively charged POPS and POPG (Figure A.5.4). In the 5:1 POPE:POPG and *E. coli* membrane models, multiple interactions between PE-type lipids and Hv1 sidechains are observed (Figure A.5.21). According to bioinformatics analysis, the sidechains of Hv1 interacting with lipid membranes tend to be conserved (Figure 5.14). This suggest that lipid-protein anchoring may be crucial for controlling how Hv1 is oriented in relation to the membrane interface. In every Hv1 simulation with a varied lipid composition, K121, R96, and R216 interact with the lipid headgroups (Figures A.5.23). On the cytoplasmic side, arginines and lysines R85, R87, K159, and K223 engage with the negatively charged headgroups PS and PG, whereas on the

extracellular side, carboxylates D119 or E115 interact with the amine group of zwitterionic PE (Figure A.5.23). When K121, E115, and D119 are changed to Ala, the voltage threshold for proton current detection rises, whereas R96A has the reverse effect [92, 230]. These mutagenesis research, however, employed the same cell line without lipid composition differentiation. As the lipid anchors differ based on the nature and charge of lipid headgroups, mutagenesis analysis of these lipid anchors in lipid membranes with different lipid composition might lead to new insights.

## 5.6 H-bond dynamics of Hv1 towards drug design

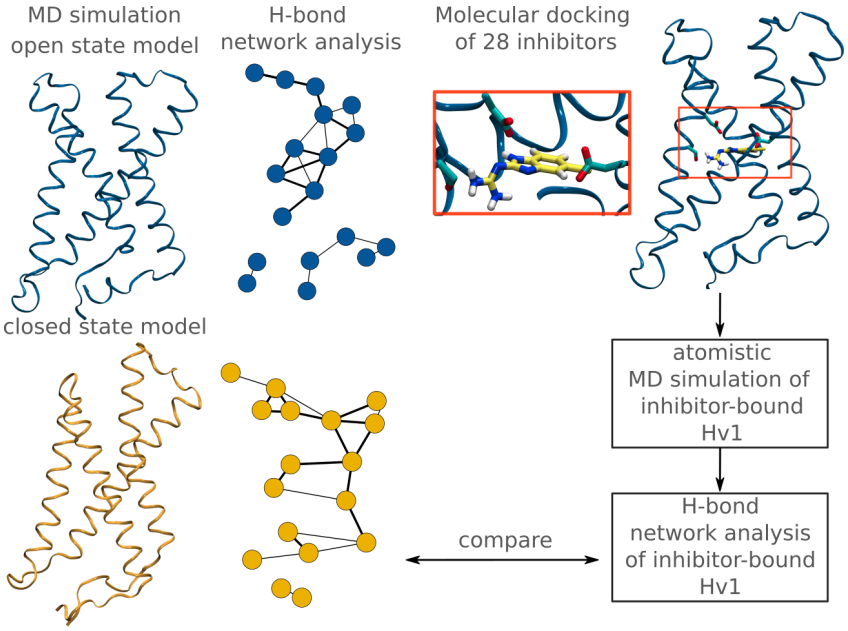


**Figure 5.15.** H-bond dynamics of Hv1 towards drug design.

Hv1 is associated with cancer [86, 88, 204], neuroinflammatory diseases [257, 258], sperm cell capacitation [259, 260] and ischemis stroke [261, 262], making it an important drug target and an aid to male contraceptive treatments [259]. Development of Hv1 inhibitors has been focused on targeting the extracellular side with peptide toxins [178, 236, 263] or the intracellular side with small organic molecules [242, 264]. Previous studies have reported zinc ion [148, 228], 2-guanidinobenzimidazole (2GBI) [237, 265], 5-chloro-2-guanidinobenzimidazole (ClGBI) [237], Corza6 (C6) [178] and HIF (Hv1 Inhibitor Flexibles) [231, 232] as Hv1 inhibitors. As discussed in the previous sections of Chapter 5 and reported by previous studies [27, 85, 91–93], the functioning of Hv1 is regulated by a network of H-bonds. The presence of inhibitors could impact the dynamics of this H-bond network and thus effect its functioning. Taking this into account, in this section, I dock the known

inhibitors of Hv1 and setup Hv1-inhibitor systems for MD simulations that can be used to characterize the impact of the inhibitor binding on H-bond networks of Hv1.

The crystal structure of a resting state of chimeric Hv1 is available [148] whereas the open and closed state models have been proposed by Tobias group [27] using MD simulations. So for docking studies, the suggested open and closed model [27] were used. MD simulations 100 ns long of open and closed state models of Hv1 without the inhibitors were performed using the protocol described in Chapter 2.

*Docking of known inhibitors of Hv1*

28 known inhibitors of Hv1 (Table 5.1) were docked on the last frame of 100 ns long trajectory of open state model of Hv1. Inhibitors 1-18 are from ref. [237], inhibitors 19-24 are HIFs from ref. [231, 232] and inhibitors 25-28 are from ref. [233]. AutoDock Vina [145] was used for docking and binding energy calculation. The center of the Hv1 open state structure was set as the center of docking box. The box size was set to 24 Å in each dimension ensuring that the known binding pocket is within the defined box. The exhaustiveness of the global search was set to 8, a reasonable choice maintaining balance between the accuracy of docking results and computational efficiency [266]. The maximum number of binding modes was 10 capturing diverse binding poses of ligand. The docking results were found to be in alignment to the experimental studies done before [231, 232, 242].

Docking results show binding energies ranging from -4.2 to -11.3 kcal/mol (Figure 5.16A). The binding site for the inhibitors under study is located on the cytoplasmic or intracellular side (Figure 5.15B). The interaction of inhibitors is stabilized by H-bonds formed with the titratable sidechains of Hv1. The conserved carboxylates D112 and D185, and the voltage sensing R211 interacts with a total of 17 out of 28 inhibitors. D112 serves as the selectivity filter of Hv1 [228] whereas R211 forms salt bridges with D112 and D185 that are imported for gating mechanism of Hv1 [27, 91]. S181 interacts with the NH2 group of 5 guanidine derivative inhibitors. These four aminoacid residues are located close to the hydrophobic gasket of Hv1 formed by V178, I177, V109, and F150 (numbering as hHv1) (Figure 5.2B). Another inhibitor binding site includes the carboxylate E225 and arginine R223 located on dynamic non-helical region at the end of S4 helix. N214 (N210 in mHv1), a conserved amino acid residue (Figure 5.14) also interacts with Hv1 inhibitors. In this chapter in previous discussion, N214 is proposed to be a linker between the internal and cytoplasmic H-bond network of Hv1.

Out of these 28 compounds, 4 activity cliffs with large differences in potency were selected for further analysis. As reported by ref. [237], at 10 µM concentration, the highest difference in the inhibition (%) was found between inhibitors 1 and 4 whereas at 200 µM a difference in activity is observed for inhibitors 1,3 and 11. Thus, inhibitors 1, 3, 4 and 11 were chosen. Ligand-protein interaction maps were generated using ProLif [267]. Inhibitor bound Hv1 systems were prepared for MD simulations for future use. H-bond network analysis of these simulations could give insights into the role of water mediated H-bond networks in Hv1 functioning.

**Table 5.1.** Inhibitors of Hv1. The molecular images of the inhibitors are shown in Figure A.5.24.

| No. | Inhibitor |
|---|---|
| 1 | 2-guanidinobenzimidazole (2GBI) |
| 2 | 2-(2-benzimidazolylamino)-imidazole-4,5-dione |
| 3 | 4-phenyl-1,4-dihydro[1,3,5]triazino[1,2-a]benzimidazol-2-amine |
| 4 | 5-chloro-2-guanidinobenzimidazole |
| 5 | 5-nitro-2-guanidinobenzimidazole |
| 6 | 1-[5-(morpholin-4-ylsulfonyl)-1H-benzimidazol-2-yl]guanidine |
| 7 | N-(4-chlorophenyl)-4H-1,2,4-triazole-3,5-diamine |
| 8 | S-1H-benzimidazol-2-yl-carbamothioate |
| 9 | 1-(benzimidazol-2-yl)urea |
| 10 | N-(4-chlorophenyl)-1,3,5-triazine-2,4-diamine |
| 11 | 2-guanidino-benzoxazole |
| 12 | 1-(benzimidazol-2-yl)-3-(2-phenylethyl)guanidine |
| 13 | amiloride |
| 14 | 3a,8a-dihydroxy-2-imino-2,3,3a,8a-tetrahydroindeno[1,2-d]imidazol-8(1H)-one |
| 15 | isoproyl6-(guanidinoimino)-6-phenylhexanoate |
| 16 | creatinine |
| 17 | 1-[2-(5-methoxy-1H-indol-3-yl)ethyl] guanidine |
| 18 | leonurine |
| 19 | 3-(2-amino-5-methyl-1H-imidazol-4-yl)-1-(3,5-difluorophenyl)propan-1-one (HIF) |
| 20 | 3-(2-amino-5-methyl-1H-imidazol-4-yl)-1-phenyl-propan-1-one (HIF_NF) |
| 21 | N-[(2-amino-5-methyl-1H-imidazol-4-yl)methyl]-3,5-difluorobenzamide (HIF_NH) |
| 22 | 3-(2-amino-5-methyl-1H-imidazol-4-yl)-1-(3,5-difluorophenyl)propan-1-ol (HIF_OH) |
| 23 | (2E)-3-(2-amino-5-methyl-1H-imidazol-4-yl)-1-(3,5-difluorophenyl)prop-2-en-1-one (HIF_EN) |
| 24 | 2-aminobenzimidazole (ABI) |
| 25 | YHV98-1 |
| 26 | YHV98-2 |
| 27 | YHV98-3 |
| 28 | YHV98-4 |

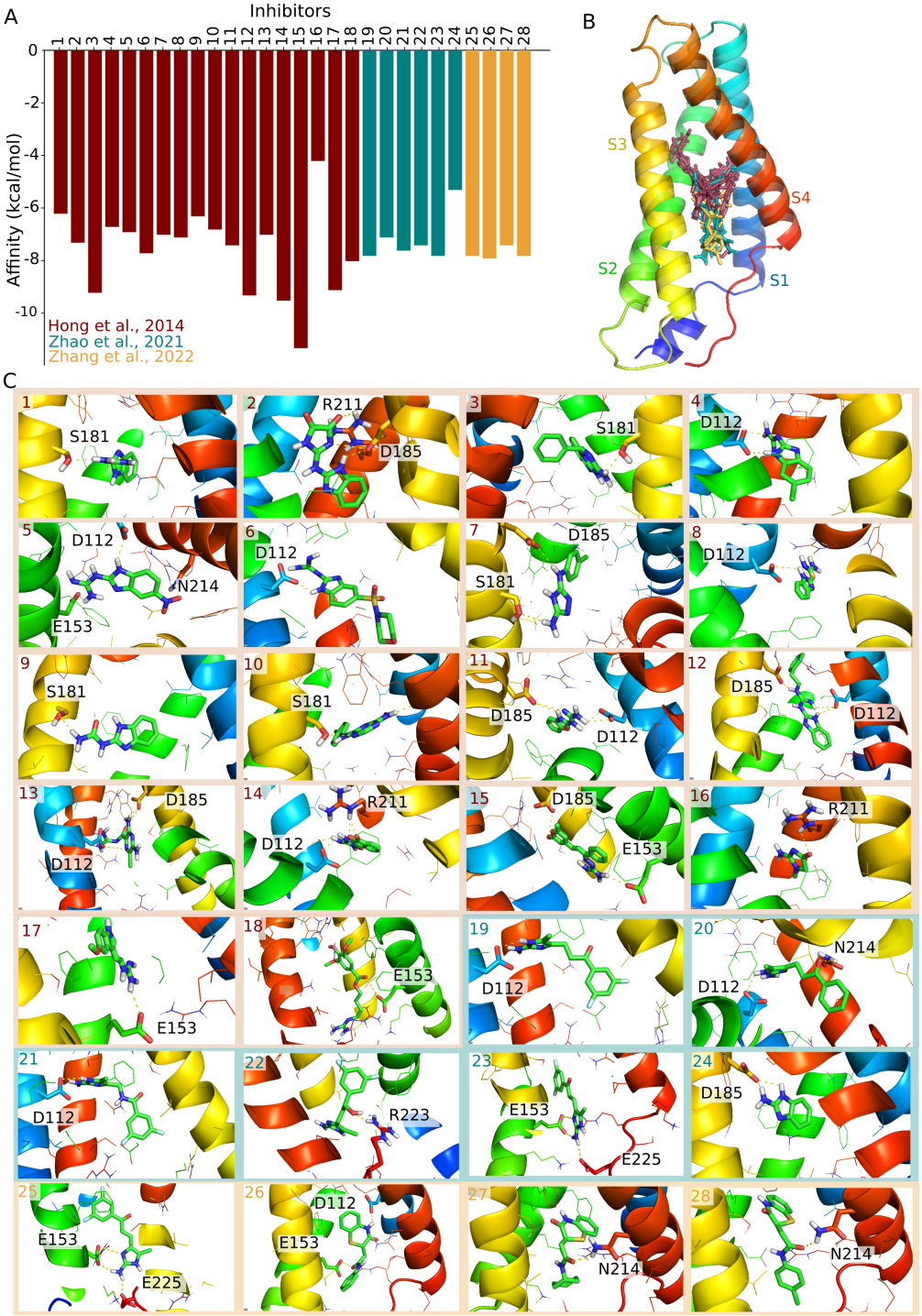


**Figure 5.16.** Docking results of known inhibitors of Hv1 docked on open state model of human Hv1. (A) Binding energies of 28 known inhibitors bound to open state of Hv1. (B) Molecular graphics showing the binding pocket of all the inhibitors under study here. (C) Close view of interactions of 28 known inhibitors with Hv1. The molecular graphics were prepared using PyMol [146].

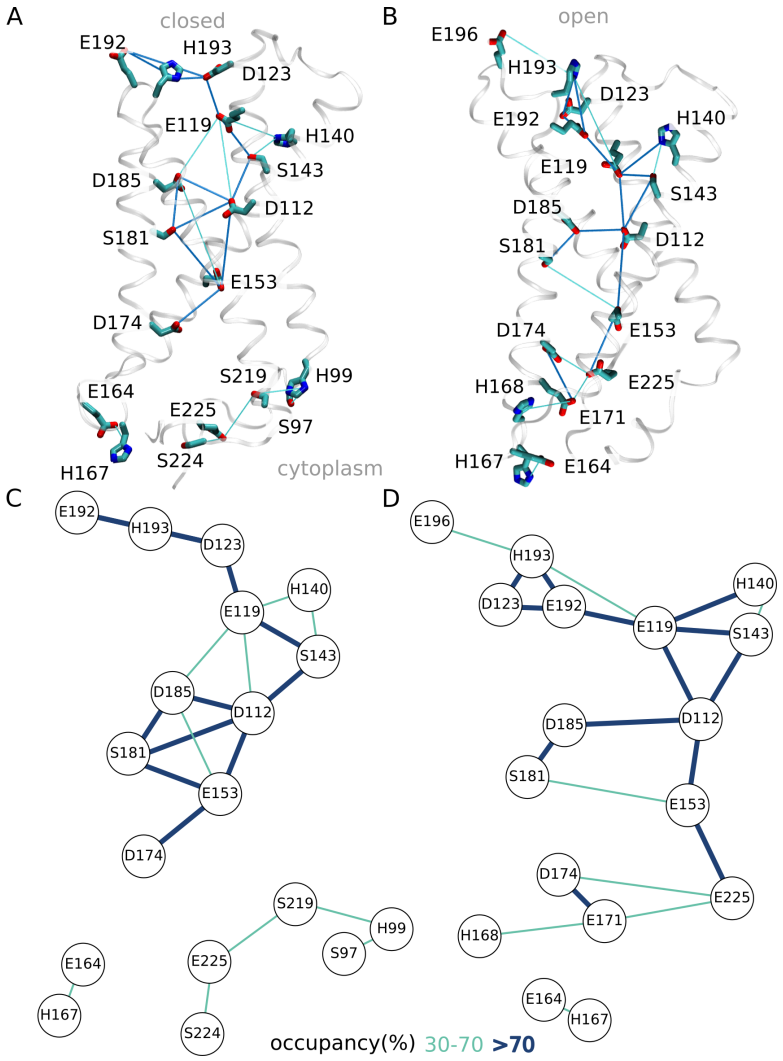


**Figure 5.17.** Dynamic H-bond network of closed and open state models of human Hv1 without inhibitors. (A-B) Molecular graphics of closed (Panel A) and open (Panel B) state model's water mediated H-bond network formed by titratable sidechains (Asp, Glu, Ser, Thr and His) of Hv1. (C-D) Graphical representation of closed (Panel C) and open (Panel D) state H-bond network of Hv1 as shown in Panels A and B respectively. Upto 3 waters are taken into consideration for H-bond calculation done using Bridge [34, 128]. The molecular graphics were prepared using VMD [144].

*H-bond network analysis of open and closed state of Hv1*

H-bond network analysis for open and closed was performed using Bridge [34, 128]. An interruption in the water mediated H-bond network via titratable sidechains is observed at D174 (numbering as hHv1, D170 in mouse Hv1) in closed state in contrast to the open state model where a continuous H-bond network spans the proton channels (Figure 5.17). E153 connects to E225 via water mediated H-bonds which allows the formation of a continuous H-bond network in open state model of Hv1 in contrast to closed state model. The

amino acid residues D112, D185, R211, E153 and E225 involved in inhibitor binding of Hv1 are part of the H-bond network formed by Hv1 in open an closed state. This further suggests that the interaction of inhibitors with the H-bonding amino acid residues of Hv1 could result in an interrupted H-bond network leaving the proton channel nonfunctional.

# 6

# Conclusions and future aspects

H-bonds play an essential role in many biological functions such as providing conformational flexibility to proteins [20, 21, 41, 44], regulating physical properties of lipid membranes [22–24] and serving as proton transfer pathways [27, 28, 30, 38, 171] (Chapter 1). Understanding the dynamics of H-bond networks in biological systems can give insights that drive drug discovery. In this thesis, I compute and analyse dynamic H-bond networks of lipid membranes and a protein using atomistic MD simulations along with graph theory based approach (Chapter 2). I characterize and identified the dynamic H-bond networks in (i) lipid membranes containing anionic lipids (Chapter 3, 4) and (ii) Human voltage gated proton channel Hv1 embedded in lipid bilayers (Chapter 5).

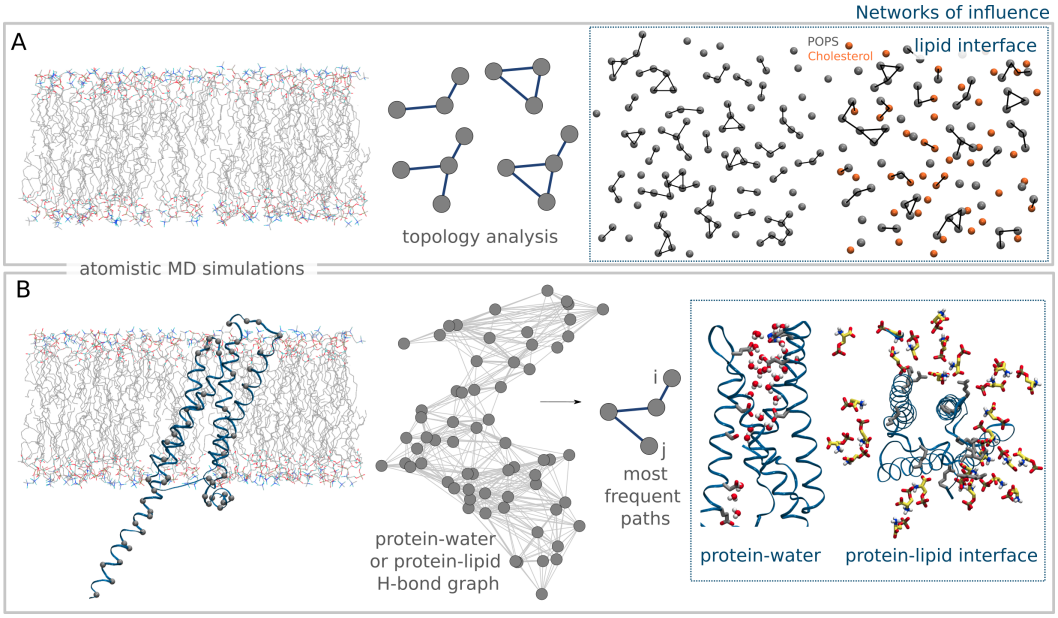


**Figure 6.1.** Networks of influence in lipid membranes and transmembrane proton channel. (A) Approach to characterize lipid clusters in bilayers with varying lipid composition based on their topology. (B) Approach to identify and characterize H-bond networks of transmembrane proteins and at protein-lipid interface.

Lipid clusters can be formed on the lipid membrane via dynamic H-bonding mediated by water molecules. The nature of lipid headgroups can play a role in governing the dynamics of these H-bonded lipid clusters [83, 165, 170]. To investigate the role of lipid headgroups in formation of H-bonded lipid

clusters, I performed MD simulations of hydrated lipid bilayers containing zwitterionic and anionic lipids. I implemented a previously developed DFS based graph algorithm [42] to analyze the topology of H-bonded lipid clusters in six different systems distinguished by lipid composition (Table 2.1, Chapter 2, Sec 2.5). Using the DFS algorithm [42], the topologies are classified into 4 main topologies - linear, star & linear, circular, star & linear & circular (Figure 2.4). In all simulations the most common topology sampled is linear irrespective of the lipid composition or nature of lipid headgroup (Chapter 3). This suggests that the mechanism of proton transfer might be independent of the lipid headgroup. However, anionic lipids mainly phosphatidylserine tend to form extended water mediated H-bonded lipid clusters with 3 or more lipids (Chapter 3) [42]. In this case, protons might move along the H-bonded water wires and the lipid-lipid interactions would position the waters in the water wire facilitating formation of extended H-bond networks.

Phosphatidylserine, an anionic lipid, shows a higher tendency to form H-bonds as compared to other anionic or zwitterionic lipids (Chapter 3) [42]. Extended water-mediated H-bond networks are formed by POPS (Chapter 3). Cholesterol can H-bond to phosphatidylserine [84] and can thus impact the properties of phosphatidyleserine bilayers. To evaluate the impact of cholesterol and to characterize the H-bond dynamics of phosphatidylserine:cholesterol membranes, I did topology analysis of bilayers of phosphatidylserine containing varying concentrations (10 to 40 %) of cholesterol (Chapter 4). Eukaryotic plasma membranes contains a complex mixture of 11 different types of lipids along with 10-40 % cholesterol [62]. Thus, the systems discussed in Chapter 4 are limited to being model membranes.

The presence of cholesterol results in influencing the properties such as area per lipid, thickness and ordering of lipid tails [71–74, 176] of the lipid bilayer (Chapter 4). A decrease in area per lipid, an increase in membrane thickness and order parameters is observed (Chapter 4, Sec 4.1) in the presence of cholesterol. To understand the distribution of H-bond dynamics at different depths of lipid bilayers, I identified and characterized the H-bonds formed by different H-bonding groups of the lipid headgroup - phosphate, serine, ester, phosphate & serine and all the groups together (Chapter 4, Sec 4.2). Regardless of the presence of cholesterol, POPS samples dynamic (low-occupancy) water-mediated H-bond networks. Water-mediated H-bonding is found to be predominant between the phosphate & serine and serine groups. The topology analysis of phosphatidylserine:cholesterol membranes gave insights about how the H-bonded lipid clusters tend to arrange spatially. As reported previously [42] and discussed in Chapter 3, POPS tends to form linear clusters with 3-4 lipids. Irrespective of the presence of cholesterol, this

tendency of POPS to form short linear clusters via direct or water-mediated H-bonding is maintained. However, based on the topology analysis, the presence of cholesterol seems to hinder the formation of extended water-mediated H-bond networks in phosphatidylserine membranes. Cholesterol forms H-bonded clusters with POPS but these clusters are less frequent then POPS-POPS clusters. On the other hand, cholesterol-cholesterol clusters are rarely sampled and whenever sampled they are usually sampled in pairs (Chapter 4, Sec 4.3). These results are compatible with previous studies reporting formation of cholesterol dimers. The protocol used in Chapter 4 may prove beneficial to analyze the dynamic H-bond lipid clusters in cholesterol-containing complex bilayers with proton binding interfaces. It can also be utilized to assess the impact of cations on preferred topologies of lipid clusters.

Closely spaced anionic lipid headgroups and/or titratable sidechains of transmembrane proteins can form proton antennas (Chapter 1) facilitating proton transfer along the lipid bilayers [95, 96, 104]. In order to decipher the mechanism of proton transfer mechanism across proton transporters, it is essential to identify and characterize these proton-binding clusters and the H-bond pathways between them. In order to identify these important H-bond paths, I developed a graph theory based protocol to find the most frequently sampled water-mediated H-bond paths via titratable groups of transmembrane proteins and/or lipid headgroups (Figure 2.5) (Chapter 2, Sec 2.6). This developed protocol provides a significant advantage by enriching the sampling of H-bond paths in comparison to the shortest path approach (Chapter 5). In Chapter 5, I discuss the results of the implementation of this protocol on the human voltage gated proton channel Hv1.

Hv1, a voltage gated proton channel, is responsible for pH regulation [85, 86]. It's main function is proton extrusion. A dynamic network of H-bonds between the titratable sidechains of Hv1 regulate the functioning of Hv1 (Chapter 5, Sec 5.1) [27, 85, 91–93]. In alignment with previous studies, I find that the H-bond network of Hv1 in POPC bilayer and standard protonation state is interrupted at D108-D170 near the hydrophobic gasket (Chapter 5, Sec 5.1) [225]. The internal H-bond network extends to the extracellular side from D108 to E115, H136, D119, E192 via D181 and to the cytoplasmic side from D170 to E167. This internal network is connected further to a cytoplasmic H-bond network via conserved amino acid residues N210 or S215 whereas T133 or Q128 connects to an extracellular H-bond network. These amino acid residues are defined as linkers in this work. Mutagenesis studies of the linkers could provide further insights into the functioning mechanism of Hv1.

Hv1 has a pH dependent gating mechanism [238, 239]. Thus, change in pH can affect the H-bond network of Hv1 and thus it's functioning and gating. To probe the impact of protonation state on Hv1 H-bond network dynamics, I performed MD simulations of ten systems of Hv1 embedded in hydrated lipid bilayers and distinguished by protonation state of carboxylates and histidines (Table 2.1) lining up the transmembrane region. Protonation of D108 and D181 results in a continuous water-mediated H-bond network spanning the transmembrane region (Chapter 5, Sec 5.2). In other simulations, H-bond network is found to be interrupted at either D108-D181 or E115, suggesting a key role of these amino acid residues in proton transfer pathways. The H-bond network extends or collapses on the intracellular or extracellular side depending on the location of the protonated carboxylate or histidine (Chapter 5, Sec 5.2).

Hv1 has several titratable groups that can interact with the lipid bilayer. To investigate whether Hv1-lipid interactions could affect the H-bond dynamics of Hv1, I performed MD simulations of Hv1 embedded in 5 different bilayers with varying lipid composition. I find that in contrast to bacterial cell membranes and POPC bilayer, a continuous H-bond network is sampled in POPS bilayer (Chapter 5, Sec 5.3). How does the pH and lipid composition of the membrane affects the H-bond network of Hv1 remains an open question. I apply the newly developed protocol to study the protonation and lipid coupled H-bond dynamics of Hv1 ( Figure 2.5). Taking a closer look at the lipid-protein interface reveals that acidic lipids can participate in H-bonding with Hv1 (Chapter 5, Sec 5.4). Along with the bulk exposed closely spaced carboxylates and histidines of Hv1, lipid headgroups might form proton antennas on the lipid membrane bilayer. I use the newly developed protocol to find the most frequent H-bond paths between carboxylates, histidines and lipid headgroups. Using the protocol, I identify potential proton antennas of Hv1 in POPS bilayer and bacterial cell membranes (Chapter 5, Sec 5.4). I also identify conserved amino acid residues of Hv1 that can serve as lipid anchors (Chapter 5, Sec 5.5). All the above results discussed for Hv1, are based on the resting state [148] and a monomer of Hv1. Hv1 exists as a dimer. However, each monomer is functional on its own [241]. As the crystal structure of the open and closed state of Hv1 are not yet available, the analysis of Hv1 discussed above is limited to the resting state model of chimeric Hv1.

Hv1 is an important drug target for cancer [86–89], neuroinflammatory diseases [90] and male contraceptives [259]. As discussed in previous studies and Chapter 5, the functioning of Hv1 is influenced by H-bond network between titratable sidechains. Hv1 inhibitors can be thus designed targeting

the H-bond network of Hv1. In this thesis (Chapter 5, Sec 5.6), I present the work done on characterizing the impact of Hv1 inhibitors on H-bond networks of Hv1. For the docking studies, I use open and closed models proposed by MD simulations [27]. I dock 28 known inhibitors [165, 231, 232, 237] of Hv1 on the open state model and prepare the ligand-protein systems with the best poses that can be used for MD simulations. I also calculate the H-bond network of closed and open models without the inhibitors that can be used as a reference while comparing with inhibitor-bound systems. Further MD simulations and H-bond network analysis can give insights about the impact of inhibitor binding on Hv1 H-bond network.

The protocol to find the most frequent H-bond paths between titratable sidechains developed and implemented in Chapter 5, can be applied to find H-bond networks of influence in transmembrane proteins. Identifying the most frequent H-bond paths between titratable sidechains can give insights into the proton transport mechanism. Apart from putative proton antennas (Chapter 5), the protocol can be used to identify key protein sidechains involved in substrate binding and recognition, or in protein-protein interactions. The important residues in the protein-ligand interactions can be characterized by studying the impact of inhibitor on H-bond network dynamics.

The methods to identify and characterize H-bond networks of influence discussed in this thesis, have a broad applicability from lipid membranes with varying lipid composition, lipid membranes with cholesterol to transmembrane proteins such as ion channels, transporters, enzymes, G-protein coupled receptors, or neurotransmitters. The insights from MD simulations and H-bond network analysis can lead to the development of novel drugs.

# 7

# Appendix

## 7.1 Appendix Tables

**Table A.3.1.** Average number of lipid clusters and total number of lipids forming clusters per frame.

| | Average # lipid clusters | | | Total lipids forming clusters | | |
|---|---|---|---|---|---|---|
| Simulation | direct | 1-water bridged | ion-bridged | direct | 1-water bridged | ion-bridged |
| POPC | - | 21 ± 3 | 1 ± 0 | - | 55 ± 6 | 2 ± 1 |
| POPE | 21 ± 3 | 21 ± 3 | 1 ± 0 | 81 ± 5 | 56 ± 7 | 2 ± 1 |
| POPS | 18 ± 3 | 13 ± 3 | 14 ± 2 | 94 ± 4 | 89 ± 4 | 38 ± 6 |
| POPG | 20 ± 3 | 21 ± 3 | 13 ± 3 | 48 ± 7 | 72 ± 6 | 33 ± 6 |
| POPA | 16 ± 3 | 22 ± 3 | 13 ± 2 | 34 ± 6 | 69 ± 6 | 34 ± 6 |
| 5:1 POPG:POPE | 4 ± 2 | 21 ± 3 | 2 ± 1 | 8 ± 3 | 58 ± 7 | 4 ± 2 |
| *E. coli* | 4 ± 2 | 21 ± 3 | 2 ± 1 | 9 ± 3 | 57 ± 6 | 4 ± 2 |

**Table A.4.1.** Average number of lipid clusters and total number of lipids forming clusters per frame.

| | Average # lipid clusters | | | Total lipids forming clusters | | |
|---|---|---|---|---|---|---|
| Cholesterol (%) | direct | 1-water bridged | ion-bridged | direct | 1-water bridged | ion-bridged |
| 0 | 18 ± 3 | 13 ± 3 | 14 ± 2 | 93 ± 4 | 88 ± 5 | 37 ± 6 |
| 10 | 17 ± 3 | 13 ± 3 | 13 ± 2 | 82 ± 4 | 79 ± 4 | 34 ± 6 |
| 20 | 16 ± 2 | 12 ± 3 | 12 ± 2 | 77 ± 4 | 75 ± 5 | 30 ± 6 |
| 30 | 15 ± 2 | 13 ± 3 | 10 ± 2 | 68 ± 4 | 68 ± 5 | 26 ± 6 |
| 40 | 14 ± 2 | 13 ± 3 | 8 ± 2 | 58 ± 4 | 59 ± 5 | 19 ± 5 |

**Table A.5.1.** Protonated amino acid residues corresponding to Hv1 models and the effect of mutations of these residues.

| | | | Effects of mutation | | |
|---|---|---|---|---|---|
| *Mus Musculus (3wkv)* | *Homo sapiens (5oqk)* | Mutations studied | Selectivity | Voltage threshold for detecting proton current | Interaction with inhibitors |
| D108 | D112 | D112E [228, 268] | H+ | decreases | interacts with guanidine derivatives [237] and HIFs [231, 232] |
| D108 | D113 | D112A [92, 228] | Cl- | increases | - |
| D108 | D114 | D112F [228] | Cl- | increases | - |
| D108 | D115 | D112V [228] | no proton current detected | increases | - |
| D108 | D116 | D112I [229] | no proton current detected | increases | - |
| D108 | D117 | D112N /D185A [92] | - | increases | - |
| D108 | D118 | D112K [228] | Cl- | increases | - |
| D108 | D119 | D112H [228] | Cl- | increases | - |
| D108 | D120 | D112V /V116D [269] | H+ selectivity recovered | - | - |
| D108 | D121 | D112N [92, 228] | Cl- | increases | - |
| D108 | D122 | D112S [228] | Cl- | increases | - |
| D108 | D123 | D112S /R211S [268] | Gu+ | increases | - |
| D108 | D124 | D112R /R211D [268] | H+ | - | - |
| D170 | D174 | D174A [92] | - | decreases | non-functional channel with saturating concentration of YHV98-1 [233] |
| D170 | D175 | D174N [92] | - | decreases | - |
| D170 | D176 | D174H [92] | - | decreases | - |

| | | | Effects of mutation | | |
|---|---|---|---|---|---|
| *Mus Musculus (3wkv)* | *Homo sapiens (5oqk)* | Mutations studied | Selectivity | Voltage threshold for detecting proton current | Interaction with inhibitors |
| D170 | D177 | D174E [92] | - | decreases | Extent of HIF inhibition was reduced [231, 232] |
| E115 | E119 | E119A [92] | - | increases | - |
| D119 | D123 | D123A [92] | - | increases | - |
| D181 | D185 | D185N [228] | H+ | increases | - |
| D181 | D185 | D185A [228] | H+ | increases | Prevents binding of hanatoxin [236], no effect on binding of HIF [231, 232] |
| D181 | D185 | D185M [228] | H+ | increases | - |
| D181 | D185 | D185V [228] | H+ | increases | - |
| H136 | H140 | H140A [93] | H+ | - | Decreased Zn2+ binding |
| H95 | H99 | H99A [92] | H+ | increases | - |
| E167 | E171 | E164A /E171A [92] | - | decreases | - |
| E167 | E171 | E171A /D174A [92] | - | decreases | - |
| E167 | E171 | E171Q [231, 232] | - | - | Extent of HIF inhibition was reduced |
| D149 | E153 | E153A [92] | - | decreases | - |
| D149 | E153 | E153N [92] | - | decreases | - |
| D149 | E153 | E153C [92] | - | decreases | Reduced ability of Hv1 to release HIF from its binding site [231, 232] |
| D149 | E153 | E153D [92] | - | decreases | - |
| D149 | E153 | E153D /D174E [92] | - | decreases | - |

**Table A.5.2.** Illustration of the most frequent H-bond path calculation. Most frequent H-bond paths from D108 and D181 sampled in MD simulations of Hv1 in hydrated POPS lipid bilayer with all amino acid residues in their standard protonation state. The table is taken from ref. [162] (manuscript under preparation).

| From | To | Path | Path length | 1-water | 2-water | 3-water |
|---|---|---|---|---|---|---|
| D108 | D181 | - | 1 | - | 77 | 86 |
| D108 | D119 | D181, E115 | 2 | - | - | 22 |
| D108 | D119 | D181, E115, E192 | 3 | - | - | 17 |
| D108 | D119 | D181, E115, H136 | 3 | - | - | 16 |
| D108 | D119 | D181, E115, S139, H136 | 4 | - | - | 8 |
| D108 | E115 | D181 | 1 | - | - | 27 |
| D108 | E192 | D181, E115 | 2 | - | - | 19 |
| D108 | E192 | D181, E115, D119 | 3 | - | - | 19 |
| D108 | E192 | D181, E115, H136, D119 | 4 | - | - | 14 |
| D108 | E192 | D181, E115, S139, H136, D119 | 5 | - | - | 7 |
| D108 | H136 | D181, E115 | 2 | - | - | 24 |
| D108 | H136 | D181, E115, D119 | 3 | - | - | 15 |
| D108 | H136 | D181, E115, S139 | 3 | - | - | 13 |
| D108 | H136 | D181, E115, E192, D119 | 4 | - | - | 12 |
| D181 | D108 | | 1 | - | 77 | 86 |
| D181 | D119 | E115 | 1 | - | - | 27 |
| D181 | D119 | E115, E192 | 2 | - | - | 21 |
| D181 | D119 | E115, H136 | 2 | - | - | 20 |
| D181 | D119 | E115, S139, H136 | 3 | - | - | 10 |
| D181 | E115 | | 1 | - | - | 34 |
| D181 | E192 | E115 | 1 | - | - | 24 |
| D181 | E192 | E115, D119 | 2 | - | - | 23 |
| D181 | E192 | E115, H136, D119 | 3 | - | - | 16 |
| D181 | E192 | E115, S139, H136, D119 | 4 | - | - | 9 |
| D181 | H136 | E115 | 1 | - | - | 29 |
| D181 | H136 | E115, D119 | 2 | - | - | 19 |
| D181 | H136 | E115, S139 | 2 | - | - | 17 |
| D181 | H136 | E115, E192, D119 | 3 | - | - | 14 |

**Table A.5.3.** Illustration of the shortest H-bond path calculation. Shortest H-bond paths from D108 and D181 sampled in MD simulations of Hv1 in hydrated POPS lipid bilayer with all amino acid residues in their standard protonation state.

| From | To | Path | Path length | 1-water | 2-water | 3-water |
|---|---|---|---|---|---|---|
| D108 | D181 | - | 1 | - | 77 | 86 |
| D108 | D119 | D181, E115 | 2 | - | - | 22 |
| D108 | E115 | D181 | 1 | - | - | 27 |
| D108 | E192 | D181, E115 | 2 | - | - | 19 |
| D108 | H136 | D181, E115 | 2 | - | - | 24 |
| D181 | D108 | | 1 | - | 77 | 86 |
| D181 | D119 | E115 | 1 | - | - | 27 |
| D181 | E115 | | 1 | - | - | 34 |
| D181 | E192 | E115 | 1 | - | - | 24 |
| D181 | H136 | E115 | 1 | - | - | 29 |

## 7.2 Appendix Figures

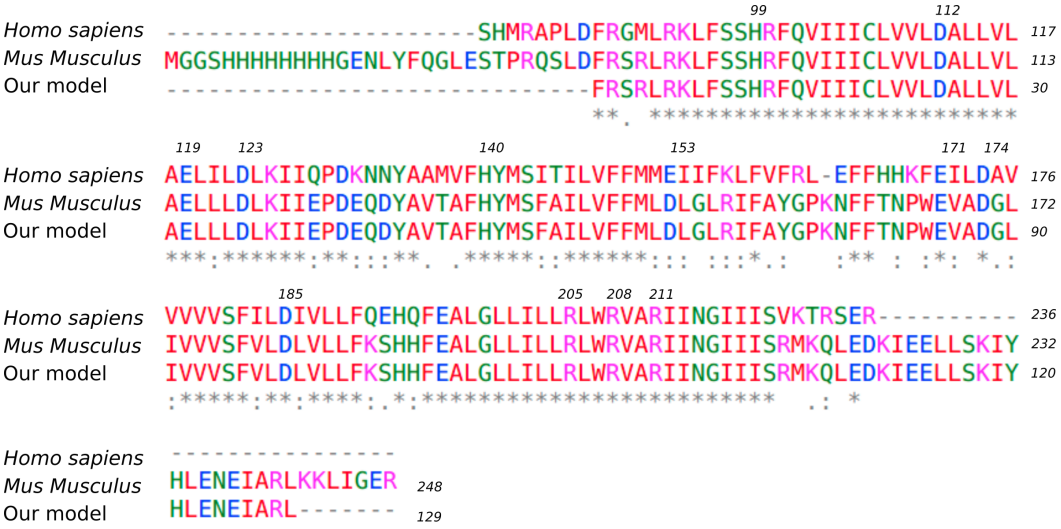


**Figure A.5.1.** Multiple sequence alignment of Hv1 resting state model with *Mus musculus* and *Homo sapiens* Hv1. The sequence alignment was performed by Clustal Omega [270]. The figure is from ref. [162] (manuscript under preparation).

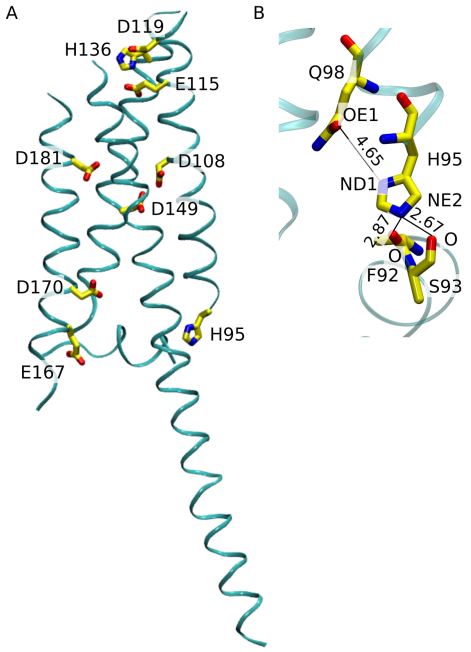


**Figure A.5.2.** Amino acid residues of Hv1 that are protonated in individual membrane simulations. (A) Molecular graphics of Hv1 *Mus musculus* crystal structure (PDB ID: 3wkv) [148] before modeling of missing loops. Protein is shown as thin cyan ribbons and protein sidechains in yellow licorice representation. (B) The distance between H95 and neighboring residues. The distances of H95 from neighboring residues raise the possibility of singly protonation on the N$\epsilon$ atom. The numbering scheme is based on *Mus musculus* crystal structure of Hv1. The figure is from ref. [162] (manuscript under preparation).

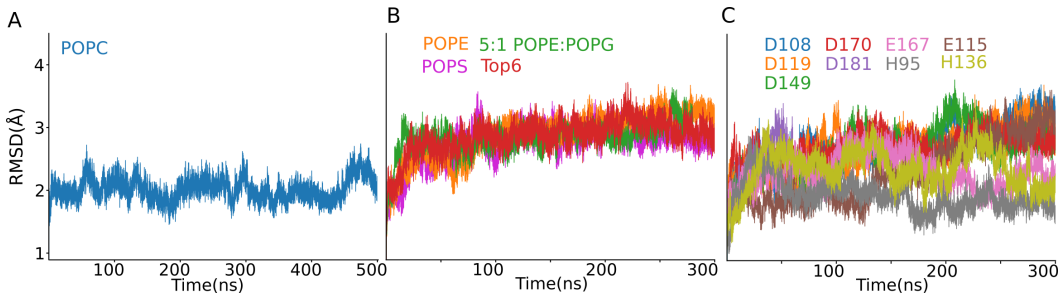


**Figure A.5.3.** C$\alpha$ RMSD profiles for helical regions of Hv1. (A-C) Time series of C$\alpha$ RMSD of helical regions of Hv1 in pure POPC membrane in with all aminoacid residues in their standard protonation state (Panel A), pure POPE membrane, 5:1 POPE:POPG membrane, *E. coli* Top6 bacterial cell membrane with all aminoacid residues in their standard protonation state (Panel B) and Hv1 in pure POPC membrane with D108, D119, D149, D170, D181, E115, E167, H95 and H136 protonated in individual simulations (Panel C). The figure is from ref. [162] (manuscript under preparation).

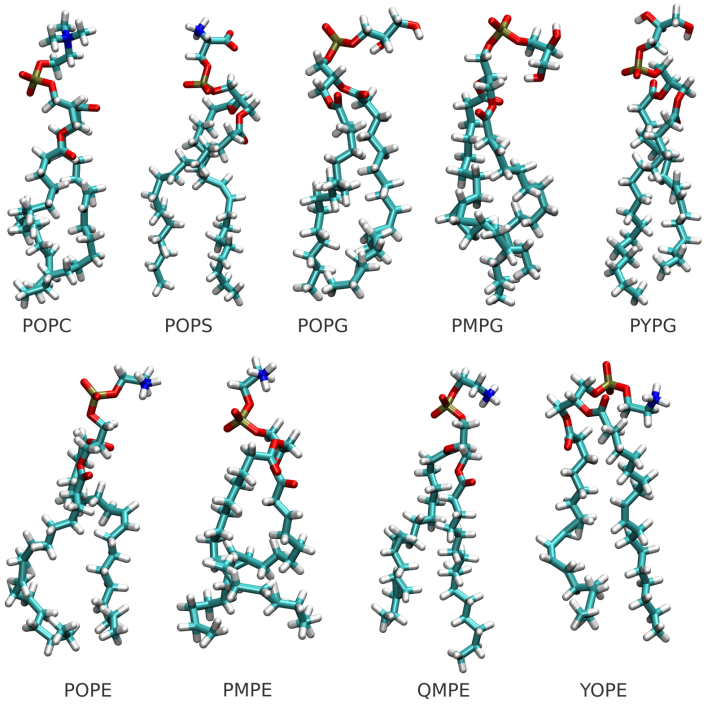


**Figure A.5.4.** Molecular graphics of lipids in Hv1-lipid membrane simulations. The figure is from ref. [162] (manuscript under preparation).

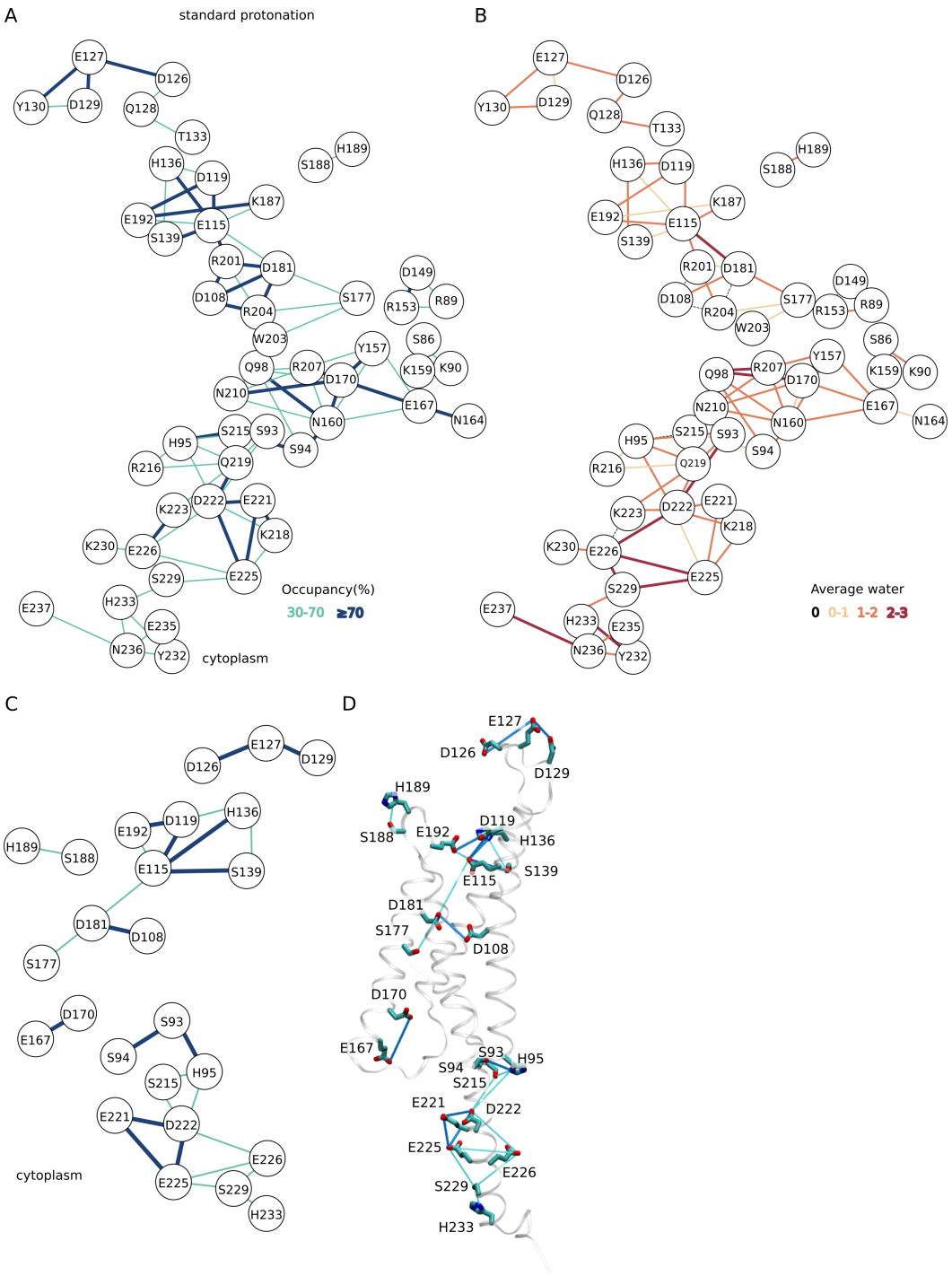


**Figure A.5.5.** H-bond network of Hv1 in POPC with standard protonation state. (A-B) Complete H-bond network via waterwires with upto 3 water molecules of Hv1 with occupancy (%) (Panel A) and average number of waters in waterwires (Panel B) on the edges. (C) H-bond network of Hv1 via putative proton carriers. (D) Molecular graphics of H-bond network in Panel C. The molecular graphics was prepared using the last frame of 500 ns MD simulation. Panels A-B are adpated and Panels C-D are taken from ref. [162] (manuscript under preparation).

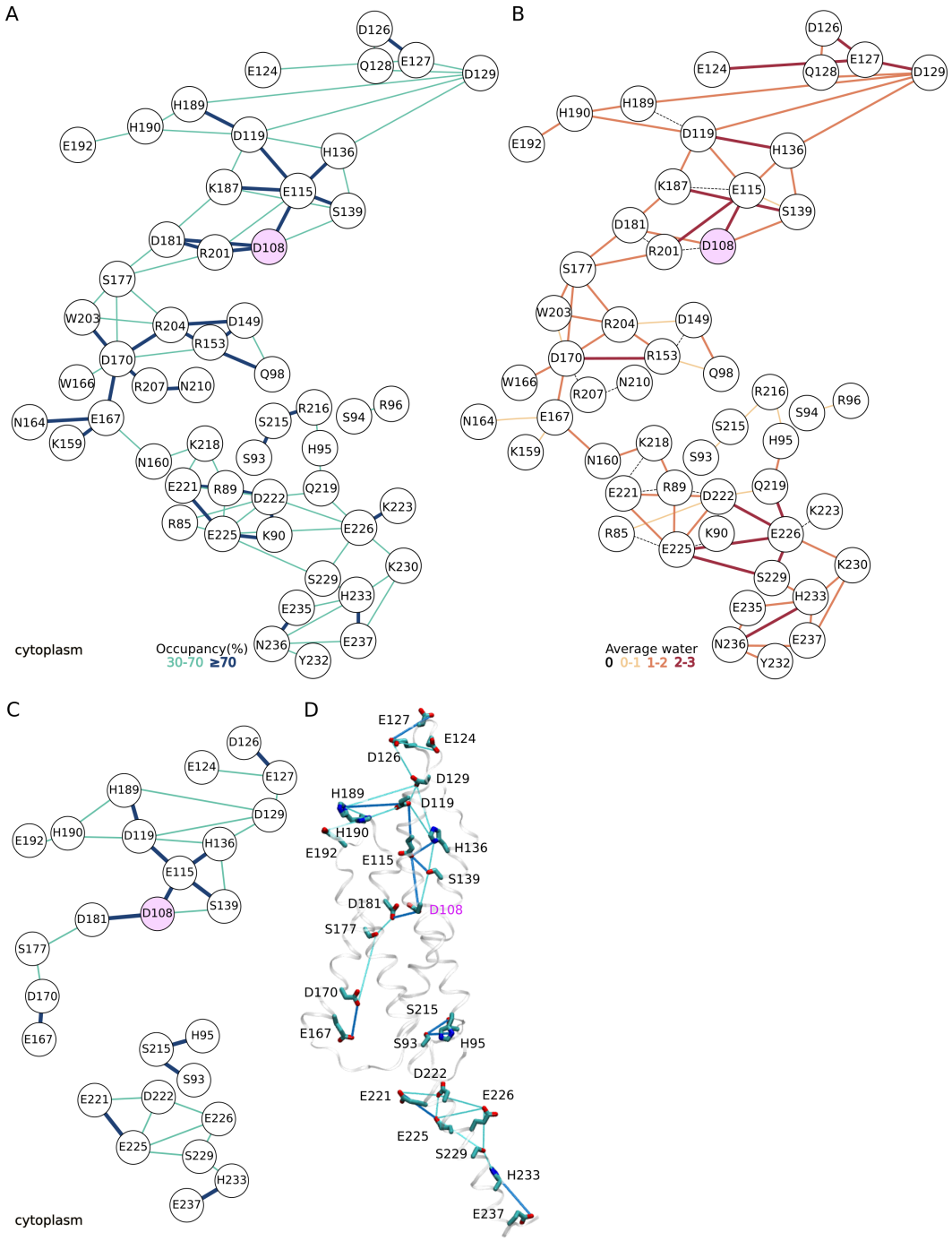


**Figure A.5.6.** H-bond network of Hv1 in POPC with D108 protonated. (A-B) Complete H-bond network via waterwires with upto 3 water molecules of Hv1 with occupancy (%) (Panel A) and average number of waters in waterwires (Panel B) on the edges. (C) H-bond network of Hv1 via putative proton carriers. (D) Molecular graphics of H-bond network in Panel C. The molecular graphics was prepared using the last frame of 300 ns MD simulation. Panels A-B are adpated and Panels C-D are taken from ref. [162] (manuscript under preparation).

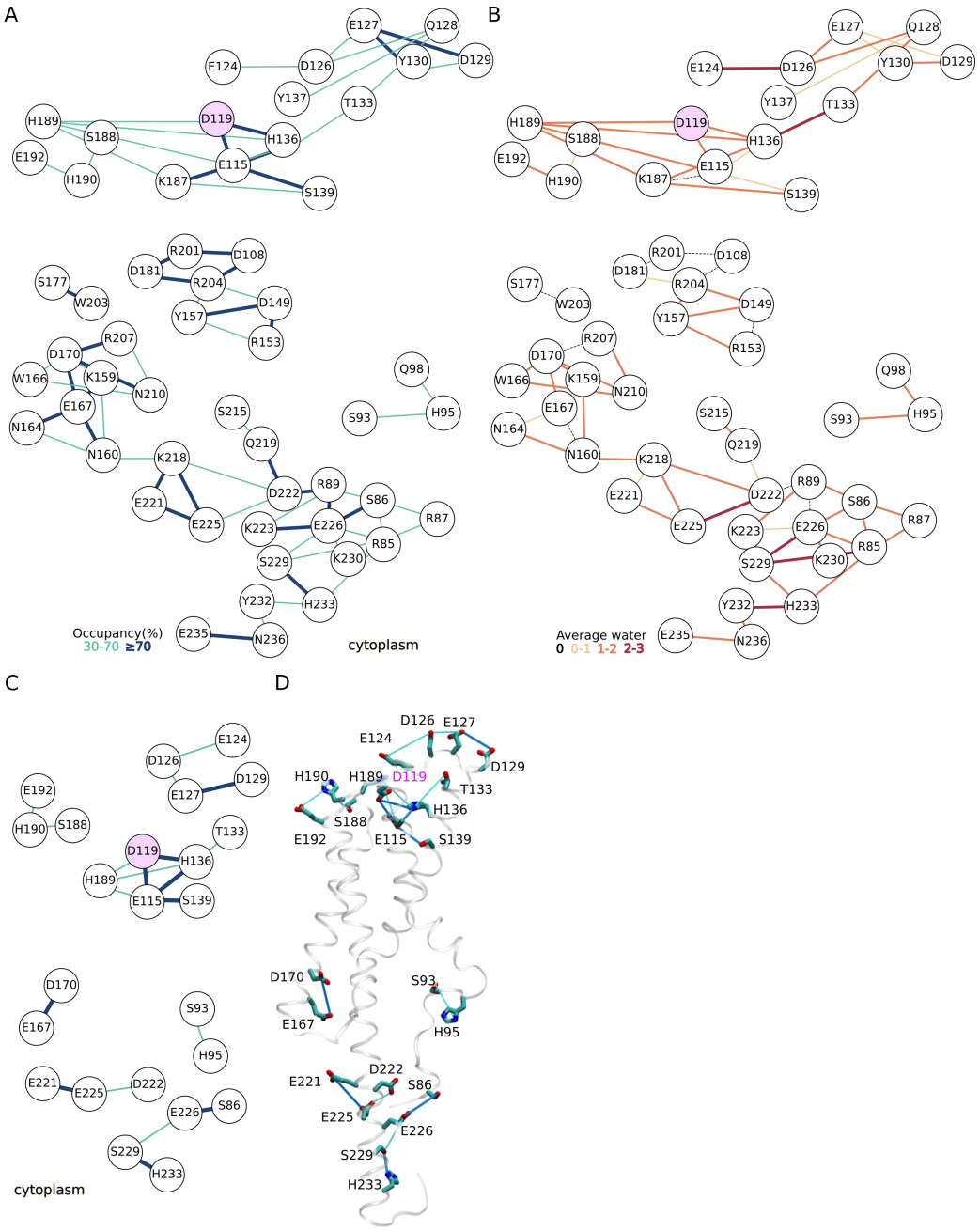


**Figure A.5.7.** H-bond network of Hv1 in POPC with D119 protonated.(A-B) Complete H-bond network via waterwires with upto 3 water molecules of Hv1 with occupancy (%) (Panel A) and average number of waters in waterwires (Panel B) on the edges. (C) H-bond network of Hv1 via putative proton carriers. (D) Molecular graphics of H-bond network in Panel C. The molecular graphics was prepared using the last frame of 300 ns MD simulation. Panels A-B are adpated and Panels C-D are taken from ref. [162] (manuscript under preparation).

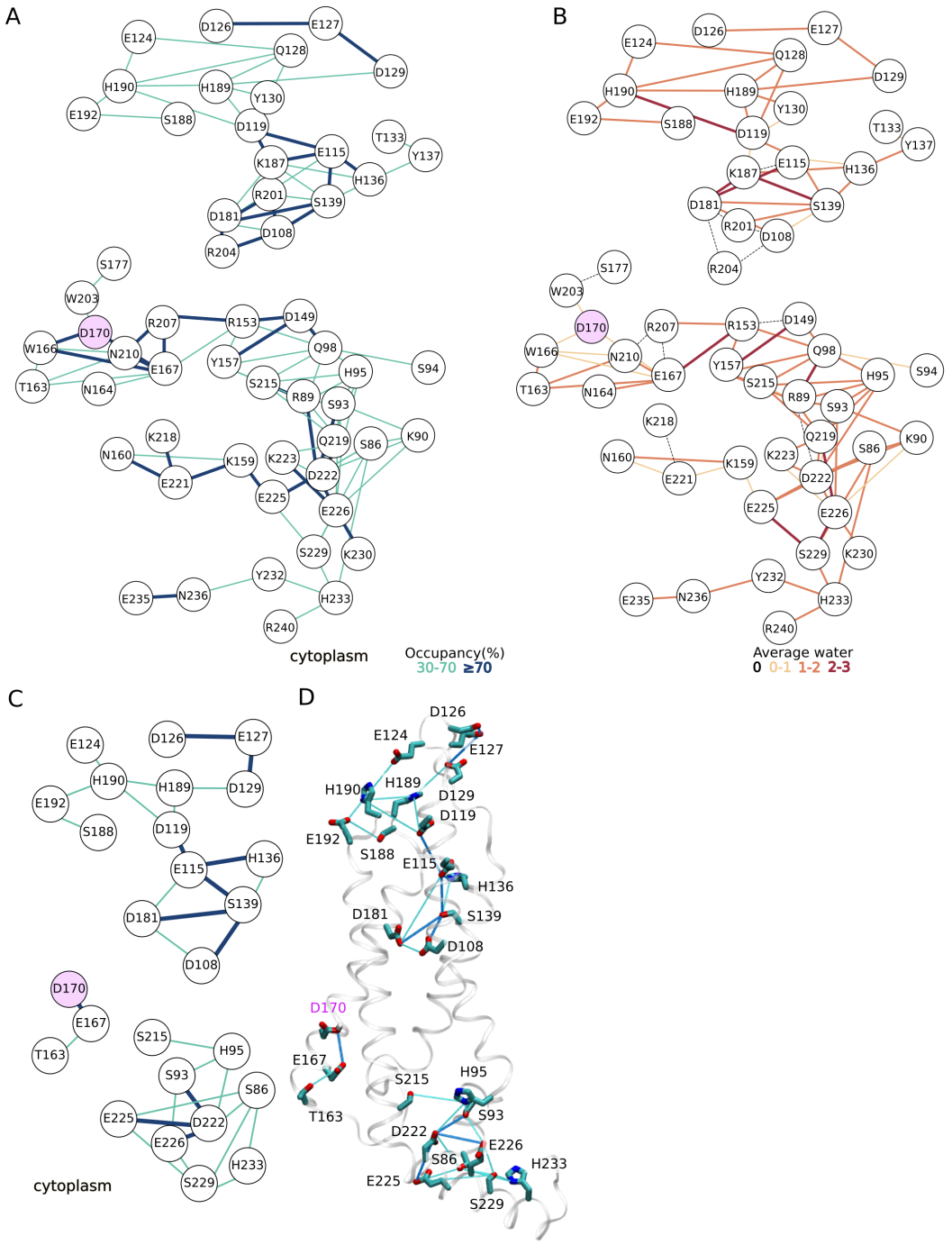


**Figure A.5.8.** H-bond network of Hv1 in POPC with D170 protonated.(A-B) Complete H-bond network via waterwires with upto 3 water molecules of Hv1 with occupancy (%) (Panel A) and average number of waters in waterwires (Panel B) on the edges. (C) H-bond network of Hv1 via putative proton carriers. (D) Molecular graphics of H-bond network in Panel C. The molecular graphics was prepared using the last frame of 300 ns MD simulation. Panels A-B are adpated and Panels C-D are taken from ref. [162] (manuscript under preparation).

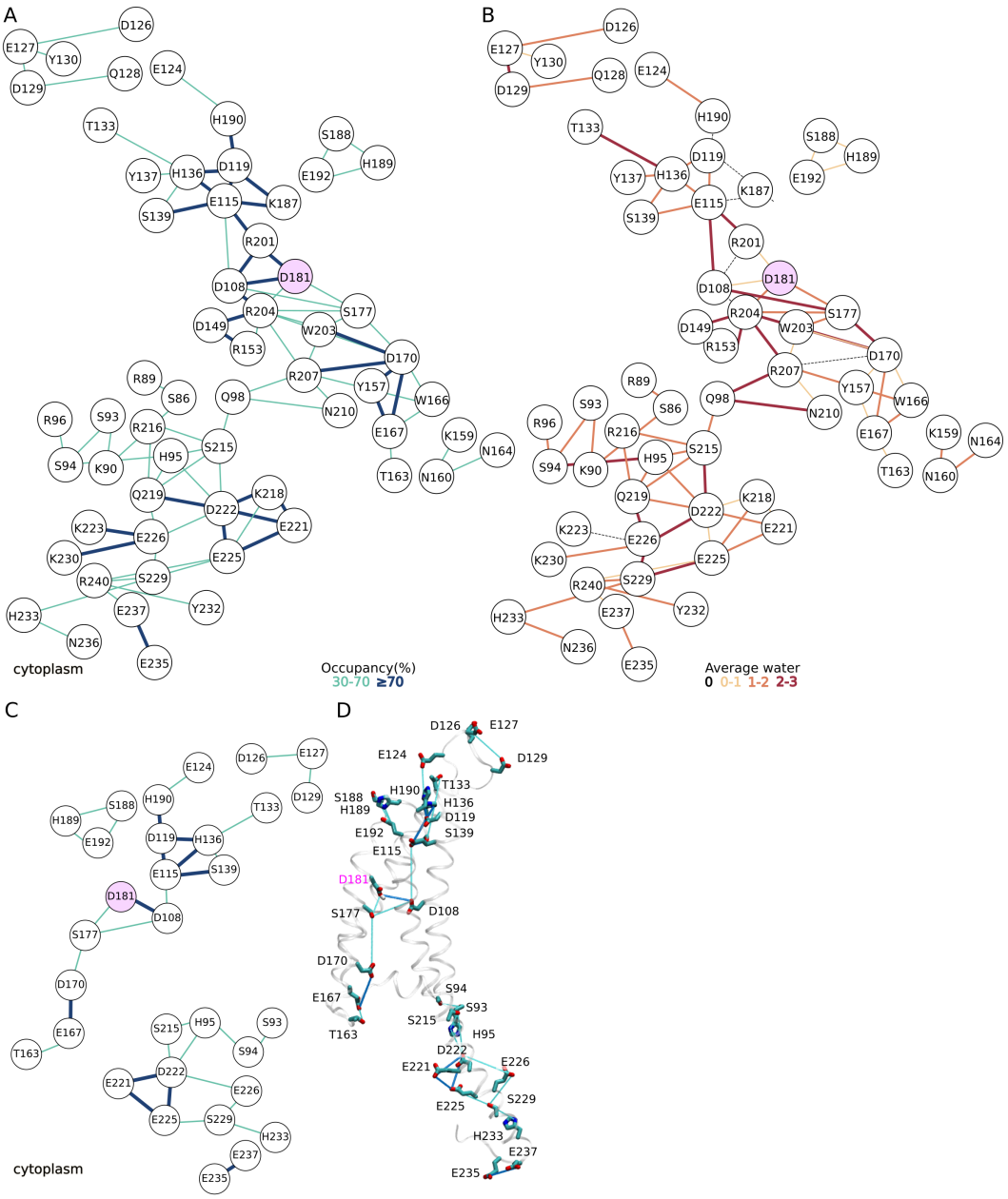


**Figure A.5.9.** H-bond network of Hv1 in POPC with D181 protonated.(A-B) Complete H-bond network via waterwires with upto 3 water molecules of Hv1 with occupancy (%) (Panel A) and average number of waters in waterwires (Panel B) on the edges. (C) H-bond network of Hv1 via putative proton carriers. (D) Molecular graphics of H-bond network in Panel C. The molecular graphics was prepared using the last frame of 300 ns MD simulation. Panels A-B are adpated and Panels C-D are taken from ref. [162] (manuscript under preparation).

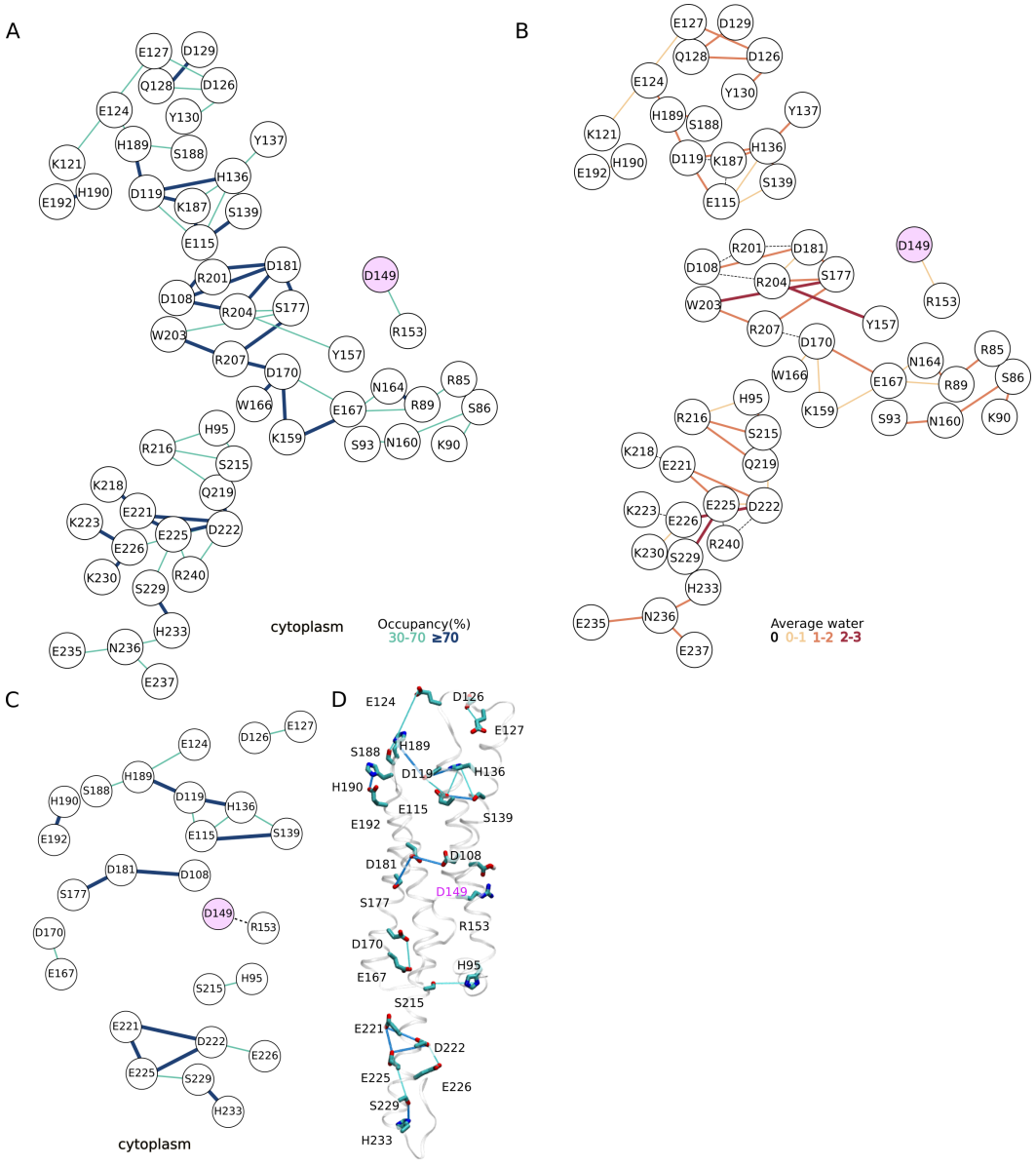


**Figure A.5.10.** H-bond network of Hv1 in POPC with D149 protonated.(A-B) Complete H-bond network via waterwires with upto 3 water molecules of Hv1 with occupancy (%) (Panel A) and average number of waters in waterwires (Panel B) on the edges. (C) H-bond network of Hv1 via putative proton carriers. (D) Molecular graphics of H-bond network in Panel C. The molecular graphics was prepared using the last frame of 300 ns MD simulation. Panels A-B are adpated and Panels C-D are taken from ref. [162] (manuscript under preparation).

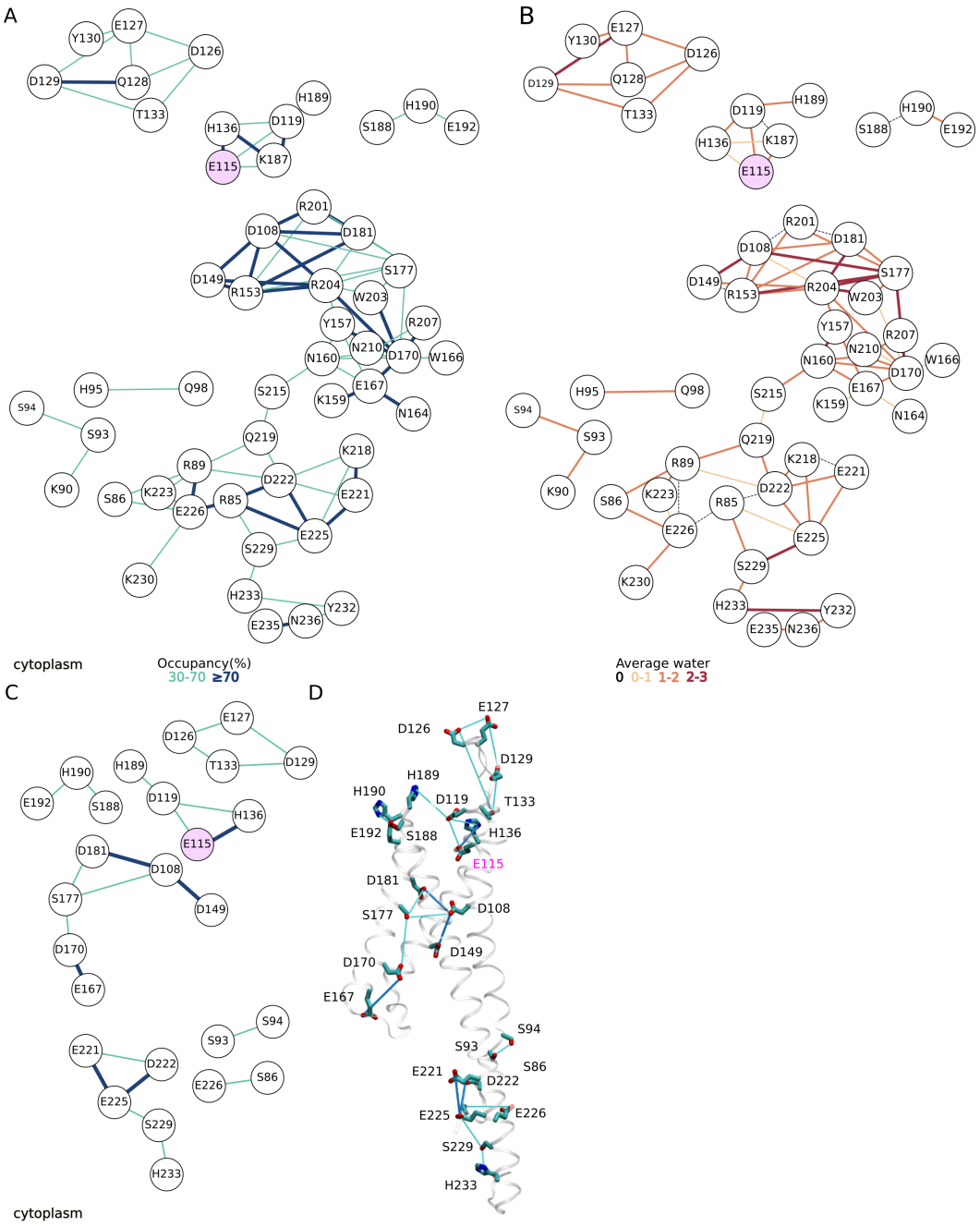


**Figure A.5.11.** H-bond network of Hv1 in POPC with E115 protonated.(A-B) Complete H-bond network via waterwires with upto 3 water molecules of Hv1 with occupancy (%) (Panel A) and average number of waters in waterwires (Panel B) on the edges. (C) H-bond network of Hv1 via putative proton carriers. (D) Molecular graphics of H-bond network in Panel C. The molecular graphics was prepared using the last frame of 300 ns MD simulation. Panels A-B are adpated and Panels C-D are taken from ref. [162] (manuscript under preparation).

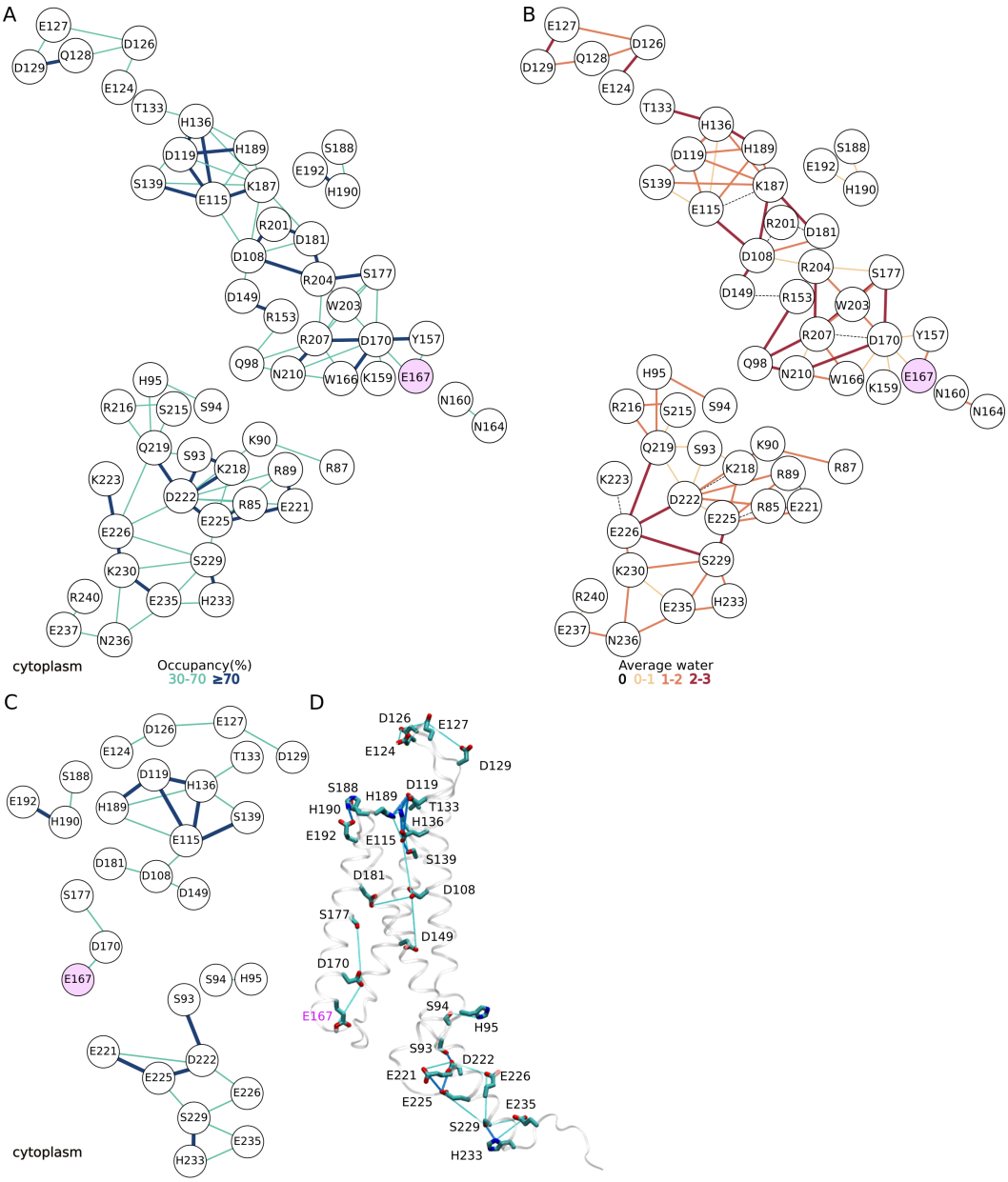


**Figure A.5.12.** H-bond network of Hv1 in POPC with E167 protonated.(A-B) Complete H-bond network via waterwires with upto 3 water molecules of Hv1 with occupancy (%) (Panel A) and average number of waters in waterwires (Panel B) on the edges. (C) H-bond network of Hv1 via putative proton carriers. (D) Molecular graphics of H-bond network in Panel C. The molecular graphics was prepared using the last frame of 300 ns MD simulation. Panels A-B are adpated and Panels C-D are taken from ref. [162] (manuscript under preparation).

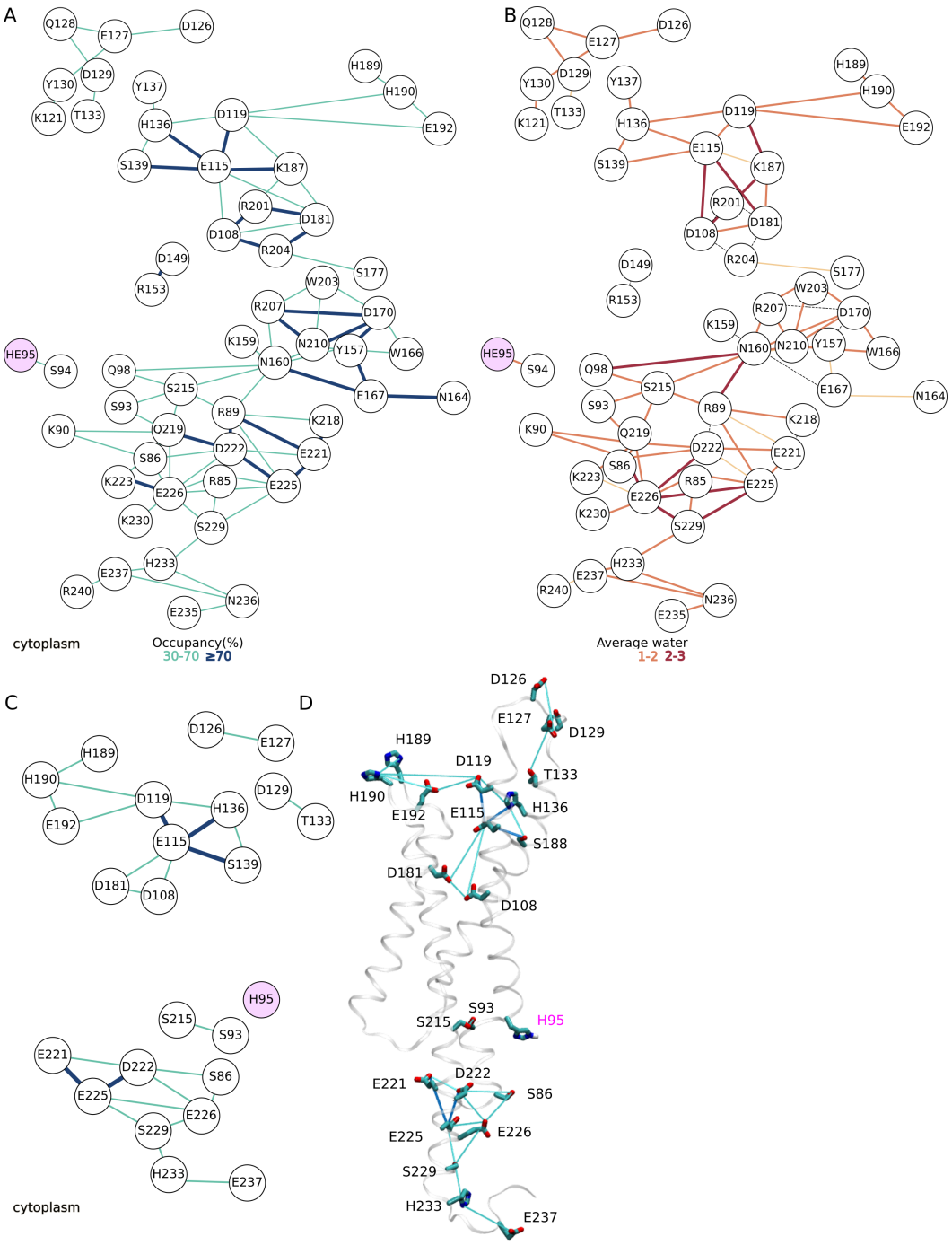


**Figure A.5.13.** H-bond network of Hv1 in POPC with H95 protonated.(A-B) Complete H-bond network via waterwires with upto 3 water molecules of Hv1 with occupancy (%) (Panel A) and average number of waters in waterwires (Panel B) on the edges. (C) H-bond network of Hv1 via putative proton carriers. (D) Molecular graphics of H-bond network in Panel C. The molecular graphics was prepared using the last frame of 300 ns MD simulation. Panels A-B are adpated and Panels C-D are taken from ref. [162] (manuscript under preparation).

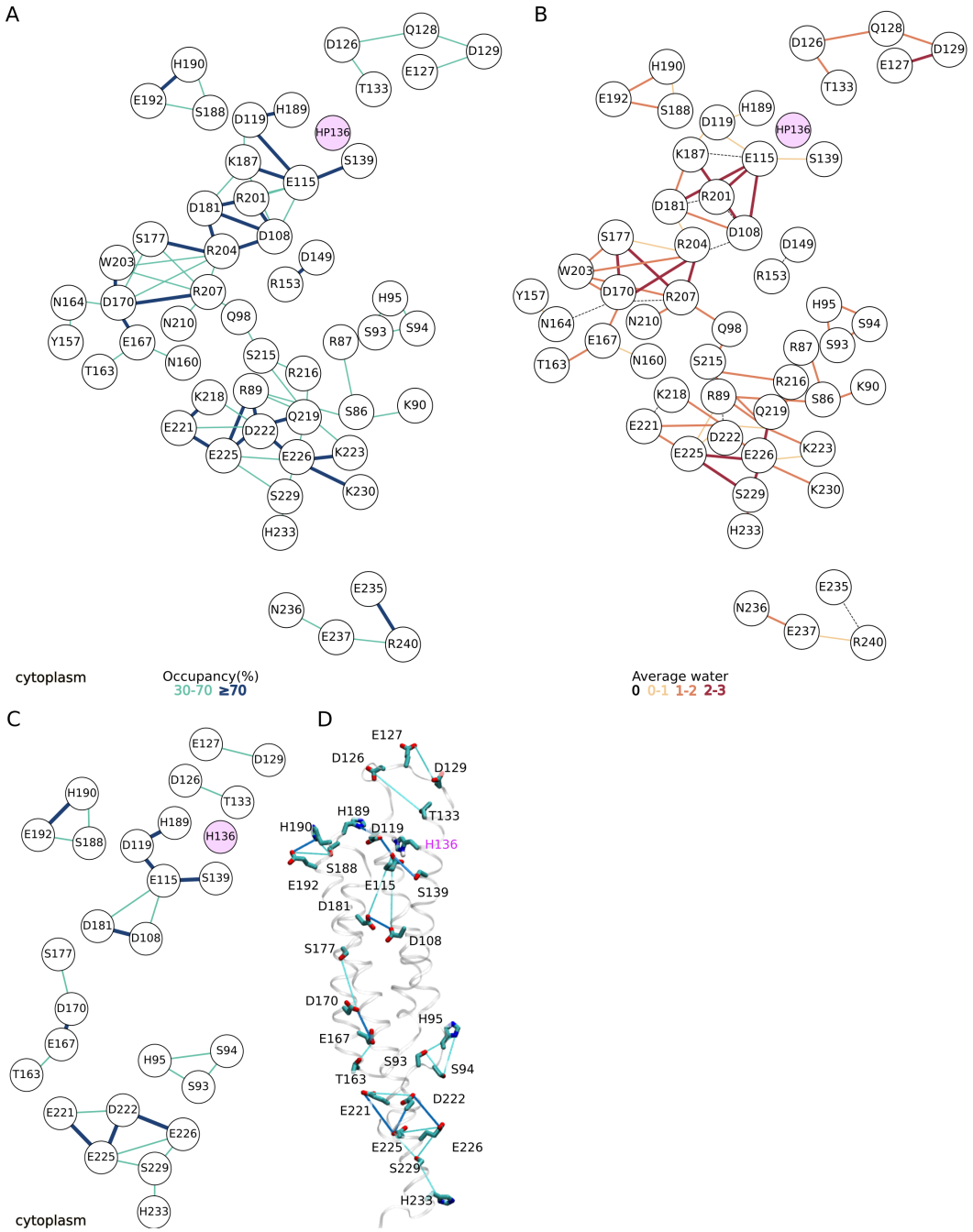


**Figure A.5.14.** H-bond network of Hv1 in POPC with H136 protonated.(A-B) Complete H-bond network via waterwires with upto 3 water molecules of Hv1 with occupancy (%) (Panel A) and average number of waters in waterwires (Panel B) on the edges. (C) H-bond network of Hv1 via putative proton carriers. (D) Molecular graphics of H-bond network in Panel C. The molecular graphics was prepared using the last frame of 300 ns MD simulation. Panels A-B are adpated and Panels C-D are taken from ref. [162] (manuscript under preparation).

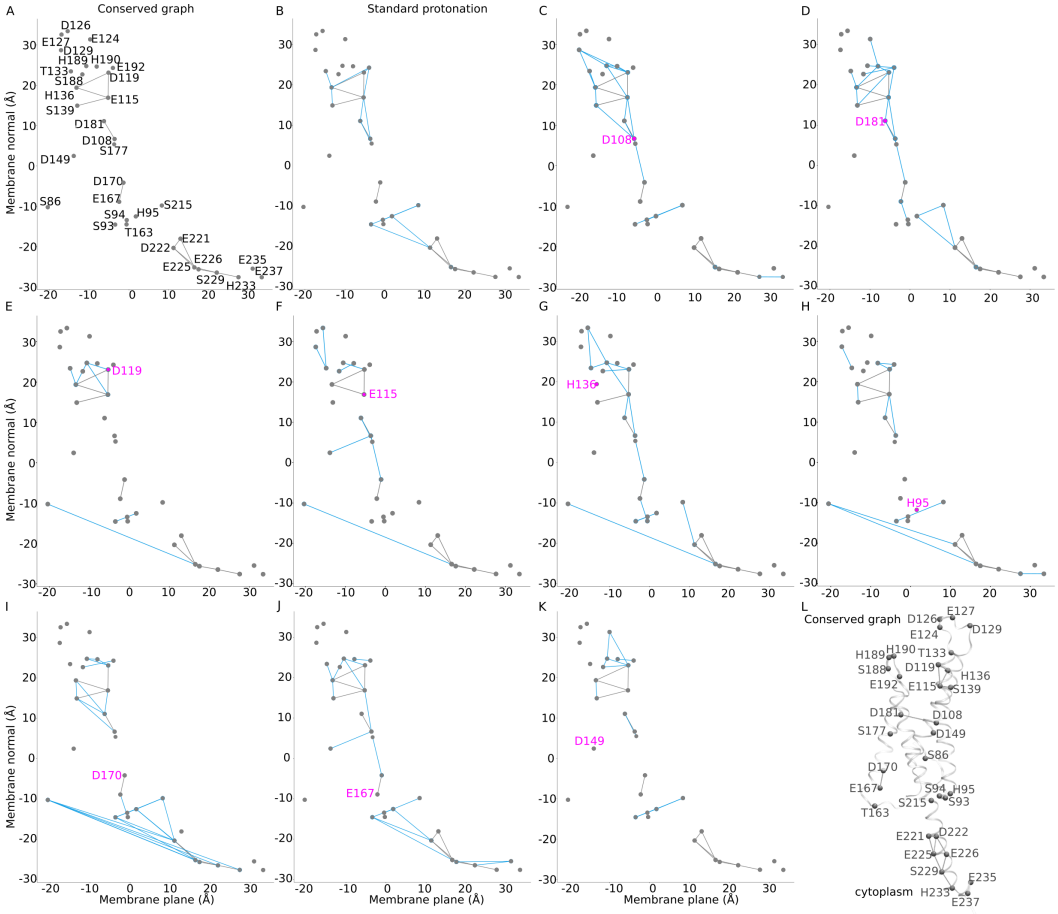


**Figure A.5.15.** Conserved H-bond network across protonated Hv1 systems. (A) Graph representation of conserved H-bond network mediated by upto 3 waters and via potential proton carriers. (B-K) Difference H-bond graphs of Hv1 from simulations with standard protonation for all titratable sidechains (Panel B), with neutral D108 (Panel C), neutral D181 (Panel D), neutral D119 (Panel E), neutral E115 (Panel F), doubly protonated H136 (Panel G), N$\epsilon$ protonated H95 (Panel H), neutral D170 (Panel I), neutral E167 (Panel J) and neutral D149 (Panel K). Conserved H-bonds and H-bonding groups conserved are shown in grey whereas the difference between conserved H-bonds and H-bonding groups is shown in blue, The protonated H-bonding group is shown magenta. Cgraph was used to generate H-bond graphs [271] with an occupancy filter of 30% and conservation threshold of 80%. (L) Molecular graphics of conserved graph from Panel A. The figure is from ref. [162] (manuscript under preparation).

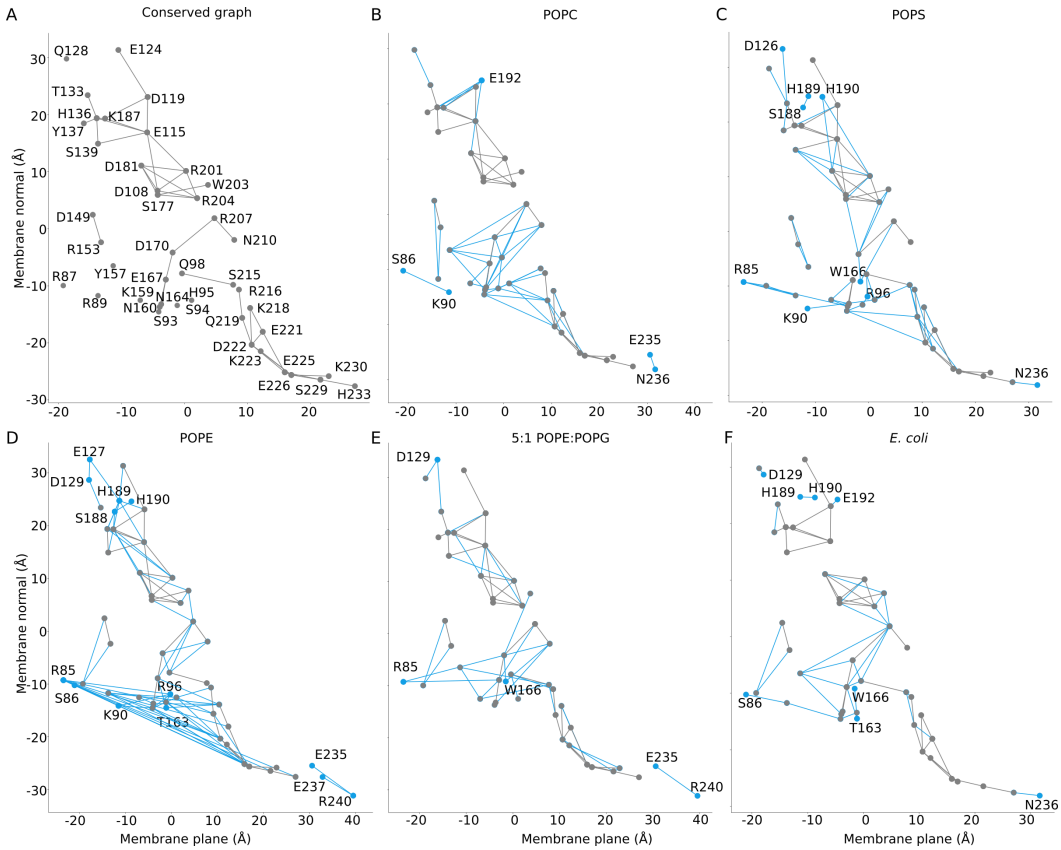


**Figure A.5.16.** Conserved Hv1 H-bond network in different lipid bilayers. (A) Graph representation of conserved H-bond network mediated via upto 3 waters. (B-F) Difference H-bond graphs of Hv1 from simulations with standard protonation for all titratable sidechains in pure POPC (Panel B), pure POPS (Panel C), pure POPE (Panel D), 5:1 POPE:POPG (Panel E) and *E. coli* (Panel F) bilayers. H-bonds and H-bonding groups conserved across simulations are shown in grey. Conserved H-bonds and H-bonding groups conserved are shown in grey whereas the difference between conserved H-bonds and H-bonding groups is shown in blue, The protonated H-bonding group is shown magenta. Cgraph was used to generate H-bond graphs [271] with an occupancy filter of 30% and conservation threshold of 80%. The figure is from ref. [162] (manuscript under preparation).

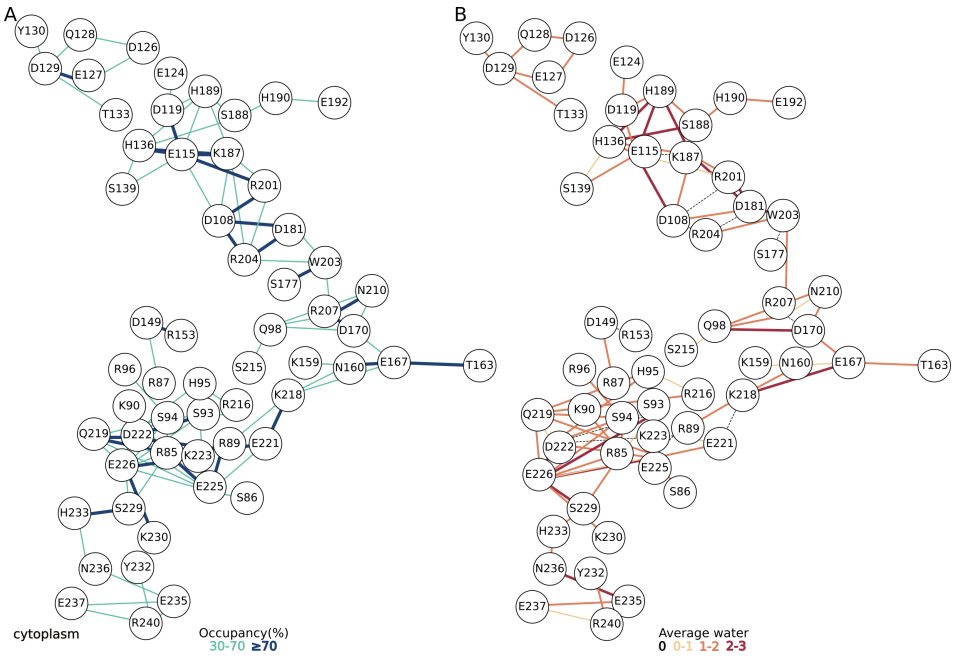


**Figure A.5.17.** H-bond network of Hv1 in POPE bilayer.(A-B) Complete H-bond network via waterwires with upto 3 water molecules of Hv1 with occupancy (%) (Panel A) and average number of waters in waterwires (Panel B) on the edges. Adapted from ref. [162] (manuscript under preparation).

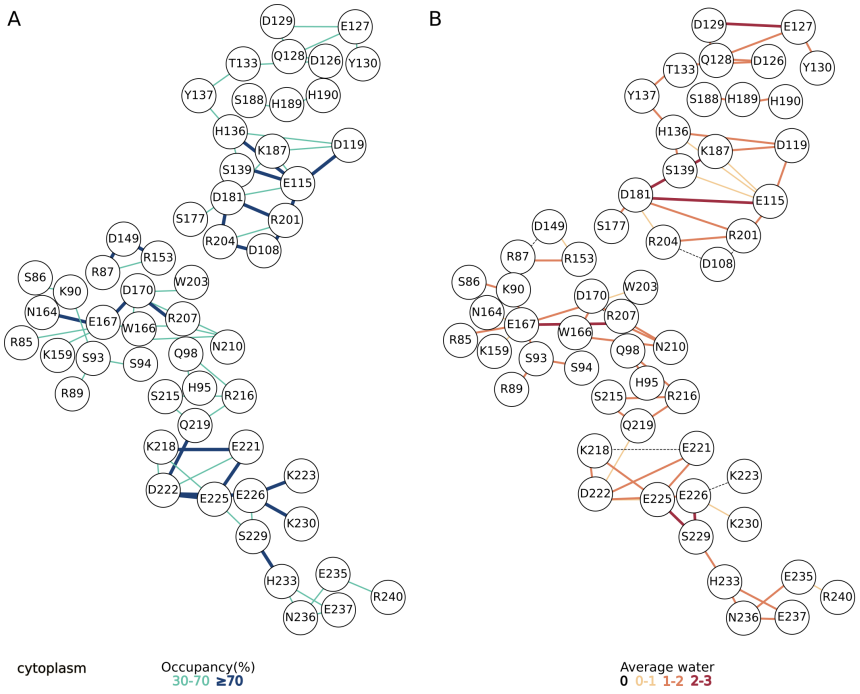


**Figure A.5.18.** H-bond network of Hv1 in 5:1 POPE:POPG bilayer.(A-B) Complete H-bond network via waterwires with upto 3 water molecules of Hv1 with occupancy (%) (Panel A) and average number of waters in waterwires (Panel B) on the edges. Adapted from ref. [162] (manuscript under preparation).

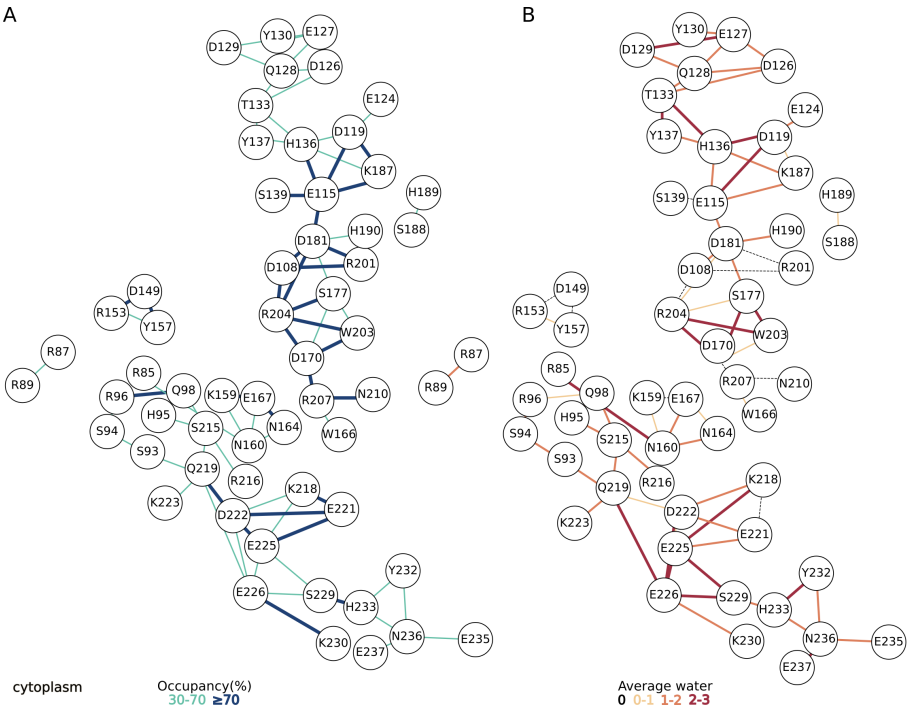


**Figure A.5.19.** H-bond network of Hv1 in POPS bilayer. (A-B) Complete H-bond network via waterwires with upto 3 water molecules of Hv1 with occupancy (%) (Panel A) and average number of waters in waterwires (Panel B) on the edges. Adapted from ref. [162] (manuscript under preparation).

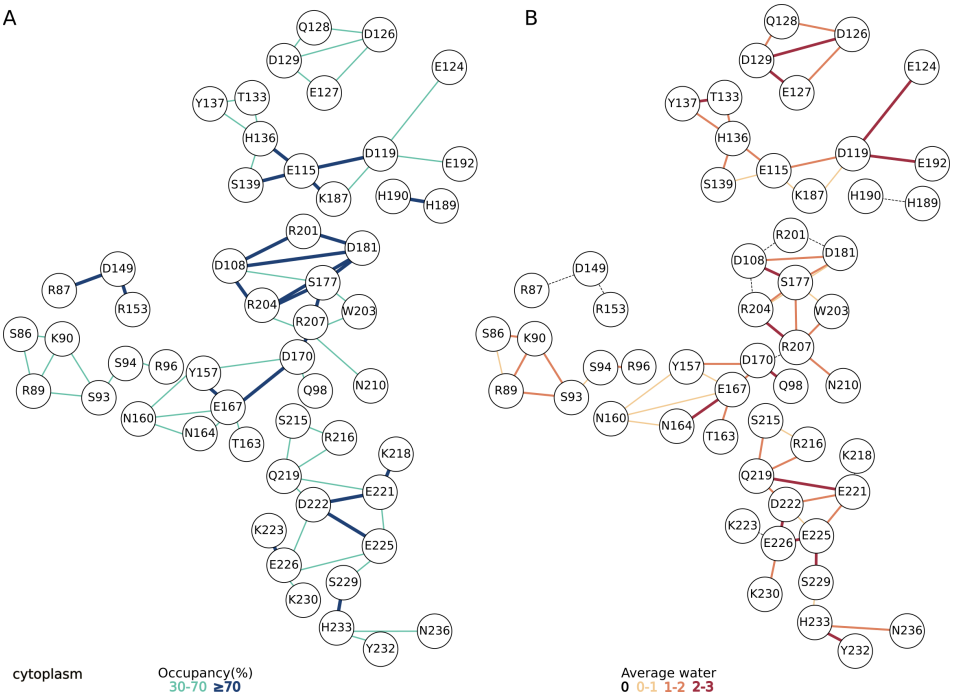


**Figure A.5.20.** H-bond network of Hv1 in *E. coli* bilayer.(A-B) Complete H-bond network via waterwires with upto 3 water molecules of Hv1 with occupancy (%) (Panel A) and average number of waters in waterwires (Panel B) on the edges. Adapted from ref. [162] (manuscript under preparation).

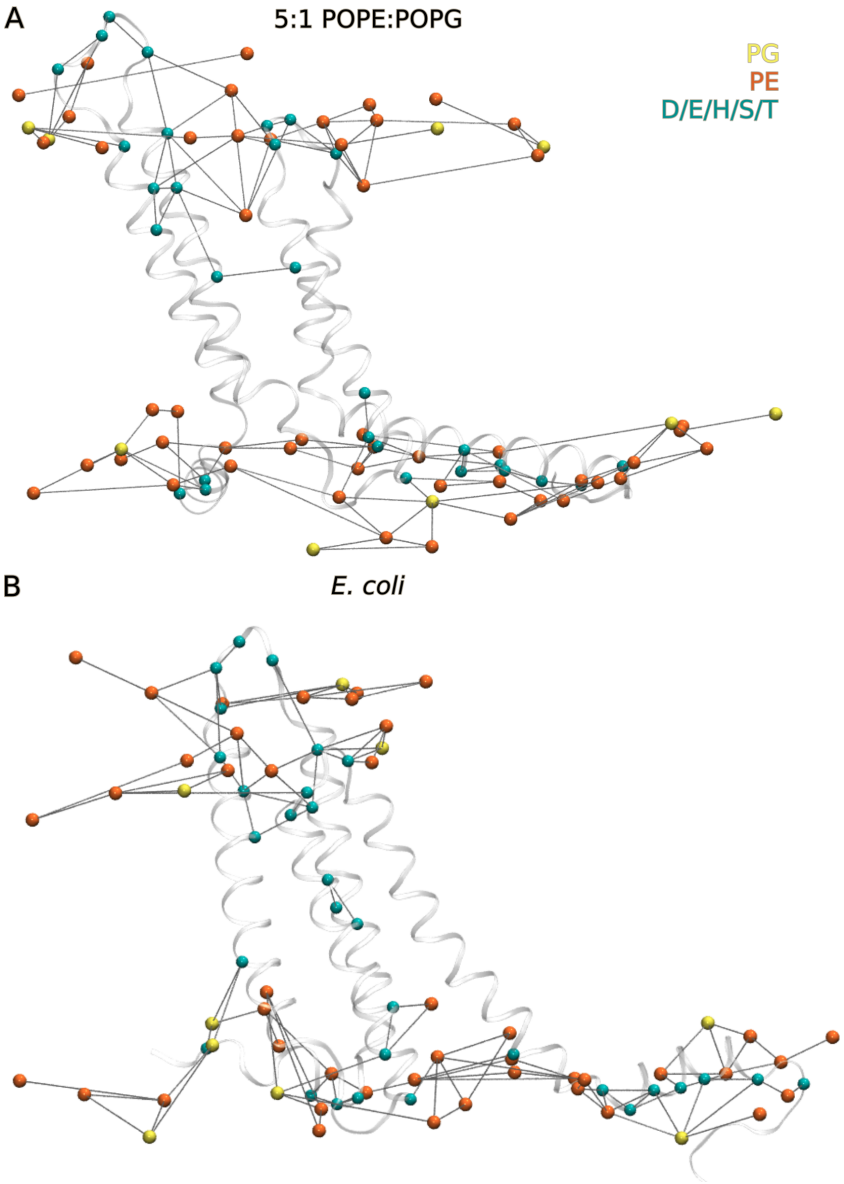


**Figure A.5.21.** Lipid interactions of Hv1 in bacterial membranes. (A-B) Lipid-Hv1 water mediated H-bond in 5:1 POPE:POPG bilayer (Panel A) vs *E. coli* bilayer (Panel B). The figure is adpated from ref. [162] (manuscript under preparation).

```
Karlodinium veneficum MHEEHEAEDHGEHRVSDAAGSLEAPLQKGSFEQHAK--GTSGVHHARSQASSNREGREGC 245
Ciona intestinalis    TVKTKA--DDRVHEIKKKNSELELQIHNLEEKLSQKEQDMSRLHEILRCNNIDIPPTVPL 326
Nicoletia phytophila  SVKMQA--EHQLEREKQRGMALEGELSRCRQVCAAQQRELDVLRAVLQHHGLDQQLPDGN 228
Danio rerio           SVQNRA--NHRVEKLKEINESLVHQVNELKEQNTKMDQENVRLRALLKDHSIDF------ 235
Xenopus laevis        SVKTRA--EEKMHKLKEQKGSLLEKVAQLEQQCAQQEQEIGRLHKLLQEHNVFPAS---- 230
Xenopus tropicalis    SVKTQA--EDKIHRLKENQESLLEKVAHLEQQCAQQEQEIVRLQTLLQQHNVFPAS---- 230
Gallus gallus         SVKTRS--EQQVSKLKQVNLKLATKVEQLQHSCVEKEQEIERLTRMLKQHGLLSEQT--- 235
Mus musculus chimera  SRMKQL--EDKIEELL-------SKIYH-------LENEIARLKKLIGER---------- 196
Homo sapiens          SVKTRS--ERQLLRLKQMNVQLAAKIQHLEFSCSEKEQEIERLNKLLRQHGLLGEVN--- 273
Mus Musculus          SVKTRS--ERQILRLKQINIQLATKIQHLEFSCSEKEQEIERLNKLLKQNGLLGDVN--- 269
                        :  :    .          : .          :
```

**Figure A.5.22.** Multiple sequence alignment of cytoplasmic helix of Hv1. The sequence alignment was performed by Clustal Omega [270]. The figure is from ref. [162] (manuscript under preparation).

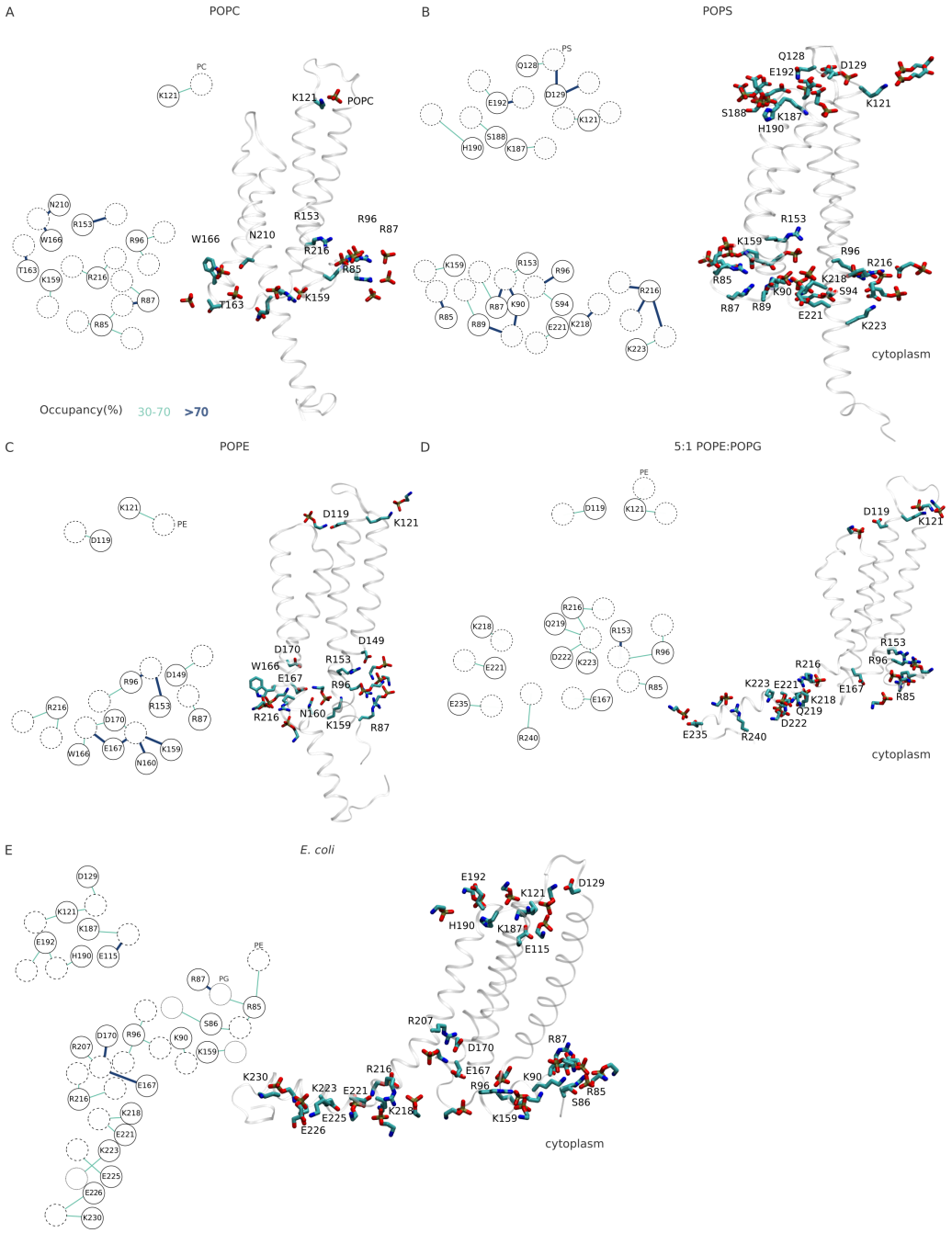


**Figure A.5.23.** Lipid anchors of Hv1. (A-E) Molecular graphics and graph representation of lipid anchors of Hv1 in POPC (Panel A), POPS (Panel B), POPE (Panel C), 5:1 POPE:POPG (Panel D) and *E. coli* (Panel E) bilayers. The figure is adapted from ref. [162] (manuscript under preparation).

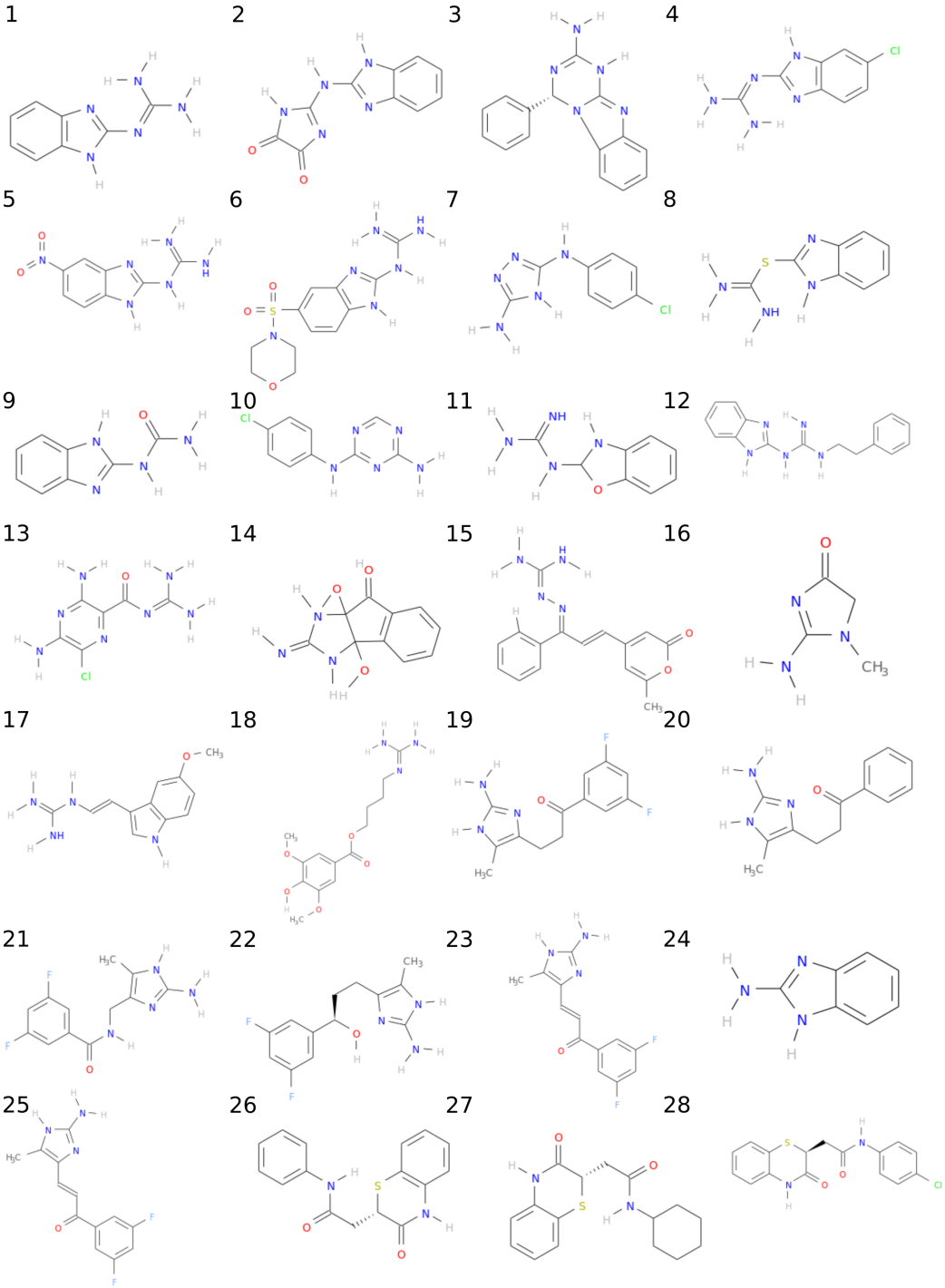


**Figure A.5.24.** Molecular images of inhibitors of Hv1. The numbering on the top left corner describes the inhibitor number corresponding to Table 5.1.

## 7.3 Publications arising from this thesis

biomolecules

MDPI

*Article*

# Graph-Based Analyses of Dynamic Water-Mediated Hydrogen-Bond Networks in Phosphatidylserine: Cholesterol Membranes

**Honey Jain [1,2], Konstantina Karathanou [2] and Ana-Nicoleta Bondar [1,3,*]**

[1] Faculty of Physics, University of Bucharest, Atomiștilor 405, 077125 Măgurele, Romania
[2] Department of Physics, Freie Universität Berlin, Arnimallee 14, 14195 Berlin, Germany
[3] IAS-5/INM-9, Forschungszentrum Jülich, Institute of Computational Biomedicine, Wilhelm-Johnen Straße, 52428 Jülich, Germany
* Correspondence: nbondar@fizica.unibuc.ro or a.bondar@fz-juelich.de

**Abstract:** Phosphatidylserine lipids are anionic molecules present in eukaryotic plasma membranes, where they have essential physiological roles. The altered distribution of phosphatidylserine in cells such as apoptotic cancer cells, which, unlike healthy cells, expose phosphatidylserine, is of direct interest for the development of biomarkers. We present here applications of a recently implemented Depth-First-Search graph algorithm to dissect the dynamics of transient water-mediated lipid clusters at the interface of a model bilayer composed of 1-palmytoyl-2-oleoyl-sn-glycero-2-phosphatidylserine (POPS) and cholesterol. Relative to a reference POPS bilayer without cholesterol, in the POPS:cholesterol bilayer there is a somewhat less frequent sampling of relatively complex and extended water-mediated hydrogen-bond networks of POPS headgroups. The analysis protocol used here is more generally applicable to other lipid:cholesterol bilayers.

**Keywords:** depth-first-search algorithm; lipid–water hydrogen-bond network; hydrogen-bond network topology; POPS-cholesterol hydrogen-bond networks



**Citation:** Jain, H.; Karathanou, K.; Bondar, A.-N. Graph-Based Analyses of Dynamic Water-Mediated Hydrogen-Bond Networks in Phosphatidylserine: Cholesterol Membranes. *Biomolecules* **2023**, *13*, 1238. https://doi.org/10.3390/biom13081238

Academic Editor: Angelika Chroni

Received: 20 June 2023
Revised: 3 August 2023
Accepted: 7 August 2023
Published: 11 August 2023



## 1. Introduction

Hydrogen (H)-bonds and H-bond networks shape the structure and dynamics of lipid–lipid interactions [1] and the fluidity of the lipid bilayer [2–4]. H-bonding properties depend on the nature of the lipid headgroup. The anionic phosphatidylserine (PS) has more inter-lipid H-bonds than, e.g., the zwitterionic phosphatidylethanolamine (PE) and phosphatidylcholine (PC), or than the anionic phosphatidylglycerol (PG) and phosphatidic acid (PA) [5–7]. This propensity for intermolecular H-bonding of PS may be associated with somewhat larger bilayer thicknesses [7].

Lipid clusters can be defined as groups of lipids H-bonded via direct H-bonds, water molecules, or ion interactions. The clustering of PS appears to be associated with the formation of nanometer-sized domains [8–10] that could provide, e.g., a platform for peripheral protein recruitment [11], viral assembly [12], and the binding to the membrane of the influenza A virus matrix protein [9]. Altered distribution of PS has been associated with a number of human diseases [13], including cancer [14–16]. The formation of lipid clusters, particularly in the case of PS [17–19], PG [17], and phosphatidylinositol 4,5-bisphosphate (PIP2) [20], might be promoted by the presence of cations. Experiments using, e.g., time-resolved fluorescence spectroscopy [18], fluorescence correlation spectroscopy [20,21], steady-state probe-partitioning fluorescence resonance energy transfer (SP-FRET) [20], and molecular dynamics (MD) simulations [18,19,22] suggested that the presence of sodium [9,18,21,23–26], potassium [18,22], calcium [19,22,25–28], or magnesium ions [28] may be associated with the clustering of lipids. Details of ion-mediated lipid cluster formation depend both on the cation and on the lipid headgroup. For example,

compared to potassium, the presence of sodium ions tends to be associated with larger clusters in PIP2 bilayers [22] and shows a higher affinity to a membrane composed of 1-palmytoyl-2-oleoyl-*sn*-glycero-2-phosphatidylcholine (POPC) and 1-palmytoyl-2-oleoyl-*sn*-glycero-2-phosphatidylserine (POPS) [18]. At the interface of a POPS/POPC bilayer, sodium ions have reduced mobility relative to POPC [18]. Likewise, sodium and potassium ions have weaker binding at a PC than a PE lipid membrane interface [29].

Cholesterol favors interactions with anionic lipids (PS and PG) as compared to the zwitterionic PC and PE [30–33], and it can H-bond to lipid headgroups [34]. Cholesterol prefers H-bond to single phospholipids [35], typically with the lipid carbonyl or phosphate oxygen atoms [35–37]. Intercalation of cholesterol molecules could influence the packing of anionic lipids [30], looser at the lipid headgroups and tighter at the tails [38] and be associated with reduced sodium ion binding at the interface [39].

MD studies have shown that lipids can form H-bond networks mediated by direct or water-mediated H-bonds between lipid headgroups [5,17]. The water dynamics at the lipid interface is slower than the bulk [1,40,41]. The slower relaxation rates of interfacial waters H-bonded to lipids suggest that H-bond networks in the hydration layer facilitate lipid–lipid interactions [1]. The number of H-bonds between water molecules at the interface of DMPC [1] and DOPS [42] bilayers decreases with an increasing membrane depth.

To identify and characterize dynamic water-mediated clusters of lipid headgroups, we have recently implemented a Depth-First-Search (DFS)-based graph algorithm that uses Connected Component searches to explore the nodes of the H-bond graphs and identify four main types of lipid H-bond clusters [17]. Clusters are then characterized according to properties such as cluster size, which is given by the number of nodes (lipid headgroups) that constitute the cluster, and cluster length, which is given by the number of H-bonds within the longest H-bond path within the cluster [17]. Using the DFS-based algorithm we implemented, we dissected the water-mediated H-bond clusters at the interface of hydrated lipid bilayers composed of POPE, POPG, 3:1 POPE:POPG, 5:1 POPE:POPG, POPS, and an *Escherichia coli* lipid membrane model, all without cholesterol [17]. We found that, regardless of the lipid membrane composition, short linear H-bond arrangements, typically two lipid headgroups that H-bond directly or via one water molecule, were sampled frequently during atomistic MD simulations [17]; relative to the other lipids studied, POPS could engage more frequently in circular arrangements of three lipid headgroups [17].

Here, we apply the DFS graph algorithm to characterize dynamic water-mediated interactions in a POPS:cholesterol membrane with 10% cholesterol, which is in the range of cholesterol concentrations relevant to the plasma membrane of a healthy eukaryotic cell [43]. As a reference, we use a hydrated POPS bilayer without cholesterol. We compute separately H-bond clusters contributed by phosphate, serine vs. ester groups; likewise, we compute separately H-bond clusters that involve direct POPS:POPS H-bonds, vs. one-water bridges or ion-mediated bridges between POPS headgroups. We find that cholesterol disfavors the transient formation of H-bonded POPS clusters.

## 2. Methods

### *2.1. MD Simulations of Hydrated Lipid Membranes*

CHARMM-GUI [44–46] was used to generate coordinates for two distinct hydrated POPS bilayers (Table 1): (i) without cholesterol; (ii) with 10% cholesterol. All simulation systems have 0.15 M neutralizing KCl salt and a starting size of approximately 81 Å × 81 Å × 85 Å.

We used the CHARMM36 force field for lipids and ions [47–52] and the TIP3P water model [53]. All simulations were performed with NAMD 2.13 [54,55]. The standard CHARMM-GUI scheme for the initial equilibration was used. For the production runs, we used a Langevin dynamics scheme [56,57] with an oscillation period of 200 fs, a damping time scale of 100 fs, and a damping coefficient of 5 $ps^{-1}$ in the *NPT* ensemble (constant number of particles $N$, constant pressure $P$ = 1 bar, and constant temperature $T$ = 310.15 K). We used the smooth particle mesh Ewald summation to compute Coulomb

interactions [58,59] and a 10–12 Å switch function for real-space interactions; covalent bonds to H-atoms were fixed. An integration step of 1 fs was used throughout equilibration and the first 1 ns of the production runs; for the production runs, we used a multiple time-step integration scheme [60,61] with 1 fs for bonded interactions and 2 fs for short-range nonbonded forces and long-range electrostatics. Coordinates were saved every 10 ps for data analyses. The total sampling time of the two simulations was 1 μs.

**Table 1.** MD simulations performed. We report the length of the production runs performed without any constraints. The total number of atoms we report includes atoms of the lipids and water molecules, and the ions.

| Sim | #POPS/Chol Molecules per Leaflet | #Atoms | Length (μs) |
|---|---|---|---|
| POPS | POPS (109) | 53,680 | 0.5 |
| POPS:chol (10%) | POPS/Chol (98/11) | 51,859 | 0.5 |

### *2.2. H-bond Criteria, H-bond Graphs, H-bond Paths, and H-bond Occupancies*

We identified H-bonds using a distance criterion whereby two groups were considered as H-bonded if the distance between the H-atom and acceptor hetero-atom was within 2.5 Å. This single distance criterion gives results largely equivalent to a combined distance and angle criterion of H-bond distances $\leq$3.5 Å between the H-bond donor and acceptor hetero-atoms, and H-bond angles within 60° [62]. For potassium ion-mediated bridges between two POPS phosphate groups, we used a distance criterion of 4 Å.

A H-bond graph consists of nodes, which here are the POPS or cholesterol headgroups, and the edges, which are direct, 1 water-mediated, or ion-mediated H-bond connections between the nodes. A H-bond path between two lipid headgroups connects these two headgroups via the shortest distance H-bond path, i.e., via the smallest number of intermediate H-bonds. The occupancy of a H-bond is the percentage of coordinate sets utilized in analyses in which the H-bond criterion is satisfied [24,63]. We used Bridge [63,64] to compute H-bond occupancies.

### *2.3. H-bond Clusters, Topology, Cluster Size, Path Length, and Occupancy of Lipid Clusters*

A H-bond cluster consists of nodes and edges that interconnect with each other. The topology of a H-bond lipid cluster is defined as the geometric arrangement of the nodes and edges in that cluster. To identify lipid clusters, we used the recently developed DFS algorithm [17] that analyses the H-bond graph to identify transient lipid clusters and the topologies of these clusters. Briefly, the DFS algorithm treats the nodes and edges of the H-bond graph as, respectively, data points and relationships between these data points. The algorithm explores all graph nodes, monitors H-bond distances in the coordinate dataset (MD trajectory), and constructs adjacency or connection matrices that represent the H-bond connections between pairs of nodes. The nodes of the graph are clustered, according to the H-bonding relationships between them, into four main topologies—linear, star and linear, circular, and complex combinations of these three arrangements. A lipid cluster is then characterized by its size, which is given by the number of lipid headgroups that constitute the cluster, and by the path length $L$, which is given by the number of edges (H-bonds) in the longest path connecting two nodes of the H-bond cluster.

The occupancy of a lipid cluster is the percentage of coordinate sets utilized in analyses in which the cluster is present. The length of the water wire that connects two lipid headgroups is given by the number of bridging H-bonded water molecules [63]; for simplicity, and because water bridges between lipids tend to have very small occupancies, here we considered only one-water bridges. All topology calculations were performed using the VMD [65] and MATLAB data analysis scripts of the DFS algorithm [17] as deposited in the Mendeley repository [66]. For data analyses, the complete trajectories of the production runs were used.

### *2.4. Structure Factors and the Number of H-bonds per POPS*

We used the MEMBPLUGIN [67] in VMD [65] to evaluate the average thickness of each bilayer, area per lipid, and order parameters. The H-bonds per lipid are reported as the average number of H-bonds sampled by the specific lipid group in each coordinate set.

All molecular graphics were prepared using VMD 1.9.4 [65]. Boxplots of H-bond occupancy values extracted with Bridge [63,64] were prepared using Python. Files pertaining to the simulations reported here are released as a public Mendeley repository (see the Data Availability Statement).

## 3. Results and Discussion

The simulations reported here have average membrane thickness, area per lipid, and order parameter values close to previous experiments and simulations. For the POPS membrane without cholesterol, the average membrane thickness we calculate is 41.2 ± 0.5 Å, which is close to values reported from previous MD simulations, e.g., 43.2 ± 0.5 Å [68], 40.6 Å [69], 42.4 ± 0.2 Å [70], 42.1 ± 0.5 Å [17], and to the 42.2 Å thickness measured by neutron and X-ray scattering in the presence of NaCl [69]. In the presence of 10% cholesterol, the POPS membrane is ~1.5 Å thicker (Table 1, Figure 1A,C), which is compatible with the ~2.2 Å increase, relative to pure DMPC, in the thickness of DMPC/cholesterol membranes with 10% cholesterol [71]. The calculated area per lipid for the POPS membrane is 59.8 ± 1.9 Å$^2$, which is relatively close to previously reported values from MD simulations (58.4 Å$^2$ [72], 57.5 ± 1.2 Å$^2$ [70], and 62.0 Å$^2$ [69]). A decrease of ~5 Å$^2$ in the area per lipid and an increase in the order parameters found here in the presence of cholesterol (Figure 1B,D) are in reasonable qualitative agreement with the decrease by ~6–7 Å$^2$ [73,74] in the area per lipid of a DOPC/cholesterol membrane with 10% cholesterol. Likewise, the order parameters for the POPS membrane (Figure 1D) are compatible with previous studies [70,72].

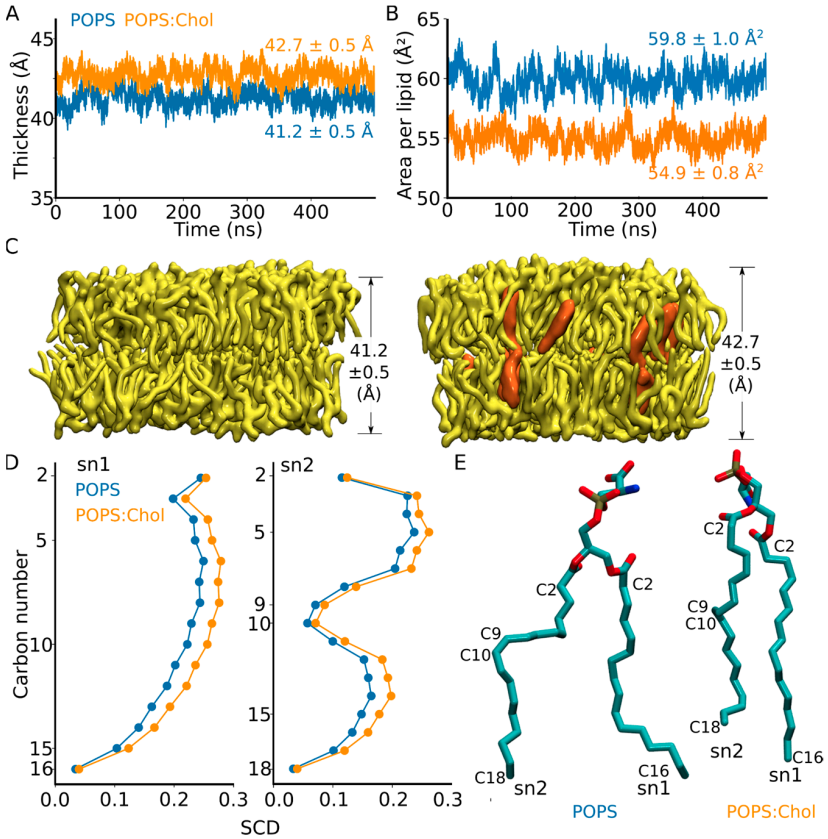


**Figure 1.** Basic features of the hydrated POPS and POPS:chol membranes. (**A**) Time series and average values of the lipid bilayer thickness computed from POPS membranes (cyan profile) vs.

POPS:chol (orange profile). (**B**) Time series of the area per lipid computed from POPS and POPS:chol membranes. (**C**) Molecular graphics based on coordinate snapshots from simulations of POPS (**left**) vs. POPS:chol (**right**). POPS are shown as yellow bonds; when present, cholesterol is shown as orange bonds. (**D**) SCD order parameter profiles. (**E**) Molecular graphics illustrating POPS with selected atoms labeled.

### *3.1. Direct and One-Water-Mediated H-bonding of POPS Headgroups*

On average, each POPS headgroup has 1.5 ± 0.1 H-bonds with another POPS (Figure 2A), which is close to the 1.1–1.2 H-bonds/POPS headgroup reported previously from CHARMM36 MD simulations [7]. Each POPS headgroup also has, on average, 2.3 ± 0.2 H-bonds from one-water bridges (Figure 2B) and 1.5 ± 0.1 potassium ion interactions (Figure 2C). Each phosphate and serine group has about 1.3–1.4 H-bonds to a bridging water molecule (Figure 2), slightly higher than the ~1.1 one-water-mediated H-bonds per ester group (Figure 2B). When the ester groups are included in the H-bond computation, the average number of one-water-mediated H-bonds increases from 1.9 ± 0.1 (when only the POPS phosphate and serine groups are included in the H-bond computation) to 2.3 ± 0.2 (Figure 2), but these ester H-bonds have very low occupancies (Figure 3). The total average number of H-bonds per POPS is similar in membranes with and without cholesterol (Figure 2).

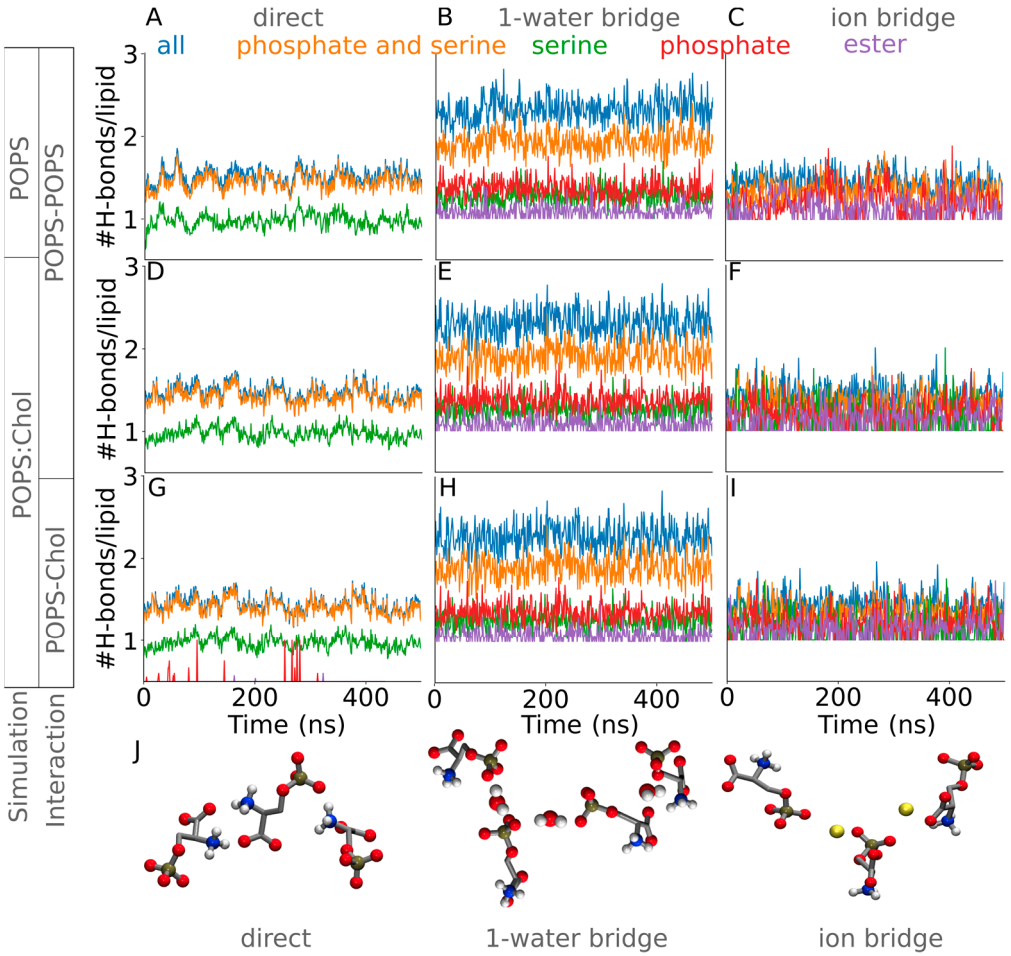


**Figure 2.** Number of H-bonds per POPS. (**A**–**C**) Time series of interactions sampled in simulations of the POPS membrane without cholesterol. We show the number of direct lipid H-bonds (panel **A**) and

1-water-mediated (panel **B**) and ion-mediated bridges between POPS (panel **C**). The total number of H-bonds per POPS is shown by the blue profile. For groups of atoms of POPS, we use the following color code: serine, green; phosphate, red; ester, purple; phosphate and serine, orange; all, blue. For clarity, coordinate sets were read each 1 ns. (**D**–**F**) Interactions sampled in POPS:chol membrane simulations. We show the number of direct lipids H-bonds (panel **C**), 1-water-mediated (panel **D**) vs. ion-mediated bridges between POPS (panel **D**). (**G**–**I**) POPS-cholesterol interactions. We monitor the number of direct POPS-cholesterol H-bonds (panel **G**), 1-water-mediated (panel **H**) vs. ion-mediated bridges (panel **I**). (**J**) Molecular graphics illustrating, from left to right, direct POPS H-bonds, 1-water bridging, and potassium ion-mediated bridges.

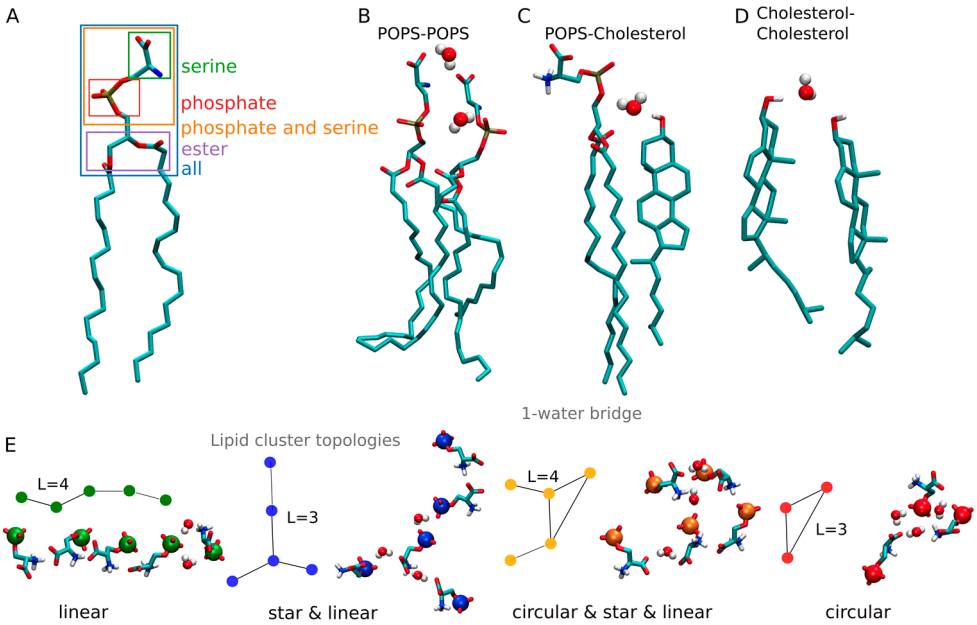


**Scheme 1.** H-bonds and lipid cluster topologies sampled in hydrated POPS bilayers. (**A**) H-bonding groups used for topology analysis and H-bond calculations of POPS. (**B**–**D**) Molecular graphics illustrating 1-water mediated H-bond interaction between POPS headgroups (Panel **B**), POPS-cholesterol (Panel **C**), and between two cholesterol molecules (Panel **D**). (**E**) Illustrations of the topologies studied here with the DFS algorithm [17]. H-bond clusters with path lengths L = 3 and L = 4 are shown.

Overall, both the direct and one-water-mediated bridges between POPS have small occupancies: 83–93% of the direct H-bonds have occupancies within 10–15% (Figure 3A,C), and 69–100% of the one-water bridges computed for the different POPS H-bonding groups have occupancies within about 5% (Figure 3B,D), suggesting these interactions are quite dynamic. In the distribution of the occupancies of direct H-bonds and one-water-mediated bridges, there are also outliers: for each of the H-bonds and water-mediated bridges presented in Figure 3, about 4–8% of the data points are outliers, i.e., these are H-bonds and water-mediated bridges with occupancy values significantly larger than the average (Figure 3). The highest-occupancy H-bonds are, in the POPS membrane, a pair of POPS headgroups that remain within H-bond distance for 306.2ns (i.e., 61.2% POPS simulation) and, in the POPS:cholesterol simulation, a pair of POPS headgroups within H-bond distance for 360.2 ns (72% of the simulation).

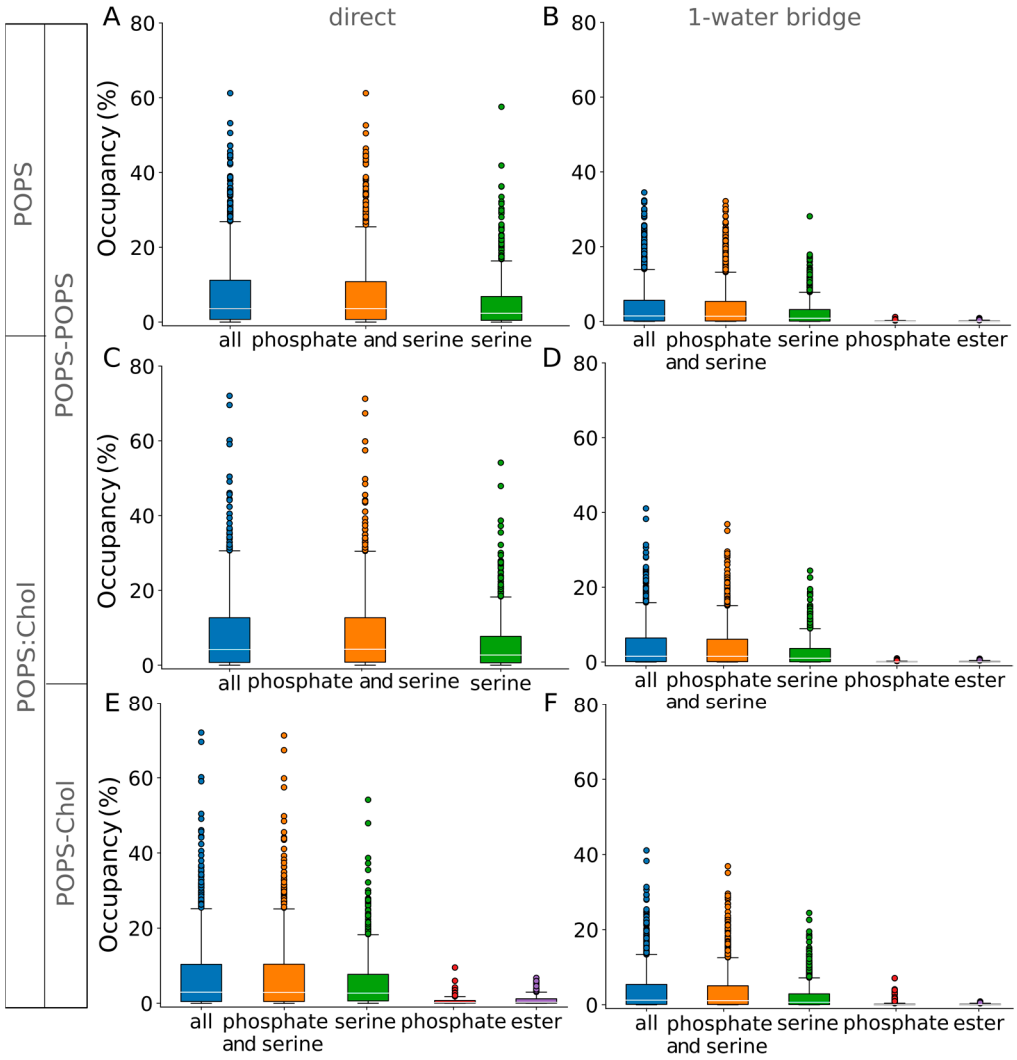


**Figure 3.** H-bonds and water-mediated bridges have low occupancies. We present boxplots of H-bond occupancy values for interactions between phosphate, serine, and ester groups, and for all three groups (see Scheme 1A). (**A**–**D**) Occupancies (%) of direct H-bonds (panels **A**, **C**) and for one-water bridges (panels **B**, **D**). In panels **A** and **C**, note that direct H-bonds between phosphate or ester groups are not found. (**E**,**F**) Occupancies (%) of direct POPS-cholesterol H-bonds (panel **E**) and one-water bridges between POPS and cholesterol (panel **F**). Overall, the same pairs of headgroups tend to give the high-occupancy H-bonding and water bridging presented here for the distinct moieties.

### *3.2. Water-Mediated H-bond Clusters in the POPS:Cholesterol Membrane*

We used the DFS algorithm as illustrated in Scheme 1 to characterize POPS clusters in membranes with cholesterol, using as a reference the results obtained for the POPS membrane without cholesterol [17,66].

We first considered all unique H-bonds sampled during the simulations. At any given time, about 15–18 clusters are likely to be sampled in the POPS:cholesterol membrane, that is, because each leaflet has 109 lipids (Table 1), at any moment of time about 81% of the lipids participate in dynamic, low-occupancy H-bond paths of at least two lipids. About half of these H-bond paths (8–9) are linear (Scheme 1, Figure 4A). Linear, relatively short H-bond paths are favoured by POPS irrespective of whether cholesterol is present or not (Figures 4A and 5) and are exclusively sampled in cholesterol clusters (Figure 6). Circular and star and linear clusters are rare and, when sampled, have minimal sizes (3 and 4–5 lipids, respectively, Figure 4A,B). Star and linear and circular arrangements may also

be sampled transiently, such that, overall, most of the H-bond paths sampled are either linear or a more complex topology that includes a linear path segment (Figure 4).

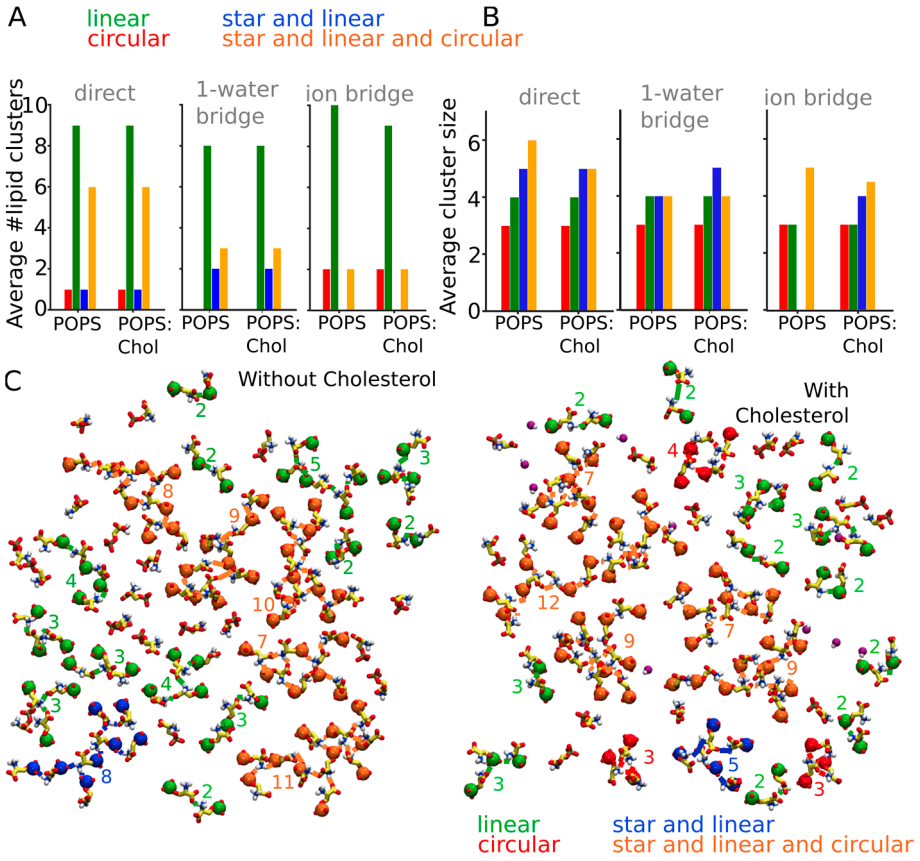


**Figure 4.** POPS clusters sampled during simulations without and with cholesterol. (**A**,**B**) Bar graphs of the average number of lipids clusters (panel **A**) and of the average cluster size (panel **B**) computed separately for H-bond clusters mediated by direct POPS and POPS-cholesterol H-bonds, one-water bridges, and potassium ion bridges. (**C**) Illustration of lipid clusters mediated by direct POPS H-bonds in coordinate snapshots from simulations of POPS bilayers without (**left**) and with cholesterol (**right**). POPS headgroups are shown with yellow bonds, and cholesterol oxygen atoms are shown as purple spheres.

As reported previously for a hydrated POPS bilayer [17], linear H-bond paths (Scheme 1) mediated by one water molecule are sampled throughout the entire POPS simulation: on average, at least one linear path is sampled at any moment in time (Figure 5E). The one-water-mediated linear H-bond paths tend to be relatively short, composed of 2–3 lipids, that is, these are singular H-bonds, or two H-bonds with one common POPS headgroup (Figure 5E). These results for the reference POPS simulation are in qualitatively good agreement with our previous computations on hydrated POPS [17] and 4:1 POPC:POPG membranes [23]. In the presence of cholesterol, direct singular H-bonds (H-bond paths with length L = 1) between POPS headgroups are slightly less likely than in the POPS membrane (Figure 5A), though such paths are sampled throughout the entire simulation (Figure 5F). Taken together with the H-bond occupancy analysis summarized in Figure 3, the time series of the H-bond paths of different lengths (Figure 5) suggest that, overall, most H-bond clusters at the POPS headgroup interface are short and transient. It should also be noted that the exact number of H-bond paths, or clusters, sampled throughout the simulation trajectories (Figure 5), depends on the size of the lipid bilayer, and the time series presented in Figure 5 are meant as an illustration of the H-bond dynamics at the lipid headgroup interface of the hydrated membrane patches used here (Table 1).

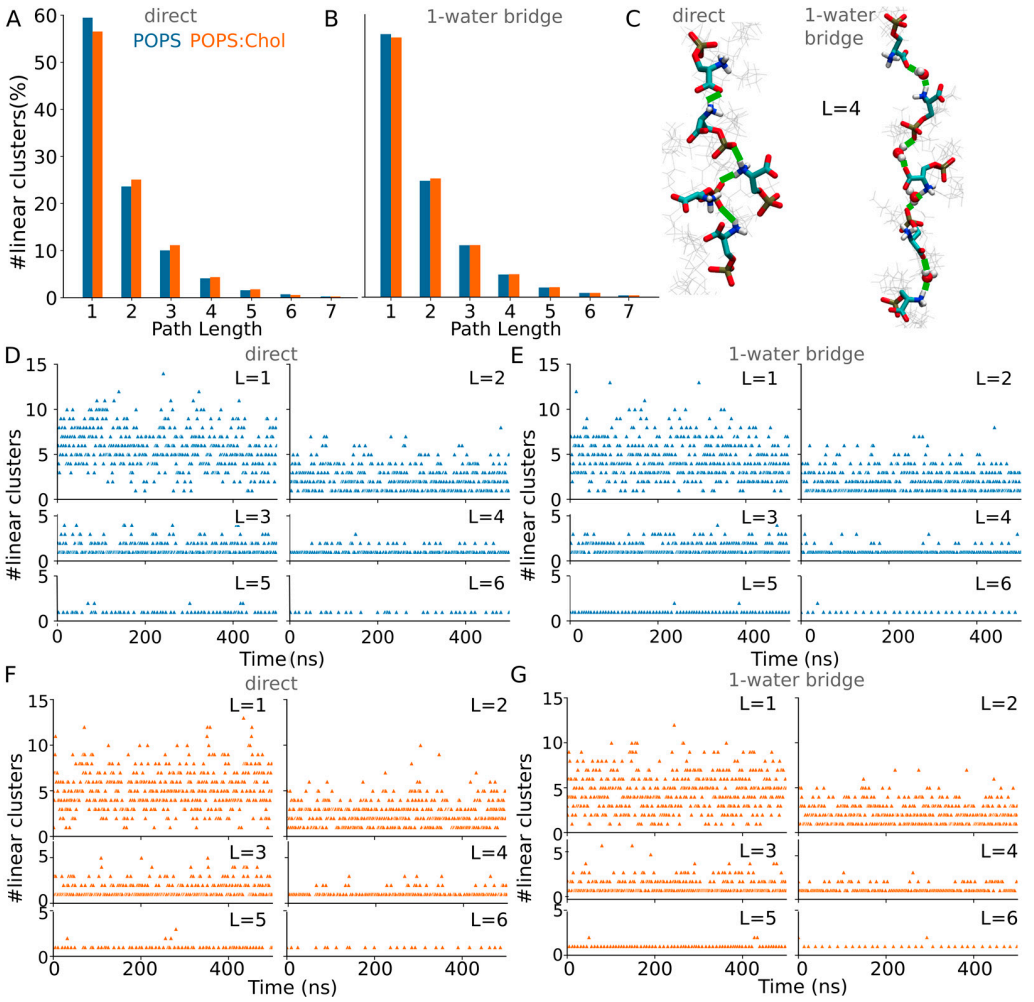


**Figure 5.** Path lengths for linear clusters in the POPS and POPS:chol bilayer. (**A**,**B**) Percentage of number of linear clusters with different path lengths mediated by direct H-bonds (panel **A**) vs. one-water bridges (panel **B**) in POPS (blue) vs. POPS:chol (orange) bilayers. Note that most of these paths are transient, as most H-bonds and water-mediated bridges have small occupancies (Figure 3). (**C**) Water-mediated linear clusters with path length L = 4; the four connecting H-bonds are shown as thick green lines. (**D**,**E**) Time series of the number of direct (panel **D**) and one-water bridges (panel **E**) linear clusters with path lengths between 1 and 6, computed from simulations of POPS without cholesterol. (**F**,**G**) Time series of the number of direct (panel **F**) and one-water bridges (panel **G**) linear clusters with path lengths between 1 and 6, computed from simulations of POPS with cholesterol.

As noted before for a hydrated POPS bilayer [17], linear paths with more than 2–3 lipids are sampled but only very rarely (Figures 4 and 5A,B). Most (~60%) of the linear H-bond clusters sampled by POPS headgroups have a path length L = 1, and a significant percentage (25%) of the linear clusters have a path length L = 2. That is, when sampled, linear H-bond paths are typically short, only 2–3 lipids; longer linear paths with more lipids may be sampled but very rarely (Figure 5A,B). Cholesterol molecules may, infrequently, sample small clusters (L = 1, i.e., two cholesterol molecules); longer linear H-bond clusters with 3–4 cholesterol molecules H-bonded via one-water bridges are very rarely sampled (Figure 6). The infrequent sampling of cholesterol clusters can be attributed to its preference for H-bonding to single phospholipids [35]. Even in 1:1 concentrations, cholesterol–lipid is more likely than cholesterol–cholesterol interactions [35–37]. We also note that the sampling frequency of specific clusters can depend on the length of the simulation.

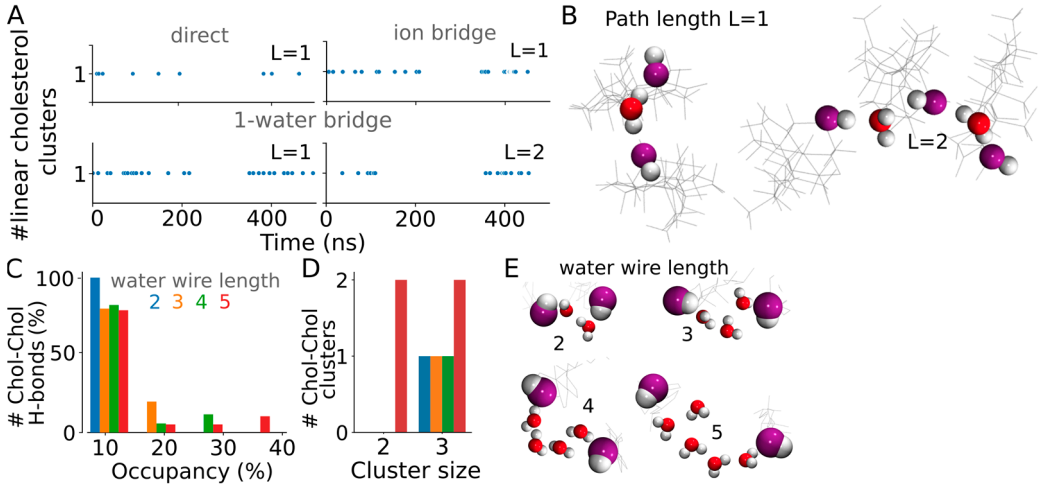


**Figure 6.** Cholesterol H-bond clusters. (**A**) Time series of the number of linear clusters mediated by direct cholesterol–cholesterol H-bonds, one-water bridges, and ion bridges between cholesterol molecules with path lengths 1–2. (**B**) Illustration of linear paths mediated via one-water bridging between 2 and 3 cholesterol molecules. (**C**) Occupancy (%) of cholesterol–cholesterol H-bonds mediated by 2, 3, 4, or 5 water molecules. (**D**) Cluster size. (**E**) Illustration of linear cholesterol paths formed via water wires of length 2, 3, 4, or 5 water molecules.

## 4. Conclusions

Anionic PS lipid headgroups have a high propensity to H-bond [5–7], and topology analyses have revealed preferred arrangements of POPS bridged by water molecules [17]. Because the H-bond dynamics of PS can be affected by cholesterol [30–32,34], here we studied the dynamics of H-bond clusters sampled in atomistic simulations of a POPS membrane with cholesterol and compared the results with those for a cholesterol-free POPS bilayer.

The concentration of cholesterol used here, 10%, approximates that of a healthy eukaryotic plasma membrane [43]. We stress, however, that the POPS:cholesterol membrane studied here is but a model membrane, because the eukaryotic plasma membrane is a complex mixture of no fewer than 11 different types of lipids [43]. As anticipated based on previous results reported in the literature [75], the POPS membrane is about 1.5 Å thicker when cholesterol is present (Figure 1A,C).

Regardless of the presence of cholesterol, POPS samples dynamic (low-occupancy) water-mediated H-bond networks (Figure 3). As reported before, linear H-bond clusters are sampled more frequently than more complex topologies (Scheme 1, Figure 4), yet more complex arrangements may be sampled, particularly in the absence of cholesterol (Figure 4).

Regardless of the presence of cholesterol, POPS tends to form small linear lipid clusters with 2–3 lipids directly H-bonded or one-water-bridged (Figures 4 and 5). Cholesterol is associated with fewer POPS being part of complex H-bond clusters (Figure 4).

POPS-cholesterol clusters are sampled less frequently than POPS-POPS clusters, and cholesterol–cholesterol clusters are rare (Figure 6). When sampled, cholesterol-only clusters are small, typically only two cholesterol molecules (Figure 6); this finding is compatible with the previous study [76] reporting a preference of cholesterol molecules to form dimers. POPS clusters mediated by potassium ions prefer a linear arrangement of 3–4 lipids, whereas the more complex topologies are much less frequent (Figure 4). This is compatible with previous work [17] indicating that sodium-mediated POPS lipid clusters tend to prefer linear topologies with two lipid clusters; we note, however, that the number of cation-mediated clusters sampled during the simulations, and the size of the clusters, might depend on the length of the simulations and on the size of the lipid membrane patch.

We anticipate that the protocol used here to evaluate the H-bonding of a simple cholesterol-containing model bilayer could become useful to dissect dynamic H-bond clusters sampled in simulations of more complex lipid mixtures, including for water-mediated lipid headgroup H-bond paths of potential interest for lateral proton transfer along lipid membrane interfaces, and to evaluate how different cations influence the sampling of transient H-bond clusters, and the preferred topologies of these clusters, in hydrated membranes with distinct lipid composition.

**Author Contributions:** Conceptualization, A.-N.B.; methodology, H.J., K.K. and A.-N.B.; software, K.K.; validation, H.J., K.K. and A.-N.B.; formal analysis, H.J.; investigation, H.J.; resources, A.-N.B.; data curation, H.J. and K.K.; writing—original draft preparation, H.J.; writing—review and editing, H.J. and A.-N.B.; visualization, H.J. and A.-N.B.; supervision, A.-N.B.; project administration, A.-N.B.; funding acquisition, A.-N.B. All authors have read and agreed to the published version of the manuscript.

**Funding:** This research was funded by the European Union's Horizon 2020 Research and Innovation Program under the Marie Sklodowska-Curie grant agreement No H2020 MSCA-ITN-2019-860592, Innovative Training Network 'Proton and proton-coupled transport' (to A.-N.B.).

**Institutional Review Board Statement:** Not applicable.

**Informed Consent Statement:** Not applicable.

**Data Availability Statement:** Input coordinate and protein structure files, and trajectory files with coordinate sets from the simulations reported here, are openly available at Jain, Honey (2023), "Graph-based analyses of dynamic water-mediated hydrogen-bond networks in phosphatidylserine:cholesterol membranes", Mendeley Data, V1, doi: 10.17632/h8y6zjckcw.1 as accessed on 11 August 2023.

**Acknowledgments:** Research was supported by funds from the European Union's Horizon 2020 Research and Innovation Program under the Marie Sklodowska-Curie grant agreement No. H2020 MSCA-ITN-2019-860592, Innovative Training Network 'Proton and proton-coupled transport' (to A-NB). MD simulations were performed using computing resources of the Physics Department at the Freie Universität Berlin, and data analyses were performed using computer resources of the Faculty of Physics of the University of Bucharest. The authors are grateful to Jens Dreger (Freie Universität Berlin) for technical support.

**Conflicts of Interest:** The authors declare no conflict of interest.

## References

1. Srivastava, A.; Debnath, A. Hydration Dynamics of a Lipid Membrane: Hydrogen Bond Networks and Lipid-Lipid Associations. *J. Chem. Phys.* **2018**, *148*, 094901. [CrossRef]
2. Boggs, J.M. Lipid Intermolecular Hydrogen Bonding: Influence on Structural Organization and Membrane Function. *Biochim. Biophys. Acta* **1987**, *906*, 353–404. [CrossRef]
3. Seu, K.J.; Cambrea, L.R.; Everly, R.M.; Hovis, J.S. Influence of Lipid Chemistry on Membrane Fluidity: Tail and Headgroup Interactions. *Biophys. J.* **2006**, *91*, 3727–3735. [CrossRef]
4. Pasenkiewicz-Gierula, M.; Takaoka, Y.; Miyagawa, H.; Kitamura, K.; Kusumi, A. Hydrogen Bonding of Water to Phosphatidylcholine in the Membrane As Studied by a Molecular Dynamics Simulation: Location, Geometry, and Lipid-Lipid Bridging via Hydrogen-Bonded Water. *J. Phys. Chem. A* **1997**, *101*, 3677–3691. [CrossRef]
5. Pyrkova, D.V.; Tarasova, N.V.; Krylov, N.A.; Nolde, D.E.; Pentkovsky, V.M.; Efremov, R.G. Dynamic Clustering of Lipids in Hydrated Two-Component Membranes: Results of Computer Modeling and Putative Biological Impact. *J. Biomol. Struct. Dyn.* **2013**, *31*, 87–95. [CrossRef]
6. Lewis, R.N.A.H.; McElhaney, R.N. Calorimetric and Spectroscopic Studies of the Thermotropic Phase Behavior of Lipid Bilayer Model Membranes Composed of a Homologous Series of Linear Saturated Phosphatidylserines. *Biophys. J.* **2000**, *79*, 2043–2055. [CrossRef]
7. Jiang, L.; Dávila-Contreras, E.M.; Beaven, A.H.; Im, W.; Klauda, J.B. An Extensive Simulation Study of Lipid Bilayer Properties with Different Head Groups, Acyl Chain Lengths, and Chain Saturations. *Biochim. Biophys. Acta Biomembr.* **2016**, *1858*, 3093–3104. [CrossRef]
8. Fairn, G.D.; Schieber, N.L.; Ariotti, N.; Murphy, S.; Kuerschner, L.; Webb, R.I.; Grinstein, S.; Parton, R.G. High-Resolution Mapping Reveals Topologically Distinct Cellular Pools of Phosphatidylserine. *J. Cell Biol.* **2011**, *194*, 257–275. [CrossRef]

9. Bobone, S.; Hilsch, M.; Storm, J.; Dunsing, V.; Herrmann, A.; Chiantia, S. Phosphatidylserine Lateral Organization Influences the Interaction of Influenza Virus Matrix Protein 1 with Lipid Membranes. *J. Virol.* **2017**, *91*, 10–1128. [CrossRef]
10. Hirama, T.; Das, R.; Yang, Y.; Ferguson, C.; Won, A.; Yip, C.M.; Kay, J.G.; Grinstein, S.; Parton, R.G.; Fairn, G.D. Phosphatidylserine Dictates the Assembly and Dynamics of Caveolae in the Plasma Membrane. *J. Biol. Chem.* **2017**, *292*, 14292–14307. [CrossRef]
11. Lucas, N.; Cho, W. Phosphatidylserine Binding Is Essential for Plasma Membrane Recruitment and Signaling Function of 3-Phosphoinositide-Dependent Kinase-1. *J. Biol. Chem.* **2011**, *286*, 41265–41272. [CrossRef]
12. Husby, M.L.; Amiar, S.; Prugar, L.I.; David, E.A.; Plescia, C.B.; Huie, K.E.; Brannan, J.M.; Dye, J.M.; Pienaar, E.; Stahelin, R.V. Phosphatidylserine Clustering by the Ebola Virus Matrix Protein Is a Critical Step in Viral Budding. *EMBO Rep.* **2022**, *23*, e51709. [CrossRef]
13. Zwaal, R.F.A.; Comfurius, P.; Bevers, E.M. Surface Exposure of Phosphatidylserine in Pathological Cells. *Cell. Mol. Life Sci.* **2005**, *62*, 971–988. [CrossRef]
14. Ran, S.; Thorpe, P.E. Phosphatidylserine Is a Marker of Tumor Vasculature and a Potential Target for Cancer Imaging and Therapy. *Int. J. Radiat. Oncol. Biol. Phys.* **2002**, *54*, 1479–1484. [CrossRef]
15. Riedl, S.; Rinner, B.; Asslaber, M.; Schaider, H.; Walzer, S.M.; Novak, A.; Lohner, K.; Zweytick, D. In Search of a Novel Target—Phosphatidylserine Exposed by Non-Apoptotic Tumor Cells and Metastases of Malignancies with Poor Treatment Efficacy. *Biochim. Biophys. Acta Biomembr.* **2011**, *1808*, 2638–2645. [CrossRef]
16. Tan, L.T.H.; Chan, K.-G.; Pusparajah, P.; Lee, W.L.; Chuah, L.H.; Khan, T.M.; Lee, L.H.; Goh, B.H. Targeting Membrane Lipid a Potential Cancer Cure? *Front. Pharmacol.* **2017**, *8*, 12. [CrossRef]
17. Karathanou, K.; Bondar, A.-N. Algorithm to Catalogue Topologies of Dynamic Lipid Hydrogen-Bond Networks. *Biochim. Biophys. Acta Biomembr.* **2022**, *1864*, 183859. [CrossRef]
18. Jurkiewicz, P.; Cwiklik, L.; Vojtiskova, A.; Jungwirth, P.; Hof, M. Structure, Dynamics, and Hydration of POPC/POPS Bilayers Suspended in NaCl, KCl, and CsCl Solutions. *Biochim. Biophys. Acta Biomembr.* **2012**, *1818*, 609–616. [CrossRef]
19. Boettcher, J.M.; Davis-Harrison, R.L.; Clay, M.E.; Nieuwkoop, A.J.; Ohkubo, Y.Z.; Tajkhorshid, E.; Morrissey, J.H.; Rienstra, C.M. Atomic View of Calcium-Induced Clustering of Phosphatidylserine in Mixed Lipid Bilayers. *Biochemistry* **2011**, *50*, 2264–2273. [CrossRef]
20. Wang, Y.H.; Slochower, D.R.; Janmey, P.A. Counterion-Mediated Cluster Formation by Polyphosphoinositides. *Chem. Phys. Lipids* **2014**, *182*, 38–51. [CrossRef]
21. Mukhopadhyay, P.; Monticelli, L.; Tieleman, D.P. Molecular Dynamics Simulation of a Palmitoyl-Oleoyl Phosphatidylserine Bilayer with Na+ Counterions and NaCl. *Biophys. J.* **2004**, *86*, 1601–1609. [CrossRef]
22. Böckmann, R.A.; Hac, A.E.; Heimburg, T.; Grubmüller, H. Effect of Sodium Chloride on a Lipid Bilayer. *Biophys. J.* **2003**, *85*, 1647–1655. [CrossRef]
23. Han, K.; Kim, S.H.; Venable, R.M.; Pastor, R.W. Design Principles of PI(4,5)P2 Clustering under Protein-Free Conditions: Specific Cation Effects and Calcium-Potassium Synergy. *Proc. Natl. Acad. Sci. USA* **2022**, *119*, e2202647119. [CrossRef]
24. Karathanou, K.; Bondar, A.-N. Dynamic Water Hydrogen-Bond Networks at the Interface of a Lipid Membrane Containing Palmitoyl-Oleoyl Phosphatidylglycerol. *J. Membr. Biol.* **2018**, *251*, 461–473. [CrossRef]
25. Filippov, A.V.; Orädd, G.; Lindblom, G. Effect of NaCl and $CaCl_2$ on the Lateral Diffusion of Zwitterionic and Anionic Lipids in Bilayers. *Chem. Phys. Lipids* **2009**, *159*, 81–87. [CrossRef]
26. Porasso, R.D.; Cascales, J.J.L. Study of the Effect of $Na^+$ and $Ca^{2+}$ Ion Concentration on the Structure of an Asymmetric DPPC/DPPC+DPPS Lipid Bilayer by Molecular Dynamics Simulation. *Colloids Surf. B Biointerfaces* **2009**, *73*, 42–50. [CrossRef]
27. Mao, L.; Yang, L.; Zhang, Q.; Jiang, H.; Yang, H. Effects of Ion Interactions with a Cholesterol-Rich Bilayer. *Biochem. Biophys. Res. Commun.* **2015**, *468*, 125–129. [CrossRef]
28. Bradley, R.; Slochower, D.R.; Janmey, P.A.; Radhakrishnan, R. Divalent Cations Bind to Phosphoinositides to Induce Ion and Isomer Specific Propensities for Nano-Cluster Initiation in Bilayer Membranes. *R. Soc. Open Sci.* **2020**, *7*, 192208. [CrossRef]
29. Gurtovenko, A.A.; Vattulainen, I. Effect of NaCl and KCl on Phosphatidylcholine and Phosphatidylethanolamine Lipid Membranes: Insight from Atomic-Scale Simulations for Understanding Salt-Induced Effects in the Plasma Membrane. *J. Phys. Chem. B* **2008**, *112*, 1953–1962. [CrossRef]
30. Yesylevskyy, S.O.; Demchenko, A.P. Cholesterol Behavior in Asymmetric Lipid Bilayers: Insights from Molecular Dynamics Simulations. In *Methods in Molecular Biology*; Springer Science + Business Media: New York, NY, USA, 2014; pp. 291–306.
31. Silvius, J.R. Role of Cholesterol in Lipid Raft Formation: Lessons from Lipid Model Systems. *Biochim. Biophys. Acta Biomembr.* **2003**, *1610*, 174–183. [CrossRef]
32. Simons, K.; Vaz, W.L.C. Model Systems, Lipid Rafts, and Cell Membranes. *Annu. Rev. Biophys. Biomol. Struct.* **2004**, *33*, 269–295. [CrossRef]
33. Van Dijck, P.W.M. Negatively Charged Phospholipids and Their Position in the Cholesterol Affinity Sequence. *Biochim. Biophys. Acta Biomembr.* **1979**, *555*, 89–101. [CrossRef]
34. Rowlands, L.J.; Marks, A.; Sanderson, J.E.; Law, R.V. $^{17}O$ NMR Spectroscopy as a Tool to Study Hydrogen Bonding of Cholesterol in Lipid Bilayers. *Chem. Commun.* **2020**, *56*, 14499–14502. [CrossRef]
35. Bhide, S.Y.; Zhang, Z.; Berkowitz, M.L. Molecular Dynamics Simulations of SOPS and Sphingomyelin Bilayers Containing Cholesterol. *Biophys. J.* **2007**, *92*, 1284–1295. [CrossRef]

36. Hénin, J.; Chipot, C. Hydrogen-Bonding Patterns of Cholesterol in Lipid Membranes. *Chem. Phys. Lett.* **2006**, *425*, 329–335. [CrossRef]
37. Chiu, S.C.; Jakobsson, E.; Mashl, R.J.; Scott, H.L. Cholesterol-Induced Modifications in Lipid Bilayers: A Simulation Study. *Biophys. J.* **2002**, *83*, 1842–1853. [CrossRef]
38. Zocher, F.; Van Der Spoel, D.; Pohl, P.; Hub, J.S. Local Partition Coefficients Govern Solute Permeability of Cholesterol-Containing Membranes. *Biophys. J.* **2013**, *105*, 2760–2770. [CrossRef]
39. Magarkar, A.; Dhawan, V.; Kallinteri, P.; Viitala, T.; Elmowafy, M.; Róg, T.; Bunker, A. Cholesterol Level Affects Surface Charge of Lipid Membranes in Saline Solution. *Sci. Rep.* **2014**, *4*, 5005. [CrossRef]
40. Flanagan, J.C.; Valentine, M.L.; Baiz, C.R. Ultrafast Dynamics at Lipid–Water Interfaces. *Acc. Chem. Res.* **2020**, *53*, 1860–1868. [CrossRef]
41. Higuchi, Y.; Asano, Y.; Kuwahara, T.; Hishida, M. Rotational Dynamics of Water at the Phospholipid Bilayer Depending on the Head Groups Studied by Molecular Dynamics Simulations. *Langmuir* **2021**, *37*, 5329–5338. [CrossRef]
42. Efremov, R.G. Dielectric-Dependent Strength of Interlipid Hydrogen Bonding in Biomembranes: Model Case Study. *J. Chem. Inf. Model.* **2019**, *59*, 2765–2775. [CrossRef]
43. Symons, J.; Cho, K.-J.; Chang, J.T.; Du, G.; Waxham, M.N.; Hancock, J.F.; Levental, I.; Levental, K.R. Lipidomic Atlas of Mammalian Cell Membranes Reveals Hierarchical Variation Induced by Culture Conditions, Subcellular Membranes, and Cell Lineages. *Soft Matter* **2021**, *17*, 288–297. [CrossRef]
44. Jo, S.; Kim, T.H.; Iyer, V.; Im, W. CHARMM-GUI: A Web-Based Graphical User Interface for CHARMM. *J. Comput. Chem.* **2008**, *29*, 1859–1865. [CrossRef]
45. Lee, J.; Cheng, X.; Swails, J.M.; Yeom, M.S.; Eastman, P.; Lemkul, J.A.; Wei, S.; Buckner, J.; Jeong, J.J.; Zhang, J.Z.H.; et al. CHARMM-GUI Input Generator for NAMD, GROMACS, AMBER, OpenMM, and CHARMM/OpenMM Simulations Using the CHARMM36 Additive Force Field. *J. Chem. Theory Comput.* **2015**, *12*, 405–413. [CrossRef]
46. Wu, E.L.; Cheng, X.; Jo, S.; Rui, H.; Song, K.W.; Dávila-Contreras, E.M.; Zhang, J.Z.H.; Lee, J.; Monje-Galvan, V.; Venable, R.M.; et al. CHARMM-GUI *Membrane Builder* toward Realistic Biological Membrane Simulations. *J. Comput. Chem.* **2014**, *35*, 1997–2004. [CrossRef]
47. Brooks, B.R.; Bruccoleri, R.E.; Olafson, B.D.; States, D.J.; Swaminathan, S.; Karplus, M. CHARMM: A Program for Macromolecular Energy, Minimization, and Dynamics Calculations. *J. Comput. Chem.* **1983**, *4*, 187–217. [CrossRef]
48. Feller, S.E.; MacKerell, A.D. An Improved Empirical Potential Energy Function for Molecular Simulations of Phospholipids. *J. Phys. Chem. B* **2000**, *104*, 7510–7515. [CrossRef]
49. Klauda, J.B.; Venable, R.M.; Freites, J.A.; O'Connor, J.K.; Tobias, D.J.; Mondragon-Ramirez, C.; Vorobyov, I.; MacKerell, A.D.; Pastor, R.W. Update of the CHARMM All-Atom Additive Force Field for Lipids: Validation on Six Lipid Types. *J. Phys. Chem. B* **2010**, *114*, 7830–7843. [CrossRef]
50. Beglov, D.; Roux, B. Finite Representation of an Infinite Bulk System: Solvent Boundary Potential for Computer Simulations. *J. Chem. Phys.* **1994**, *100*, 9050–9063. [CrossRef]
51. MacKerell, A.D.; Feig, M.; Brooks, C.L. Extending the Treatment of Backbone Energetics in Protein Force Fields: Limitations of Gas-Phase Quantum Mechanics in Reproducing Protein Conformational Distributions in Molecular Dynamics Simulations. *J. Comput. Chem.* **2004**, *25*, 1400–1415. [CrossRef]
52. MacKerell, A.D.; Bashford, D.; Bellott, M.; Dunbrack, R.L.; Evanseck, J.D.; Field, M.J.; Fischer, S.M.; Gao, J.R.; Guo, H.; Ha, S.; et al. All-Atom Empirical Potential for Molecular Modeling and Dynamics Studies of Proteins. *J. Phys. Chem. B* **1998**, *102*, 3586–3616. [CrossRef]
53. Jorgensen, W.L.; Chandrasekhar, J.; Madura, J.D.; Impey, R.; Klein, M.L. Comparison of Simple Potential Functions for Simulating Liquid Water. *J. Chem. Phys.* **1983**, *79*, 926–935. [CrossRef]
54. Kale, L.V.; Skeel, R.D.; Bhandarkar, M.; Brunner, R.J.; Gursoy, A.; Krawetz, N.; Phillips, J.G.; Shinozaki, A.; Varadarajan, K.; Schulten, K. NAMD2: Greater Scalability for Parallel Molecular Dynamics. *J. Comput. Phys.* **1999**, *151*, 283–312. [CrossRef]
55. Phillips, J.G.; Braun, R.; Wang, W.; Gumbart, J.C.; Tajkhorshid, E.; Villa, E.; Chipot, C.; Skeel, R.D.; Kale, L.V.; Schulten, K. Scalable Molecular Dynamics with NAMD. *J. Comput. Chem.* **2005**, *26*, 1781–1802. [CrossRef]
56. Martyna, G.J.; Tobias, D.J.; Klein, M.L. Constant Pressure Molecular Dynamics Algorithms. *J. Chem. Phys.* **1994**, *101*, 4177–4189. [CrossRef]
57. Feller, S.E.; Zhang, Y.; Pastor, R.W.; Brooks, B.R. Constant Pressure Molecular Dynamics Simulation: The Langevin Piston Method. *J. Chem. Phys.* **1995**, *103*, 4613–4621. [CrossRef]
58. Darden, T.; York, D.M.; Pedersen, L.G. Particle Mesh Ewald: An(*N*)·log(*N*) Method for Ewald Sums in Large Systems. *J. Chem. Phys.* **1993**, *98*, 10089–10092. [CrossRef]
59. Essmann, U.; Perera, L.; Berkowitz, M.L.; Darden, T.; Lee, H.F.; Pedersen, L.G. A Smooth Particle Mesh Ewald Method. *J. Chem. Phys.* **1995**, *103*, 8577–8593. [CrossRef]
60. Grubmüller, H.; Heller, H.; Windemuth, A.; Schulten, K. Generalized Verlet Algorithm for Efficient Molecular Dynamics Simulations with Long-Range Interactions. *Mol. Simul.* **1991**, *6*, 121–142. [CrossRef]
61. Tuckerman, M.E.; Berne, B.J.; Martyna, G.J. Reversible Multiple Time Scale Molecular Dynamics. *J. Chem. Phys.* **1992**, *97*, 1990–2001. [CrossRef]

62. Karathanou, K.; Lazaratos, M.; Bertalan, É.; Siemers, M.; Buzar, K.; Schertler, G.F.X.; Del Val, C.; Bondar, A.-N. A Graph-Based Approach Identifies Dynamic H-Bond Communication Networks in Spike Protein S of SARS-CoV-2. *J. Struct. Biol.* **2020**, *212*, 107617. [CrossRef]
63. Siemers, M.; Lazaratos, M.; Karathanou, K.; Guerra, F.; Brown, L.S.; Bondar, A.-N. Bridge: A Graph-Based Algorithm to Analyze Dynamic H-Bond Networks in Membrane Proteins. *J. Chem. Theory Comput.* **2019**, *15*, 6781–6798. [CrossRef]
64. Siemers, M.; Bondar, A.-N. Interactive Interface for Graph-Based Analyses of Dynamic H-Bond Networks: Application to Spike Protein S. *J. Chem. Inf. Model.* **2021**, *61*, 2998–3014. [CrossRef]
65. Humphrey, W.; Dalke, A.; Schulten, K. VMD: Visual Molecular Dynamics. *J. Mol. Graph.* **1996**, *14*, 33–38. [CrossRef]
66. Karathanou, K. Graph-Based Algorithm for Common Topologies of Dynamic Lipid Clusters. *Mendeley Data* **2022**, V2. [CrossRef]
67. Guixà-González, R.; Giorgino, T.; Ramírez-Anguita, J.M.; Carrió-Gaspar, P.; Martinez-Seara, H.; Hansen, T.V.; Selent, J. MEMB-PLUGIN: Studying Membrane Complexity in VMD. *Comput. Appl. Biosci.* **2014**, *30*, 1478–1480. [CrossRef]
68. Shahane, G.; Ding, W.; Palaiokostas, M.; Orsi, M. Physical Properties of Model Biological Lipid Bilayers: Insights from All-Atom Molecular Dynamics Simulations. *J. Mol. Model.* **2019**, *25*, 76. [CrossRef]
69. Pan, J.; Cheng, X.; Monticelli, L.; Katsaras, J.; Kučerka, N.; Tieleman, D.P.; Katsaras, J. The Molecular Structure of a Phosphatidylserine Bilayer Determined by Scattering and Molecular Dynamics Simulations. *Soft Matter* **2014**, *10*, 3716. [CrossRef]
70. Skjevik, Å.A.; Madej, B.D.; Dickson, C.J.; Lin, C.P.; Teigen, K.; Walker, R.C.; Gould, I.R. Simulation of Lipid Bilayer Self-Assembly Using All-Atom Lipid Force Fields. *Phys. Chem. Chem. Phys.* **2016**, *18*, 10573–10584. [CrossRef]
71. Róg, T.; Pasenkiewicz-Gierula, M. Cholesterol Effects on the Phospholipid Condensation and Packing in the Bilayer: A Molecular Simulation Study. *FEBS Lett.* **2001**, *502*, 68–71. [CrossRef]
72. Venable, R.M.; Luo, Y.; Gawrisch, K.; Roux, B.; Pastor, R.W. Simulations of Anionic Lipid Membranes: Development of Interaction-Specific Ion Parameters and Validation Using NMR Data. *J. Phys. Chem. B* **2013**, *117*, 10183–10192. [CrossRef]
73. Hung, W.-C.; Lee, M.-T.; Chen, F.-Y.; Huang, H.W. The Condensing Effect of Cholesterol in Lipid Bilayers. *Biophys. J.* **2007**, *92*, 3960–3967. [CrossRef]
74. Alwarawrah, M.; Dai, J.S.; Huang, J. A Molecular View of the Cholesterol Condensing Effect in DOPC Lipid Bilayers. *J. Phys. Chem. B* **2010**, *114*, 7516–7523. [CrossRef]
75. Doktorova, M.; Katsaras, J.; Kingston, R.L.; Khelashvili, G.; Cuendet, M.A.; Wen, Y.; Feigenson, G.W.; Vogt, V.M.; Dick, R.P. Cholesterol Promotes Protein Binding by Affecting Membrane Electrostatics and Solvation Properties. *Biophys. J.* **2017**, *113*, 2004–2015. [CrossRef]
76. Bandara, A.; Panahi, A.; Pantelopulos, G.A.; Straub, J.E. Exploring the Structure and Stability of Cholesterol Dimer Formation in Multicomponent Lipid Bilayers. *J. Comput. Chem.* **2016**, *38*, 1479–1488. [CrossRef]

Manuscript in preparation

# Fluctuating hydrogen bond networks couple protonation, lipid interactions, and conformational dynamics of the Hv1 ion channel

Honey Jain[1,2] , Michalis Lazaratos[1], Peter Pohl[3], Ana-Nicoleta Bondar[1,2,4,*,#]

[1]Freie Universität Berlin, Department of Physics, Theoretical Molecular Biophysics, Arnimallee 14, D-14195 Berlin, Germany

[2]University of Bucharest, Faculty of Physics, Atomiștilor 405, Măgurele 077125, Romania

[3]Institute of Biophysics, Johannes Kepler University, Gruberstraße 40, 4020 Linz, Austria

[4]Forschungszentrum Jülich, Institute of Computational Biomedicine, IAS-5/INM-9, Wilhelm-Johnen Straße, 5428 Jülich, Germany

*Correspondence to nbondar@fizica.unibuc.ro, a.bondar@fz-juelich.de

#Current affiliations: University of Bucharest and Forschungszentrum Jülich

# Abstract

Hv1, a human voltage gated proton channel, aids highly metabolically active cancer cells to dispose of excess acid from their intracellular environment to the negatively charged extracellular environment. Protons may transiently bind to bulk exposed negatively charged protein sidechains or lipid headgroups at lipid membrane interfaces and facilitate the proton transfer along and across the cells. Using a graph-based approach, we investigate dynamic water mediated lipid-protein hydrogen bonded networks at Hv1-lipid membrane interfaces relevant to proton binding. The protocol described here identifies the most frequent hydrogen bonded paths between the protein sidechains. We identify and characterize the dynamic H-bond network of Hv1 embedded in 5 different lipid bilayers and with different protonation states of the titratable protein sidechains. We find that anionic lipids can participate in the water-mediated H-bond network of Hv1 and form extensive H-bond networks on the membrane interface. We further identify frequently sampled water-mediated Hv1-lipid H-bonded clusters that might serve as putative proton antennae.


# Introduction

Mammalian voltage-gated proton channel Hv are involved in the control of intracellular pH. They are expressed in various tissues, such as the brain, lung, sperm, and skeletal muscle, and a number of blood cells. The Hv1 channel, initially denoted as Voltage-sensor-domain-only protein (VSOP), is implicated in key physiological processes such as control of intracellular pH in neurons and in phagocytes during the respiratory burst, and in human disease –Hv1 has been linked to a worsening of tissue damage during ischemia, and to faster tumorigenesis.[1,2] The importance of Hv1 for human physiology and disease make Hv1 a major target for developing therapies and a potential bio-marker for cancer.[3,4] Description of the mechanisms used by Hv1 to collect protons from the bulk and direct them towards the interior of distinct cell membranes could guide and inform the design of drugs with

desired Hv1 binding properties. To this aim, here we conducted an extensive set of atomistic simulations of Hv1 in hydrated membranes with different lipid composition, and implemented a graph-based protocol to characterize dynamic hydrogen(H)-bond networks that could be used by Hv1 to collect and guide protons in cell membranes.

A peculiar aspect of Hv1 is that it lacks a classic ion channel domain –as the alternative nomenclature suggests, Hv1 uses the same protein domain for voltage sensing and proton permeation.[5] R201, R204, and R207 (mouse Hv1 numbering, *m*HV1) (Figure 1B) are the essential structural elements of voltage gating. In the resting, closed state of Hv1, these three gating Arg groups salt-bridge to D108 and D170.[6,7] During activation of the channel, structural changes occur in two stages: First, R201 reorients relative to F146, R204 reorients to interact with D108, and R207, with D170. Then, in the second step, movement of helix S4 associates with reorientations of R201 and R204 towards the extracellular side, and formation of salt bridge pairs R201-D119, R204-E192/E115, and R207-D108.[7]

The carboxylic groups that interact with the gating Arg in the resting state of the channel are important for function: D108 (D112 in human Hv1, *h*HV1) is the carboxylic group that makes Hv1 selective for protons,[8] as its mutation to Ala,[8,9] Phe, Lys, His, Asn, or Ser[9] makes Hv1 permeable to anions, and its mutation to Val[8] or Ile[10] makes Hv1 unfunctional; by contrast, D108E remains proton selective[8,11] D170 is known to be a binding site for Hv1 inhibitors[12–14] and mutating it to Ala causes the opening of the channel at 0 mV.[15] Relatively close to the extracellular side, H136 is required for the binding of $Zn^{2+}$ which inhibits hHv1.[16] A hydrophobic cluster composed of denoted as the hydrophobic gasket (Figure 2B) blocks the flow of water and ion when the channel is closed.[17]

The inner region of Hv1 contains a number of carboxylic and His groups (Figure 1B) whose mutation impacts the voltage threshold needed to elicit proton current, and the binding of inhibitors. Relative to the wild-type channel, the voltage threshold at which proton current could be detected was higher when, close to the extracellular side of the channel, D119 or E115 were mutated to Ala,[9] D108 to Ala, Asn, Phe, Ser, Lys, or His,[8,9] D181A,[8]

or D181 to Asn, Met or Val.[8] By contrast, the voltage threshold for detecting proton current decreased when carboxylic groups closer to the cytoplasmic side, D170, D149 (E153 in hHv1), E167 were mutated to Ala;[9] similarly, a decrease in the voltage threshold was observed for H95A.[9] The effect of mutations on the binding of inhibitors differs somewhat on the inhibitor that was probed – for example, D181A binds inhibitors known as HIFs (Hv1 Inhibitor Flexibles),[12,13] but not hanatoxin,[18] whereas E167Q and D170E have reduced HIF inhibition.[12,13]

With variations in pH, the sidechains of titratable amino acids change their protonation status, which in turn substantially regulates the voltage-gated proton channel Hv1.[19–21] The pH- and ΔpH-dependent gating of the human Hv1 channel was investigated using constant pH molecular dynamics simulations under symmetrical and asymmetrical pH circumstances.[19] Amino acids near the extracellular entrance of the channel are involved in Hv1 activation as the outer pH rises, extending the network of interactions from the external solution down to the hydrophobic gap. In contrast, amino acids near the channel's cytoplasmic entry play a role in activation when the inner pH drops and in a network of interactions that extends from the cytoplasm all the way up to the hydrophobic gap.[19]

At the cytoplasmic side, the long helix contains six carboxylic groups whose functional role is unclear. This extended helix from the membrane into the cytoplasm creates a dimeric interface and forms a coiled coil region that induces cooperative gating of the dimer[22–24] and mediates thermosensitivity of the channel.[25] In the crystal structure of *Mus musculus* Hv1 chimera (PDB ID: 3WKV), this C-terminal coiled coil region is replaced by the GCN4 leucine-zipper transcriptional activator from *S. cerevisiae* to increase the thermostability of the channel.[16] Conserved residues of the coiled coil domain present in heptad repeats stabilize the dimer formation by hydrophobic interactions, salt bridges, disulfide bonds, and hydrogen bonds.[24] Multiple sequence alignment of the cytoplasmic coiled coil region shows conserved carboxylates E221, E235, and E237 whose functional role remains to be explored (Figure S34). Truncating of the C-terminal coiled coil region affects the localization of Hv1.[26]

At the interface with the lipid bilayer, Hv1 has several Arg, Lys, and Trp sidechains that could anchor Hv1 to membranes (Figure 2A). Potential lipid anchors of Hv1 include previously reported significant residues in Hv1 function - R96, K121 and W203. Mutation of R96 to Ala decreases whereas K121 to Ala increases the voltage threshold for detecting the proton currents.[9] W203 (207 in hHv1) is highly conserved along with the voltage sensing Arginines in Hv1. Mutagenesis studies show that W203 is important for four unique properties of Hv1: proton selectivity, slow channel opening, highly temperature-dependent gating kinetics, and $\Delta$pH-dependent gating.[20] Though little is known about the coupling between Hv1 and the lipid bilayer that surrounds it, voltage-gated ion channels are known to couple to the lipid bilayer. For KvAP, a voltage gated potassium channel, variation in the lipid composition of a bilayer switches the voltage sensing domains between open and close state conformations without any change in the transmembrane voltage.[27,28] Voltage sensors on potassium channels embedded in lipid bilayers become immobile when the lipid phospho-head groups are removed[28–31] whereas removal of the choline group leads to apparent activation of the channels.[28,29,31] The Arginies on the S4 helix of the voltage sensing domains have been suggested to interact with the lipids providing a stabilizing effect for either the open or closed state of the channel in the specific type of lipid bilayer.[28,30]

The discussion summarized above on how mutation of specific sidechains impact the function of Hv1 suggests that the ion channel is robust: except for D108, mutation of any of the other carboxylic sidechains to a non-titratable sidechain impacts, but does not abolish proton conductance. Likewise, Hv1 can function in lipid bilayers of various composition –from the widely different lipid composition of the tissues in which it is expressed, to membranes that are used for reconstitution in the lab, including the *Escherichia coli* membrane. Recent studies report Hv1 as a novel target for neuroprotection since it is upregulated in parkinsonian mice and mediates the generation of pro-inflammatory cytokines by microglia.[32] The genetic deletion of Hv1 suppresses tumor formation.[33]

The pH variation leading to protonation of titratable amino acids of Hv1 has been linked

to the extension of the network of interactions formed on the extracellular or cytoplasmic site.[19] The robustness of Hv1's functioning and its gating mechanisms have been investigated, however more insights are still needed to understand how Hv1 interacts with lipids and how protonation of specific titratable side chains affects the dynamics of its H-bonds and its conformation. Here, we use a graph-theory based procedure for investigating Hv1's protonation and lipid-coupled hydrogen bond dynamics in various lipid bilayers. Instead of adopting the shortest path, the protocol described here characterizes the most frequent hydrogen-bonded path between the titratable side chains, enriching the sampling of H-bond paths. The H-bond paths identified could be used by Hv1 to facilitate proton transfer along and across the cell membranes.

Mammalian Hv1 is a dimer, but each monomer has its own proton-conduction path and can function on its own.[26] Okumura group suggested that in Hv1 dimers VSDs interact via S4 segments[16,34] whereas Li et al. and Mony et al.[26,35] proposed the S1-S4 interactions between dimers. For simplicity, and since the dimer interface remains unclear,[16,26,34,35] all computations were performed on a single copy of Hv1.

# Methods

*Starting protein coordinates, protonations, and lipid membrane composition.* Protein coordinates were taken from the crystal structure of *m*Hv1 (PDB ID:3WKV).[16] Missing internal loops were generated using Modeller[36] (Figure S1). The structure of Hv1 was oriented along the membrane normal using the OPM server[37] and placed in the membrane with CHARMM-GUI.[38–40] We used 0.15M neutralizing KCl , for a total of ∼96K to ∼107K atoms. We prepared 14 independent simulations distinguished by the protonation of selected titratable sidechains, and by the composition of the lipid bilayer, as follows (Table 1).

To probe the dynamics of Hv1 in bilayers with different lipid composition, we used standard protonations for all titratable protein sidechains, i.e., we considered all Asp/Glu as

negatively charged, Lys and Arg, positively charged, and all His neutral and described as Nd1 tautomers. We placed Hv1 with standard protonation in membranes composed of *i)* 1-palmitoyl-2-oleoylphosphatidylcholine (POPC) lipids; *ii)* 1-palmitoyl-2-oleoyl-sn-glycero-3-phosphoethanolamine (POPE) lipids; *iii)* 5:1 POPE:POPG 1-palmitoyl-2-oleoyl-sn-glycero-3-phosphatidylglycerol; *iv)* 1-palmitoyl-2-oleoyl-sn-glycero-3-phospho-L-serine (POPS) lipids; *v)* the *E. coli* membrane model Top6 from ref.[41]

To probe the impact of protonation on the dynamics of Hv1, we used a hydrated POPC lipid bilayer to perform independent simulations in which *i)* neutral H95 was described as an N$\epsilon$2 tautomer; *ii)* H136 was protonated at both the N$\delta$1 and N$\epsilon$2 atoms, *i.e.*, it has a net charge of +1e; *iii)* Seven independent simulations in which one of the following carboxylates was protonated - E115, D108, D119, D149, E167, D170, D181 (Table 1, Figure S2).

Table 1: Summary of simulations performed. 'Protonation' indicates whether all titratable sidechains were considered in their standard protonation or, when a sidechain has non-standard protonation, the identity of that sidechain.

| Sim | Lipid bilayer / #lipids | Protonation | #Atoms | Length (ns) | RMSD (Å) [a)] |
|---|---|---|---|---|---|
| Sim1 | POPC / 218 | standard | 107348 | 500 | 2.0 ± 0.2 |
| Sim2 | | D119 | 107291 | 300 | 2.8 ± 0.3 |
| Sim3 | | E167 | 107297 | 300 | 2.4 ± 0.3 |
| Sim4 | | D108 | 107295 | 300 | 2.9 ± 0.3 |
| Sim5 | | E115 | 107267 | 300 | 2.5 ± 0.5 |
| Sim6 | | D181 | 107247 | 300 | 2.4 ± 0.4 |
| Sim7 | | D170 | 107396 | 300 | 2.8 ± 0.2 |
| Sim8 | | D149 | 107286 | 300 | 2.8 ± 0.3 |
| Sim9 | | H95 | 107331 | 300 | 1.8 ± 0.3 |
| Sim10 | | H136 | 107309 | 300 | 2.4 ± 0.3 |
| Sim11 | POPE / 218 | standard | 96095 | 300 | 3.2 ± 0.4 |
| Sim12 | 5:1 POPE/POPG (180/36) | standard | 95918 | 280 | 3.0 ± 0.2 |
| Sim13 | Top6[b)] | standard | 99141 | 300 | 3.0 ± 0.3 |
| Sim14 | POPS /218 | standard | 97775 | 300 | 2.9 ± 0.3 |

[a)] We report the C$\alpha$ RMSD and the standard deviation are computed from the last 200ns of each simulation. [b)] Top6 consists of 28 POPE lipids, 16 YOPE, 20 PYPG, 28 QMPE, 104 PMPE, and 22 PMPG lipids.

*Protocol for MD simulations.* We used CHARMM36 for the protein, lipids, and ions,[42–47] and the TIP3P water model.[48] All simulations were performed with NAMD version 2.13.[49,50] We used the smooth particle mesh Ewald summation[51,52] for Coulomb interactions, and a

switch function between 10 Å and 12 Å for real space interactions. Equilibration for ∼1 ns was performed according to the standard CHARMM-GUI protocol. All production runs were performed in the $NPT$ ensemble (constant number of particles $N$, constant pressure $P$ = 1bar, and constant temperature $T = 310.15$ K) using a Langevin dynamics scheme[53,54] with an oscillation period of 200 fs, a damping time scale of 100 fs, and a damping coefficient of 5 $ps^{-1}$. Covalent bonds to H atoms were fixed using SHAKE.[55] Equilibration and the first 1 ns of the production runs were performed with an integration step of 1 fs. All remaining production runs were performed with a multiple time step integration scheme[56,57] with integration steps 1 fs for the bonded interactions, 2 fs for short-range nonbonded forces, and 4 fs for long-range electrostatics. Coordinates were saved every 10 ps.

*Cα Root-mean-squared distances (RMSD) profiles.* Time series of the Cα RMSD profiles were monitored separately for the entire protein, for the transmembrane helical region and for the loops and termini of Hv1 (Figure S3). Average RMSD values were computed from the last 200 ns of each simulation.

*H-bond criteria, H-bond occupancy, H-bond graphs, local H-bond clusters, and H-bond paths.* We used standard distance and angle criteria for H-bonding, whereby two groups were considered as H-bonded if the distance between the donor and acceptor heavy atoms was within 3.5 Å, and the H-bond angle, within $60^{o}$. The *occupancy of an H-bond* gives the percentage of the coordinate sets used for analyses during which the H-bond criteria are met.

*An H-bond graph* consists of nodes, which here are the protein H-bonding groups, and edges, which are direct or water-mediated H-bonds between protein sidechains. *The local H-bond cluster* or local network of a specific protein sidechain consists of the nodes and edges that connect to that specific group of interest. *An H-bond path* between two nodes (protein groups) of interest consists of the nodes and edges that inter-connect those two protein groups via intermediate H-bonds. The *Joint Occupancy (JO) of an H-bond path* is given by the percentage of the coordinate sets used for analyses during which all intermediate

path segments meet the H-bond criteria at the same moment of time.

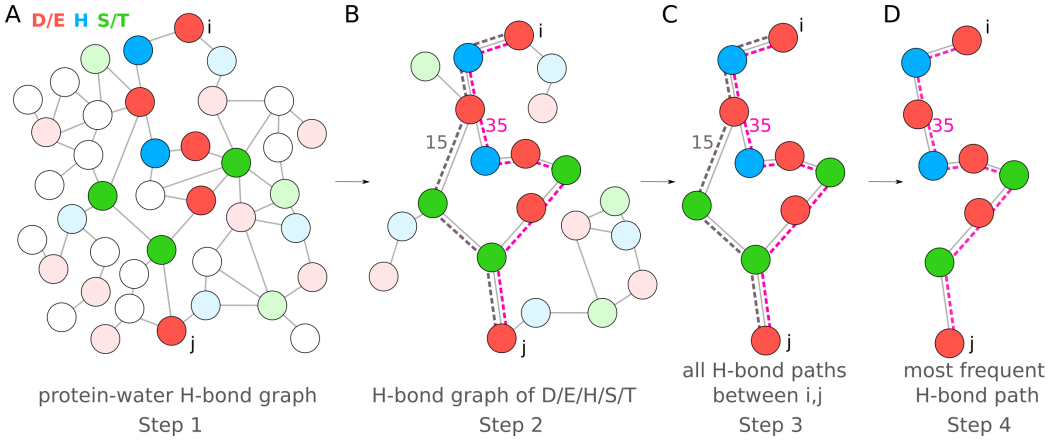


Scheme 1: Schematic illustration of how H-bond paths between Asp, Glu, and His sidechains are extracted from the protein-water H-bond graph. (A) Complete protein-water H-bond graphs (Step 1). (B) Extracted graph of Asp, Glu, His, Ser, Thr (Step 2). (C) Computation of all H-bond paths and joint occupancies of these paths between carboxylates/histidines of interest (Step 3). (D) Most frequent H-bond path between carboxylates and/or histidines in MD simulations. Here, each circle represents a H-bonding group (Step 4). An edge represents a H-bond. Asp/Glu, His, Ser/Thr are shown as red, blue and green circles. Amino-acid residues in the selected paths are shown as bright colors whereas the faded circles represent the remaining amino acid residues in the extracted H-bond graph.

*Implementation of H-bond path calculations for titratable protein sidechains.* To identify H-bond paths that inter-connect Asp, Glu and His sidechains via water molecules and protein sidechains that could participate in proton transfer, we proceeded as follows (Scheme 1). First, we computed protein-water H-bond graphs from the last 200ns of each simulation trajectory; we considered water bridges of up to three H-bonded waters. In the second step, we extract the H-bond graph of Asp, Glu, His, Ser, and Thr. Then in the third step, for all unique pairs of Asp, Glu, and His side chains, we use the depth-first search algorithm from the NetworkX package[58] to compute all the H-bond paths mediated via up to three water molecules. In the fourth step, we compute the JO value of each path, and rank the paths according to their JO. We then report the most frequent paths between the carboxylates and/or histidines of interest.

*Protocol for H-bond and H-bond path calculations.* All H-bond graph computations were

performed with Bridge.[59,60] Local H-bond clusters and H-bond paths were extracted from the H-bond graphs using Connected Component Analyses[61] in Bridge. Unless specified otherwise, water-mediated bridges between protein sidechains include up to three H-bonded water molecules; for clarity, we include in data analyses only H-bonds with occupancies higher than 30%. We only report H-bond paths with a joint occupancy greater than 5%.

# Results and discussion

We report the results from 14 independent simulations distinguished by the composition of the lipid bilayer and protonation of selected titratable sidechains with a total sampling time of 4.38 µs. Twelve of our simulations are 300 ns, one is 500 ns and one is 280 ns long (Table 1). Structure of Hv1 models becomes stable in all simulations with C$\alpha$ RMSD of TM helices within 3.5 Å relative to starting crystal structure with resolution of 3.45 Å (Figure S3).[16] The modeled loops and non-helical regions are dynamic and show C$\alpha$ RMSD values upto 45 Å. In 5:1 POPE:POPG and Top6 bilayers, the cytoplasmic part of S4 helix orients towards the lipid headgroups, resulting in high RMSD values for non-helical regions of Hv1.

We report the most frequent H-bond paths between carboxylates of Hv1 sampled during the MD simulations. The protocol used here takes into account all the H-bond paths rather than only the shortest path i.e. the H-bond paths with minimum number of nodes (Figure 1A). This enriches the sampling of H-bond paths for calculation of the most frequent H-bond paths.

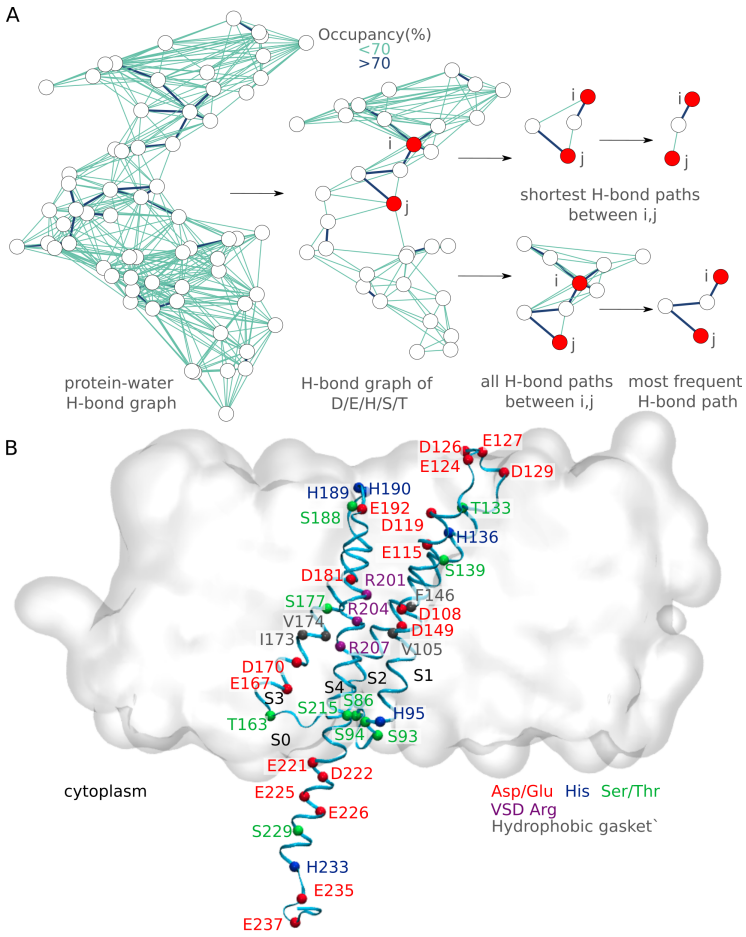


Figure 1: Protocol for finding most frequent paths of Hv1 and architecture of Hv1. (A) Graphical representation showing comparison between shortest path approach and our protocol to find the most frequent H-bond paths between carboxylates of Hv1. (B) Cut-away view of Hv1 in membrane. The membrane Hv1 is shown schematically as a surface colored grey, the protein is shown as thin cyan ribbons, and the C$\alpha$ atoms of selected protein groups are shown as small spheres.

*A dynamic H-bond network inter-connects acidic and histidine sidechains of Hv1.* As a reference simulation, we consider Hv1 with standard protonation of all titratable sidechains and embedded in a hydrated POPC lipid membrane (Table 1). From H-bond path calculations for this simulation, we identified a dynamic network that contains carboxylic and histidine sidechains (Figure 2C). Though extensive, this internal H-bond network is interrupted at approximately the center of the membrane plane, where D108 and D170 connect to either side of the membrane but not to each other: D108 connects to the extracellular side

via water-mediated paths that include seven other carboxylic and His sidechains, whereas D170 connects to E167 at the cytoplasmic side (Figures 2C,D,E). The interruption of the internal H-bond network of Hv1 is likely due to a cluster of hydrophobic side chains (V174, I173, V105, and F146) known as the hydrophobic gasket (Figure 2B).[17]

To further analyze the interruption of the H-bond network, we calculate the minimal distances between the carboxylates D108, D181, and D170 and their respective interaction partners. We find that D108 maintains a stable salt bridge interaction with R201, whereas D181 toggles between R201 and R204 (Figure S4). D170, on the cytoplasmic side, prefers R207 as its interaction partner for most of the trajectory (Figure S4). These salt bridge interactions are consistent with earlier research.[6,7]

We report the most frequent water mediated H-bond paths formed between acidic and histidine sidechains (Figure 2D,E, Table S1). On the extracellular side the most frequent H-bond paths between titratable sidechains extend from D108 to E115, H136, D119, E192 via D181 with joint occupancy in the range of 7-27% and mediated via 1,2 or 3 water molecules on an average (Figure 2E). On the cytoplasmic side, D170 and E167 form the most frequent H-bond path with joint occupancy of 91% and mediated by an average of 2 waters (Figure 2E).

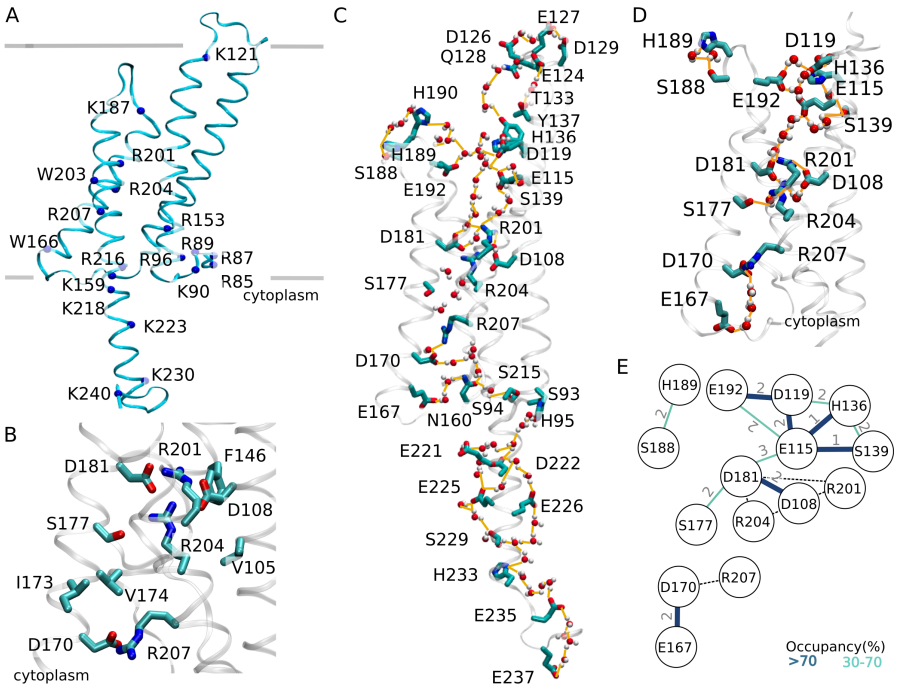


Figure 2: H-bonding groups, hydrophobic gasket and H-bond network of Hv1. (A) Arg, Lys and Trp sidechains that could anchor to lipid membranes and Arginines forming the Voltage sensing domain(VSD). (B) Hv1 groups in and around the hydrophobic gasket. (C) Close view of the H-bond network between selected protein side chains and water molecules. (D) Close view of the internal H-bond network and interruption at D108-D170. The most frequent water mediated H-bond paths connecting the hydrophobic core to the extracellular and cytoplasmic side are shown here. (E) Graphs of the H-bond networks computed from simulations illustrated in Panel D. The numbers on edges represent the average number of waters per water wire of the graph. The molecular graphics were prepared with Visual Molecular Dynamics (VMD)[62] based on a coordinate snapshot from the simulation of Hv1 with standard protonation and embedded in a hydrated POPC lipid membrane environment. The protein is shown as thin cyan (Panel A) and white (Panel B, C, D, E) ribbons, the selected protein groups are shown as licorice and water molecules are shown as CPK representation.

*Uncharged polar amino acid residues serve as linkers connecting the internal H-bond network to cytoplasmic and extracellular sides.* Several Ser, Thr, Asn and Gln represent in the proximity of carboxylates and histidines that form H-bond network in Hv1. We observe that the connection between internal and cytoplasmic H-bond network is mediated by N160, N210 or S215 whereas the extracellular carboxylates and internal H-bond network are connected by T133 or Q128 (Figure 3, S5). We call these H-bonding groups "linkers" (Figure 3). The extracellular and cytoplasmic H-bond networks are formed by amino acid residues located

in the highly dynamic part of Hv1 however N210 and S215 are highly conserved. N210C or N210A blocks proton permeation whereas N210R is proton permeable.[9,63,64] Mutation of N210 to Lys decreased the voltage threshold for detection of proton currents whereas Arg had the opposite effect.[9,64] S215, located at the beginning of the cytoplasmic helix, has been reported to interact with Hv1 inhibitor and its mutation to Ala showed reduced inhibitory effect.[14] Thus we can suggest that the linker groups N210 and S215 play a role in determining the connectivity between the internal H-bond network and extracellular and cytoplasmic networks.

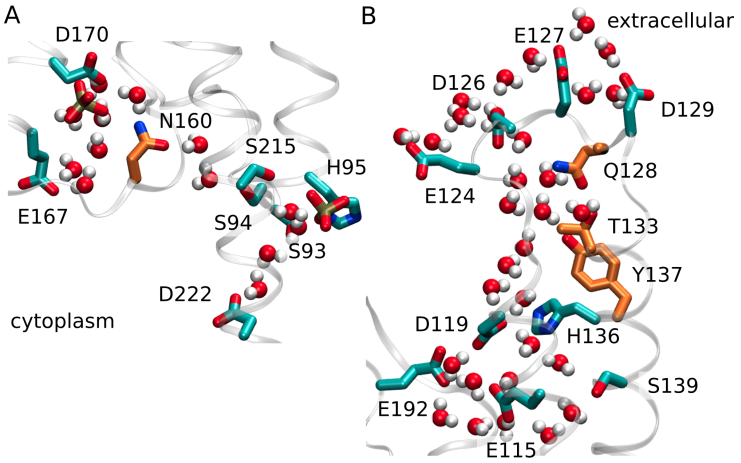


Figure 3: Linkers between internal and cytoplasmic and extracellular H-bond networks of Hv1. Molecular graphics showing (A) N160, N210 and S215 connecting D170 and E167 from internal H-bond network to the cytoplasmic H-bond network via water mediated H-bonds and (B) Q128 or T133 connecting D119 and H136 from internal H-bond network to D126 or E124 of the extracellular H-bond network via water mediated H-bonds. The linkers and selected H-bonding groups are shown in orange and cyan licorice representation respectively. The molecular graphics were prepared with Visual Molecular Dynamics (VMD)[62] based on a coordinate snapshot from the simulation of Hv1 with standard protonation and embedded in a hydrated POPC lipid membrane environment.

*Protonation of acidic and histidine sidechains affects the internal H-bond dynamics of Hv1.* To study the effect of protonation state on the H-bond network dynamics of Hv1, we analyzed 10 independent simulations with different protonation states of carboxylates and histidines present in the most frequent H-bond paths (Figure 2D,E) and of significance in the proton conduction pathway as described in the literature. We observe that waterwire span

across Hv1 depends on the protonation state of the carboxylates and histidines forming the most frequent paths (Figures 4,5). A continuous H-bonded waterwire between D/E/H/S/T spans the transmembrane region only in simulations where D108 and D181 are protonated (Figures 4B,4C,5). This continuous water mediated H-bond network is interrupted at two sites: (1) at E115 when carboxylates on the extracellular side D119 or E115 are protonated (Figure 4D,E); and (2) at D108/D181 in standard protonation state and when carboxylates on the cytoplasmic side D170, E167 or D149 are protonated (Figure 4F-H). Disruption of waterwire in the resting state of Hv1 at only two specific sites suggests a significant role of carboxylates D108, D181 and E115 in mediating proton transfer pathway. H136 no longer remains part of the H-bond network on double protonation (Figure 5J) whereas the cytoplasmic H-bond network is lost when H95 is epsilon protonated (Figure 5I). Depending on the location of the protonated amino acid residue, the cytoplasmic H-bond network cluster extends or collapses (Figures S6-S15). This cytoplasmic cluster is present when carboxylates on the cytoplasmic side below E115 are protonated whereas an interruption is observed when carboxylates at the extracellular side E115 or D119 are protonated (Figures 4, 5). The conserved graph analysis using Cgraphs software[65] shows the rearrangement of the dynamic water-mediated H-bond network depending on the protonation state of the carboxylates and histidines (Figure S16). This suggests that location of protonated amino acid residues regulates the continuity of the waterwire on a specific side of the Hv1. It aligns with the discussion of increase in outer or inner pH leading to extended H-bond network on the extracellular or intracellular side.[19] If we include all the titratable sidechains of Hv1 in H-bond network calculations, we still observe the interruption of H-bond network in simulations with standard protonation (Figure S17), protonated D119 (Figure S18), D149 (Figure S19), D170 (Figure S20), E115 (Figure S21), H95 (Figure S22) and a continuous H-bond network when D108 (Figure S23), D181 (Figure S24) are protonated. For simulations with E167 protonated (Figure S25) and H136 doubly protonated (Figure S26), we observe that R204, R207 and W203 form water mediated H-bonds with neighbouring carboxylates D108, D181,

D149 and D170 leading to a formation of continuous H-bond network. These H-bonds are usually mediated by 2-3 water molecules on an average (Figure S25-S26).

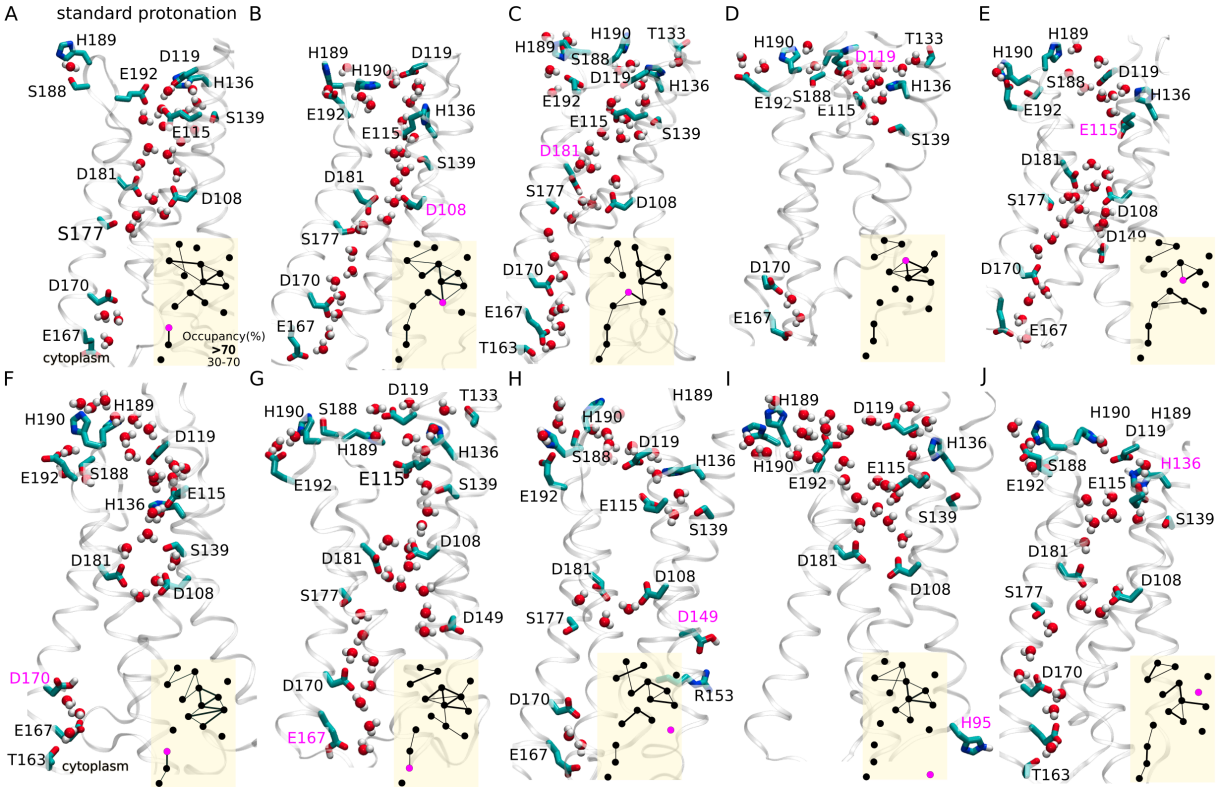


Figure 4: Protonation coupled H-bond network dynamics of Hv1. (A-J) Molecular graphics of Hv1 from simulations with standard protonation for all titratable sidechains (Panel A), with neutral D108 (Panel B), neutral D181 (Panel C), neutral D119 (Panel D), neutral E115 (Panel E), neutral D170 (Panel F), neutral E167 (Panel G), neutral D149 (Panel H), Nϵ protonated H95 (Panel I) and doubly protonated H136 (Panel J). The protein is shown as thin white ribbons, the selected protein groups are shown as licorice and water molecules are shown as CPK representation. H-bond paths shown here are mediated by water bridges with up to 3 H-bonded waters in chains. Graphs of the H-bond networks computed from simulations illustrated as insets on the bottom right of each Panel. The molecular graphics were prepared with Visual Molecular Dynamics (VMD)[62] based on a coordinate snapshot from the simulation of Hv1 embedded in a hydrated POPC lipid membrane environment.

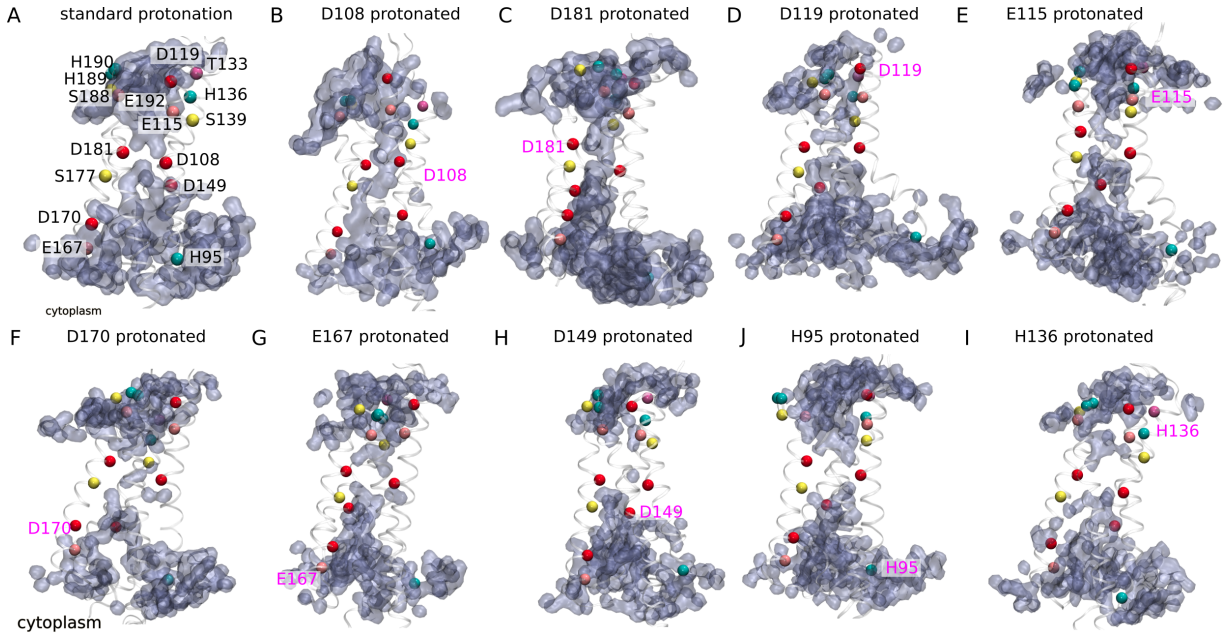


Figure 5: Water-wire span across Hv1 varies depending on the protonation state of carboxylates and histidines forming the most frequent H-bond paths. (A-J) Molecular graphics of Hv1 from simulations with standard protonation for all titratable sidechains (Panel A), with neutral D108 (Panel B), neutral D181 (Panel C), neutral D119 (Panel D), neutral E115 (Panel E), neutral D170 (Panel F), E167 (Panel G), D149 (Panel H), doubly protonated H136 (Panel I) and with N$\epsilon$ protonated H95 (Panel J). The protein is shown as thin white ribbons. The selected protein groups Asp, Glu, His, Ser, Thr are shown as red, pink, cyan, yellow and purple spheres. Water molecules are shown as iceblue QuickSurf representation. The molecular graphics were prepared with Visual Molecular Dynamics (VMD)[62] based on a coordinate snapshot from the simulation of Hv1 embedded in a hydrated POPC lipid membrane environment.

*Lipid composition influences the internal H-bond network dynamics.* We characterize internal H-bond network dynamics of Hv1 in bilayers distinguished by lipid composition (Table 1). This network is interrupted at the hydrophobic cluster surrounding D108-D170 in pure POPC, pure POPE and 5:1 POPE:POPG bilayers and at E115-D108 in *E. coli* bilayer (Figures 6, S17, S29- S32). The internal H-bond network of Hv1 may become continuous in the POPS membrane (Figures 6B,F, S28, S31). This suggests that, in POPS, helix S3 reorients relative to the remaining of Hv1, and this associates with a number of rearrangements of internal amino acid residues of the H-bond network. In all simulations with acidic lipids, titratable sidechains of Hv1 can be part of dynamic water-mediated H-bond clusters with

lipid molecules. This suggests that Hv1 sidechains and the lipid headgroups could collectively bind protons and the interface. To test this hypothesis, more advanced computations with quantum mechanics would be necessary.

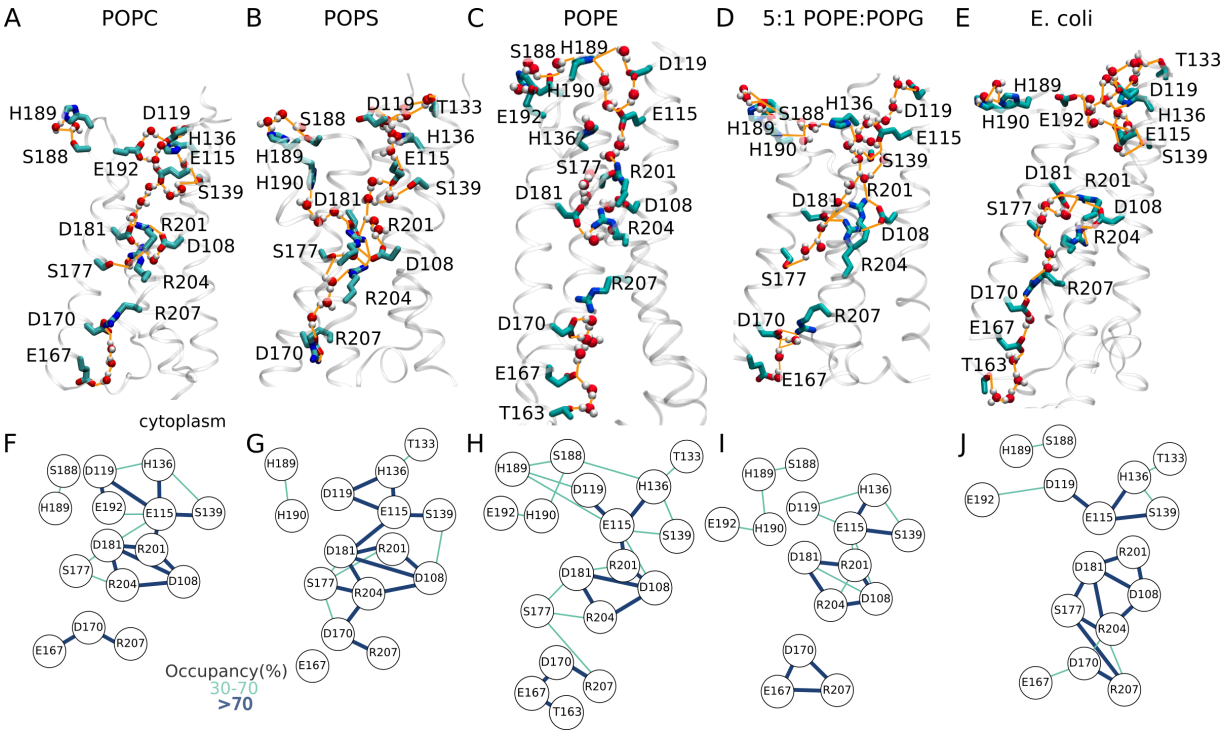


Figure 6: Illustration of the internal H-bond network of Hv1 in bilayers of distinct lipid composition. We present a molecular graphics of the H-bond network, and the corresponding graph representation of the network, for Hv1 in POPC (Panel A, E), POPS (Panel B, F), POPE( Panel C, G), 5:1 POPE:POPG (Panel D, H) and the *E. coli* membrane mode (Panel E, I).

*Acidic lipids can participate in water-mediated H-bond clusters with Hv1.* Close proximity of Hv1 sidechains to lipid headgroups indicates the possibility of formation of extended water mediated H-bond network on the extracellular and cytoplasmic sides (Figure 1C). To derive insights into how acidic lipids could participate in proton binding to Hv1, we performed atomistic simulations of membrane-embedded Hv1 with distinct compositions of the lipid membrane. At the membrane interface, POPS tend to engage in extended H-bond networks (Figure 7). POPE and POPG in 5:1 POPE:POPG and the Top6 *E. coli* membrane model have somewhat less extended H-bond networks than POPS (Figure 7). Whereas, POPC

lipids barely participate in water-mediated H-bond networks with protein sidechains (Figure 7). We further characterized the dynamic H-bond paths that can transiently connect internal titratable sidechains and lipid headgroups to the bulk using our protocol for calculation of water mediated H-bond paths. To derive clues about paths that could function as proton wires, we rank the paths according to how frequently all intermediate path segments are sampled during the independent simulations performed. We identified water-mediated H-bond clusters that contain POPS lipid headgroups and carboxylic sidechains of Hv1 (Figure 8). At the extracellular side of Hv1, an H-bond cluster extends from D108 to POPS lipid headgroups (Figure 8A). At the cytoplasmic side, there is an H-bond cluster that includes E167 and lipid headgroups, and another protein-water-lipid H-bond cluster that includes carboxylic sidechains of the S4 helix (Figure 8A).

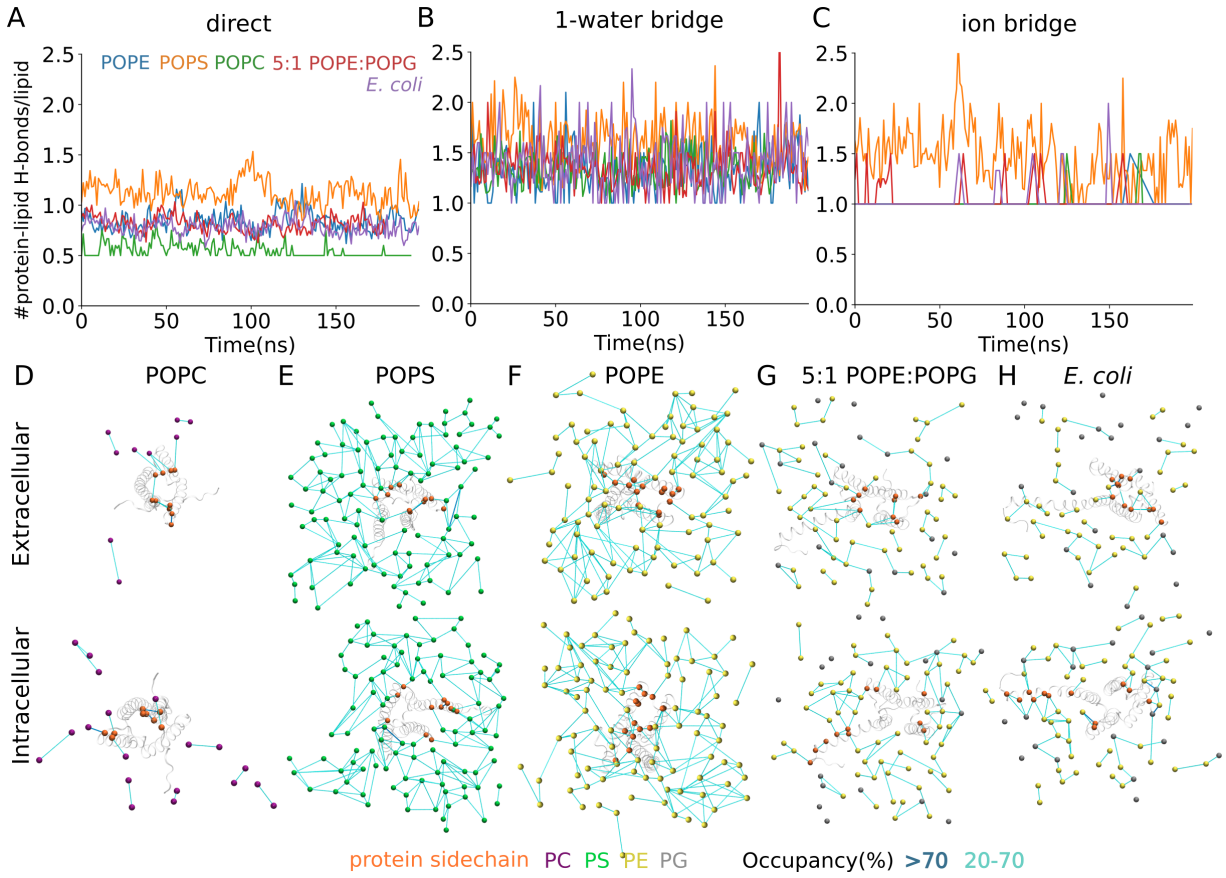


Figure 7: Water-mediated H-bond network at membrane interfaces with Hv1. (A-C) Time series of the number of direct (Panel A), one-water mediated bridges (Panel B), and potassium-ion-mediated bridges between lipid headgroups (Panel C). For clarity, coordinate sets were read each 1 ns. (D-H) Illustration of water-mediated H-bond network at membrane interfaces with Hv1. For each simulation, the top Panel shows a view from the extracellular side of Hv1, and the bottom Panel, from the cytoplasmic side. H-bond network at the interfaces of POPC (Panel D), POPS (Panel E), POPE (Panel F), 5:1 POPE:POPG (Panel G), and *E. coli* Top6 membranes (Panel H). The H-bond networks were computed using Bridge.[59,60] H-bonds with occupancy greater than 20% are shown here.

The two simulations of Hv1 embedded in bilayers that contain acidic PG-type lipids (Table 1) suggest that, similarly to the POPS membrane, PG-type lipids may be part of dynamic H-bond clusters at membrane interfaces of Hv1 (Figure 9, 10). In both the POPE:POPG and *E. coli* membranes, PG-type lipids are part of water-mediated H-bond clusters with H189, S188 and D129 at the extracellular side, and with E167, E226, H233 and S86, at the cytoplasmic side (Figure 9, 10). Likewise, both lipid membranes allow water-mediated

lipid-Hv1 H-bond clusters at the extracellular E115 site (Figure 9, 10). The finding here that E115 participates in H-bonding with water molecules and PG-type lipids is relevant for considerations of proton transfer, because E115 is thought important for proton transfer by Hv1.[1,6,7,9,66] Relative to the wild-type channel, the voltage threshold at which proton current could be detected was higher when E115 was mutated to Ala.[9]

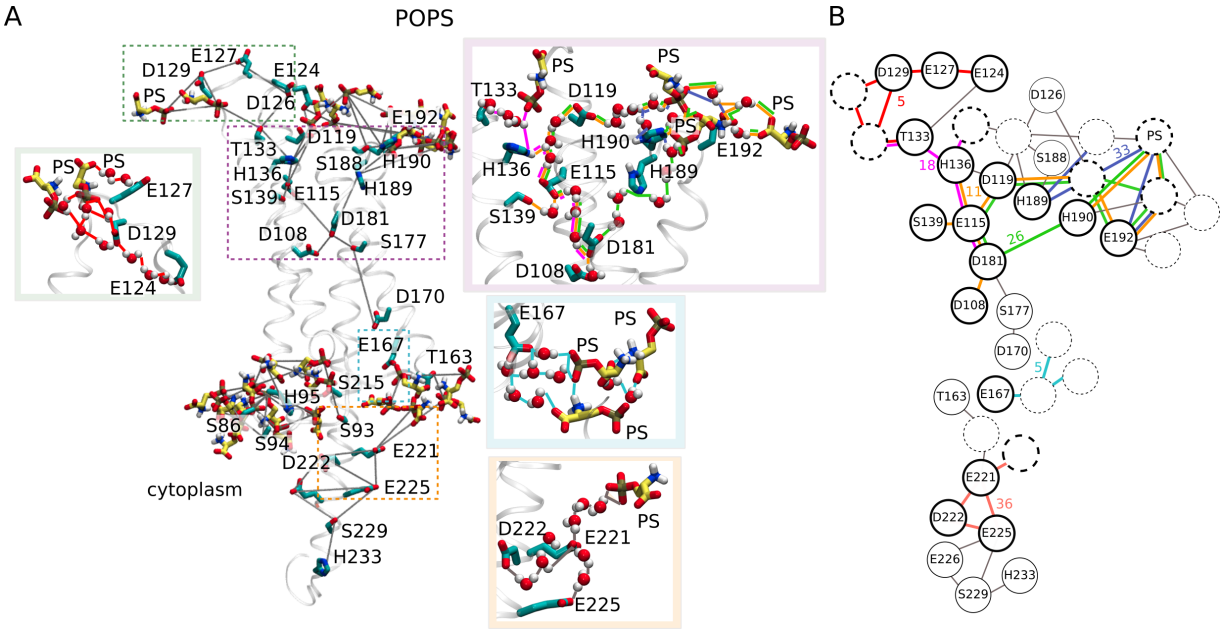


Figure 8: Water-mediated Hv1-POPS H-bond clusters. (A) Molecular graphics illustrating selected H-bond clusters at distinct sites of Hv1. (B) Schematic graph representation of the H-bond clusters shown in Panel A. For clarity, only H-bonds present during at least 30% of the time are present, and paths with minimum $JO$ value of 5%

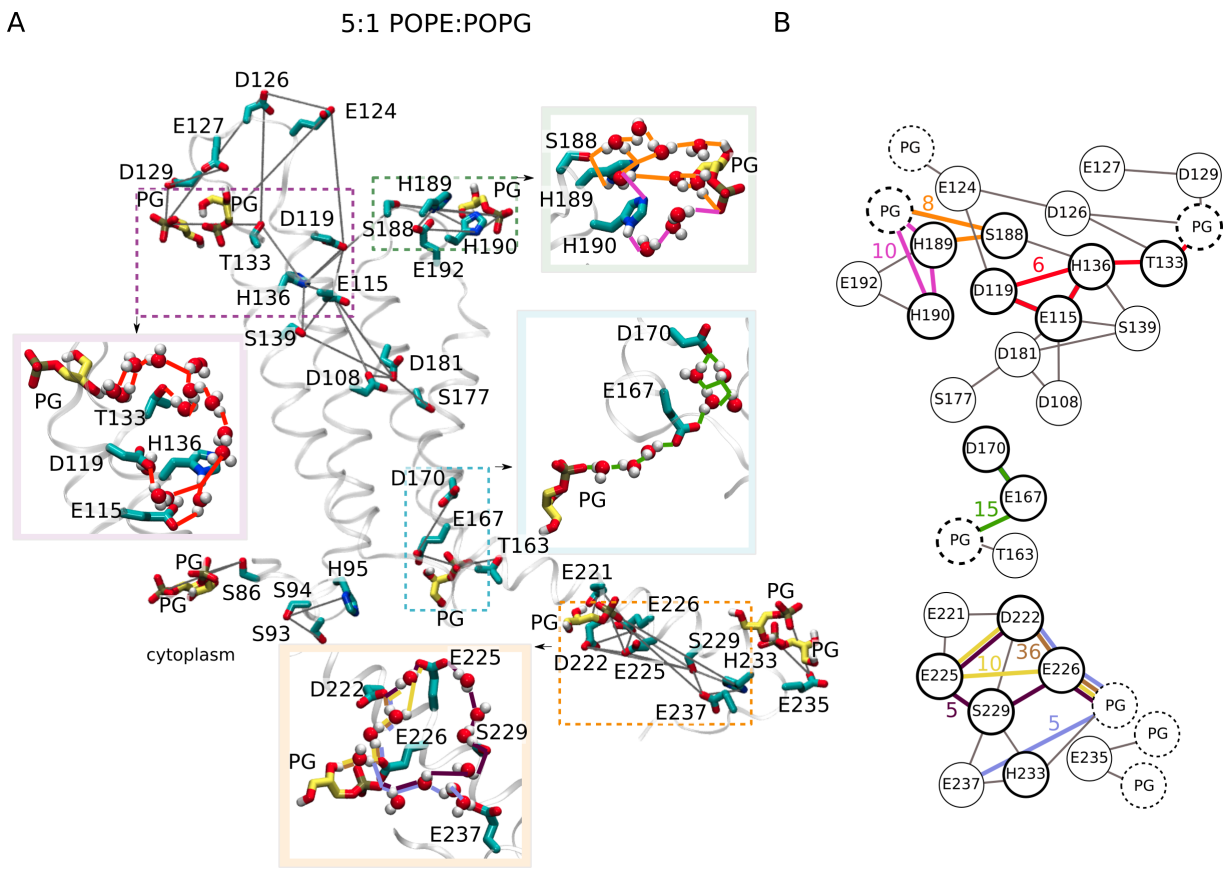


Figure 9: Water-mediated protein-lipid H-bond clusters of Hv1 in a hydrated membrane with 5:1 POPE:POPG lipids. (A) Molecular graphics illustrating selected H-bond clusters at distinct sites of Hv1. (B) Schematic graph representation of the H-bond clusters shown in Panel A.

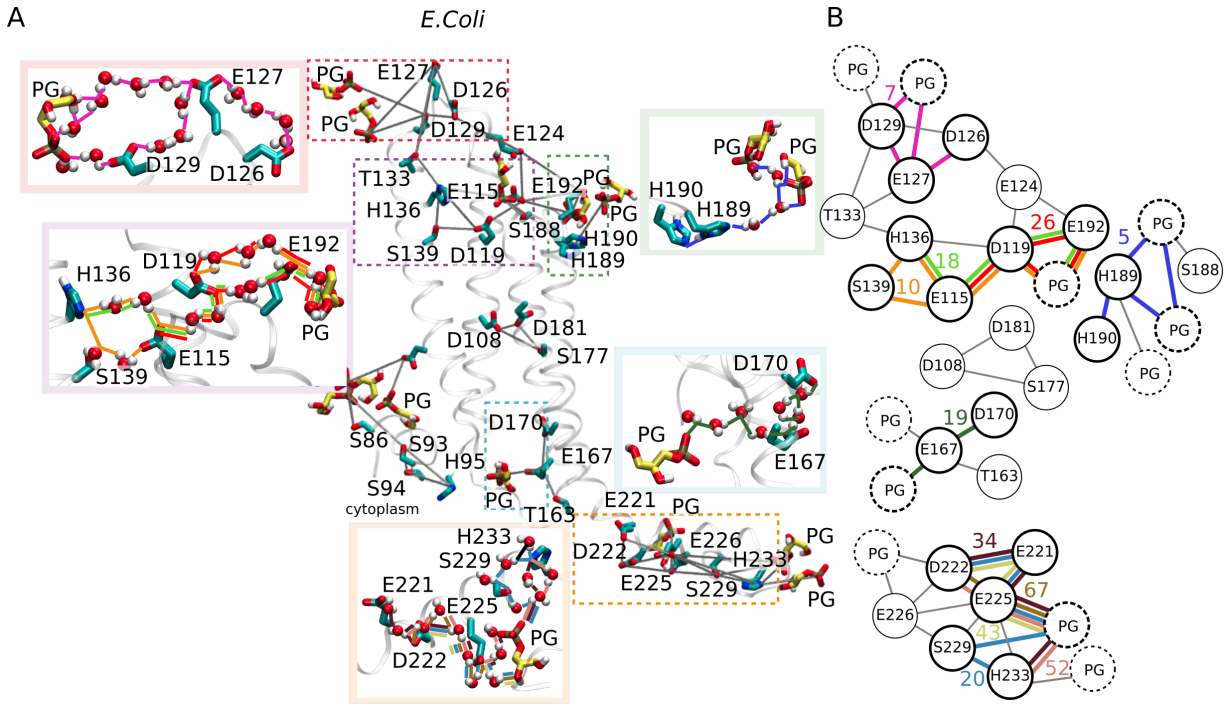


Figure 10: Water-mediated protein-lipid H-bond clusters of Hv1 in a model *E. coli* bilayer. (A) Molecular graphics illustrating selected H-bond clusters at distinct sites of Hv1. (B) Schematic graph representation of the H-bond clusters shown in Panel A.

*Lipid anchors of Hv1.* We identified amino acid residues of Hv1 that interact with lipid headgroups in nine different types of lipids: neutral POPC, zwitterionic POPE, PMPE, QMPE, YOPE, negatively charged POPS and POPG (Figure S27). In addition to the lipid-Hv1 H-bond clusters above, both the 5:1 POPE:POPG and *E. coli* membrane models allow multiple interactions between PE-type lipids and Hv1 sidechains (Figure S33). Bioinformatics analyses suggest that sidechains found here to anchor Hv1 to the membrane tend to be conserved (Figure 11), suggesting lipid-protein anchoring could be important – for example, to control the orientation of Hv1 relative to the membrane interface. K121, R96 and R216 interact with the lipid headgroups in all the Hv1 simulations with different lipid composition (Figures S35). Arginines and Lysines on the cytoplasmic side - R85, R87, K159 and K223 interact with negatively charged headgroups PS and PG (Figures S35) whereas carboxylates D119 or E115 on extracellular side interacts with the amine group of zwitterionic PE (Figure S35). K121, E115 and D119 when mutated to Ala increases the voltage thresh-

old for detection of proton current whereas R96A has an opposite effect.[9,64] However these mutagenesis studies were done using the same cell line without differentiation in the lipid composition. As the lipid anchors differ based on the nature and charge of lipid headgroups, we suggest mutagenesis analysis of these lipid anchors in lipid membranes with different lipid composition.

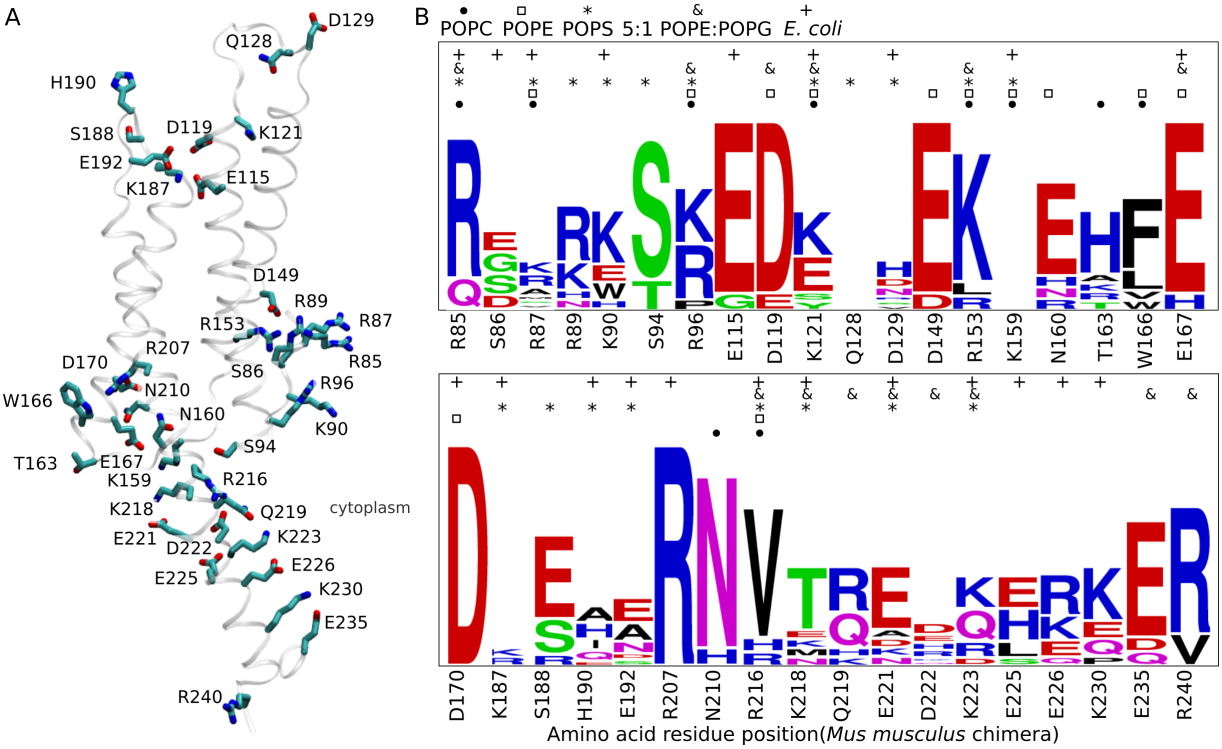


Figure 11: Conserved lipid anchors of Hv1. (A) Molecular graphics showing lipid anchors of Hv1. The protein is shown as thin white ribbons, and the protein groups that anchor to the lipid headgroups are shown as licorice. The molecular graphics were prepared with Visual Molecular Dynamics (VMD)[62] based on a coordinate snapshot from the simulation of Hv1 with standard protonation and embedded in a hydrated POPC lipid membrane environment. (B) Logos diagram for multiple sequence alignment of lipid anchors of Hv1. The height of each symbol represents the conservation of that residue in 10 different Hv1 sequences from 9 species. The Logos diagram was generated using WebLogo.[67,68]

# Conclusions

The simulations we performed were on the closed state of the channel, in the absence of external voltage. Hv1 is thought to have a complex energy landscape, with multiple con-

formations of the closed state.[64] Our atomistic simulations (Table 1) capture the impact of protonation and lipid composition on the conformational and hydrogen bond dynamics of the closed state of the Hv1 channel. Our graph-theory based protocol to identify the most frequent H-bond paths rather than the shortest H-bond paths enriches the sampling of H-bond paths and provides valuable insights to understand the functioning of Hv1 (Scheme 1, Figure 1). We identify a dynamic H-bond network that interconnects acidic and histidine sidechains of Hv1 (Figure 1). This network extends from D108 to the extracellular side and from D170 to E167 on the cytoplasmic side and is interrupted at the hydrophobic gasket of the Hv1 channel (Figure 2). The internal H-bond network is connected to the cytoplasmic and extracellular sides via conserved uncharged polar amino acid residues - N210 and S215 (Figure 3). We examined 10 independent simulations with various protonation states of carboxylates and histidines that are significant in the proton conduction pathway and present in the most common H-bond paths (Figure 2D,E) in order to study the impact of protonation state on the H-bond network dynamics of Hv1. As seen in Figures 4 and 5, the protonation state of the carboxylates and histidines forming the most frequent pathways affects the waterwire span across Hv1.

We for the first time explore the lipid interactions of Hv1 embedded in lipid bilayers of different lipid compositions. To probe the impact of lipid composition on the H-bond network dynamics of Hv1, we examined 5 independent simulations with Hv1 embedded in pure POPC, pure POPE, pure POPS, 5:1 POPE:POPG and *E. coli* bilayer. We observe a continuous H-bond network spanning across the Hv1 channel in pure POPS bilayers in contrast to the other bilayers in study where the H-bond network is interrupted at the hydrophobic gasket (Figure 6). This suggests that lipid composition influences the internal H-bond network dynamics. Hv1 has carboxylate and histidine groups in close proximity to the lipid headgroups suggesting formation of proton antennas. In our simulations of Hv1 in different lipid bilayers we observe that acidic lipids can participate in water-mediated H-bond clusters with Hv1 (Figure 7). Using our protocol to find the most frequent H-bond paths,

we identify potential proton antennas connecting the Hv1 sidechains and lipid headgroups - POPS (Figure 8), POPE and POPG (Figure 9) and in model *E. coli* (Figure 10) bilayers. We further investigated the lipid anchors of Hv1. According to bioinformatics analysis, sidechains that connect Hv1 to the membrane tend to be conserved (Figure 11), indicating that lipid-protein anchoring may be crucial for controlling, for instance, how Hv1 is oriented in relation to the membrane interface. We find that the lipid anchors vary depending on the nature and charge of the lipid membranes. A mutagenesis analysis of these lipid anchors in lipid membranes with various lipid compositions would provide further insights into the role of lipid composition in functioning of Hv1.


## Acknowledgement

Research was supported by funds from the European Union's Horizon 2020 Research and Innovation Program under the Marie Sklodowska-Curie grant agreement No. H2020 MSCA-ITN-2019-860592, Innovative Training Network 'Proton and proton-coupled transport' (to A-NB). MD simulations were performed using computing resources of the Physics Department at the Freie Universität Berlin, and data analyses were performed using computer resources of the Faculty of Physics of the University of Bucharest. The authors are grateful to Jens Dreger (Freie Universität Berlin) for technical support.

## Funding

This research was funded by the European Union's Horizon 2020 Research and Innovation Program under the Marie Sklodowska-Curie grant agreement No H2020 MSCA-ITN-2019-860592, Innovative Training Network 'Proton and proton-coupled transport' (to A.-N.B.).

# Supplementary Information

Table S1: Illustration of the most frequent H-bond path calculation. Most frequent H-bond paths from D108 and D181 sampled in MD simulations of Hv1 in hydrated POPS lipid bilayer with all amino acid residues in their standard protonation state.

| From | To | Path | Path length | 1-water | 2-water | 3-water |
|---|---|---|---|---|---|---|
| D108 | D181 | - | 1 | - | 77 | 86 |
| D108 | D119 | D181, E115 | 2 | - | - | 22 |
| D108 | D119 | D181, E115, E192 | 3 | - | - | 17 |
| D108 | D119 | D181, E115, H136 | 3 | - | - | 16 |
| D108 | D119 | D181, E115, S139, H136 | 4 | - | - | 8 |
| D108 | E115 | D181 | 1 | - | - | 27 |
| D108 | E192 | D181, E115 | 2 | - | - | 19 |
| D108 | E192 | D181, E115, D119 | 3 | - | - | 19 |
| D108 | E192 | D181, E115, H136, D119 | 4 | - | - | 14 |
| D108 | E192 | D181, E115, S139, H136, D119 | 5 | - | - | 7 |
| D108 | H136 | D181, E115 | 2 | - | - | 24 |
| D108 | H136 | D181, E115, D119 | 3 | - | - | 15 |
| D108 | H136 | D181, E115, S139 | 3 | - | - | 13 |
| D108 | H136 | D181, E115, E192, D119 | 4 | - | - | 12 |
| D181 | D108 | | 1 | - | 77 | 86 |
| D181 | D119 | E115 | 1 | - | - | 27 |
| D181 | D119 | E115, E192 | 2 | - | - | 21 |
| D181 | D119 | E115, H136 | 2 | - | - | 20 |
| D181 | D119 | E115, S139, H136 | 3 | - | - | 10 |
| D181 | E115 | | 1 | - | - | 34 |
| D181 | E192 | E115 | 1 | - | - | 24 |
| D181 | E192 | E115, D119 | 2 | - | - | 23 |
| D181 | E192 | E115, H136, D119 | 3 | - | - | 16 |
| D181 | E192 | E115, S139, H136, D119 | 4 | - | - | 9 |
| D181 | H136 | E115 | 1 | - | - | 29 |
| D181 | H136 | E115, D119 | 2 | - | - | 19 |
| D181 | H136 | E115, S139 | 2 | - | - | 17 |
| D181 | H136 | E115, E192, D119 | 3 | - | - | 14 |

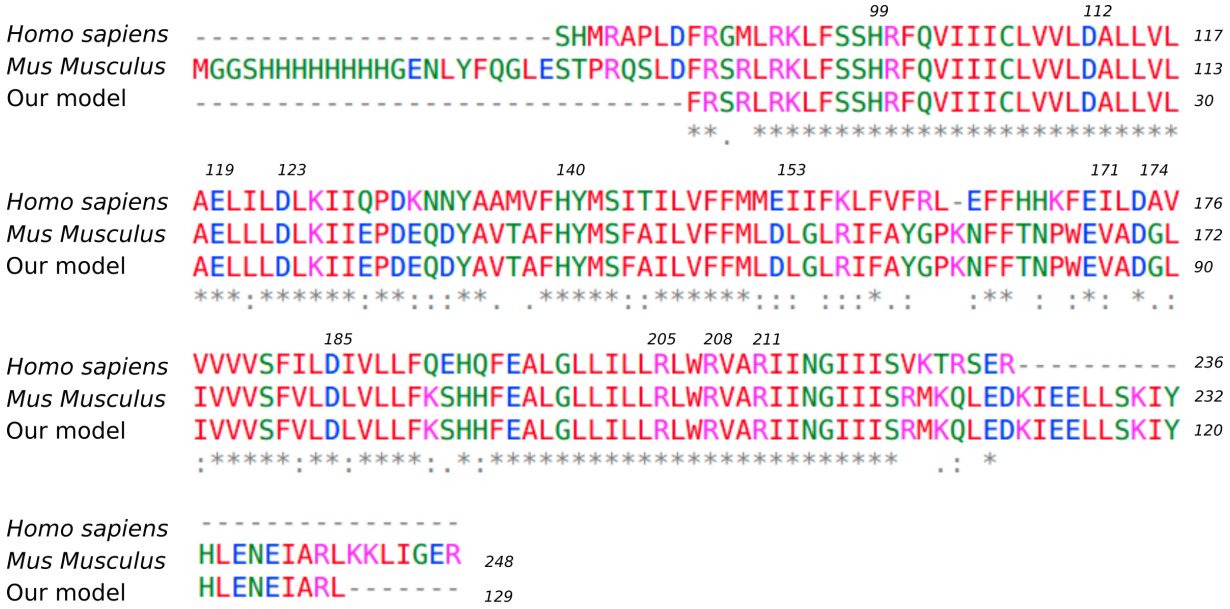


Figure S1: Multiple sequence alignment of our Hv1 model with *Mus musculus* and *Homo sapiens* Hv1. The sequence alignment was performed by Clustal Omega.[69]

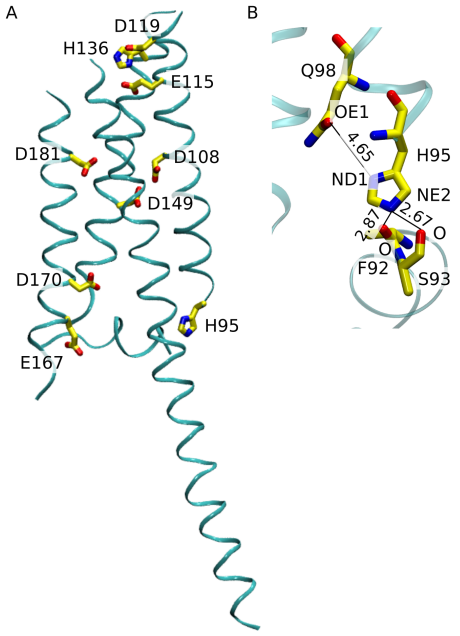


Figure S2: Protonated residues of Hv1 in individual membrane simulations. (A) *Mus musculus* crystal structure of Hv1 (PDB ID: 3wkv) before modeling of missing loops. Protonated residues of Hv1 in individual simulations displayed in yellow licorice representation. (B) Distances of H95 from neighboring residues raise the possibility of singly protonation on the N$\epsilon$ atom. The numbering scheme in the figure is based on *Mus musculus* crystal structure of Hv1.

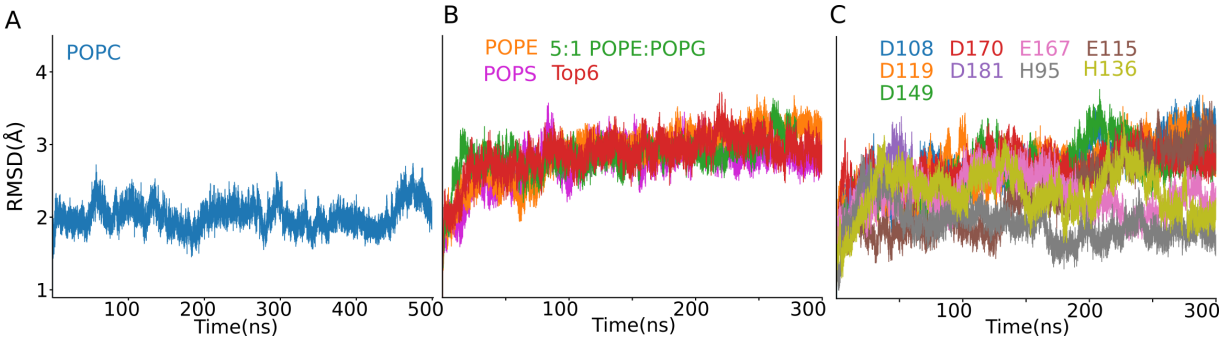


Figure S3: Structural stability of Hv1 in membrane simulations. C$\alpha$ RMSD profiles for helical regions of Hv1. (A) C$\alpha$ RMSD profiles computed for helical regions of Hv1 in pure POPC membrane in with all aminoacid residues in their standard protonation state (Panel A), pure POPE membrane, 5:1 POPE:POPG membrane, Top6 bacterial cell membrane with all aminoacid residues in their standard protonation state (Panel B) and Hv1 in pure POPC membrane with D108, D119, D149, D170, D181, E115, E167, H95 and H136 protonated in individual simulations (Panel C).

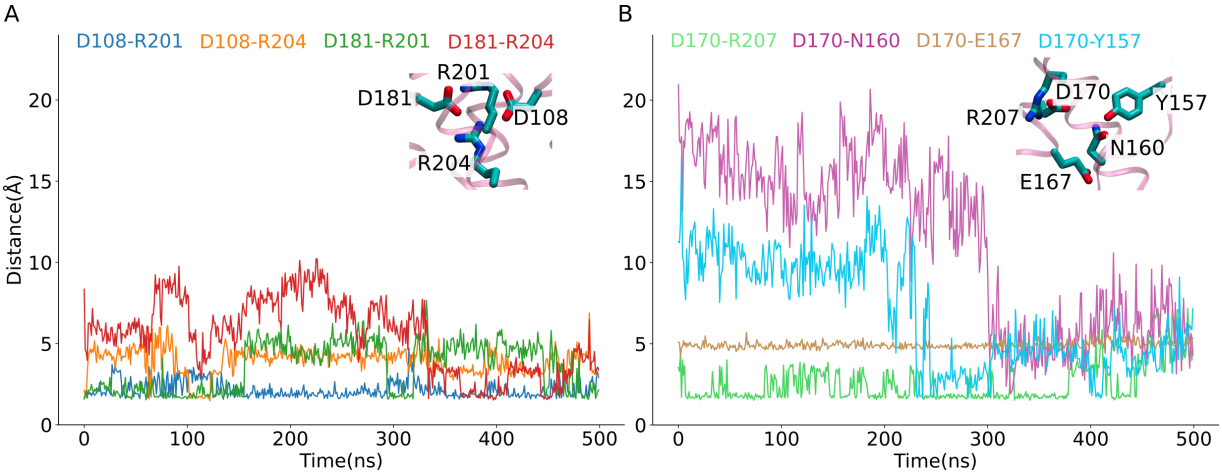


Figure S4: Dynamics of Aspartates forming salt-bridge in Hv1. Time series of the minimal distance between H-bond forming groups of D108-R201, D108-R204, D181-R201, D181-R204 Panel A) and D170-R207, D170-N160, D170-Y157, D170-E167 (Panel B). The coordinates used for calculation of minimal distances were read every 1ns from 500 ns trajectory.

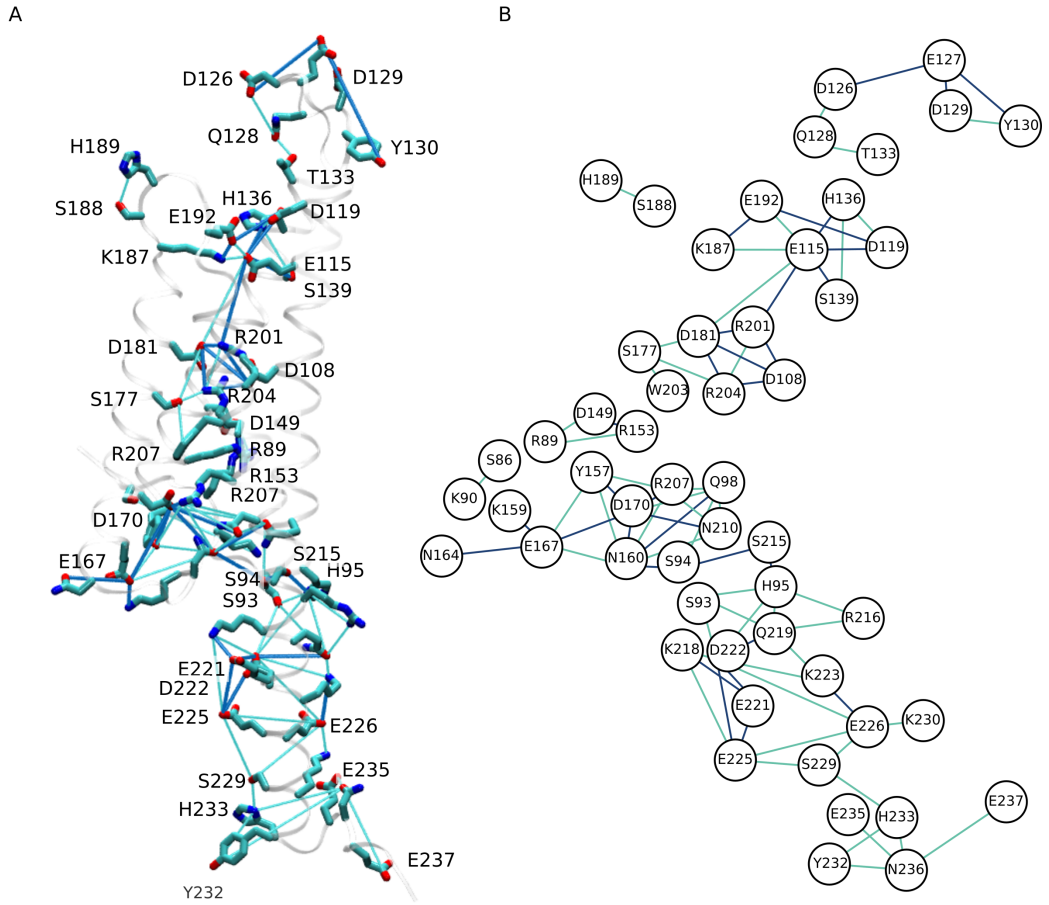


Figure S5: Dynamic H-bond network of Hv1. (A) Molecular graphics representation of water-mediated H-bond network of Hv1 in POPC bilayer in standard protonation state. The protein is shown as thin white ribbons, and the selected protein groups are shown as licorice. (B) Graph view of the H-bond network from Panel A. The molecular graphics were prepared with Visual Molecular Dynamics (VMD)[62] based on a coordinate snapshot from the simulation of Hv1 with standard protonation and embedded in a hydrated POPC lipid membrane environment.

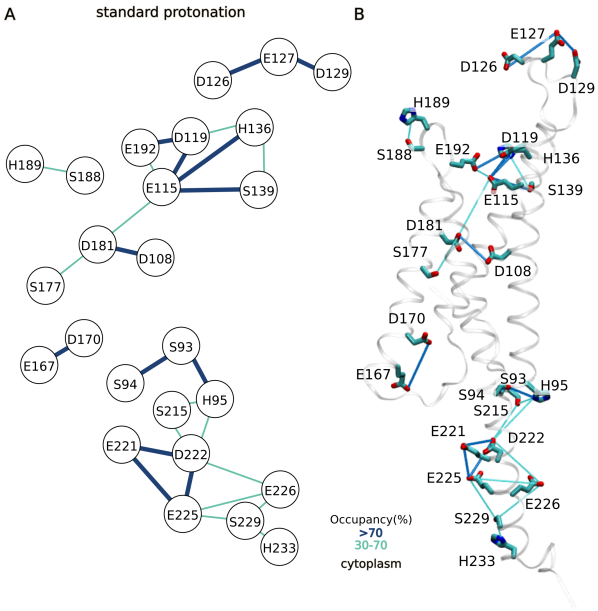


Figure S6: H-bond dynamics of Hv1 in POPC with standard protonation state. (A) H-bond network via possible proton carriers mediated by waterwires of maximum length 3. (B) Molecular graphics of H-bond network in Panel A. The last frame of 500 ns MD simulation is used for molecular graphics representation. Here the minimum occupancy of the H-bonds is 30%.

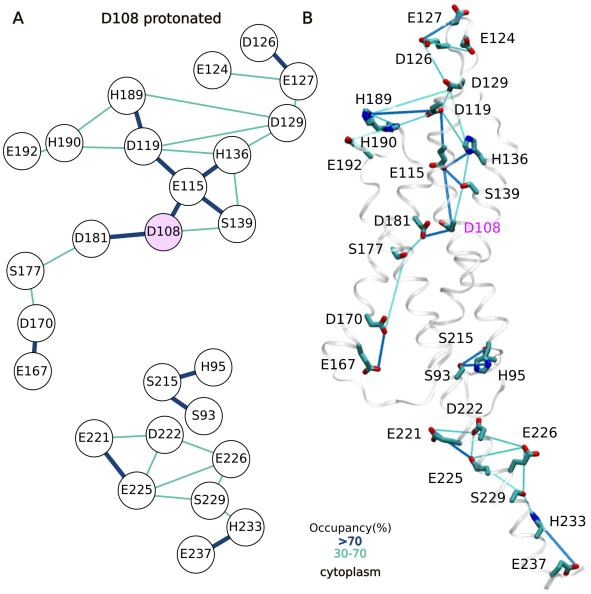


Figure S7: H-bond dynamics of Hv1 in POPC with D108 protonated. (A) H-bond network via possible proton carriers mediated by waterwires of maximum length 3. (B) Molecular graphics of H-bond network in Panel A. The last frame of 300 ns MD simulation is used for molecular graphics representation. Here the minimum occupancy of the H-bonds is 30%.

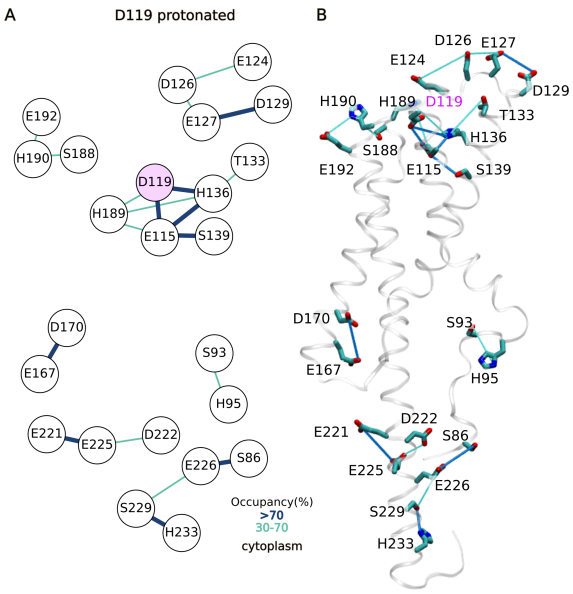


Figure S8: H-bond dynamics of Hv1 in POPC with D119 protonated. (A) H-bond network via possible proton carriers mediated by waterwires of maximum length 3. (B) Molecular graphics of H-bond network in Panel A. The last frame of 300 ns MD simulation is used for molecular graphics representation. Here the minimum occupancy of the H-bonds is 30%.

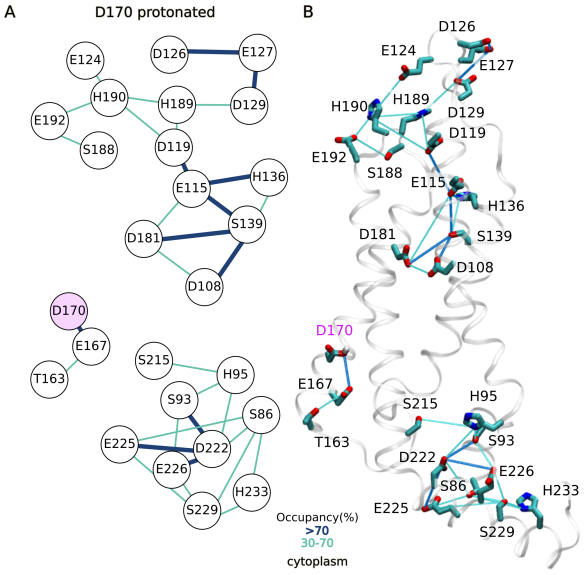


Figure S9: H-bond dynamics of Hv1 in POPC with D170 protonated. (A) H-bond network via possible proton carriers mediated by waterwires of maximum length 3. (B) Molecular graphics of H-bond network in Panel A. The last frame of 300 ns MD simulation is used for molecular graphics representation. Here the minimum occupancy of the H-bonds is 30%.

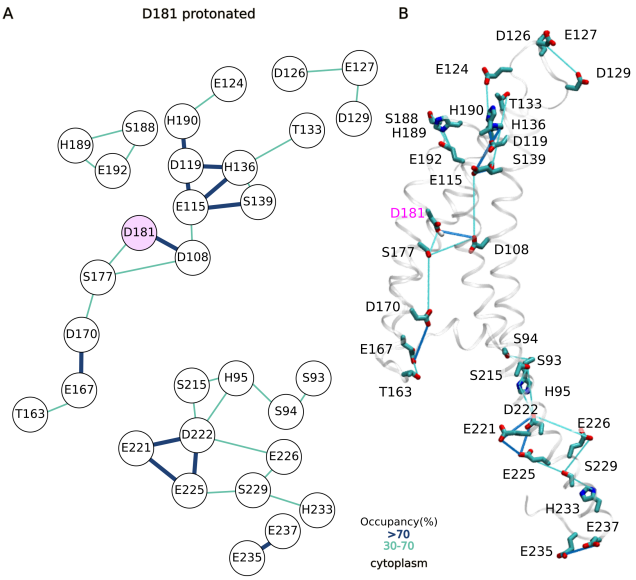


Figure S10: H-bond dynamics of Hv1 in POPC with D181 protonated. (A) H-bond network via possible proton carriers mediated by waterwires of maximum length 3. (B) Molecular graphics of H-bond network in Panel A. The last frame of 300 ns MD simulation is used for molecular graphics representation. Here the minimum occupancy of the H-bonds is 30%.

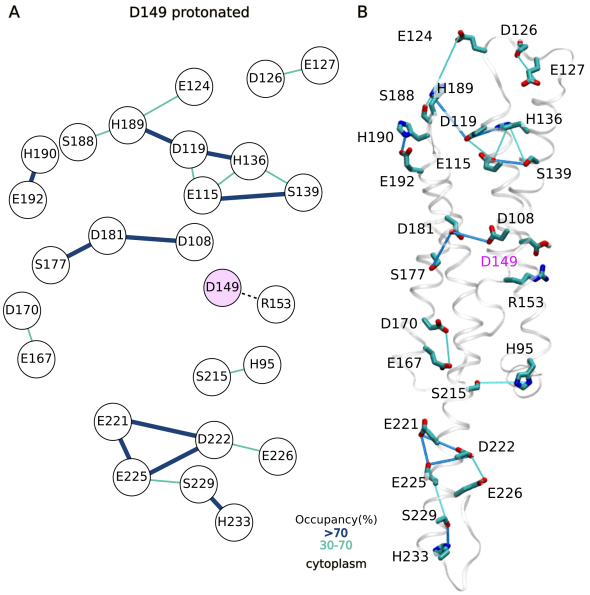


Figure S11: H-bond dynamics of Hv1 in POPC with D149 protonated. (A) H-bond network via possible proton carriers mediated by waterwires of maximum length 3. (B) Molecular graphics of H-bond network in Panel A. The last frame of 300 ns MD simulation is used for molecular graphics representation. Here the minimum occupancy of the H-bonds is 30%.

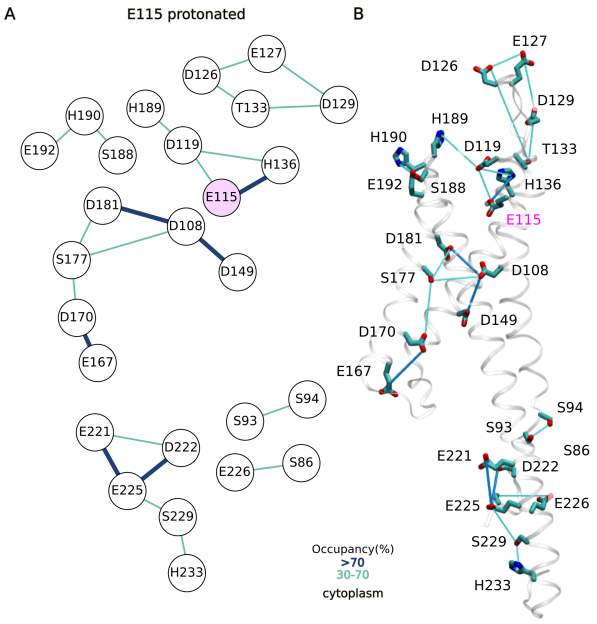


Figure S12: H-bond dynamics of Hv1 in POPC with E115 protonated. (A) H-bond network via possible proton carriers mediated by waterwires of maximum length 3. (B) Molecular graphics of H-bond network in Panel A. The last frame of 300 ns MD simulation is used for molecular graphics representation. Here the minimum occupancy of the H-bonds is 30%.

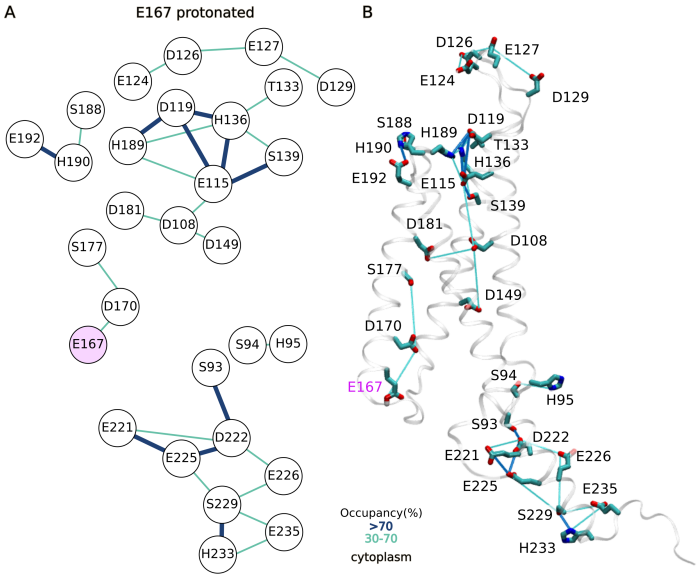


Figure S13: H-bond dynamics of Hv1 in POPC with E167 protonated. (A) H-bond network via possible proton carriers mediated by waterwires of maximum length 3. (B) Molecular graphics of H-bond network in Panel A. The last frame of 300 ns MD simulation is used for molecular graphics representation. Here the minimum occupancy of the H-bonds is 30%.

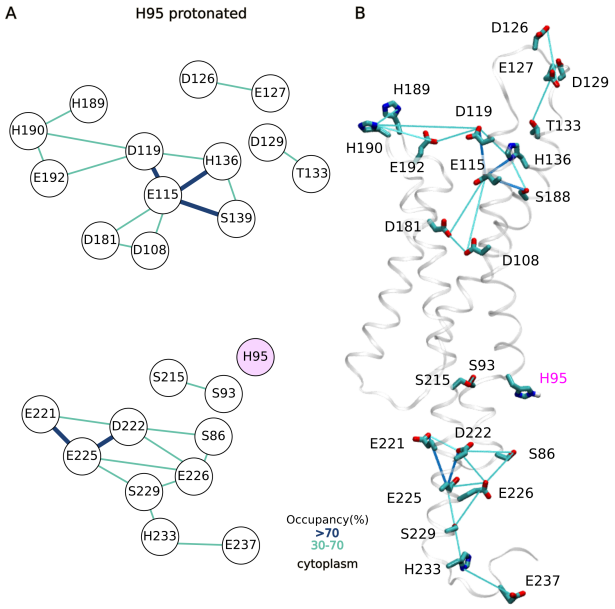


Figure S14: H-bond dynamics of Hv1 in POPC with H95 protonated. (A) H-bond network via possible proton carriers mediated by waterwires of maximum length 3. (B) Molecular graphics of H-bond network in Panel A. The last frame of 300 ns MD simulation is used for molecular graphics representation. Here the minimum occupancy of the H-bonds is 30%.

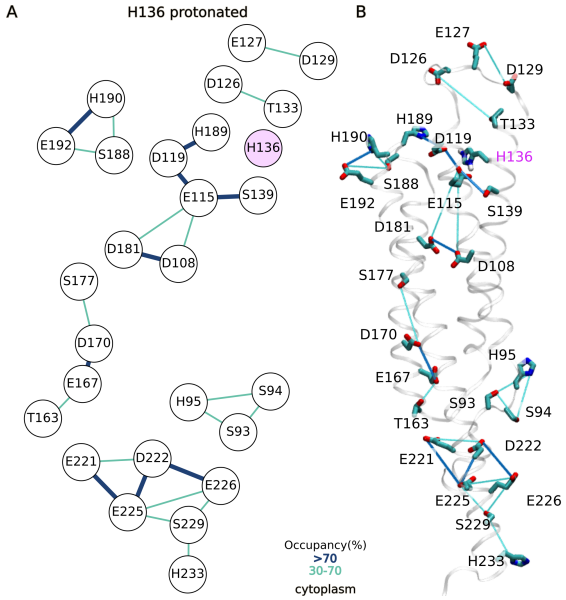


Figure S15: H-bond dynamics of Hv1 in POPC with H136 protonated. (A) H-bond network via possible proton carriers mediated by waterwires of maximum length 3. (B) Molecular graphics of H-bond network in Panel A. The last frame of 300 ns MD simulation is used for molecular graphics representation. Here the minimum occupancy of the H-bonds is 30%.

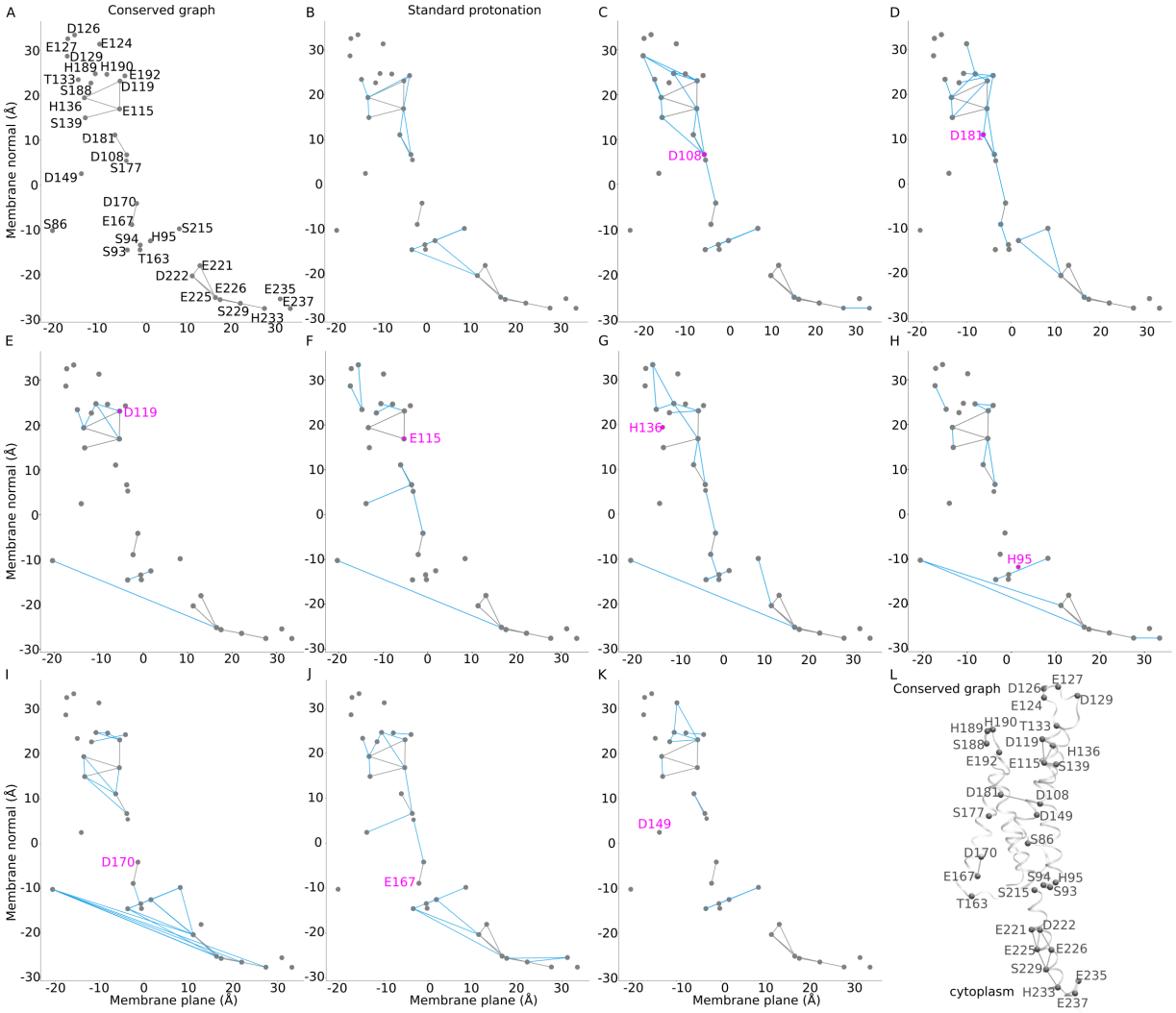


Figure S16: Conserved H-bond network via potential proton carriers across protonated Hv1 systems under study. (A) Graph of conserved H-bond network mediated by waterwires of maximum length 3. (B-K) Difference H-bond graphs of Hv1 from simulations with standard protonation for all titratable sidechains (Panel B), with neutral D108 (Panel C), neutral D181 (Panel D), neutral D119 (Panel E), neutral E115 (Panel F), doubly protonated H136 (Panel G), N$\epsilon$ protonated H95 (Panel H), neutral D170 (Panel I), neutral E167 (Panel J) and neutral D149 (Panel K). H-bonds and H-bonding groups conserved across simulations are shown in grey. The difference between conserved H-bonds and H-bonding groups is shown in blue whereas protonated H-bonding group is shown magenta. The H-bond graphs were generated using Cgraph[70] with an occupancy filter of 30% and conservation threshold of 80%. (L) Molecular graphics of conserved graph from Panel A.

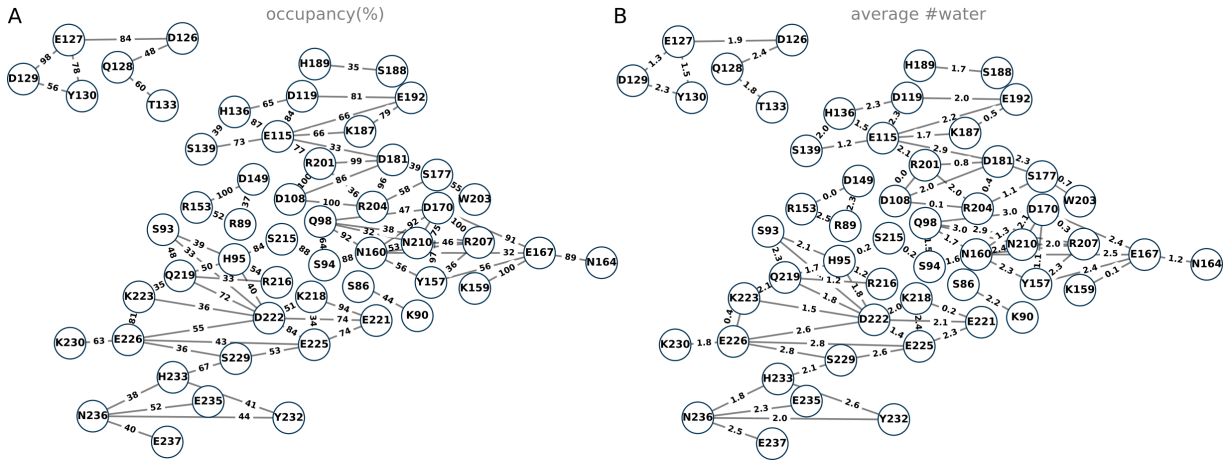


Figure S17: H-bond network of Hv1 in POPC with standard protonation. (A-B) H-bond network mediated by waterwires of maximum length 3 with H-bond occupancies (Panel A) and average number of waters in a waterwire (Panel B) shown on the edges. Here the minimum occupancy of the H-bonds is 30%.

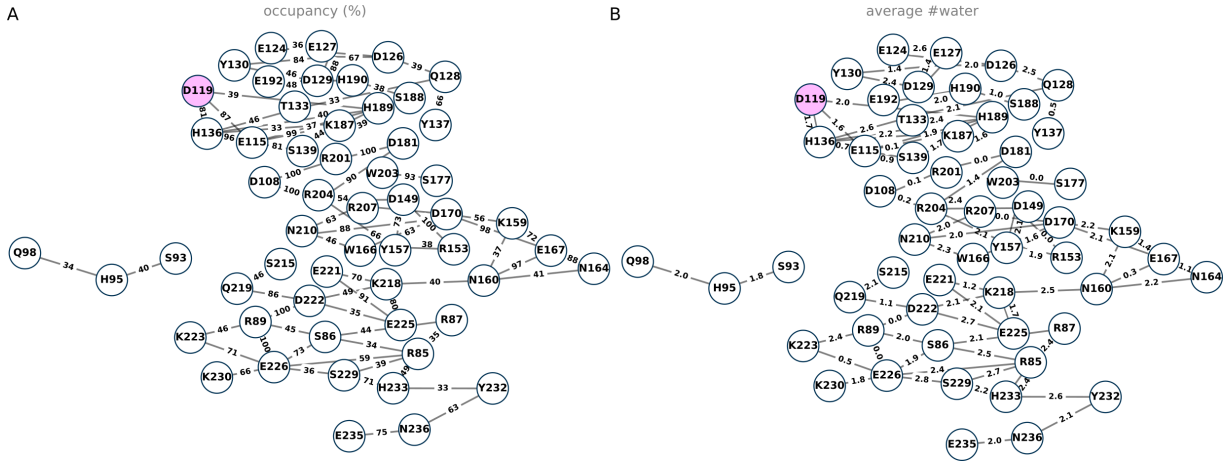


Figure S18: H-bond network of Hv1 in POPC with D119 protonated. (A-B) H-bond network mediated by waterwires of maximum length 3 with H-bond occupancies (Panel A) and average number of waters in a waterwire (Panel B) shown on the edges. Here the minimum occupancy of the H-bonds is 30%.

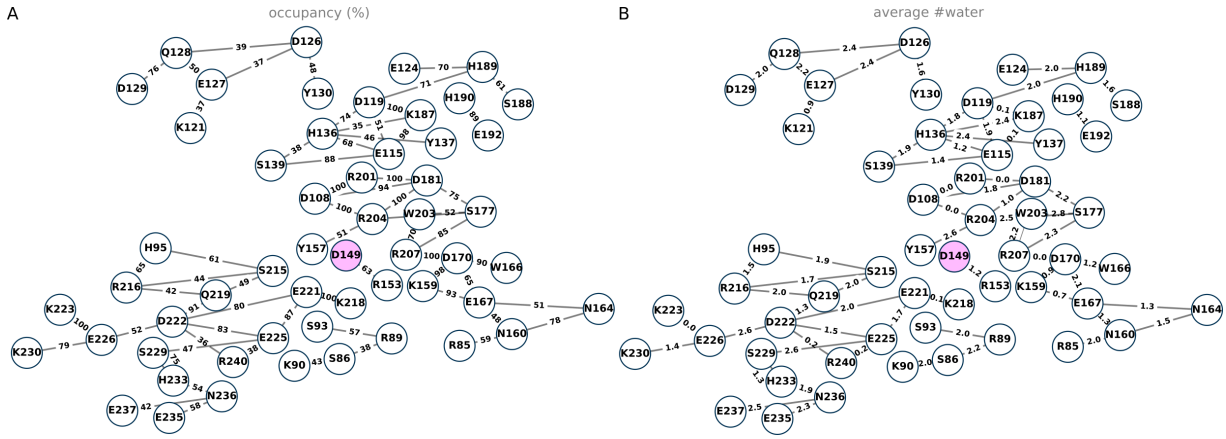


Figure S19: H-bond network of Hv1 in POPC with D149 protonated. (A-B) H-bond network mediated by waterwires of maximum length 3 with H-bond occupancies (Panel A) and average number of waters in a waterwire (Panel B) shown on the edges. Here the minimum occupancy of the H-bonds is 30%.

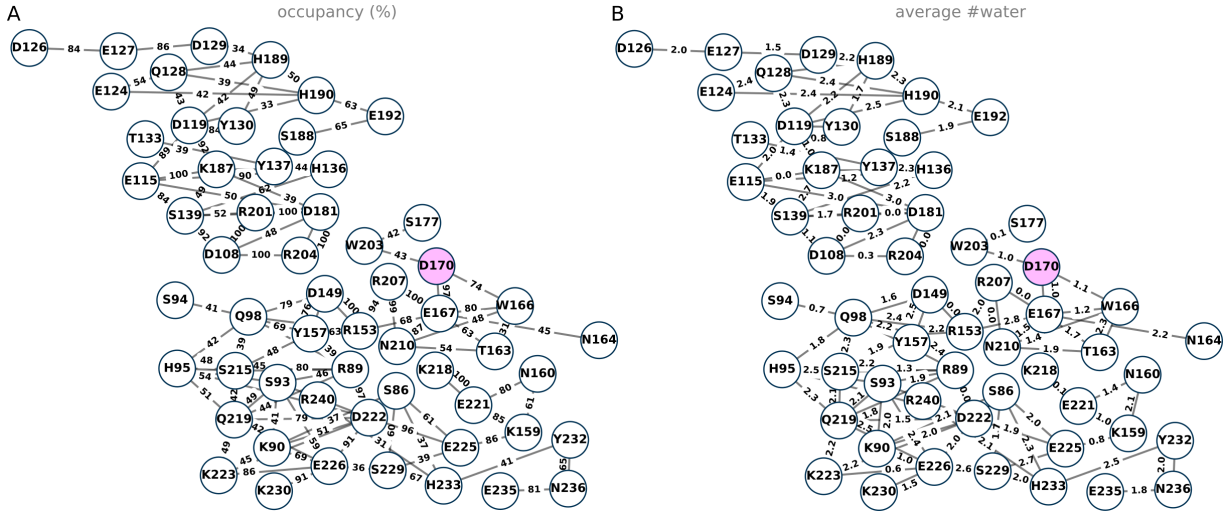


Figure S20: H-bond network of Hv1 in POPC with D170 protonated. (A-B) H-bond network mediated by waterwires of maximum length 3 with H-bond occupancies (Panel A) and average number of waters in a waterwire (Panel B) shown on the edges. Here the minimum occupancy of the H-bonds is 30%.

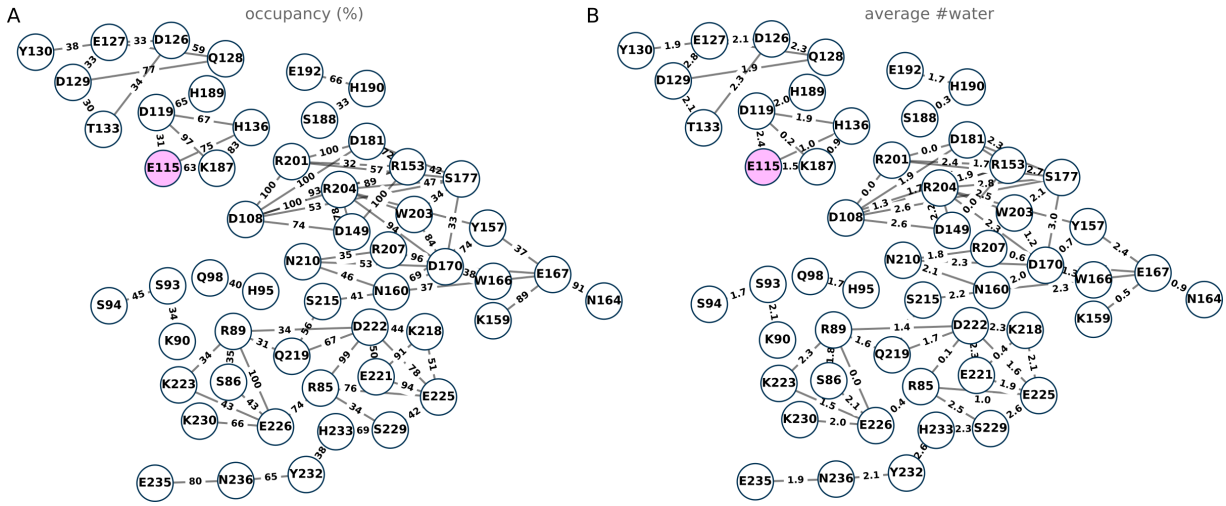


Figure S21: H-bond network of Hv1 in POPC with E115 protonated. (A-B) H-bond network mediated by waterwires of maximum length 3 with H-bond occupancies (Panel A) and average number of waters in a waterwire (Panel B) shown on the edges. Here the minimum occupancy of the H-bonds is 30%.

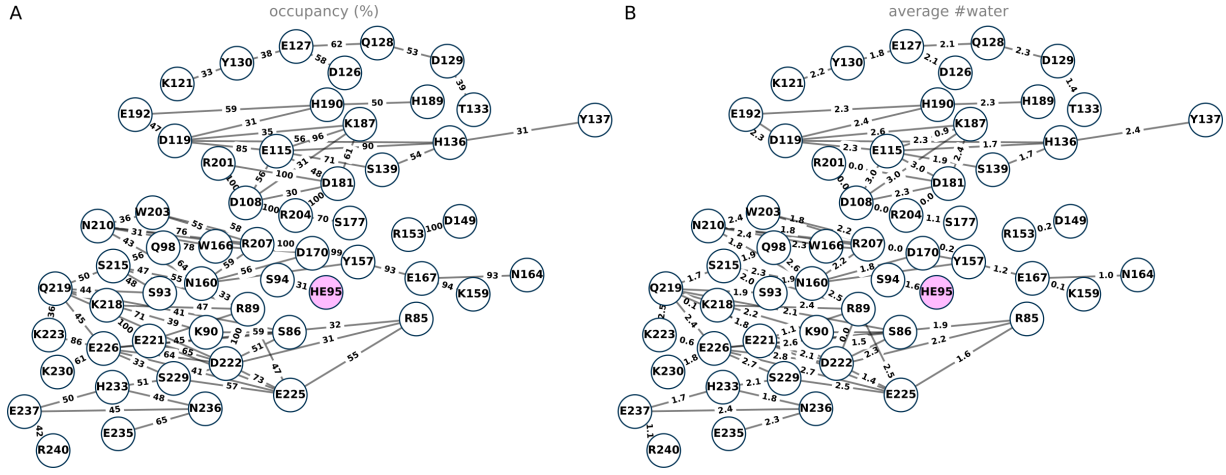


Figure S22: H-bond network of Hv1 in POPC with H95 protonated. (A-B) H-bond network mediated by waterwires of maximum length 3 with H-bond occupancies (Panel A) and average number of waters in a waterwire (Panel B) shown on the edges. Here the minimum occupancy of the H-bonds is 30%.

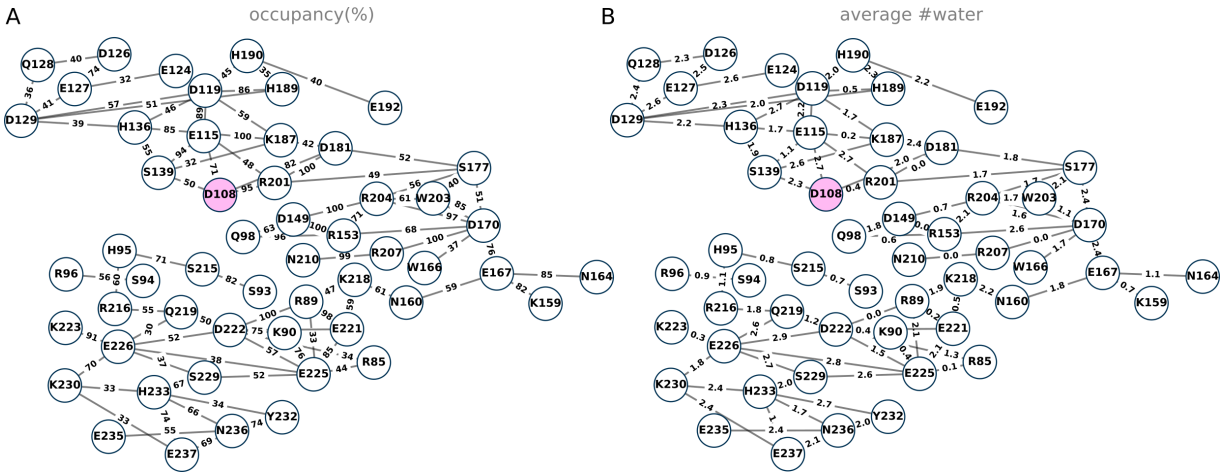


Figure S23: H-bond network of Hv1 in POPC with D108 protonated. (A-B) H-bond network mediated by waterwires of maximum length 3 with H-bond occupancies (Panel A) and average number of waters in a waterwire (Panel B) shown on the edges. Here the minimum occupancy of the H-bonds is 30%.

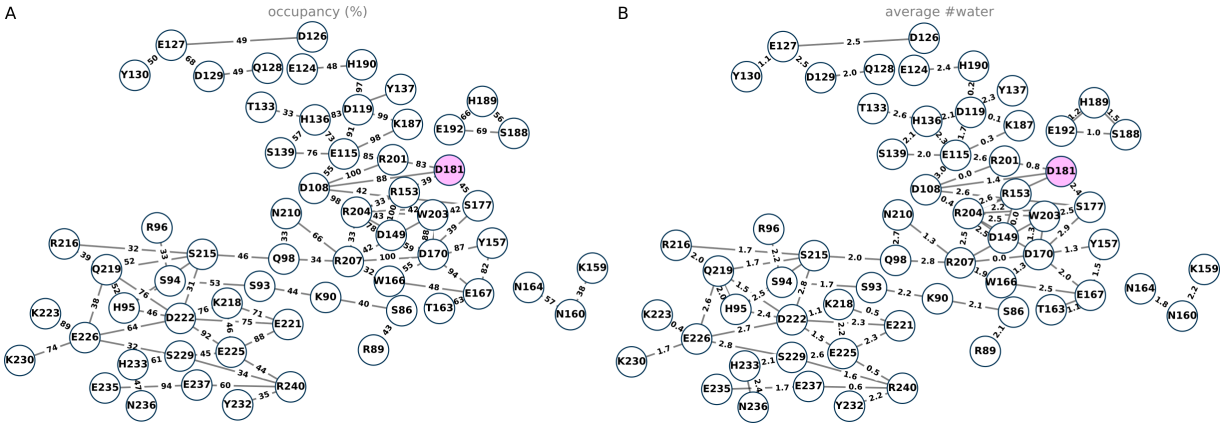


Figure S24: H-bond network of Hv1 in POPC with D181 protonated. (A-B) H-bond network mediated by waterwires of maximum length 3 with H-bond occupancies (Panel A) and average number of waters in a waterwire (Panel B) shown on the edges. Here the minimum occupancy of the H-bonds is 30%.

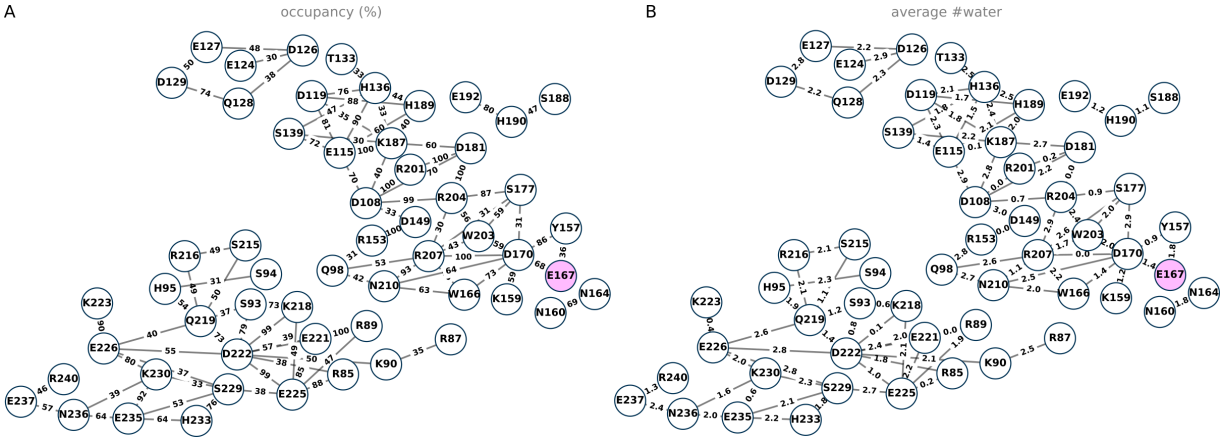


Figure S25: H-bond network of Hv1 in POPC with E167 protonated. (A-B) H-bond network mediated by waterwires of maximum length 3 with H-bond occupancies (Panel A) and average number of waters in a waterwire (Panel B) shown on the edges. Here the minimum occupancy of the H-bonds is 30%.

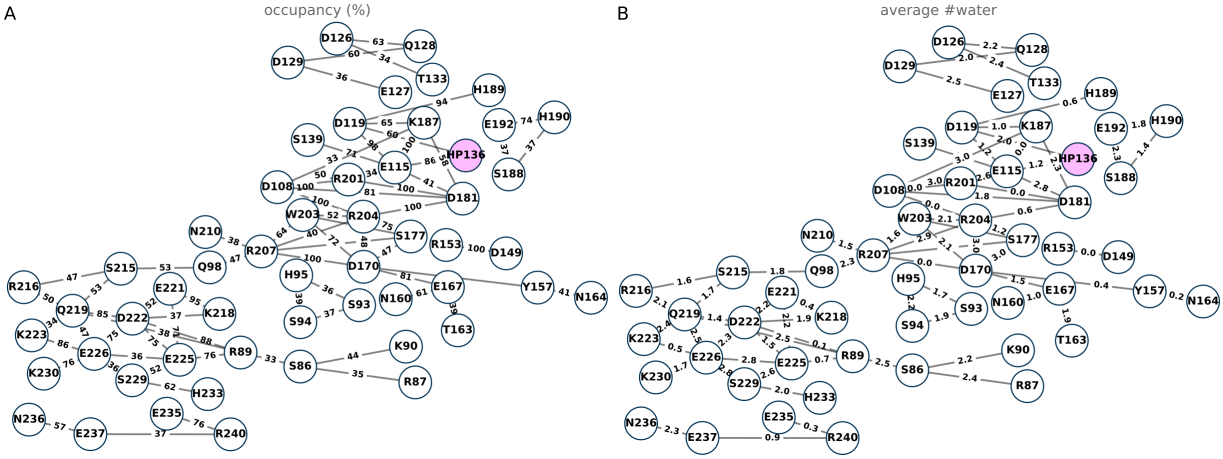


Figure S26: H-bond network of Hv1 in POPC with H136 protonated. (A-B) H-bond network mediated by waterwires of maximum length 3 with H-bond occupancies (Panel A) and average number of waters in a waterwire (Panel B) shown on the edges. Here the minimum occupancy of the H-bonds is 30%.

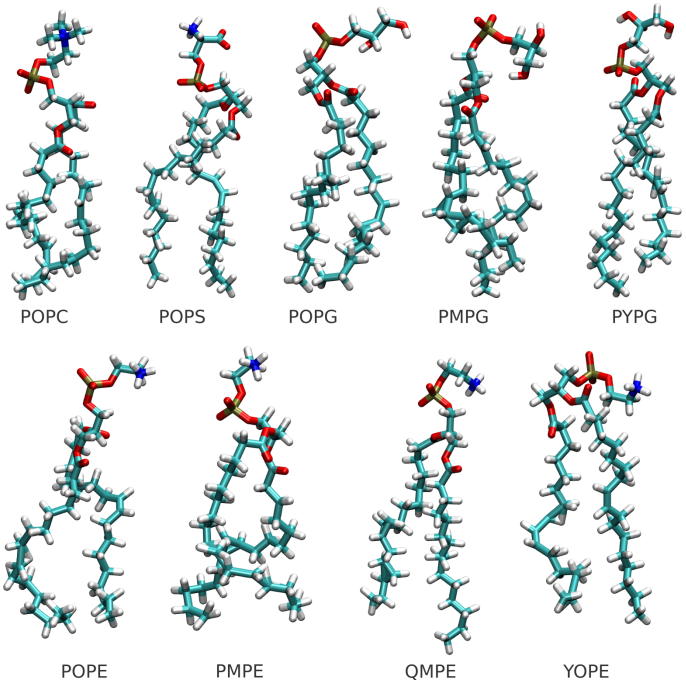


Figure S27: Types of lipids in Hv1 and lipid membrane simulations.

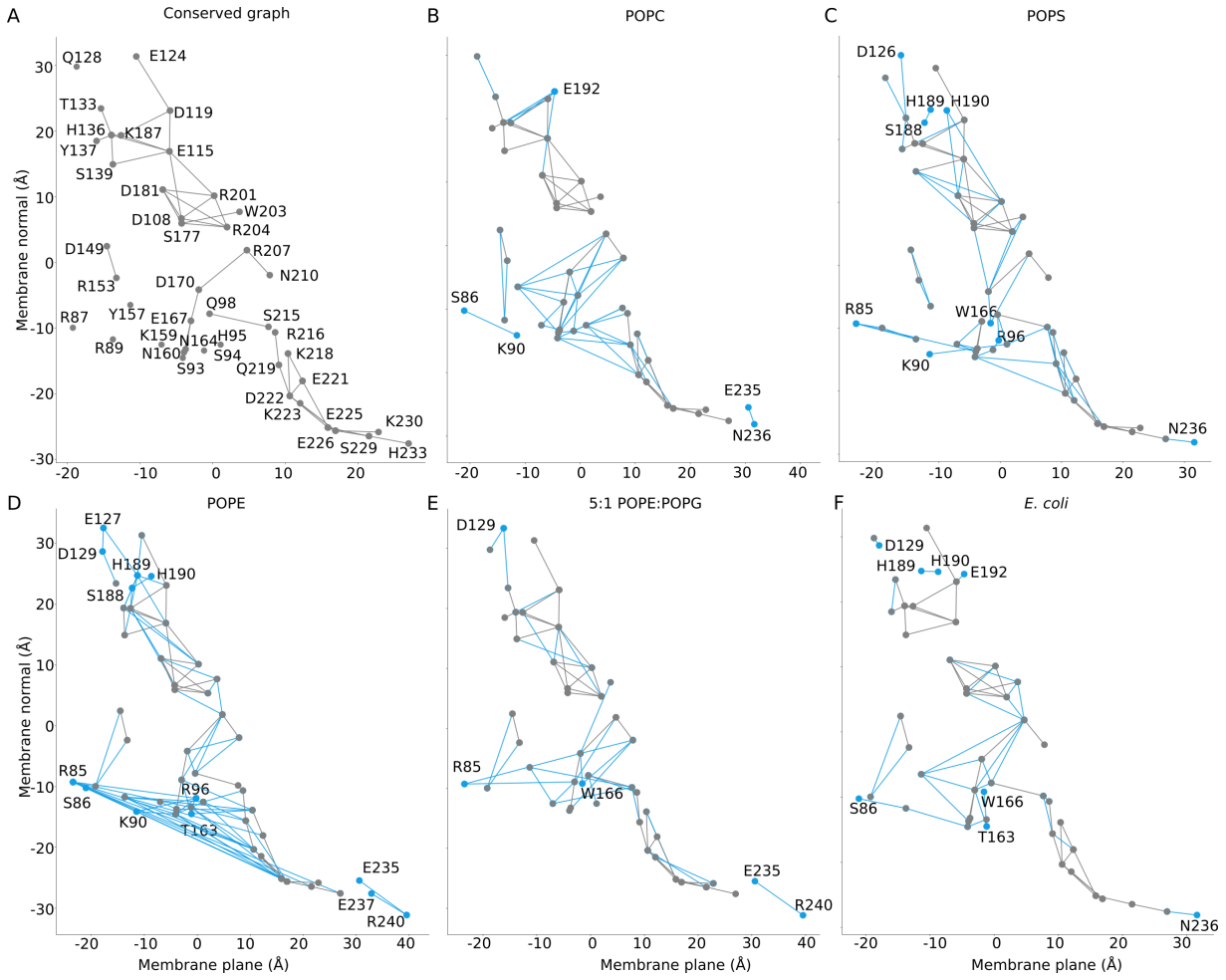


Figure S28: Conserved H-bond network across Hv1 systems in different lipid bilayers. (A) Graph of conserved H-bond network mediated by waterwires of maximum length 3. (B-F) Difference H-bond graphs of Hv1 from simulations with standard protonation for all titratable sidechains in pure POPC (Panel B), pure POPS (Panel C), pure POPE (Panel D), 5:1 POPE:POPG (Panel E) and *E. coli* (Panel F) bilayers. H-bonds and H-bonding groups conserved across simulations are shown in grey. The difference between conserved H-bonds and H-bonding groups is shown in blue whereas protonated H-bonding group is shown magenta. The H-bond graphs were generated using Cgraph[70] with an occupancy filter of 30 % and conservation threshold of 80 %.

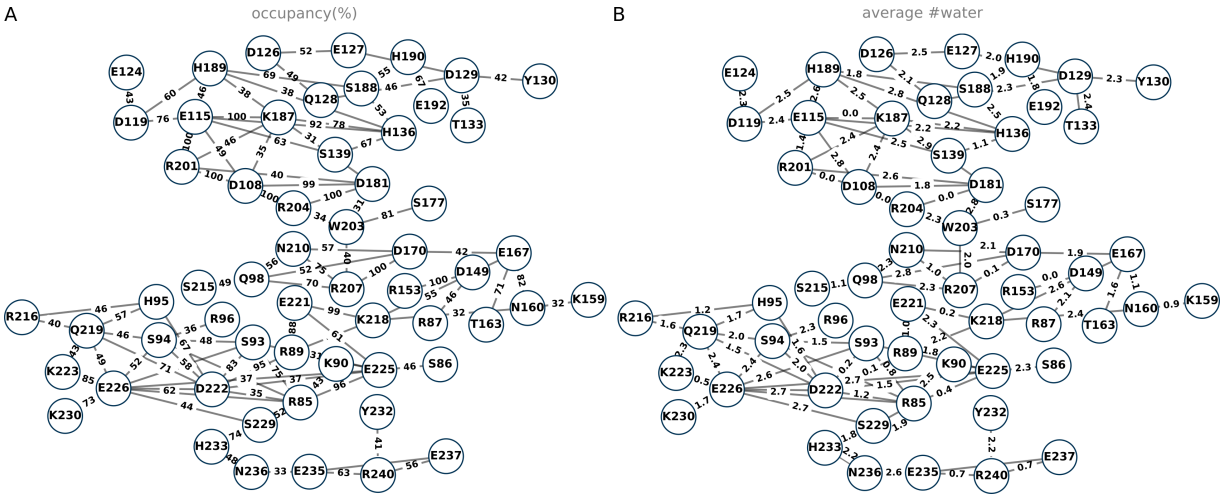


Figure S29: H-bond network of Hv1 in POPE bilayer. (A-B) H-bond network mediated by waterwires of maximum length 3 with H-bond occupancies (Panel A) and average number of waters in a waterwire (Panel B) shown on the edges. Here the minimum occupancy of the H-bonds is 30%.

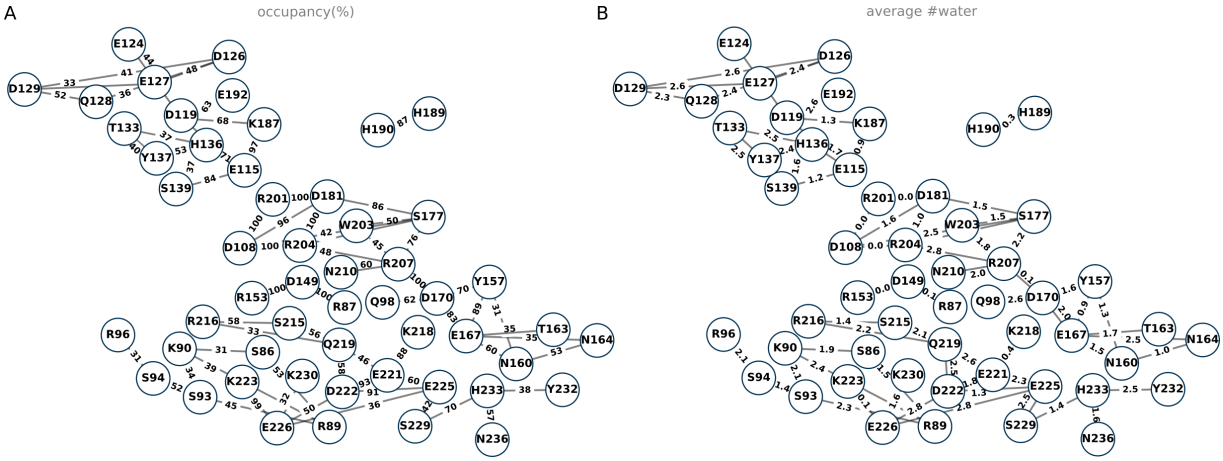


Figure S30: H-bond network of Hv1 in 5:1 POPE:POPG bilayer. (A-B) H-bond network mediated by waterwires of maximum length 3 with H-bond occupancies (Panel A) and average number of waters in a waterwire (Panel B) shown on the edges. Here the minimum occupancy of the H-bonds is 30%.

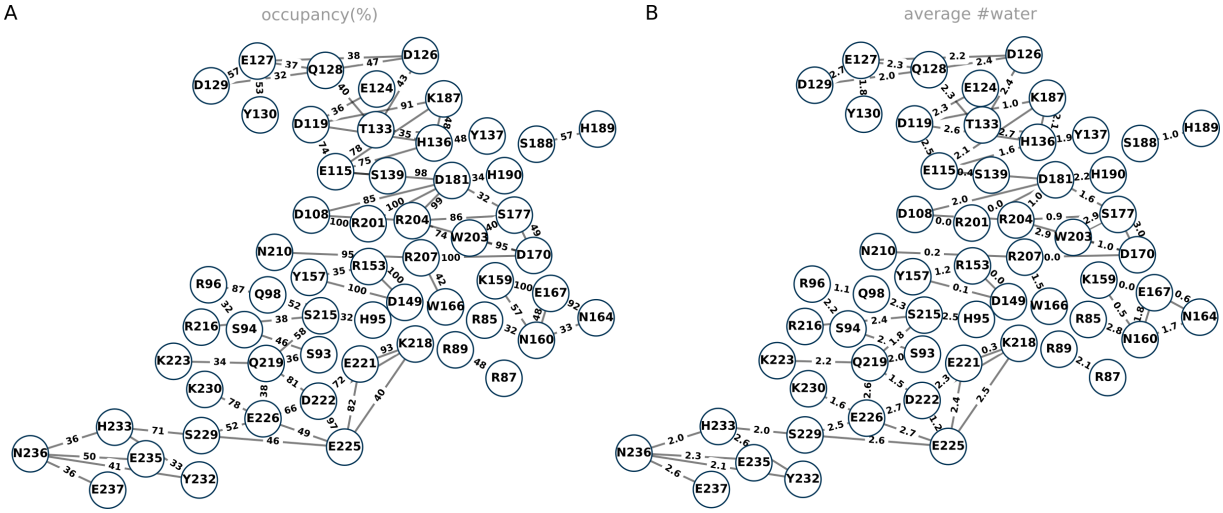


Figure S31: H-bond network of Hv1 in POPS bilayer. (A-B) H-bond network mediated by waterwires of maximum length 3 with H-bond occupancies (Panel A) and average number of waters in a waterwire (Panel B) shown on the edges. Here the minimum occupancy of the H-bonds is 30%.

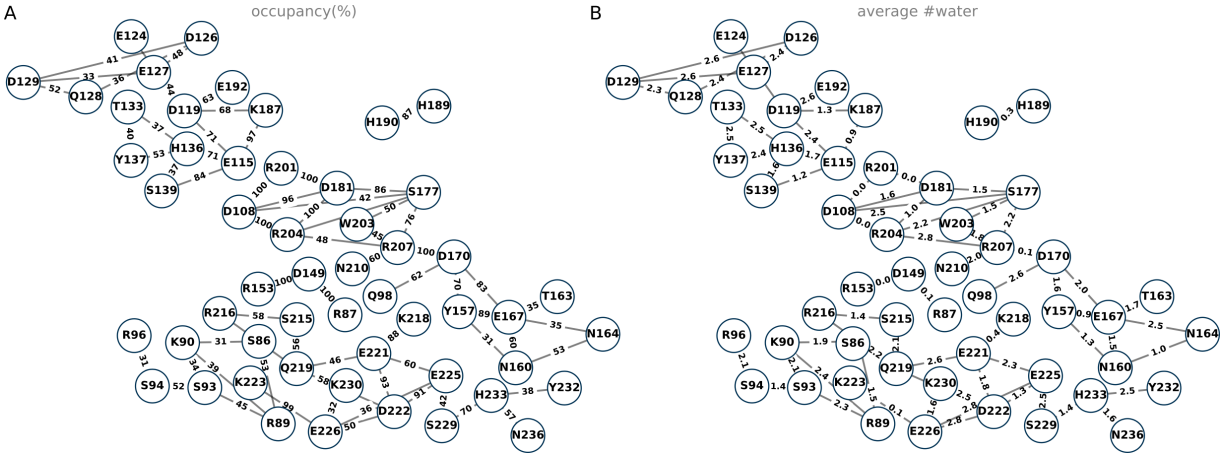


Figure S32: H-bond network of Hv1 in *E. coli* bilayer. (A-B) H-bond network mediated by waterwires of maximum length 3 with H-bond occupancies (Panel A) and average number of waters in a waterwire (Panel B) shown on the edges. Here the minimum occupancy of the H-bonds is 30%.

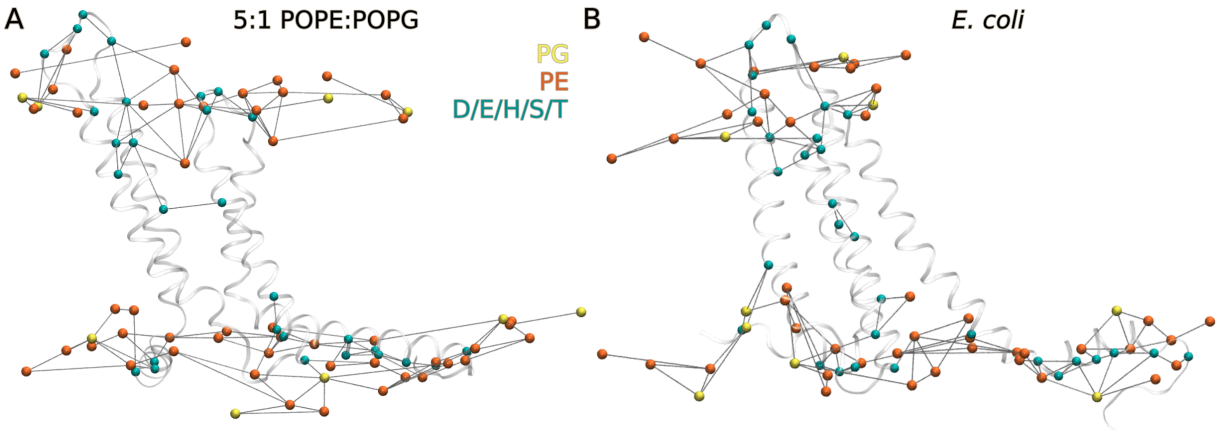


Figure S33: Lipid interactions of Hv1. (A-B) Water-mediated lipid interactions of Hv1 in 5:1 POPE:POPG bilayer (Panel A) vs *E. coli* bilayer (Panel B).

```
Karlodinium veneficum  MHEEHEAEDHGEHRVSDAAGSLEAPLQKGSFEQHAK--GTSGVHHARSQASSNREGREGC  245
Ciona intestinalis     TVKTKA--DDRVHEIKKKNSELELQIHNLEEKLSQKEQDMSRLHEILRCNNIDIPPTVPL  326
Nicoletia phytophila   SVKMQA--EHQLEREKQRGMALEGELSRCRQVCAAQQRELDVLRAVLQHHGLDQQLPDGN  228
Danio rerio            SVQNRA--NHRVEKLKEINESLVHQVNELKEQNTKMDQENVRLRALLKDHSIDF------  235
Xenopus laevis         SVKTRA--EEKMHKLKEQKGSLLEKVAQLEQQCAQQEQEIGRLHKLLQEHNVFPAS----  230
Xenopus tropicalis     SVKTQA--EDKIHRLKENQESLLEKVAHLEQQCAQQEQEIVRLQTLLQQHNVFPAS----  230
Gallus gallus          SVKTRS--EQQVSKLKQVNLKLATKVEQLQHSCVEKEQEIERLTRMLKQHGLLSEQT---  235
Mus musculus chimera   SRMKQL--EDKIEELL-------SKIYH-------LENEIARLKKLIGER----------  196
Homo sapiens           SVKTRS--ERQLLRLKQMNVQLAAKIQHLEFSCSEKEQEIERLNKLLRQHGLLGEVN---  273
Mus Musculus           SVKTRS--ERQILRLKQINIQLATKIQHLEFSCSEKEQEIERLNKLLKQNGLLGDVN---  269
                               :  :    .          : .             :
```

Figure S34: Multiple sequence alignment of cytoplasmic helix of Hv1. The sequence alignment was performed by Clustal Omega.[69]

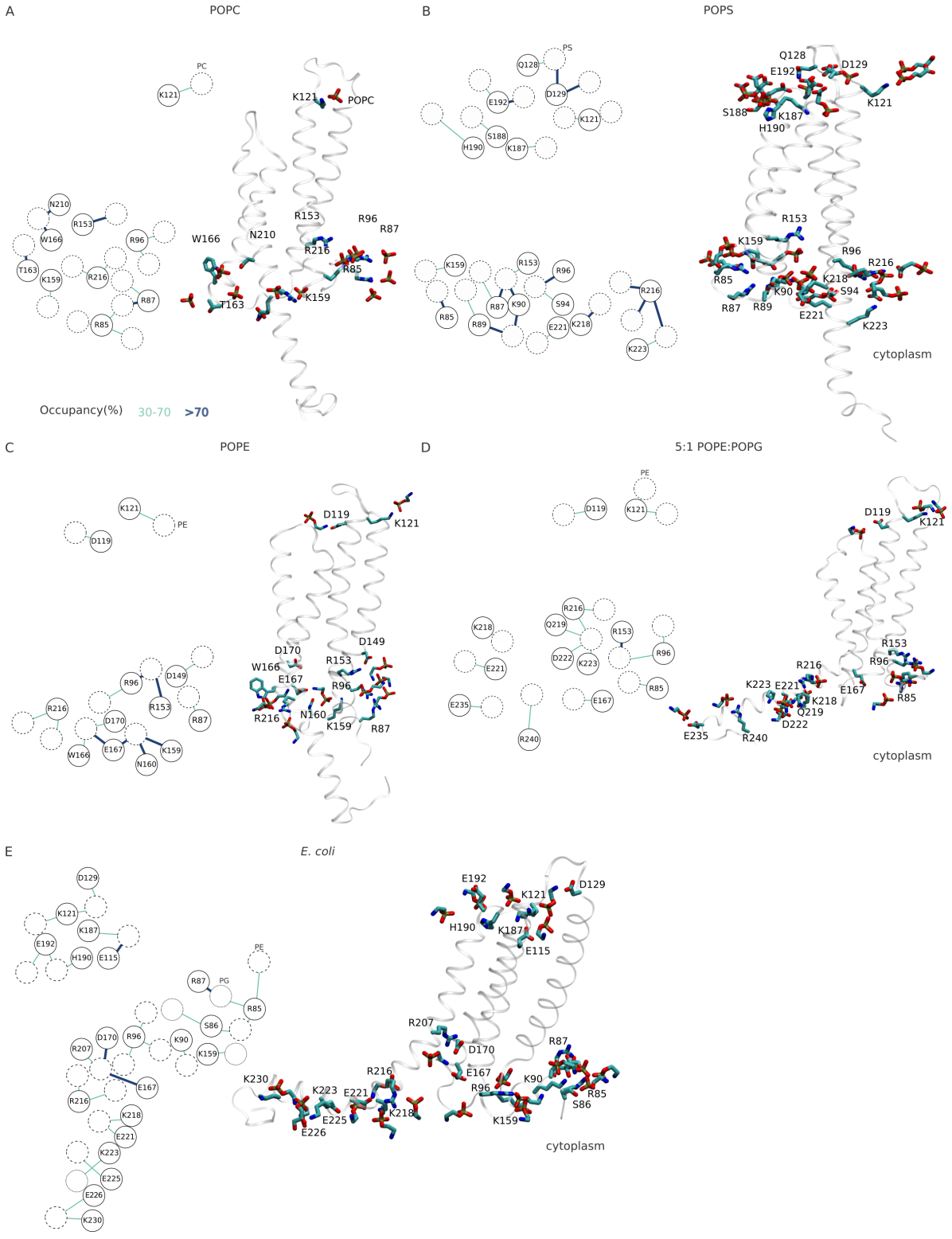


Figure S35: Lipid anchors of Hv1. (A-E) Lipid-Hv1 interactions in POPC (Panel A), POPS (Panel B), POPE (Panel C), 5:1 POPE:POPG (Panel D) and *E. coli* (Panel E) bilayers.

# References


(1) DeCoursey, T. E. *Physiological Reviews* **2013**, *93*, 599–652.

(2) Wang, Y.; Li, S. J.; Juncheng, P.; Che, Y.; Yin, J.; Zhao, Q. *Biochemical and Biophysical Research Communications* **2011**, *412*, 353–359.

(3) Wang, Y.; Wu, X.; Li, Q.; Zhang, S.; Li, S. J. *PLOS ONE* **2013**, *8*, e70550.

(4) Alvear-Arias, J. J.; Peña-Pichicoi, A.; Carrillo, C.; Fernandez, M. a. L.; Gonzalez, T.; Garate, J. A.; Gonzalez, C. *Frontiers in Pharmacology* **2023**, *14*.

(5) Ramsey, I. S.; Moran, M. M.; Chong, J. A.; Clapham, D. E. *Nature* **2006**, *440*, 1213–1216.

(6) Bayrhuber, M.; Maslennikov, I.; Kwiatkowski, W.; Sobol, A. A.; Wierschem, C.; Eichmann, C.; Frey, L.; Riek, R. *Biochemistry* **2019**, *58*, 4017–4027.

(7) Geragotelis, A. D.; Wood, M. L.; Göddeke, H.; Luan, H.; Webster, P. D.; Wong, E.; Freites, J. A.; Tombola, F.; Tobias, D. J. *Proceedings of the National Academy of Sciences of the United States of America* **2020**, *117*, 13490–13498.

(8) Musset, B.; Smith, S.; Rajan, S.; Morgan, D.; Cherny, V. V.; DeCoursey, T. E. *Nature* **2011**,

(9) Ramsey, I. S.; Mokrab, Y.; Carvacho, I.; Sands, Z. A.; Sansom, M. S. P.; Clapham, D. E. *Nature Structural & Molecular Biology* **2010**, *17*, 869–875.

(10) DeCoursey, T. E. *Biochemistry* **2015**, *54*, 3250–3268.

(11) Berger, T.; Isacoff, E. Y. *Neuron* **2011**, *72*, 991–1000.

(12) Zhao, C.; Luan, H.; Riahi, S.; Lim, V. T.; Tobias, D. J.; Tombola, F. *The Journal of General Physiology* **2021**, *153*.

(13) Zhao, C.; Luan, H.; Galpin, J. D.; Riahi, S.; Lim, V. T.; Webster, P. D.; Tobias, D. J.; Ahern, C. A.; Tombola, F. *The Journal of General Physiology* **2021**, *153*.

(14) Zhang, Q. et al. *Cell Research* **2022**, *32*, 461–476.

(15) Boytsov, D.; Brescia, S.; Chaves, G.; Koefler, S.; Hannesschlaeger, C.; Siligan, C.; Goessweiner-Mohr, N.; Musset, B.; Pohl, P. *bioRxiv (Cold Spring Harbor Laboratory)* **2022**,

(16) Takeshita, K.; Sakata, S.; Yamashita, E.; Fujiwara, Y.; Kawanabe, A.; Kurokawa, T.; Okochi, Y.; Matsuda, M.; Narita, H.; Okamura, Y.; Nakagawa, A. *Nature Structural & Molecular Biology* **2014**, *21*, 352–357.

(17) Banh, R. L.; Cherny, V. V.; Morgan, D.; Musset, B.; Thomas, S.; Kulleperuma, K.; Smith, S.; Pomes, R.; DeCoursey, T. E. *Proceedings of the National Academy of Sciences of the United States of America* **2019**, *116*, 18951–18961.

(18) Alabi, A. A.; Bahamonde, M. I.; Jung, H. C.; Kim, J. I.; Swartz, K. J. *Nature* **2007**, *450*, 370–375.

(19) Jardin, C.; Ohlwein, N.; Franzen, A.; Chaves, G.; Musset, B. *Physical Chemistry Chemical Physics* **2022**, *24*, 9964–9977.

(20) Cherny, V. V.; Morgan, D.; Musset, B.; Chaves, G.; Smith, S.; DeCoursey, T. E. *The Journal of General Physiology* **2015**, *146*, 343–356.

(21) Cherny, V. V.; Morgan, D.; Thomas, S.; Smith, S.; DeCoursey, T. E. *The Journal of General Physiology* **2018**, *150*, 851–862.

(22) Luan, H.; Singh, V.; Wulff, H.; Tombola, F. *Scientific Reports* **2015**, *5*.

(23) Fujiwara, Y.; Kurokawa, T.; Okamura, Y. *The Journal of General Physiology* **2014**, *143*, 377–386.

(24) Boonamnaj, P.; Sompornpisut, P. *Journal of Physical Chemistry B* **2018**, *122*, 1037–1048.

(25) Fujiwara, Y.; Kurokawa, T.; Takeshita, K.; Kobayashi, M.; Okochi, Y.; Nakagawa, A.; Okamura, Y. *Nature Communications* **2012**, *3*.

(26) Li, S. J.; Zhao, Q.; Zhou, Q.; Unno, H.; Zhai, Y.; Sun, F. *Journal of Biological Chemistry* **2010**, *285*, 12047–12054.

(27) Zheng, H.; Liu, W.; Anderson, L.; Jiang, Q. X. *Nature Communications* **2011**, *2*.

(28) Jiang, Q. X.; Gonen, T. *Current Opinion in Structural Biology* **2012**, *22*, 529–536.

(29) Xu, Y.; Ramu, Y.; Lü, Z. *Nature* **2008**, *451*, 826–829.

(30) Schmidt, D. R.; Jiang, Q. X.; MacKinnon, R. *Nature* **2006**, *444*, 775–779.

(31) Ramu, Y.; Xu, Y.; Lü, Z. *Nature* **2006**, *442*, 696–699.

(32) Neal, M.; Beier, E. E.; Hossain, M. M.; Boyle, A.; Zheng, J.; Kim, C. K.; Mhatre-Winters, I.; Wu, L. J.; Richardson, J. *Antioxidants* **2023**, *12*, 582.

(33) Chemaly, A. E.; Jaquet, V.; Cambet, Y.; Caillon, A.; Cherpin, O.; Balafa, A.; Krause, K.; Demaurex, N. *Biochimica et Biophysica Acta (BBA) - Molecular Cell Research* **2023**, *1870*, 119415.

(34) Okuda, H.; Yonezawa, Y.; Takano, Y.; Okamura, Y.; Fujiwara, Y. *Journal of Biological Chemistry* **2016**, *291*, 5935–5947.

(35) Mony, L.; Stroebel, D.; Isacoff, E. Y. *Proceedings of the National Academy of Sciences of the United States of America* **2020**, *117*, 20898–20907.

(36) Webb, B.; Sali, A. *Current protocols in bioinformatics* **2016**, *54*.

(37) Lomize, M. A.; Pogozheva, I. D.; Joo, H.; Mosberg, H. I.; Lomize, A. L. *Nucleic Acids Research* **2011**, *40*, D370–D376.

(38) Jo, S.; Kim, T.-H.; Iyer, V.; Im, W. *Journal of Computational Chemistry* **2008**, *29*, 1859–1865.

(39) Lee, J.; Cheng, X.; Jo, S.; MacKerell, A. D.; Klauda, J. B.; Im, W. *Biophysical Journal* **2016**, *110*, 641a.

(40) Wu, E. L.; Cheng, X.; Jo, S.; Rui, H.; Song, K.; Davila-Contreras, E. M.; Qi, Y.; Lee, J.; Monje-Galvan, V.; Venable, R. M.; Klauda, J. B.; Im, W. *Journal of Computational Chemistry* **2014**, *35*, 1997–2004.

(41) Pandit, K. R.; Klauda, J. B. *Biochimica Et Biophysica Acta - Biomembranes* **2012**, *1818*, 1205–1210.

(42) Brooks, B. R.; Bruccoleri, R. E.; Olafson, B. D.; States, D. J.; Swaminathan, S.; Karplus, M. *Journal of Computational Chemistry* **1983**, *4*, 187–217.

(43) MacKerell, A. D.; Feig, M.; Brooks, C. L. *Journal of Computational Chemistry* **2004**, *25*, 1400–1415.

(44) MacKerell, A. D. et al. *Journal of Physical Chemistry B* **1998**, *102*, 3586–3616.

(45) Feller, S. E.; MacKerell, A. D. *Journal of Physical Chemistry B* **2000**, *104*, 7510–7515.

(46) Klauda, J. B.; Venable, R. M.; Freites, J. A.; O'Connor, J. W.; Tobias, D. J.; Mondragon-Ramirez, C.; Vorobyov, I.; MacKerell, A. D.; Pastor, R. W. *Journal of Physical Chemistry B* **2010**, *114*, 7830–7843.

(47) Beglov, D.; Roux, B. *Journal of Chemical Physics* **1994**, *100*, 9050–9063.

(48) Jorgensen, W. L.; Chandrasekhar, J.; Madura, J. D.; Impey, R.; Klein, M. L. *Journal of Chemical Physics* **1983**, *79*, 926–935.

(49) Kale, L. V.; Skeel, R. D.; Bhandarkar, M.; Brunner, R.; Gursoy, A.; Krawetz, N.; Phillips, J. C.; Shinozaki, A.; Varadarajan, K.; Schulten, K. *Journal of Computational Physics* **1999**, *151*, 283–312.

(50) Phillips, J. C.; Braun, R.; Wang, W.; Gumbart, J. C.; Tajkhorshid, E.; Villa, E.; Chipot, C.; Skeel, R. D.; Kale, L. V.; Schulten, K. *Journal of Computational Chemistry* **2005**, *26*, 1781–1802.

(51) Darden, T.; York, D. M.; Pedersen, L. G. *Journal of Chemical Physics* **1993**, *98*, 10089–10092.

(52) Essmann, U.; Perera, L.; Berkowitz, M. L.; Darden, T.; Lee, H.; Pedersen, L. G. *Journal of Chemical Physics* **1995**, *103*, 8577–8593.

(53) Martyna, G.; Tobias, D. J.; Klein, M. L. *Journal of Chemical Physics* **1994**, *101*, 4177–4189.

(54) Feller, S. E.; Zhang, Y.; Pastor, R. W.; Brooks, B. R. *Journal of Chemical Physics* **1995**, *103*, 4613–4621.

(55) Ryckaert, J. P.; Ciccotti, G.; Berendsen, H. J. C. *Journal of Computational Physics* **1977**, *23*, 327–341.

(56) Grubmüller, H.; Heller, H.; Windemuth, A.; Schulten, K. *Molecular Simulation* **1991**, *6*, 121–142.

(57) Tuckerman, M. E.; Berne, B. J.; Martyna, G. *Journal of Chemical Physics* **1992**, *97*, 1990–2001.

(58) Hagberg, A.; Schult, D. A.; Swart, P. J. *Proceedings of the 7th Phyton in Science Conference (SciPy 2008)* **2008**,

(59) Siemers, M.; Lazaratos, M.; Karathanou, K.; Guerra, F.; Brown, L. S.; Bondar, A. *Journal of Chemical Theory and Computation* **2019**, *15*, 6781–6798.

(60) Siemers, M.; Bondar, A.-N. *Journal of Chemical Information and Modeling* **2021**, *61*, 2998–3014.

(61) Cormen, T. H.; Leiserson, C. E.; Rivest, R. L.; Stein, C. *Introduction to Algorithms, third edition*; 2009.

(62) Humphrey, W.; Dalke, A.; Schulten, K. *Journal of Molecular Graphics* **1996**, *14*, 33–38.

(63) Sakata, S.; Kurokawa, T.; Nørholm, M. H. H.; Takagi, M.; Okochi, Y.; Von Heijne, G.; Okamura, Y. *Proceedings of the National Academy of Sciences of the United States of America* **2009**, *107*, 2313–2318.

(64) DeCoursey, T. E.; Morgan, D.; Musset, B.; Cherny, V. V. *The Journal of General Physiology* **2016**, *148*, 97–118.

(65) Bertalan, E.; Lešnik, S.; Bren, U.; Bondar, A.-N. *Journal of Structural Biology* **2020**, *212*, 107634.

(66) Van Keulen, S. C.; Gianti, E.; Carnevale, V.; Klein, M. L.; Röthlisberger, U.; Delemotte, L. *Journal of Physical Chemistry B* **2016**, *121*, 3340–3351.

(67) Crooks, G. E.; Hon, G. C.; Chandonia, J.-M.; Brenner, S. E. *Genome Research* **2004**, *14*, 1188–1190.

(68) Scheiner, S. *Hydrogen bonding: A theoretical perspective*; 1997.

(69) Sievers, F.; Wilm, A.; Dineen, D.; Gibson, T. J.; Karplus, K.; Li, W.; Lopez, R.; McWilliam, H.; Remmert, M.; Söding, J.; Thompson, J.; Higgins, D. G. *Molecular Systems Biology* **2011**, *7*.

(70) Bertalan, e.; Lesca, E.; Schertler, G.; Bondar, A. *Journal of Chemical Information and Modeling* **2021**, *61*, 5692–5707.

# Bibliography


1. Bränden, C.-I. & Tooze, J. *Introduction to protein structure* (2012).
2. Pace, C. N., Fu, H., Fryar, K. L., Landua, J. D., Trevino, S., Schell, D., Thurlkill, R. L., Imura, S., Scholtz, J. M., Gajiwala, K., Sevcik, J., Urbanikova, L., Myers, J. K., Takano, K., Hebert, E., Shirley, B. A. & Grimsley, G. R. Contribution of hydrogen bonds to protein stability. *Protein Science* **23,** 652–661 (2014).
3. Vanderkooi, J. M., Dashnau, J. L. & Zelent, B. Temperature excursion infrared (TEIR) spectroscopy used to study hydrogen bonding between water and biomolecules. *Biochimica et Biophysica Acta (BBA) - Proteins and Proteomics* **1749,** 214–233 (2005).
4. Cooper, G. M. *The Cell: A Molecular Approach 2nd edition* (2000).
5. Kollman, P. A. & Allen, L. C. Theory of the hydrogen bond. *Chemical Reviews* **72,** 283–303 (1972).
6. Jeffrey, G. A. & Saenger, W. *Hydrogen bonding in biological structures* (1991).
7. Arunan, E., Desiraju, G. R., Klein, R. A., Sadlej, J., Scheiner, S., Alkorta, I., Clary, D. C., Crabtree, R. H., Dannenberg, J. J., Hobza, P., Kjaergaard, H. G., Legon, A. C., Mennucci, B. & Nesbitt, D. J. Defining the hydrogen bond: An account (IUPAC Technical Report). *Pure and Applied Chemistry* **83,** 1619–1636 (2011).
8. Harris, T. K. & Mildvan, A. S. High-Precision measurement of hydrogen bond lengths in proteins by nuclear magnetic resonance methods. *Proteins: Structure, Function, and Bioinformatics* **35,** 275–282 (1999).
9. Hibbert, F. & Emsley, J. *Hydrogen bonding and chemical reactivity* 255–379 (1990).
10. Shan, S.-o. & Herschlag, D. The change in hydrogen bond strength accompanying charge rearrangement: Implications for enzymatic catalysis. *Proceedings of the National Academy of Sciences of the United States of America* **93,** 14474–14479 (1996).
11. Eswar, N. & Ramakrishnan, C. Deterministic features of side-chain main-chain hydrogen bonds in globular protein structures. *Protein Engineering Design & Selection* **13,** 227–238 (2000).
12. Myers, J. K. & Pace, C. N. Hydrogen bonding stabilizes globular proteins. *Biophysical Journal* **71,** 2033–2039 (1996).
13. Ben-Naim, A. The role of hydrogen bonds in protein folding and protein association. *The Journal of Physical Chemistry* **95,** 1437–1444 (1991).

14. Deechongkit, S., Nguyen, H., Powers, E. T., Dawson, P. E., Gruebele, M. & Kelly, J. W. Context-dependent contributions of backbone hydrogen bonding to $\beta$-sheet folding energetics. *Nature* **430,** 101–105 (2004).

15. Rose, G. D., Fleming, P., Banavar, J. R. & Maritan, A. A backbone-based theory of protein folding. *Proceedings of the National Academy of Sciences of the United States of America* **103,** 16623–16633 (2006).

16. Bordo, D. & Argos, P. The role of side-chain hydrogen bonds in the formation and stabilization of secondary structure in soluble proteins. *Journal of Molecular Biology* **243,** 504–519 (1994).

17. Eswar, N. & Ramakrishnan, C. Secondary structures without backbone: an analysis of backbone mimicry by polar side chains in protein structures. *Protein Engineering Design & Selection* **12,** 447–455 (1999).

18. Fersht, A. R. The hydrogen bond in molecular recognition. *Trends in Biochemical Sciences* **12,** 301–304 (1987).

19. Thurlkill, R. L., Grimsley, G. R., Scholtz, J. M. & Pace, C. N. Hydrogen bonding markedly reduces the PK of buried carboxyl groups in proteins. *Journal of Molecular Biology* **362,** 594–604 (2006).

20. Bondar, A.-N. & White, S. H. Hydrogen bond dynamics in membrane protein function. *Biochimica et Biophysica Acta (BBA) - Biomembranes* **1818,** 942–950 (2012).

21. Corin, K. & Bowie, J. U. How bilayer properties influence membrane protein folding. *Protein Science* **29,** 2348–2362 (2020).

22. Boggs, J. M. Lipid intermolecular hydrogen bonding: influence on structural organization and membrane function. *Biochimica et biophysica acta* **906,** 353–404 (1987).

23. Seu, K. J., Cambrea, L. R., Everly, R. M. & Hovis, J. S. Influence of lipid chemistry on membrane fluidity: tail and headgroup interactions. *Biophysical Journal* **91,** 3727–3735 (2006).

24. Pasenkiewicz-Gierula, M., Takaoka, Y., Miyagawa, H., Kïtamura, K. & Kusumi, A. Hydrogen Bonding of Water to Phosphatidylcholine in the Membrane As Studied by a Molecular Dynamics Simulation: Location, Geometry, and Lipid-Lipid Bridging via Hydrogen-Bonded Water. *Journal of Physical Chemistry A* **101,** 3677–3691 (1997).

25. Slater, S. J., Ho, C., Taddeo, F. J., Kelly, M. B. & Stubbs, C. D. Contribution of hydrogen bonding to lipid-lipid interactions in membranes and the role of lipid order: Effects of cholesterol, increased phospholipid unsaturation, and ethanol. *Biochemistry* **32,** 3714–3721 (1993).

26. Coimbra, J. T. S., Feghali, R., Ribeiro, R. P., Ramos, M. J. & Fernandes, P. A. The importance of intramolecular hydrogen bonds on the translocation of the small drug piracetam through a lipid bilayer. *RSC Advances* **11,** 899–908 (2021).

27. Geragotelis, A. D., Wood, M. L., Göddeke, H., Luan, H., Webster, P. D., Wong, E., Freites, J. A., Tombola, F. & Tobias, D. J. Voltage-dependent structural models of the human Hv1 proton channel from long-timescale molecular dynamics simulations. *Proceedings of the National Academy of Sciences of the United States of America* **117,** 13490–13498 (2020).

28. Guerra, F., Siemers, M., Mielack, C. & Bondar, A.-N. Dynamics of Long-Distance Hydrogen-Bond networks in Photosystem II. *Journal of Physical Chemistry B* **122,** 4625–4641 (2018).

29. Bondar, A.-N. & Smith, J. C. Protonation-state-Coupled conformational dynamics in reaction mechanisms of channel and pump rhodopsins. *Photochemistry and Photobiology* **93,** 1336–1344 (2017).

30. Del Val, C., Bondar, L. N. & Bondar, A.-N. Coupling between inter-helical hydrogen bonding and water dynamics in a proton transporter. *Journal of Structural Biology* **186,** 95–111 (2014).

31. Joh, N. H., Min, A., Faham, S., Whitelegge, J. P., Yang, D., Woods, V. L. & Bowie, J. U. Modest stabilization by most hydrogen-bonded side-chain interactions in membrane proteins. *Nature* **453,** 1266–1270 (2008).

32. Lazaratos, M., Karathanou, K. & Bondar, A.-N. Graphs of dynamic H-bond networks: from model proteins to protein complexes in cell signaling. *Current Opinion in Structural Biology* **64,** 79–87 (2020).

33. Karathanou, K. & Bondar, A.-N. Using Graphs of Dynamic Hydrogen-Bond Networks To Dissect Conformational Coupling in a Protein Motor. *Journal of Chemical Information and Modeling* **59,** 1882–1896 (2019).

34. Siemers, M., Lazaratos, M., Karathanou, K., Guerra, F., Brown, L. S. & Bondar, A.-N. Bridge: a Graph-Based algorithm to analyze dynamic H-Bond networks in membrane proteins. *Journal of Chemical Theory and Computation* **15,** 6781–6798 (2019).

35. Harris, A. L., Lazaratos, M., Siemers, M., Ethan, W., Anh, H., Tomida, S., Schubert, L., Saita, M., Heberle, J., Furutani, Y., Kandori, H., Bondar, A.-N. & Brown, L. S. Mechanism of inward proton transport in an Antarctic microbial rhodopsin. *Journal of Physical Chemistry B* **124,** 4851–4872 (2020).

36. Karathanou, K., Lazaratos, M., Bertalan, E., Siemers, M., Buzar, K., Schertler, G., Del Val, C. & Bondar, A.-N. A graph-based approach identifies dynamic H-bond communication networks in spike protein S of SARS-CoV-2. *Journal of Structural Biology* **212,** 107617 (2020).

37. Krishnamurthy, S., Eleftheriadis, N., Karathanou, K., Smit, J. H., Portaliou, A. G., Chatzi, K., Karamanou, S., Bondar, A.-N., Gouridis, G. & Economou, A. A nexus of intrinsic dynamics underlies translocase priming. *Structure* **29,** 846–858.e7 (2021).

38. Shinobu, A. & Agmon, N. Mapping proton wires in proteins: carbonic anhydrase and GFP chromophore biosynthesis. *Journal of Physical Chemistry A* **113,** 7253–7266 (2009).

39. Cai, X., Haider, K., Lu, J., Radic, S., Son, C. Y., Cui, Q. & Gunner, M. R. Network analysis of a proposed exit pathway for protons to the P-side of cytochrome c oxidase. *Biochimica et Biophysica Acta (BBA) - Bioenergetics* **1859,** 997–1005 (2018).

40. Rahat, O., Alon, U., Levy, Y. & Schreiber, G. Understanding hydrogen-bond patterns in proteins using network motifs. *Bioinformatics* **25,** 2921–2928 (2009).

41. Ghane, T., Gorriz, R. F., Wrzalek, S., Volkenandt, S., Dalatieh, F., Reidelbach, M. & Imhof, P. Hydrogen-Bonded Network and Water Dynamics in the D-channel of Cytochrome c Oxidase. *The Journal of Membrane Biology* **251,** 299–314 (2018).

42. Karathanou, K. & Bondar, A.-N. Algorithm to catalogue topologies of dynamic lipid hydrogen-bond networks. *Biochimica et Biophysica Acta (BBA) - Biomembranes* **1864,** 183859 (2022).

43. Karathanou, K. & Bondar, A.-N. Dynamic water Hydrogen-Bond networks at the interface of a lipid membrane containing Palmitoyl-Oleoyl phosphatidylglycerol. *The Journal of Membrane Biology* **251,** 461–473 (2018).

44. Hubbard, R. E. & Haider, M. K. Hydrogen bonds in proteins: role and strength. *eLS* (2010).

45. Espinosa, E., Sarwat, M., Lachekar, H. & Lecomte, C. Topological analysis of the electron density in hydrogen bonds. *Acta crystallographica* **55,** 563–572 (1999).

46. Scheiner, S. *Hydrogen bonding: A theoretical perspective* (1997).

47. Tsubomura, H. The Nature of the Hydrogen-Bond. I. The Delocalization Energy in the Hydrogen-Bond as Calculated by the Atomic-orbital Method. *Bulletin of the Chemical Society of Japan* **27,** 445–450 (1954).

48. Espinosa, E., Molins, E. & Lecomte, C. Hydrogen bond strengths revealed by topological analyses of experimentally observed electron densities. *Chemical Physics Letters* **285,** 170–173 (1998).

49. Adalsteinsson, H., Maulitz, H., A. & Bruice, T. C. Calculation of the Potential Energy Surface for Intermolecular Amide Hydrogen Bonds Using Semiempirical and *Ab Initio* Methods. *Journal of the American Chemical Society* **118,** 7689–7693 (1996).

50. Uphoff, A., Hermansson, M., Haimi & Somerharju, P. *Analysis of complex lipidomes* 223–249 (Elsevier Scientific Publ. Co., 2007).

51. Dowhan, W. MOLECULAR BASIS FOR MEMBRANE PHOSPHOLIPID DIVERSITY: Why Are There So Many Lipids? *Annual Review of Biochemistry* **66,** 199–232 (1997).

52. Bigay, J. & Antonny, B. Curvature, lipid packing, and electrostatics of membrane organelles: defining cellular territories in determining specificity. *Developmental Cell* **23,** 886–895 (2012).

53. Gennis, R. Biomembranes: molecular structure and function. *Choice Reviews Online* **27,** 27–0304 (1989).

54. Ji, J., Sun, L., Luo, Z., Zhang, Y., Wang, X., Liao, Y., Xie, T. & Shan, J. Potential therapeutic applications of pulmonary surfactant lipids in the host defence against respiratory viral infections. *Frontiers in Immunology* **12** (2021).

55. Numata, M., Chu, H. W., Dakhama, A. & Voelker, D. R. Pulmonary surfactant phosphatidylglycerol inhibits respiratory syncytial virus–induced inflammation and infection. *Proceedings of the National Academy of Sciences of the United States of America* **107,** 320–325 (2009).

56. Numata, M., Kandasamy, P., Nagashima, Y., Fickes, R., Murphy, R. C. & Voelker, D. R. Phosphatidylinositol inhibits respiratory syncytial virus infection. *Journal of Lipid Research* **56,** 578–587 (2015).

57. Blankenberg, F. G. & Norfray, J. F. Multimodality Molecular imaging of apoptosis in oncology. *American Journal of Roentgenology* **197,** 308–317 (2011).

58. Rivel, T., Ramseyer, C. & Yesylevskyy, S. O. The asymmetry of plasma membranes and their cholesterol content influence the uptake of cisplatin. *Scientific Reports* **9** (2019).

59. Zwaal, R., Comfurius, P. & Bevers, E. M. Surface exposure of phosphatidylserine in pathological cells. *Cellular and Molecular Life Sciences* **62,** 971–988 (2005).

60. Yeung, T., Gilbert, G. E., Shi, J., Silvius, J. R., Kapùs, A. & Grinstein, S. Membrane phosphatidylserine regulates surface charge and protein localization. *Science* **319,** 210–213 (2008).

61. Xu, P., Baldridge, R. D., Richard, J., Burd, C. G. & Graham, T. R. Phosphatidylserine flipping enhances membrane curvature and negative charge required for vesicular transport. *Journal of Cell Biology* **202,** 875–886 (2013).

62. Symons, J. L., Cho, K.-J., Chang, J. T., Du, G., Waxham, M. N., Hancock, J. F., Levental, I. & Levental, K. R. Lipidomic atlas of mammalian cell membranes reveals hierarchical variation induced by culture conditions, subcellular membranes, and cell lineages. *Soft Matter* **17,** 288–297 (2021).

63. Oldfield, E., Meadows, M. D., Rice, D. & Jacobs, R. E. Spectroscopic studies of specifically deuterium labeled membrane systems. Nuclear magnetic resonance investigation of the effects of cholesterol in model systems. *Biochemistry* **17,** 2727–2740 (1978).

64. Urbina, J. A., Pekerar, S., Le, H. B., Patterson, J., Montez, B. & Oldfield, E. Molecular order and dynamics of phosphatidylcholine bilayer membranes in the presence of cholesterol, ergosterol and lanosterol: a comparative study using 2H-, 13C- and 31P-NMR spectroscopy. *Biochimica et Biophysica Acta (BBA) - Biomembranes* **1238,** 163–176 (1995).

65. Mills, T. T., Toombes, G. E. S., Tristram-Nagle, S., Smilgies, D.-M., Feigenson, G. W. & Nagle, J. F. Order parameters and areas in Fluid-Phase oriented lipid membranes using wide angle X-Ray scattering. *Biophysical Journal* **95,** 669–681 (2008).

66. Shahane, G., Ding, W., Palaiokostas, M. & Orsi, M. Physical properties of model biological lipid bilayers: insights from all-atom molecular dynamics simulations. *Journal of Molecular Modeling* **25** (2019).

67. Filippov, A. V., Orädd, G. & Lindblom, G. The effect of cholesterol on the lateral diffusion of phospholipids in oriented bilayers. *Biophysical Journal* **84,** 3079–3086 (2003).

68. Patra, M. Lateral pressure profiles in cholesterol–DPPC bilayers. *European Biophysics Journal* **35,** 79–88 (2005).

69. Ollila, O. H. S., Rog, T., Karttunen, M. & Vattulainen, I. Role of sterol type on lateral pressure profiles of lipid membranes affecting membrane protein functionality: Comparison between cholesterol, desmosterol, 7-dehydrocholesterol and ketosterol. *Journal of Structural Biology* **159,** 311–323 (2007).

70. Leathes, J. Croonian lectures ON THE RÔLE OF FATS IN VITAL PHENOMENA. *The Lancet* **205,** 853–856 (1925).

71. Demel, R., Van Deenen, L. & Pethica, B. A. Monolayer interactions of phospholipids and cholesterol. *Biochimica et Biophysica Acta (BBA) - Biomembranes* **135,** 11–19 (1967).

72. Phillips, M. C. *The physical state of phospholipids and cholesterol in monolayers, bilayers, and membranes* 139–221 (1972).

73. Alwarawrah, M., Dai, J. & Huang, J. A Molecular view of the cholesterol condensing effect in DOPC lipid bilayers. *Journal of Physical Chemistry B* **114,** 7516–7523 (2010).

74. Saito, H., Morishita, T., Mizukami, T., Nishiyama, K., Kawaguchi, K. & Nagao, H. Molecular dynamics study of binary POPC bilayers: molecular condensing effects on membrane structure and dynamics. *Journal of physics* **1136,** 012022 (2018).

75. Ho, T. H., Nguyen, T. & Huynh, L. K. Formation of lipid raft nanodomains in homogeneous ternary lipid mixture of POPC/DPSM/cholesterol: Theoretical insights. *Biochimica et Biophysica Acta (BBA) - Biomembranes* **1864,** 184027 (2022).

76. Luchetti, G., Sircar, R., Kong, J. H., Nachtergaele, S., Sagner, A., Byrne, E. F., Covey, D. F., Siebold, C. & Rohatgi, R. Cholesterol activates the G-protein coupled receptor Smoothened to promote Hedgehog signaling. *eLife* **5** (2016).

77. Travis, A. J. & Kopf, G. S. The role of cholesterol efflux in regulating the fertilization potential of mammalian spermatozoa. *Journal of Clinical Investigation* **110,** 731–736 (2002).

78. Simons, M., Keller, P., Dichgans, J. & Schulz, J. B. Cholesterol and Alzheimer's disease: Is there a link? *Neurology* **57,** 1089–1093 (2001).

79. Llaverias, G., Danilo, C., Mercier, I. L., Daumer, K. M., Capozza, F., Williams, T. M., Sotgia, F., Lisanti, M. P. & Frank, P. G. Role of cholesterol in the development and progression of breast cancer. *American Journal of Pathology* **178,** 402–412 (2011).

80. Ding, X., Zhang, W., Li, S. & Yang, H. The role of cholesterol metabolism in cancer. *PubMed* **9,** 219–227 (2019).

81. Yan, A., Jia, Z., Qiao, C.-F., Wang, M. & Ding, X. Cholesterol metabolism in drug-resistant cancer (Review). *International Journal of Oncology* (2020).

82. Huang, B., Song, B.-L. & Xu, C. Cholesterol metabolism in cancer: mechanisms and therapeutic opportunities. *Nature Metabolism* **2,** 132–141 (2020).

83. Pyrkova, D. V., Tarasova, N. K., Krylov, H. A., Nolde, D. E., Pentkovsky, V. M. & Efremov, R. G. Dynamic clustering of lipids in hydrated two-component membranes: results of computer modeling and putative biological impact. *Journal of Biomolecular Structure & Dynamics* **31,** 87–95 (2013).

84. Yesylevskyy, S. O. & Demchenko, A. P. *Cholesterol Behavior in Asymmetric Lipid Bilayers: Insights from Molecular Dynamics Simulations* 291–306 (2014).

85. DeCoursey, T. E. Voltage-Gated Proton Channels: Molecular Biology, Physiology, and Pathophysiology of the $H_V$Family. *Physiological Reviews* **93,** 599–652 (2013).

86. Hondares, E., Brown, M., Musset, B., Morgan, D., Cherny, V. V., Taubert, C., Bhamrah, M., Coe, D., Marelli-Berg, F. M., Gribben, J. G., Dyer, M. J. S., DeCoursey, T. E. & Capasso, M. Enhanced activation of an amino-terminally truncated isoform of the voltage-gated proton channel HVCN1 enriched in malignant B cells. *Proceedings of the National Academy of Sciences of the United States of America* **111,** 18078–18083 (2014).

87. Wang, Y., Li, S. J., Juncheng, P., Che, Y., Yin, J. & Zhao, Q. Specific expression of the human voltage-gated proton channel Hv1 in highly metastatic breast cancer cells, promotes tumor progression and metastasis. *Biochemical and Biophysical Research Communications* **412,** 353–359 (2011).

88. Wang, Y., Li, S. J., Wu, X., Che, Y. & Li, Q. Clinicopathological and biological significance of human voltage-gated proton channel HV1 protein overexpression in breast cancer. *Journal of Biological Chemistry* **287,** 13877–13888 (2012).

89. Wang, Y., Wu, X., Li, Q., Zhang, S. & Li, S. J. Human Voltage-Gated Proton Channel HV1: a new potential biomarker for diagnosis and prognosis of colorectal cancer. *PLOS ONE* **8,** e70550 (2013).

90. Neal, M., Beier, E. E., Hossain, M. M., Boyle, A., Zheng, J., Kim, C. K., Mhatre-Winters, I., Wu, L. J. & Richardson, J. Voltage-Gated proton Channel HV1 regulates neuroinflammation and dopaminergic neurodegeneration in Parkinson's disease models. *Antioxidants* **12,** 582 (2023).

91. Bayrhuber, M., Maslennikov, I., Kwiatkowski, W., Sobol, A. A., Wierschem, C., Eichmann, C., Frey, L. & Riek, R. Nuclear magnetic resonance solution structure and functional behavior of the human proton channel. *Biochemistry* **58,** 4017–4027 (2019).

92. Ramsey, I. S., Mokrab, Y., Carvacho, I., Sands, Z. A., Sansom, M. S. P. & Clapham, D. E. An aqueous H+ permeation pathway in the voltage-gated proton channel Hv1. *Nature Structural & Molecular Biology* **17,** 869–875 (2010).

93. Ramsey, I. S., Moran, M. M., Chong, J. A. & Clapham, D. E. A voltage-gated proton-selective channel lacking the pore domain. *Nature* **440,** 1213–1216 (2006).

94. Gutman, M. & Nachliel, E. The dynamic aspects of proton transfer processes. *Biochimica et Biophysica Acta (BBA) - Bioenergetics* **1015,** 391–414 (1990).

95. Sacks, V., Marantz, Y., Aagaard, A., Checover, S., Nachliel, E. & Gutman, M. The dynamic feature of the proton collecting antenna of a protein surface. *Biochimica et Biophysica Acta (BBA) - Bioenergetics* **1365,** 232–240 (1998).

96. Ädelroth, P. & Brzezinski, P. Surface-mediated proton-transfer reactions in membrane-bound proteins. *Biochimica et Biophysica Acta (BBA) - Bioenergetics* **1655,** 102–115 (2004).

97. Marantz, Y., Nachliel, E., Aagaard, A., Brzezinski, P. & Gutman, M. The proton collecting function of the inner surface of cytochrome *c* oxidase from *Rhodobacter sphaeroides*. *Proceedings of the National Academy of Sciences of the United States of America* **95,** 8590–8595 (1998).

98. Shutova, T., Klimov, V. V., Andersson, B. & Samuelsson, G. A cluster of carboxylic groups in PsbO protein is involved in proton transfer from the water oxidizing complex of Photosystem II. *Biochimica et Biophysica Acta (BBA) - Bioenergetics* **1767,** 434–440 (2007).

99. Grimsley, G. R., Scholtz, J. M. & Pace, C. N. A summary of the measured p*K* values of the ionizable groups in folded proteins. *Protein Science* **18,** 247–251 (2008).

100. Lorch, S., Capponi, S., Pieront, F. & Bondar, A.-N. Dynamic Carboxylate/Water networks on the surface of the PSBO subunit of Photosystem II. *Journal of Physical Chemistry B* **119,** 12172–12181 (2015).

101. Kemmler, L., Ibrahim, M., Dobbek, H., Zouni, A. & Bondar, A.-N. Dynamic water bridging and proton transfer at a surface carboxylate cluster of photosystem II. *Physical Chemistry Chemical Physics* **21,** 25449–25466 (2019).

102. Checover, S., Marantz, Y., Nachliel, E., Gutman, M., Pfeiffer, M., Tittor, J., Oesterhelt, D. & Dencher, N. A. Dynamics of the proton transfer reaction on the cytoplasmic surface of bacteriorhodopsin. *Biochemistry* **40,** 4281–4292 (2001).

103. Shinobu, A., Palm, G. J., Schierbeek, A. & Agmon, N. Visualizing proton antenna in a High-Resolution Green fluorescent protein structure. *Journal of the American Chemical Society* **132,** 11093–11102 (2010).

104. Gutman, M. & Nachliel, E. The dynamics of proton exchange between bulk and surface groups. *Biochimica et Biophysica Acta (BBA) - Bioenergetics* **1231,** 123–138 (1995).

105. Peitzsch, R. M., Eisenberg, M., Sharp, K. A. & McLaughlin, S. Calculations of the electrostatic potential adjacent to model phospholipid bilayers. *Biophysical Journal* **68,** 729–738 (1995).

106. Gutman, M. & Nachliel, E. TIME-RESOLVED DYNAMICS OF PROTON TRANSFER IN PROTEINOUS SYSTEMS. *Annual Review of Physical Chemistry* **48,** 329–356 (1997).

107. Medvedev, E. S. & Stuchebrukhov, A. A. Kinetics of proton diffusion in the regimes of fast and slow exchange between the membrane surface and the bulk solution. *Journal of Mathematical Biology* **52,** 209–234 (2005).

108. Yamashita, T. & Voth, G. A. Properties of Hydrated Excess Protons near Phospholipid Bilayers. *Journal of Physical Chemistry B* **114,** 592–603 (2009).

109. Georgievskii, Y., Medvedev, E. S. & Stuchebrukhov, A. A. Proton transport via coupled surface and bulk diffusion. *Journal of Chemical Physics* **116,** 1692–1699 (2002).

110. Georgievskii, Y., Medvedev, E. S. & Stuchebrukhov, A. A. Proton transport via the membrane surface. *Biophysical Journal* **82,** 2833–2846 (2002).

111. Nachliel, E. & Gutman, M. Reaction within the coulomb-cage; science in retrospect. *Biochimica et Biophysica Acta (BBA) - Biomembranes* **1865,** 184071 (2023).

112. Agmon, N. The Grotthuss mechanism. *Chemical Physics Letters* **244,** 456–462 (1995).

113. Nguyen, T. H., Zhang, C., Weichselbaum, E., Knyazev, D. G., Pohl, P. & Carloni, P. Interfacial water molecules at biological membranes: Structural features and role for lateral proton diffusion. *PLOS ONE* **13,** e0193454 (2018).

114. Smondyrev, A. M. & Voth, G. A. Molecular dynamics simulation of proton transport near the surface of a phospholipid membrane. *Biophysical Journal* **82,** 1460–1468 (2002).

115. Brooks, B. R., Bruccoleri, R. E., Olafson, B. D., States, D. J., Swaminathan, S. & Karplus, M. CHARMM: A program for macromolecular energy, minimization, and dynamics calculations. *Journal of Computational Chemistry* **4,** 187–217 (1983).

116. MacKerell, A. D., Feig, M. & Brooks, C. L. Extending the treatment of backbone energetics in protein force fields: Limitations of gas-phase quantum mechanics in reproducing protein conformational distributions in molecular dynamics simulations. *Journal of Computational Chemistry* **25,** 1400–1415 (2004).

117. MacKerell, A. D., Bashford, D., Bellott, M., Dunbrack, R. L., Evanseck, J. D., Field, M. J., Fischer, S., Gao, J., Guo, H., Ha, S., Joseph-McCarthy, D., Kuchnir, L., Kuczera, K., Lau, F. T. K., Mattos, C., Michnick, S. W., Ngo, T., Nguyen, D. T., Prod'hom, B., Reiher, W., Roux, B., Schlenkrich, M., Smith, J. C., Stote, R. H., Straub, J. E., Watanabe, M., Wiorkiewicz-Kuczera, J., Yin, D. & Karplus, M. All-Atom empirical potential for molecular modeling and dynamics studies of proteins. *Journal of Physical Chemistry B* **102,** 3586–3616 (1998).

118. Feller, S. E. & MacKerell, A. D. An improved empirical potential energy function for molecular simulations of phospholipids. *Journal of Physical Chemistry B* **104,** 7510–7515 (2000).

119. Klauda, J. B., Venable, R. M., Freites, J. A., O'Connor, J. W., Tobias, D. J., Mondragon-Ramirez, C., Vorobyov, I., MacKerell, A. D. & Pastor, R. W. Update of the CHARMM All-Atom Additive Force Field for Lipids: Validation on six lipid types. *Journal of Physical Chemistry B* **114,** 7830–7843 (2010).

120. Beglov, D. & Roux, B. Finite representation of an infinite bulk system: Solvent boundary potential for computer simulations. *Journal of Chemical Physics* **100,** 9050–9063 (1994).

121. Huang, J. & MacKerell, A. D. CHARMM36 all-atom additive protein force field: Validation based on comparison to NMR data. *Journal of Computational Chemistry* **34,** 2135–2145 (2013).

122. Best, R. B., Zhu, X. X., Shim, J., Lopes, P., Mittal, J., Feig, M. & MacKerell, A. D. Optimization of the Additive CHARMM All-Atom Protein Force Field Targeting Improved Sampling of the Backbone $\phi$, $\psi$ and Side-Chain $\chi_1$ and $\chi_2$ Dihedral Angles. *Journal of Chemical Theory and Computation* **8,** 3257–3273 (2012).

123. Brooks, B., Brooks, C., MacKerell, A. D., Nilsson, L. M., Petrella, R. J., Roux, B., Won, Y., Archontis, G., Bartels, C., Boresch, S., Caflisch, A., Caves, L., Cui, Q., Dinner, A. R., Feig, M., Fischer, S. M., Gao, J. R., Hodošček, M., Im, W., Kuczera, K., Lazaridis, T., Ma, J., Ovchinnikov, V., Paci, E., Pastor, R. W., Post, C. B., Pu, J., Schaefer, M., Tidor, B., Venable, R. M., Woodcock, H. L., Wu, X., Yang, W., York, D. G. & Karplus, M. CHARMM: The biomolecular simulation program. *Journal of Computational Chemistry* **30,** 1545–1614 (2009).

124. MacKerell, A. D., Feig, M. & Brooks, C. L. Improved treatment of the protein backbone in empirical force fields. *Journal of the American Chemical Society* **126,** 698–699 (2003).

125. Buck, M., Bouguet-Bonnet, S., Pastor, R. W. & MacKerell, A. D. Importance of the CMAP correction to the CHARMM22 protein force field: Dynamics of hen lysozyme. *Biophysical Journal* **90,** L36–L38 (2006).

126. MacKerell, A. D. Empirical force fields for biological macromolecules: Overview and issues. *Journal of Computational Chemistry* **25,** 1584–1604 (2004).

127. Gross, J. & Yellen, J. *Graph Theory and its applications* (2005).

128. Siemers, M. & Bondar, A.-N. Interactive Interface for Graph-Based Analyses of Dynamic H-Bond Networks: Application to Spike Protein S. *Journal of Chemical Information and Modeling* **61,** 2998–3014 (2021).

129. Bertalan, E., Lešnik, S., Bren, U. & Bondar, A.-N. Protein-water hydrogen-bond networks of G protein-coupled receptors: Graph-based analyses of static structures and molecular dynamics. *Journal of Structural Biology* **212,** 107634 (2020).

130. Lešnik, S., Bertalan, E., Bren, U. & Bondar, A.-N. Opioid receptors and Protonation-Coupled binding of opioid drugs. *International Journal of Molecular Sciences* **22,** 13353 (2021).

131. Lešnik, S., Bren, U., Domratcheva, T. & Bondar, A.-N. Fentanyl and the fluorinated fentanyl derivative NFEPP elicit distinct Hydrogen-Bond dynamics of the opioid receptor. *Journal of Chemical Information and Modeling* **63,** 4732–4748 (2023).

132. Bondar, A.-N. & Alfonso-Prieto, M. Hydrogen-bond networks for proton couplings in G-Protein coupled receptors. *Frontiers in Physics* **10** (2022).

133. Cormen, T. H., Leiserson, C. E., Rivest, R. L. & Stein, C. *Introduction to Algorithms, third edition* (2009).

134. Hagberg, A., Schult, D. A. & Swart, P. J. Exploring Network Structure, Dynamics, and Function using NetworkX. *Proceedings of the 7th Phyton in Science Conference (SciPy 2008)* (2008).

135. Jo, S., Kim, T.-H. & Im, W. Automated builder and database of Protein/Membrane Complexes for molecular Dynamics simulations. *PLOS ONE* **2,** e880 (2007).

136. Jo, S., Kim, T.-H., Iyer, V. & Im, W. CHARMM-GUI: A web-based graphical user interface for CHARMM. *Journal of Computational Chemistry* **29,** 1859–1865 (2008).

137. Jo, S., Lim, J. B., Klauda, J. B. & Im, W. CHARMM-GUI membrane builder for mixed bilayers and its application to yeast membranes. *Biophysical Journal* **97,** 50–58 (2009).

138. Jo, S., Cheng, X., Islam, S. M., Huang, L., Rui, H., Zhu, A., Lee, H. S., Qi, Y., Han, W., Vanommeslaeghe, K., MacKerell, A. D., Roux, B. & Im, W. *CHARMM-GUI PDB manipulator for advanced modeling and simulations of proteins containing nonstandard residues* 235–265 (2014).

139. Wu, E. L., Cheng, X., Jo, S., Rui, H., Song, K., Davila-Contreras, E. M., Qi, Y., Lee, J., Monje-Galvan, V., Venable, R. M., Klauda, J. B. & Im, W. CHARMM-GUI *Membrane Builder* toward realistic biological membrane simulations. *Journal of Computational Chemistry* **35,** 1997–2004 (2014).

140. Webb, B. & Sali, A. Comparative protein structure modeling using MODELLER. *Current protocols in bioinformatics* **54** (2016).

141. Kale, L. V., Skeel, R. D., Bhandarkar, M., Brunner, R., Gursoy, A., Krawetz, N., Phillips, J. C., Shinozaki, A., Varadarajan, K. & Schulten, K. NAMD2: Greater scalability for parallel molecular dynamics. *Journal of Computational Physics* **151,** 283–312 (1999).

142. Phillips, J. C., Braun, R., Wang, W., Gumbart, J. C., Tajkhorshid, E., Villa, E., Chipot, C., Skeel, R. D., Kale, L. V. & Schulten, K. Scalable molecular dynamics with NAMD. *Journal of Computational Chemistry* **26,** 1781–1802 (2005).

143. Bennett, L., Melchers, B. & Proppe, B. Curta: A General-purpose High-Performance Computer at ZEDAT, Freie Universität Berlin (2020).

144. Humphrey, W., Dalke, A. & Schulten, K. VMD: Visual molecular dynamics. *Journal of Molecular Graphics* **14,** 33–38 (1996).

145. Trott, O. & Olson, A. J. AutoDock Vina: Improving the speed and accuracy of docking with a new scoring function, efficient optimization, and multithreading. *Journal of Computational Chemistry* **31,** 455–461 (2009).

146. Schrodinger, L. *The PyMOL Molecular Graphics System* 2015.

147. Pandit, K. R. & Klauda, J. B. Membrane models of E. coli containing cyclic moieties in the aliphatic lipid chain. *Biochimica Et Biophysica Acta - Biomembranes* **1818,** 1205–1210 (2012).

148. Takeshita, K., Sakata, S., Yamashita, E., Fujiwara, Y., Kawanabe, A., Kurokawa, T., Okochi, Y., Matsuda, M., Narita, H., Okamura, Y. & Nakagawa, A. X-ray crystal structure of voltage-gated proton channel. *Nature Structural & Molecular Biology* **21,** 352–357 (2014).

149. Lomize, M. A., Pogozheva, I. D., Joo, H., Mosberg, H. I. & Lomize, A. L. OPM database and PPM web server: resources for positioning of proteins in membranes. *Nucleic Acids Research* **40,** D370–D376 (2011).

150. Lee, J., Cheng, X., Jo, S., MacKerell, A. D., Klauda, J. B. & Im, W. CHARMM-GUI Input Generator for NAMD, Gromacs, Amber, Openmm, and CHARMM/OpenMM Simulations using the CHARMM36 Additive Force Field. *Biophysical Journal* **110,** 641a (2016).

151. Jorgensen, W. L., Chandrasekhar, J., Madura, J. D., Impey, R. & Klein, M. L. Comparison of simple potential functions for simulating liquid water. *Journal of Chemical Physics* **79,** 926–935 (1983).

152. Darden, T., York, D. M. & Pedersen, L. G. Particle mesh Ewald: An *N*.log(*N*) method for Ewald sums in large systems. *Journal of Chemical Physics* **98,** 10089–10092 (1993).

153. Essmann, U., Perera, L., Berkowitz, M. L., Darden, T., Lee, H. & Pedersen, L. G. A smooth particle mesh Ewald method. *Journal of Chemical Physics* **103,** 8577–8593 (1995).

154. Martyna, G., Tobias, D. J. & Klein, M. L. Constant pressure molecular dynamics algorithms. *Journal of Chemical Physics* **101,** 4177–4189 (1994).

155. Feller, S. E., Zhang, Y., Pastor, R. W. & Brooks, B. R. Constant pressure molecular dynamics simulation: The Langevin piston method. *Journal of Chemical Physics* **103,** 4613–4621 (1995).

156. Ryckaert, J. P., Ciccotti, G. & Berendsen, H. J. C. Numerical integration of the cartesian equations of motion of a system with constraints: molecular dynamics of n-alkanes. *Journal of Computational Physics* **23,** 327–341 (1977).

157. Grubmüller, H., Heller, H., Windemuth, A. & Schulten, K. Generalized Verlet Algorithm for Efficient Molecular Dynamics Simulations with Long-range Interactions. *Molecular Simulation* **6,** 121–142 (1991).

158. Tuckerman, M. E., Berne, B. J. & Martyna, G. Reversible multiple time scale molecular dynamics. *Journal of Chemical Physics* **97,** 1990–2001 (1992).

159. Karathanou, K. *Graph-Based Algorithm for Common Topologies of Dynamic Lipid Clusters.* 2022.

160. Jain, H., Karathanou, K. & Bondar, A.-N. Graph-Based analyses of dynamic Water-Mediated Hydrogen-Bond networks in phosphatidylserine: cholesterol membranes. *Biomolecules* **13,** 1238 (2023).

161. Guixa-Gonzalez, R., Rodriguez-Espigares, I., Ramirez-Anguita, J. M., Carrio-Gaspar, P., Martinez-Seara, H., Giorgino, T. & Selent, J. MEMBPLUGIN: studying membrane complexity in VMD. *Computer applications in the biosciences* **30,** 1478–1480 (2014).

162. Jain, H., Lazaratos, M., Pohl, P. & Bondar, A.-N. Fluctuating hydrogen bond networks couple protonation, lipid interactions, and conformational dynamics of the Hv1 ion channel (manuscript under preparation).

163. Gowers, R., Linke, M., Barnoud, J., Reddy, T., Melo, M. N., Seyler, S. L., Domanski, J., Dotson, D., Buchoux, S., Kenney, I. M. & Beckstein, O. MDANalysis: a python package for the rapid analysis of molecular dynamics simulations. *Proceedings of the Python in Science Conferences* (2016).

164. Michaud-Agrawal, N., Denning, E. J., Woolf, T. B. & Beckstein, O. MDAnalysis: A toolkit for the analysis of molecular dynamics simulations. *Journal of Computational Chemistry* **32,** 2319–2327 (2011).

165. Zhuang, X., Davila-Contreras, E. M., Beaven, A. H., Im, W. & Klauda, J. B. An extensive simulation study of lipid bilayer properties with different head groups, acyl chain lengths, and chain saturations. *Biochimica Et Biophysica Acta - Biomembranes* **1858,** 3093–3104 (2016).

166. Van Klompenburg, W., Im, N., Von Heijne, G. & De Kruijff, B. Anionic phospholipids are determinants of membrane protein topology. *The EMBO Journal* **16,** 4261–4266 (1997).

167. Lewis, R. L. & McElhaney, R. N. Calorimetric and spectroscopic studies of the thermotropic phase behavior of lipid bilayer model membranes composed of a homologous series of linear saturated phosphatidylserines. *Biophysical Journal* **79,** 2043–2055 (2000).

168. Lopez, C. F., Nielsen, S. O., Klein, M. L. & Moore, P. B. Hydrogen Bonding Structure and Dynamics of Water at the Dimyristoylphosphatidylcholine Lipid Bilayer Surface from a Molecular Dynamics Simulation. *Journal of Physical Chemistry B* **108,** 6603–6610 (2004).

169. Pitman, M. C., Suits, F., Gawrisch, K. & Feller, S. E. Molecular dynamics investigation of dynamical properties of phosphatidylethanolamine lipid bilayers. *Journal of Chemical Physics* **122** (2005).

170. Pöyry, S. & Vattulainen, I. Role of charged lipids in membrane structures — Insight given by simulations. *Biochimica Et Biophysica Acta - Biomembranes* **1858,** 2322–2333 (2016).

171. Nachliel, E. & Gutman, M. Time-resolved proton-phospholipid interaction. Methodology and kinetic analysis. *Journal of the American Chemical Society* **110,** 2629–2635 (1988).

172. Bobone, S., Hilsch, M., Storm, J., Dunsing, V., Herrmann, A. & Chiantia, S. Phosphatidylserine Lateral Organization Influences the Interaction of Influenza Virus Matrix Protein 1 with Lipid Membranes. *Journal of Virology* **91** (2017).

173. Lucas, N. & Cho, W. Phosphatidylserine binding is essential for plasma membrane recruitment and signaling function of 3-Phosphoinositide-dependent kinase-1. *Journal of Biological Chemistry* **286,** 41265–41272 (2011).

174. Husby, M. L., Amiar, S., Prugar, L. I., David, E. A., Plescia, C. B., Huie, K. E., Brannan, J. M., Dye, J. M., Pienaar, E. & Stahelin, R. V. Phosphatidylserine clustering by the Ebola virus matrix protein is a critical step in viral budding. *EMBO Reports* **23** (2022).

175. Pasenkiewicz-Gierula, M., Takaoka, Y., Miyagawa, H., Kitamura, K. & Kusumi, A. Charge pairing of headgroups in phosphatidylcholine membranes: A Molecular Dynamics Simulation study. *Biophysical Journal* **76,** 1228–1240 (1999).

176. Hung, W.-C., Lee, M.-T., Chen, F.-Y. & Huang, H. W. The condensing effect of cholesterol in lipid bilayers. *Biophysical Journal* **92,** 3960–3967 (2007).

177. Marquer, C., Laine, J., Dauphinot, L., Hanbouch, L., Lemercier-Neuillet, C., Pierrot, N., Bossers, K., Le, M., Corlier, F., Benstaali, C., Saudou, F., Wang, S., Cartier, N., Octave, J.-N., Duyckaerts, C. & Potier, M.-C. Increasing membrane cholesterol of neurons in culture recapitulates Alzheimer's disease early phenotypes. *Molecular Neurodegeneration* **9** (2014).

178. Zhao, Z., Hao, D., Wang, L., Li, J., Yuan, M., Liu, P., Wang, Y., Zhang, C., Zhou, H., Gardner, K. & Di, L. CtBP promotes metastasis of breast cancer through repressing cholesterol and activating TGF-$\beta$ signaling. *Oncogene* **38,** 2076–2091 (2018).

179. Yang, Z., Qin, W., Chen, Y., Yuan, B., Song, X., Wang, B., Shen, F., Fu, J. & Wang, H. Cholesterol inhibits hepatocellular carcinoma invasion and metastasis by promoting CD44 localization in lipid rafts. *Cancer Letters* **429,** 66–77 (2018).

180. Zalba, S. & Hagen, T. L. T. Cell membrane modulation as adjuvant in cancer therapy. *Cancer Treatment Reviews* **52,** 48–57 (2017).

181. Szlasa, W., Zendran, I., Zalesińska, A., Tarek, M. & Kulbacka, J. Lipid composition of the cancer cell membrane. *Journal of Bioenergetics and Biomembranes* **52,** 321–342 (2020).

182. Hoejholt, K. L., Mužić, T., Jensen, S., Dalgaard, L. T., Bilgin, M., Nylandsted, J., Heimburg, T., Frandsen, S. K. & Gehl, J. Calcium electroporation and electrochemotherapy for cancer treatment: Importance of cell membrane composition investigated by lipidomics, calorimetry and in vitro efficacy. *Scientific Reports* **9** (2019).

183. Chakraborty, S., Doktorova, M., Molugu, T. R., Heberle, F. A., Scott, H. L., Dzikovski, B., Nagao, M., Stingaciu, L. R., Standaert, R. F., Barrera, F. N., Khelashvili, G., Brown, M. F. & Ashkar, R. How cholesterol stiffens unsaturated lipid membranes. *Proceedings of the National Academy of Sciences* **117,** 21896–21905 (2020).

184. MacDermaid, C. M., Kashyap, H. K., DeVane, R., Shinoda, W., Klauda, J. B., Klein, M. L. & Fiorin, G. Molecular dynamics simulations of cholesterol-rich membranes using a coarse-grained force field for cyclic alkanes. *Journal of Chemical Physics* **143,** 243144 (2015).

185. Kopecka, J., Trouillas, P., Gašparović, A. Č., Gazzano, E., Assaraf, Y. G. & Riganti, C. Phospholipids and cholesterol: Inducers of cancer multidrug resistance and therapeutic targets. *Drug Resistance Updates* **49,** 100670 (2020).

186. Hutchinson, S., Battaglia, S., Roberg-Larsen, H., Hughes, T. A. & Thorne, J. L. Cholesterol metabolism and chemo-resistance in breast cancer. *Endocrine Abstracts* (2018).

187. Rowlands, L. J., Marks, A., Sanderson, J. M. & Law, R. V. $^{17}$O NMR spectroscopy as a tool to study hydrogen bonding of cholesterol in lipid bilayers. *Chemical Communications* **56,** 14499–14502 (2020).

188. Silvius, J. R. Role of cholesterol in lipid raft formation: lessons from lipid model systems. *Biochimica Et Biophysica Acta - Biomembranes* **1610,** 174–183 (2003).

189. Simons, K. & Vaz, W. L. Model systems, lipid rafts, and cell membranes. *Annual Review of Biophysics and Biomolecular Structure* **33,** 269–295 (2004).

190. Zocher, F., Van Der Spoel, D., Pohl, P. & Hub, J. S. Local partition coefficients govern solute permeability of Cholesterol-Containing membranes. *Biophysical Journal* **105,** 2760–2770 (2013).

191. Magarkar, A., Dhawan, V., Kallinteri, P., Viitala, T., Elmowafy, M., Rog, T. & Bunker, A. Cholesterol level affects surface charge of lipid membranes in saline solution. *Scientific Reports* **4** (2014).

192. Srivastava, A. & Debnath, A. Hydration dynamics of a lipid membrane: Hydrogen bond networks and lipid-lipid associations. *Journal of Chemical Physics* **148** (2018).

193. Flanagan, J. C., Valentine, M. L. & Baiz, C. R. Ultrafast dynamics at Lipid–Water interfaces. *Accounts of Chemical Research* **53,** 1860–1868 (2020).

194. Higuchi, Y., Asano, Y., Kuwahara, T. & Hishida, M. Rotational dynamics of water at the phospholipid bilayer depending on the head groups studied by molecular dynamics simulations. *Langmuir* **37,** 5329–5338 (2021).

195. Efremov, R. G. Dielectric-Dependent strength of interlipid hydrogen bonding in biomembranes: model case study. *Journal of Chemical Information and Modeling* **59,** 2765–2775 (2019).

196. Inoue, K., Singh, P. C., Nihonyanagi, S., Yamaguchi, S. & Tahara, T. Cooperative Hydrogen-Bond dynamics at a zwitterionic Lipid/Water interface revealed by 2D HD-VSFG spectroscopy. *Journal of Physical Chemistry Letters* **8,** 5160–5165 (2017).

197. Fairn, G. D., Schieber, N. L., Ariotti, N., Murphy, S., Kuerschner, L., Webb, R. I., Grinstein, S. & Parton, R. G. High-resolution mapping reveals topologically distinct cellular pools of phosphatidylserine. *Journal of Cell Biology* **194,** 257–275 (2011).

198. Hirama, T., Das, R. K., Yang, Y., Ferguson, C., Won, A., Yip, C. M., Kay, J. G., Grinstein, S., Parton, R. G. & Fairn, G. D. Phosphatidylserine dictates the assembly and dynamics of caveolae in the plasma membrane. *Journal of Biological Chemistry* **292,** 14292–14307 (2017).

199. Henin, J. & Chipot, C. Hydrogen-bonding patterns of cholesterol in lipid membranes. *Chemical Physics Letters* **425,** 329–335 (2006).

200. Chiu, S.-W., Jakobsson, E., Mashl, R. J. & Scott, H. L. Cholesterol-Induced Modifications in lipid bilayers: a simulation study. *Biophysical Journal* **83,** 1842–1853 (2002).

201. Bhide, S. Y., Zhang, Z. & Berkowitz, M. L. Molecular dynamics simulations of SOPS and sphingomyelin bilayers containing cholesterol. *Biophysical Journal* **92,** 1284–1295 (2007).

202. Jurkiewicz, P., Cwiklik, L., Vojtiškova, A., Jungwirth, P. & Hof, M. Structure, dynamics, and hydration of POPC/POPS bilayers suspended in NaCl, KCl, and CsCl solutions. *Biochimica Et Biophysica Acta - Biomembranes* **1818,** 609–616 (2012).

203. Boettcher, J. M., Davis-Harrison, R. L., Clay, M. C., Nieuwkoop, A. J., Ohkubo, Y. Z., Tajkhorshid, E., Morrissey, J. H. & Rienstra, C. M. Atomic view of Calcium-Induced clustering of phosphatidylserine in mixed lipid bilayers. *Biochemistry* **50,** 2264–2273 (2011).

204. Wang, Y.-H., Slochower, D. R. & Janmey, P. A. Counterion-mediated cluster formation by polyphosphoinositides. *Chemistry and Physics of Lipids* **182,** 38–51 (2014).

205. Böckmann, R. A., Hac, A. E., Heimburg, T. & Grubmüller, H. Effect of sodium chloride on a lipid bilayer. *Biophysical Journal* **85,** 1647–1655 (2003).

206. Mukhopadhyay, P., Monticelli, L. & Tieleman, D. P. Molecular Dynamics Simulation of a Palmitoyl-Oleoyl Phosphatidylserine Bilayer with Na+ Counterions and NaCl. *Biophysical Journal* **86,** 1601–1609 (2004).

207. Filippov, A. V., Orädd, G. & Lindblom, G. Effect of NaCl and CaCl2 on the lateral diffusion of zwitterionic and anionic lipids in bilayers. *Chemistry and Physics of Lipids* **159,** 81–87 (2009).

208. Porasso, R. D. & Cascales, J. L. Study of the effect of Na+ and Ca2+ ion concentration on the structure of an asymmetric DPPC/DPPC+DPPS lipid bilayer by molecular dynamics simulation. *Colloids and Surfaces B: Biointerfaces* **73,** 42–50 (2009).

209. Bradley, R., Slochower, D. R., Janmey, P. A. & Radhakrishnan, R. Divalent cations bind to phosphoinositides to induce ion and isomer specific propensities for nano-cluster initiation in bilayer membranes. *Royal Society Open Science* **7,** 192208 (2020).

210. Han, K., Kim, S. H., Venable, R. M. & Pastor, R. W. Design principles of PI(4,5)$P_2$ clustering under protein-free conditions: Specific cation effects and calcium-potassium synergy. *Proceedings of the National Academy of Sciences of the United States of America* **119** (2022).

211. Gurtovenko, A. A. & Vattulainen, I. Effect of NaCl and KCl on Phosphatidylcholine and Phosphatidylethanolamine Lipid Membranes: Insight from Atomic-Scale Simulations for Understanding Salt-Induced Effects in the Plasma Membrane. *Journal of Physical Chemistry B* **112,** 1953–1962 (2008).

212. Friedman, R. Membrane–Ion interactions. *The Journal of Membrane Biology* **251,** 453–460 (2018).

213. Pantelopulos, G. A. & Straub, J. E. Regimes of complex lipid bilayer phases induced by cholesterol concentration in MD simulation. *Biophysical Journal* **115,** 2167–2178 (2018).

214. Leeb, F. & Maibaum, L. Spatially resolving the condensing effect of cholesterol in lipid bilayers. *Biophysical Journal* **115,** 2179–2188 (2018).

215. Pan, J., Cheng, X., Monticelli, L., Heberle, F. A., Kučerka, N., Tieleman, D. P. & Katsaras, J. The molecular structure of a phosphatidylserine bilayer determined by scattering and molecular dynamics simulations. *Soft Matter* **10,** 3716 (2014).

216. Skjevik, Å. A., Madej, B. D., Dickson, C. J., Lin, C., Teigen, K., Walker, R. C. & Gould, I. R. Simulation of lipid bilayer self-assembly using all-atom lipid force fields. *Physical Chemistry Chemical Physics* **18,** 10573–10584 (2016).

217. Rog, T. & Pasenkiewicz-Gierula, M. Cholesterol effects on the phospholipid condensation and packing in the bilayer: a molecular simulation study. *FEBS Letters* **502,** 68–71 (2001).

218. Doktorova, M., Heberle, F. A., Kingston, R. L., Khelashvili, G., Cuendet, M. A., Wen, Y., Feigenson, G. W., Vogt, V. M. & Dick, R. A. Cholesterol promotes protein binding by affecting membrane electrostatics and solvation properties. *Biophysical Journal* **113,** 2004–2015 (2017).

219. Venable, R. M., Luo, Y., Gawrisch, K., Roux, B. & Pastor, R. W. Simulations of anionic lipid membranes: development of Interaction-Specific ion parameters and validation using NMR data. *Journal of Physical Chemistry B* **117,** 10183–10192 (2013).

220. Bandara, A., Panahi, A., Pantelopulos, G. A. & Straub, J. E. Exploring the structure and stability of cholesterol dimer formation in multicomponent lipid bilayers. *Journal of Computational Chemistry* **38,** 1479–1488 (2016).

221. Elkins, M. R., Bandara, A., Pantelopulos, G. A., Straub, J. E. & Hong, M. Direct observation of cholesterol dimers and tetramers in lipid bilayers. *Journal of Physical Chemistry B* **125,** 1825–1837 (2021).

222. Ermilova, I. & Lyubartsev, A. P. Cholesterol in phospholipid bilayers: positions and orientations inside membranes with different unsaturation degrees. *Soft Matter* **15,** 78–93 (2019).

223. Dietrich, C., Bagatolli, L. A., Volovyk, Z., Thompson, N. L., Levi, M., Jacobson, K. A. & Gratton, E. Lipid rafts reconstituted in model membranes. *Biophysical Journal* **80,** 1417–1428 (2001).

224. Alvear-Arias, J. J., Peña-Pichicoi, A., Carrillo, C., Fernandez, M. a. L., Gonzalez, T., Garate, J. A. & Gonzalez, C. Role of voltage-gated proton channel (Hv1) in cancer biology. *Frontiers in Pharmacology* **14** (2023).

225. Banh, R. L., Cherny, V. V., Morgan, D., Musset, B., Thomas, S., Kulleperuma, K., Smith, S., Pomes, R. & DeCoursey, T. E. Hydrophobic gasket mutation produces gating pore currents in closed human voltage-gated proton channels. *Proceedings of the National Academy of Sciences of the United States of America* **116,** 18951–18961 (2019).

226. Bondar, A.-N. Proton-Binding motifs of Membrane-Bound proteins: from bacteriorhodopsin to spike protein s. *Frontiers in Chemistry* **9** (2021).

227. Lazaratos, M., Siemers, M., Brown, L. S. & Bondar, A.-N. Conserved hydrogen-bond motifs of membrane transporters and receptors. *Biochimica et Biophysica Acta (BBA) - Biomembranes* **1864,** 183896 (2022).

228. Musset, B., Smith, S., Rajan, S., Morgan, D., Cherny, V. V. & DeCoursey, T. E. Aspartate 112 is the selectivity filter of the human voltage-gated proton channel. *Nature* (2011).

229. DeCoursey, T. E. The Voltage-Gated Proton Channel: A Riddle, Wrapped in a Mystery, inside an Enigma. *Biochemistry* **54,** 3250–3268 (2015).

230. DeCoursey, T. E., Morgan, D., Musset, B. & Cherny, V. V. Insights into the structure and function of HV1 from a meta-analysis of mutation studies. *The Journal of General Physiology* **148,** 97–118 (2016).

231. Zhao, C., Luan, H., Riahi, S., Lim, V. T., Tobias, D. J. & Tombola, F. A novel Hv1 inhibitor reveals a new mechanism of inhibition of a voltage-sensing domain. *The Journal of General Physiology* **153** (2021).

232. Zhao, C., Luan, H., Galpin, J. D., Riahi, S., Lim, V. T., Webster, P. D., Tobias, D. J., Ahern, C. A. & Tombola, F. HIFs: New arginine mimic inhibitors of the Hv1 channel with improved VSD–ligand interactions. *The Journal of General Physiology* **153** (2021).

233. Zhang, Q., Ren, Y., Mo, Y., Guo, P., Liao, P., Luo, Y., Mei, J., Chen, Z., Zhang, Y., Li, Y., Yang, L., Liao, D., Fu, J., Shen, J., Huang, W., Xu, X., Guo, Y., Mei, L., Zuo, Y., Liu, J., Yang, H. & Jiang, R. Inhibiting Hv1 channel in peripheral sensory neurons attenuates chronic inflammatory pain and opioid side effects. *Cell Research* **32,** 461–476 (2022).

234. Boytsov, D., Brescia, S., Chaves, G., Koefler, S., Hannesschlaeger, C., Siligan, C., Goessweiner-Mohr, N., Musset, B. & Pohl, P. Trapped pore waters in the open proton channel $H_V1$. *bioRxiv (Cold Spring Harbor Laboratory)* (2022).

235. Van Keulen, S. C., Gianti, E., Carnevale, V., Klein, M. L., Röthlisberger, U. & Delemotte, L. Does Proton Conduction in the Voltage-Gated $H^+$Channel hHv1 Involve Grotthuss-Like Hopping via Acidic Residues? *Journal of Physical Chemistry B* **121,** 3340–3351 (2016).

236. Alabi, A. A., Bahamonde, M. I., Jung, H. C., Kim, J. I. & Swartz, K. J. Portability of paddle motif function and pharmacology in voltage sensors. *Nature* **450,** 370–375 (2007).

237. Luan, H., Kim, I. H. & Tombola, F. Molecular determinants of Hv1 proton channel inhibition by guanidine derivatives. *Proceedings of the National Academy of Sciences of the United States of America* **111,** 9971–9976 (2014).

238. Cherny, V. V., Morgan, D., Musset, B., Chaves, G., Smith, S. & DeCoursey, T. E. Tryptophan 207 is crucial to the unique properties of the human voltage-gated proton channel, hHV1. *The Journal of General Physiology* **146,** 343–356 (2015).

239. Cherny, V. V., Morgan, D., Thomas, S., Smith, S. & DeCoursey, T. E. Histidine168 is crucial for $\triangle$pH-dependent gating of the human voltage-gated proton channel, hHV1. *The Journal of General Physiology* **150,** 851–862 (2018).

240. Jardin, C., Ohlwein, N., Franzen, A., Chaves, G. & Musset, B. The pH-dependent gating of the human voltage-gated proton channel from computational simulations. *Physical Chemistry Chemical Physics* **24,** 9964–9977 (2022).

241. Li, S. J., Zhao, Q., Zhou, Q., Unno, H., Zhai, Y. & Sun, F. The role and structure of the carboxyl-terminal domain of the human voltage-gated proton Channel HV1. *Journal of Biological Chemistry* **285,** 12047–12054 (2010).

242. Luan, H., Singh, V., Wulff, H. & Tombola, F. Interrogation of the intersubunit interface of the open Hv1 proton channel with a probe of allosteric coupling. *Scientific Reports* **5** (2015).

243. Fujiwara, Y., Kurokawa, T. & Okamura, Y. Long $\alpha$ helices projecting from the membrane as the dimer interface in the voltage-gated H+ channel. *The Journal of General Physiology* **143,** 377–386 (2014).

244. Boonamnaj, P. & Sompornpisut, P. Insight into the Role of the Hv1 C-Terminal Domain in Dimer Stabilization. *Journal of Physical Chemistry B* **122,** 1037–1048 (2018).

245. Fujiwara, Y., Kurokawa, T., Takeshita, K., Kobayashi, M., Okochi, Y., Nakagawa, A. & Okamura, Y. The cytoplasmic coiled-coil mediates cooperative gating temperature sensitivity in the voltage-gated H+ channel Hv1. *Nature Communications* **3** (2012).

246. Mony, L., Stroebel, D. & Isacoff, E. Y. Dimer interaction in the Hv1 proton channel. *Proceedings of the National Academy of Sciences of the United States of America* **117,** 20898–20907 (2020).

247. Okuda, H., Yonezawa, Y., Takano, Y., Okamura, Y. & Fujiwara, Y. Direct Interaction between the Voltage Sensors Produces Cooperative Sustained Deactivation in Voltage-gated H+ Channel Dimers. *Journal of Biological Chemistry* **291,** 5935–5947 (2016).

248. Zheng, H., Liu, W., Anderson, L. & Jiang, Q. X. Lipid-dependent gating of a voltage-gated potassium channel. *Nature Communications* **2** (2011).

249. Jiang, Q. X. & Gonen, T. The influence of lipids on voltage-gated ion channels. *Current Opinion in Structural Biology* **22,** 529–536 (2012).

250. Xu, Y., Ramu, Y. & Lü, Z. Removal of phospho-head groups of membrane lipids immobilizes voltage sensors of K+ channels. *Nature* **451,** 826–829 (2008).

251. Schmidt, D. R., Jiang, Q. X. & MacKinnon, R. Phospholipids and the origin of cationic gating charges in voltage sensors. *Nature* **444,** 775–779 (2006).

252. Ramu, Y., Xu, Y. & Lü, Z. Enzymatic activation of voltage-gated potassium channels. *Nature* **442,** 696–699 (2006).

253. Noble, J. M., Thomas, T. & Ford, G. A. Effect of age on plasma membrane asymmetry and membrane fluidity in human leukocytes and platelets. *The Journals of Gerontology* **54,** M601–M606 (1999).

254. Sakata, S., Kurokawa, T., Nørholm, M. H. H., Takagi, M., Okochi, Y., Von Heijne, G. & Okamura, Y. Functionality of the voltage-gated proton channel truncated in S4. *Proceedings of the National Academy of Sciences of the United States of America* **107,** 2313–2318 (2009).

255. Crooks, G. E., Hon, G. C., Chandonia, J.-M. & Brenner, S. E. WebLogo: A sequence Logo Generator: Figure 1. *Genome Research* **14,** 1188–1190 (2004).

256. Schneider, T. D. & Stephens, R. M. Sequence logos: a new way to display consensus sequences. *Nucleic Acids Research* **18,** 6097–6100 (1990).

257. Ritzel, R. M., He, J., Li, Y., Cao, T., Khan, N., Shim, B., Sabirzhanov, B., Aubrecht, T. G., Stoica, B. A., Faden, A. I., Wu, L. & Wu, J. Proton extrusion during oxidative burst in microglia exacerbates pathological acidosis following traumatic brain injury. *Glia* **69,** 746–764 (2020).

258. Murugan, M., Zheng, J., Wu, G., Mogilevsky, R., Zheng, X., Hu, P., Wu, J. & Wu, L. The voltage-gated proton channel Hv1 contributes to neuronal injury and motor deficits in a mouse model of spinal cord injury. *Molecular Brain* **13** (2020).

259. Lishko, P. V. Contraception: Search for an ideal unisex mechanism by targeting ion channels. *Trends in Biochemical Sciences* **41,** 816–818 (2016).

260. Musset, B., Clark, R. A., DeCoursey, T. E., Petheő, G. L., Geiszt, M., Chen, Y., Cornell, J. E., Eddy, C. A., Brzyski, R. G. & Jamali, A. E. NOX5 in human spermatozoa. *Journal of Biological Chemistry* **287,** 9376–9388 (2012).

261. Li, W., Ward, R., Dong, G., Ergul, A. & O'Connor, P. Neurovascular protection in voltage-gated proton channel Hv1 knock-out rats after ischemic stroke: interaction with $Na^{+}$ /$H^{+}$ exchanger-1 antagonism. *Physiological Reports* **7** (2019).

262. Wu, L. J., Wu, G., Sharif, M. R., Baker, A. M., Jia, Y., Fahey, F. H., Luo, H., Feener, E. P. & Clapham, D. E. The voltage-gated proton channel Hv1 enhances brain damage from ischemic stroke. *Nature Neuroscience* **15,** 565–573 (2012).

263. Tang, D., Yang, Y., Zhang, X., Xu, J., Yang, Q., Han, D., Liang, S., Tang, C., Dong, H. & Z, L. Scorpion toxin inhibits the voltage-gated proton channel using a $Zn^{2+}$ -like long-range conformational coupling mechanism. *British Journal of Pharmacology* **177,** 2351–2364 (2020).

264. Luan, H., Pathak, M. A., Kim, I. H., Ta, D. T. & Tombola, F. Voltage-Sensing Domain of Voltage-Gated Proton Channel Hv1 Shares Mechanism of Block with Pore Domains. *Neuron* **77,** 274–287 (2013).

265. Lim, V. T., Geragotelis, A. D., Lim, N. M., Freites, J. A., Tombola, F., Mobley, D. L. & Tobias, D. J. Insights on small molecule binding to the Hv1 proton channel from free energy calculations with molecular dynamics simulations. *Scientific Reports* **10** (2020).

266. Agarwal, R. & Smith, J. C. Speed vs Accuracy: Effect on Ligand Pose Accuracy of Varying Box Size and Exhaustiveness in AutoDock Vina. *Molecular Informatics* **42** (2022).

267. Bouysset, C. & Fiorucci, S. ProLIF: a library to encode molecular interactions as fingerprints. *Journal of Cheminformatics* **13** (2021).

268. Berger, T. & Isacoff, E. Y. The pore of the Voltage-Gated proton channel. *Neuron* **72,** 991–1000 (2011).

269. Morgan, D., Cherny, V. V., Finnegan, A., Bollinger, J., Gelb, M. H. & DeCoursey, T. E. Sustained activation of proton channels and NADPH oxidase in human eosinophils and murine granulocytes requires PKC but not cPLA$_{2}\alpha$ activity. *The Journal of Physiology* **579,** 327–344 (2007).

270. Sievers, F., Wilm, A., Dineen, D., Gibson, T. J., Karplus, K., Li, W., Lopez, R., McWilliam, H., Remmert, M., Söding, J., Thompson, J. & Higgins, D. G. Fast, scalable generation of high-quality protein multiple sequence alignments using Clustal Omega. *Molecular Systems Biology* **7** (2011).

271. Bertalan, e., Lesca, E., Schertler, G. & Bondar, A.-N. C-Graphs Tool with Graphical User Interface to Dissect Conserved Hydrogen-Bond Networks: Applications to Visual Rhodopsins. *Journal of Chemical Information and Modeling* **61,** 5692–5707 (2021).

# Selbstständigkeitserklärung

Name: Honey
Vorname: Jain

Ich erkläre gegenüber der Freien Universität Berlin, dass ich die vorliegende Dissertation selbstständig und ohne Benutzung anderer als der angegebenen Quellen und Hilfsmittel angefertigt habe. Die vorliegende Arbeit ist frei von Plagiaten. Alle Ausführungen, die wörtlich oder inhaltlich aus anderen Schriften entnommen sind, habe ich als solche kenntlich gemacht. Diese Dissertation wurde in gleicher oder ähnlicher Form noch in keinem früheren Promotionsverfahren eingereicht. Mit einer Prüfung meiner Arbeit durch ein Plagiatsprüfungsprogramm erkläre ich mich einverstanden.

Datum:

Unterschrift: